Dilute Nitride Semiconductors

Band Structure, Scattering and High Field Transport

Masoud Seifikar
Msc in Physics
108111383

NATIONAL UNIVERSITY OF IRELAND, CORK
Department of Physics
Tyndall National Institute

Thesis submitted for the degree of Doctor of Philosophy

September 2013

Supervisors: Prof. Eoin P. O'Reilly
Prof. Stephen Fahy
Head of Department/School: Prof. John McInerney

Research supported by Science Foundation Ireland

Contents

Acknowledgements . . . vii
Abstract . . . ix

1 Introduction 1
1.1 Motivation and background . . . 1
1.2 Thesis structure . . . 3

2 Review of prior research 7
2.1 Introduction . . . 7
2.2 Band structure . . . 7
2.2.1 BAC model . . . 8
2.2.2 LCINS model . . . 9
2.2.3 Green's function method . . . 11
2.3 Mobility and scattering . . . 13
2.3.1 Carrier mobility . . . 13
2.3.2 Resonant scattering . . . 15
2.4 High field transport . . . 16
2.5 Summary . . . 19

3 Band anti-crossing model 21
3.1 Introduction . . . 21
3.2 Two-level BAC model . . . 22
3.2.1 Fractional Γ character . . . 24
3.2.2 Density of states . . . 25
3.2.3 The DOS projected to a single k state . . . 27
3.2.4 The band dispersion . . . 28
3.3 Three-level BAC model . . . 29
3.3.1 The DOS in the 3-level model . . . 31
3.3.2 Band dispersion in the 3-level model . . . 32
3.4 The LCINS model . . . 33
3.4.1 The DOS in the LCINS model . . . 34
3.4.2 The band dispersion in the LCINS model . . . 35
3.5 Summary . . . 36

4 Supercell model 37
4.1 Introduction . . . 37
4.2 Supercell model . . . 37
4.3 Fractional Γ character . . . 39
4.4 Density of states . . . 40
4.4.1 The DOS projected to a single state . . . 40
4.4.2 Density of states projected to CB . . . 42
4.4.3 Total density of states . . . 44
4.5 Participation ratio . . . 45
4.6 Summary . . . 46

5 Self-consistent Green's function method **47**
5.1 Introduction . . . 47
5.2 Self-consistent Green's function method . . . 49
5.2.1 The density of states . . . 51
5.3 The two-level SCGF . . . 52
5.3.1 The DOS for the two-level SCGF model . . . 53
5.3.2 Fractional Γ character . . . 60
5.3.3 Total density of states . . . 61
5.4 The LCINS model . . . 62
5.4.1 The DOS for the LCINS model . . . 63
5.4.2 Total density of states . . . 65
5.5 Band structure . . . 66
5.6 Discussion and conclusions . . . 68

6 Intermediate and high field mobility **71**
6.1 Introduction . . . 71
6.2 Band structure of GaN_xAs_{1-x} . . . 74
6.3 Transport calculation method . . . 75
6.3.1 Boltzmann equation . . . 75
6.3.2 Scattering processes . . . 77
6.3.2.1 Nitrogen scattering . . . 77
6.3.2.2 Polar optical scattering . . . 78
6.3.2.3 Intervalley scattering . . . 79
6.3.2.4 Acoustic phonon scattering . . . 80
6.3.3 Transport calculation method . . . 81
6.4 Transport results . . . 84
6.4.1 Carrier energy distribution . . . 84
6.4.2 Electron mobility and drift velocity: parabolic band model 86
6.4.3 Electron mobility and drift velocity: BAC model . . . 90
6.5 Discussion and conclusions . . . 94

7 Band dispersion, scattering rate and carrier mobility using the poles of the Green's function **97**
7.1 Introduction . . . 97
7.2 The poles of the SCGF . . . 98
7.2.1 The self-consistent Green's function method . . . 98
7.3 The two-band model . . . 99
7.3.1 Complex eigenvalue method of finding the poles in the 2-band model . . . 100
7.3.1.1 Exact solution for localised state with Lorentzian inhomogeneous broadening . . . 103
7.3.2 The dispersion relation . . . 104
7.3.3 Fractional Γ character . . . 104
7.3.4 Group velocity . . . 106
7.4 The LCINS model . . . 108
7.4.1 The complex eigenvalue method . . . 108

7.4.2 The band dispersion calculated using the complex eigenvalue method . . . 109
7.4.3 Fractional Γ character . . . 111
7.4.4 Group velocity . . . 113
7.5 Scattering rate . . . 114
7.6 Carrier mobility . . . 117
7.7 Discussion and conclusions . . . 120

8 Absorption spectrum of dilute nitride alloys 123
8.1 Introduction . . . 123
8.2 Absorption spectrum . . . 124
8.3 Optical absorption for III-V semiconductors . . . 126
8.3.1 CB nonparabolicity using the Kane model . . . 127
8.3.2 LH band non-parabolicity . . . 128
8.3.3 The joint density of states . . . 130
8.4 Optical absorption of dilute nitride alloys . . . 131
8.4.1 Five-level BAC model . . . 132
8.4.2 The LCINS model . . . 135
8.5 Results for $In_yGa_{1-y}N_xAs_{1-x}$ . . . 136
8.5.1 5-level model . . . 136
8.5.2 LCINS approach . . . 140
8.6 The absorption spectrum for GaN_xSb_{1-x} . . . 143
8.6.1 Absorption spectrum in the 5-level BAC model . . . 144
8.6.2 Absorption spectrum in the LCINS model . . . 146
8.7 Summary . . . 149

9 Conclusions and further work 151
9.1 Conclusions . . . 151
9.2 Future work . . . 154

A Calculating the fractional Γ character 157

B Iterative search method for finding the poles of GF 159
B.1 The two-band model . . . 160
B.2 The LCINS method . . . 161

C Contribution of individual poles of G_{nn} to the density of states 163

D The real and imaginary parts of $\gamma(E)$ and the decay rate of momentum states. 165

I, Masoud Seifikar, certify that this thesis is my own work and I have not obtained a degree in this university or elsewhere on the basis of the work submitted in this thesis.

Masoud Seifikar

To Shirin, Ryan

& my parents

Acknowledgements

First and foremost, I would like to express my sincere gratitude to my supervisors Prof. Eoin P. O'Reilly and Prof. Stephen Fahy. I am very much thankful to Prof. O'Reilly for his patience, enthusiasm, motivation, support and immense knowledge. His professional guidance has made the last five years such an amazing and unforgettable experience for me. Not only a great scientific supervisor he has also been a valuable caring adviser for me. I have been very fortunate to have Prof. Fahy as my co-supervisor who I never met without learning something interesting. I am thankful to him for his excellent guidance, constant encouragement, brilliant ideas and patience during the entire course of my Ph.D.

I appreciate all the support and help from Mary O'Regan, our lovely administrator in Theory, Modelling and Design Centre. I wish to thank my great colleague Dr. Martin Vaughan for helpful comments and discussions. I convey my gratefulness to Dr. Andreas Amann for very useful and constructive discussions and also for his generous supports. I am thankful to Chris Broderick, Stefan Schulz, Muhammad Usman, Nicola Brandonisio, Miguel CaroBayo, Oliver Marquardt and Conor Coughlan, members of Photonics Theory Group for all valuable discussions that we have had in our group meetings. Many thanks to the former and current members of Materials Theory Group; Philip Murphy, Mark Hartnett, Siobhan O'Halloran, John Buckeridge and Anna Hauber. I am extremely indebted to Andrew Lindsay for using the results of his tight-binding-based calculations. I wish his soul rests in peace and solace in the heaven.

It is a pleasure to express special thanks and appreciation to my examiners, Prof Judy Rorison and Dr. Martin Vaughan for their time in reading my thesis and for the stimulating discussions during my viva voce.

I also thank my friends especially (too many to list here but you know who you are) for providing support and friendship. I especially thank my family for all their love and encouragement; my parents who always believed, and supported me in every stage of my personal and academic life, and my brothers and sister for supporting me spiritually throughout my life.

And most of all my beloved wife Shirin, who has been by my side since 10 years ago and throughout this PhD, living every minute of it, and without whom, I would not have had the courage to embark on this journey in the first place. And to darling Ryan for being such a good little baby in the past four months, and making it possible for me to complete what I started.

Abstract

The substitution of a small fraction x of nitrogen atoms, for the group V elements in conventional III-V semiconductors such as GaAs and GaSb strongly perturbs the conduction band of the host semiconductor. In this thesis we investigate the effects of nitrogen states on the band dispersion, carrier scattering and mobility of dilute nitride alloys.

In the supercell model we solve the single particle Hamiltonian for a very large supercell containing randomly placed nitrogen. This model predicts a gap in the density of states of GaN_xAs_{1-x}, where this gap is filled in the Green's function model. Therefore we develop a self-consistent Green's function (SCGF) approach, which provides excellent agreement with supercell calculations and reveals a gap in the DOS, in contrast with the results of previous non-self-consistent Green's function calculations. However, including the distribution of N states destroys this gap, as seen in experiment.

We then examine the high field transport of carriers by solving the steady-state Boltzmann transport equation and find that it is necessary to include the full distribution of N levels in order to account for the small, low-field mobility and the absence of a negative differential velocity regime observed experimentally with increasing x. Overall the results account well for a wide range of experimental data.

We also investigate the band structure, scattering and mobility of carriers by finding the poles of the SCGF, which gives lower carrier mobility for GaN_xAs_{1-x}, compared to those already calculated, in better agreement with experiments. The calculated optical absorption spectra for $In_yGa_{1-y}N_xAs_{1-x}$ and GaN_xSb_{1-x} using the SCGF agree well with the experimental data, confirming the validity of this approach to study the band structure of these materials.

List of my Publications

[1] M. Seifikar, E. P. O'Reilly, and S. Fahy. Analysis of band-anticrossing model in GaNAs near localised states. *Physica Status Solidi B*, 248:1176–1179, 2011.

[2] M. Seifikar, E. P. O'Reilly, and S. Fahy. Theory of intermediate- and high-field mobility in dilute nitride alloys. *Physical Review B*, 84:165216, Oct 2011.

[3] M. Seifikar, E. P. O'Reilly, and S. Fahy. Self-consistent Green's function method for dilute nitride conduction band structure. *Journal of Physics: Condensed Matter*, Submitted.

[4] M. Seifikar, E. P. O'Reilly, and S. Fahy. The poles of Green's function method for alloy scattering and mobility in dilute nitride conduction band. *Physical Review B*, To be submitted.

[5] M. Seifikar, E. P. O'Reilly, and S. Fahy. Absorption spectrum of dilute nitride alloys. preprint.

Chapter 1

Introduction

1.1 Motivation and background

The band structure and physical properties of semiconductors can be engineered by alloying these materials. Such alloys have been widely used in the development and improvement of electronic and optoelectronic devices. Most such alloys are well described using the virtual crystal approximation where the properties of the materials evolve smoothly, in a linear or close to linear fashion as the composition is varied.

In the last twenty years, dilute nitrite semiconductor alloys have been a topic of intense scientific research and technological developments ever since they were discovered, because of their peculiar electronic and physical properties and potential device applications. The substitution of dilute amounts of nitrogen atoms for the group V elements in conventional III-V semiconductors such as GaAs or GaInAs strongly disturbs the conduction band (CB) of the host semiconductor, in a way which is markedly different from what will be expected using the virtual crystal approximation. This allows one to strongly modify and tailor the band structure of these semiconductors, leading to the development of novel optoelectronic devices such as light emitting diodes, edge emitting lasers, solar cells, photo detectors, and modulators [1–3].

When a small fraction of arsenic in GaAs is replaced by nitrogen to form GaN_xAs_{1-x} the energy gap decreases rapidly by about 100 meV per % of N for $x < 3\%$ [4]. This behaviour is markedly different to conventional semiconductors, and is of interest both from a fundamental perspective and because of its significant potential device applications. As an example, the strong bowing opens the possibility of using GaInNAs to get optical emission on a GaAs substrate at the technologically important wavelengths of 1.3 and 1.55 μm, considerably expand-

ing the capabilities of GaAs for optoelectronics devices [3]. In 1996 M. Kondow *et al.* [5] proposed GaInAsN as a material for long wavelength emission on GaAs. These new semiconductors offer device engineers new design opportunities for a new generation of electronic and optoelectronic devices.

The unusual electronic properties of Ga(In)NAs arise because of the marked difference between nitrogen and arsenic atoms: N is considerably more electronegative, and the equilibrium Ga-N bond length is 20% shorter than that of GaAs. This strong difference has far-reaching consequences, and underpins many features of dilute nitride alloys.

Significant progress has been achieved in understanding the electronic structure of dilute nitrides, and several theoretical approaches have been used to describe the electronic band structure of nitrogen-containing III-V compounds [6]. It is well established that because of the large difference in electronegativity and atomic size between N and As, when a single N atom replaces an As atom in GaAs, it forms a resonant defect level above the conduction band edge (CBE) of GaAs [7, 8]. A major breakthrough was achieved by Shan *et al.* [9] who demonstrated that the reduction in energy gap in dilute nitride alloys is due to a band anti-crossing (BAC) interaction between the conduction band edge of the host semiconductor material and these localised N impurity states.

The BAC model provides a good qualitative explanation of the band structure of dilute nitride alloys, but it is in many cases necessary to include the details of the distribution of N-related defect levels to obtain a quantitative understanding of the conduction band structure in dilute nitride alloys. In practice, replacing As by N introduces a range of N-related defect levels, associated with isolated N atoms, N-N pairs, where a group III atom has two N neighbours, and larger clusters of N atoms. In has been shown that the effect of such defect levels on the alloy conduction band structure is strongly dependent on the relative energy of the defect levels and the host conduction band edge [10, 11].

The incorporation of nitrogen into III-V materials is also known to cause a large drop in the electron mobility [12, 13]. In addition to the scattering from nitrogen states, the conduction band becomes highly non-parabolic, which further affects the transport properties. Adams proposed that a suppression of the electron ionisation rate might be possible in avalanche photodiodes, due to the strong perturbation by N states that could limit the ability of electrons to gain higher energy from an applied electric field in GaNAs [14]. Moreover, a strong negative differential velocity has been predicted and observed at high electric fields for GaN_xAs_{1-x} with very low N composition, x [15]. Recent Monte Carlo calcula-

tions [16] also confirms negative differential velocity at very low N compositions ($x \leq 0.2\%$).

1.2 Thesis structure

In this thesis we explore the electronic structure, scattering and high field transport of carriers in GaN_xAs_{1-x} alloys. First a review of the relevant background to this work is presented in Chapter 2. This chapter begins with an overview the current models to explain the influence of the introduction of N atoms in the band structure of the dilute nitride alloys. We first review the band-anticrossing model to describe the conduction band structure. We then discuss that there are in practice a distribution of N-related states in GaNAs, which can be described using a Linear Combination of Isolated Nitrogen States (LCINS) model [11, 17]. We then describe the Green's function approach to calculate the electronic structure. Then we describe some experiments that reported a dramatic reduction in the carrier mobility of GaN_xAs_{1-x} alloys, and review the main suggested models to understand carrier scattering and mobility in these materials. We also briefly mention some experiments that observed negative differential velocity at high field for samples containing small fraction of N, x.

Then in chapters 3 to 5 we investigate the band structure of dilute nitride alloys as a requirement to study the hot-electron, mobility and drift velocity in high electric fields in Chapter 6. We modify and develop the BAC and Green's function models in Chapter 3. The Green's function approach proposed by Wu *et al.* [18] predicts that the nitrogen state energies acquire an imaginary component, interpreted as an energy broadening, which is omitted in the usual BAC model. We introduce this N broadening by considering a complex N state energy E_N in the BAC model in Chapter 3. Moreover the usual BAC model is oversimplified as it assumes that all N atoms have the same energy E_N, and ignores a range of resonant defect level close to the conduction band edge. We modify this model in Chapter 3 by including N-N pairs and larger clusters of localised N states. Also we consider the shift in the N state energies due to their interaction with the CB states, and calculate the density of states (DOS) and band dispersion of GaN_xAs_{1-x} alloys.

In order to examine the accuracy of these models we undertake supercell calculations in Chapter 4, where by using the Anderson impurity model we directly solve a simplified random impurity model Hamiltonian for a very large GaAs supercell, and calculate the exact eigenstates of this Hamiltonian. To simplify this

model we ignore the distribution of N states and assume all the N atoms have the same energy, E_N. Thereafter we compare the band structure and the density of states of GaNAs alloys in the supercell, with those obtained using the BAC and Green's function models. This comparison confirms the validity of the BAC model at energies away from N state energies but highlights some disagreements close to the N energy, E_N. The supercell model predicts a gap in the DOS of GaN_xAs_{1-x} alloys, where this gap is filled in the Green's function and the modified BAC models. These results suggest a deeper investigation of the energy broadening model used in the Green's function approach.

Therefore, in Chapter 5 we introduce a self-consistent Green's function (SCGF) method by introducing an energy-dependent complex energy $\Delta E_j(E)$, where the imaginary and real parts of $\Delta E_j(E)$ indicate the broadening and shift in energy, respectively. This model gives a very good agreement with the results of the supercell calculations, including in the energy range close to E_N. In this chapter we also consider the effects of a distribution of N-related defect levels in the band structure by using the LCINS model. This model considers the interaction between nitrogen atoms on nearby sites leading to inhomogeneous broadening and a distribution of localised state energies. We examine the consequences of this distribution on the density of states and band structure of dilute nitride alloys. We show that it has several significant effects including a filling of the gap in the DOS of GaN_xAs_{1-x} alloys.

Having provided a clear picture of the band structure and the density of states of GaNAs alloys, we study in Chapter 6 the scattering and high field transport, by solving the steady-state Boltzmann transport equation in bulk GaN_xAs_{1-x}. Two different models of the CB structure have been studied to investigate the behaviour of electrons with increasing electric field in GaN_xAs_{1-x} alloys: (1) carriers in parabolic Γ and L bands are scattered by resonant nitrogen states, polar optic and acoustic phonons, and intervalley optical phonons; (2) carriers confined in the lower band of the BAC model are scattered by N states and by optical phonons. We consider scattering both by isolated N states and by a full LCINS distribution of N states. We conclude that it is necessary to include the full distribution of N states in order to account for the small low-field mobility and the absence of a negative differential velocity regime observed experimentally with increasing x. We note that the BAC model with carriers constrained to the lower BAC sub-band fails at high electric field as it does not allow carriers to accelerate to higher energies.

Chapter 7 aims to develop a more complete model to calculate the band

structure, scattering and mobility of bulk dilute nitride alloys by finding the poles of the Green's function. In this chapter we calculate the complex poles of the Green's function in a self-consistent manner, where we use its imaginary and real parts to calculate the scattering rate and band dispersion of carriers, respectively. Then we use the band dispersion and scattering rates to determine the carrier mean free path and mobility using the Boltzmann Transport Equation. Our results for low field mobility in Chapter 7 show a better agreement than were obtained in Chapter 6, because the model used in Chapter 7 considers the effects of nitrogen states on both the band dispersion and carrier scattering.

Then in Chapter 8 we benchmark the methods we have developed by calculating the optical absorption coefficient for InGANAs and GaNSb alloys, using the BAC and LCINS model, and comparing the results with experimental data. We consider two models for the band structure of dilute nitride alloys: (1) the BAC model including isolated and pair N levels interacting with the host matrix conduction, light hole and spin orbit split-off band; (2) the SCGF method to include the full distribution of localised state calculated using the LCINS approach, including non-parabolic CB and light hole, and parabolic heavy hole and split-off bands. The first model accounts for many features of the absorption coefficient spectrum in comparison with experiments on InGaNAs alloys; including the LCINS distribution improves this agreement. Our calculated absorption spectra for GaNSb alloys predict the band edges correctly, but show more features than seen experimentally. This suggests the presence of more disorder in GaNSb alloys in comparison with InGaNAs.

Finally in Chapter 9 we summarise our conclusions and discuss possible future works.

Chapter 2

Review of prior research

2.1 Introduction

The aim of this chapter is to provide an overview of the background theory of dilute nitride semiconductors relevant to this thesis. We start with the band structure of dilute nitride alloys, and the current models to treat the effect of substitutional nitrogen atoms in GaNAs. We begin, in § 2.2 by giving an overview of the band anticrossing (BAC), **L**inear **C**ombination of **I**solated **N**itrogen **S**tates (LCINS) and Green's function methods that have already been applied to explain the electronic structure of GaNAs alloys. Then in § 2.3 we first briefly discuss the prior carrier mobility measurements of GaNAs alloys that have shown a significant reduction of mobility in these alloys in comparison with GaAs. This is followed by a brief overview of the models which have been introduced to explain this remarkable decrease of electron mobility in dilute nitride semiconductors. Finally we review, in § 2.4, the research that has been performed on high field transport in dilute nitride alloys.

2.2 Band structure

The electronic structure of dilute nitride alloys has attracted considerable interest, both from a fundamental perspective and also because of their potential device application. Substituting a small fraction of the group V atoms by nitrogen, N, strongly perturbs the conduction band of III-VN materials. For instance, replacing a small fraction of As atoms by N introduces a series of N-related defect states into the conduction band (CB) of GaAs, and the energy gap initially decreases rapidly, at about 0.1 eV per percent of N for $x < 0.03$ [4]. A number of theoretical models have been introduced to explain the behaviour of these

materials, of which the simplest one is the two-level band anti-crossing model, as described in the next section.

2.2.1 BAC model

It is well known that the substitution of an As atoms by a single N atom, in GaAs, forms a resonant defect level above the conduction band edge (CBE) of GaAs [7]. The BAC model introduced by Walukiewicz and co-workers explains the extreme band gap bowing observed in $Ga_{1-y}In_yAs_{1-x}N_x$ in terms of an interaction between two levels, one at energy E_N associated with localised isolated N impurity states ψ_N, and the other at energy E_c associated with the extended CBE state ψ_{c0} of the GaInAs matrix, with the two states linked by a matrix element V_{Nc} describing the interaction between them [9]. The conduction band dispersion of $GaInAs_{1-x}N_x$ is then given in the BAC model by the eigenvalues of the determinant equation

$$\begin{vmatrix} E_N(x) - E & V_{Nc} \\ V_{Nc} & E_c(x) + \dfrac{\hbar^2 k^2}{2m^*} - E \end{vmatrix} = 0, \tag{2.1}$$

where the interaction V_{Nc} between the host matrix CBE and the N state increases with N concentration as $V_{Nc} = \beta x^{1/2}$ [19], β is a constant parameter, and m^* is an appropriately chosen band edge effective mass for the Ga(In)As host matrix material [20].

Figure 2.1 shows as an example the band structure of $GaN_{0.005}As_{0.995}$, where the interaction of the CB of GaAs, E_k, with the nitrogen state energy, E_N, splits the host semiconductor CB into two sub-bands E_- and E_+. The bottom of the lower band, $E_-(k)$, is pushed down to lower energy and the minimum of the upper band, $E_+(k)$, is pushed up with increasing x. Here we have taken $E_N = (1.56 - 0.22x)$ eV, $E_c = (1.42 - 3.5x)$ eV and $\beta = 2.0$ eV, based on the parameter values given in [21].

The BAC model explains many features of the electronic structure, including the strong reduction in energy gap in GaN_xAs_{1-x} with increasing x [9], the band dispersion close to and above the CBE in samples with very low N composition [22], and the measured increase in band edge effective mass in GaInAsN alloys [20]. However, because it omits the full energy distribution of N states, it fails to explain the further enhancement and non-monotonic variation of the band edge mass with x in GaN_xAs_{1-x} for $x \geq 0.05\%$ [6, 23, 24]. The BAC model is oversimplified, because it ignores the detail of the distribution of N states which are present in actual GaNAs samples, as will be discussed in the next section.

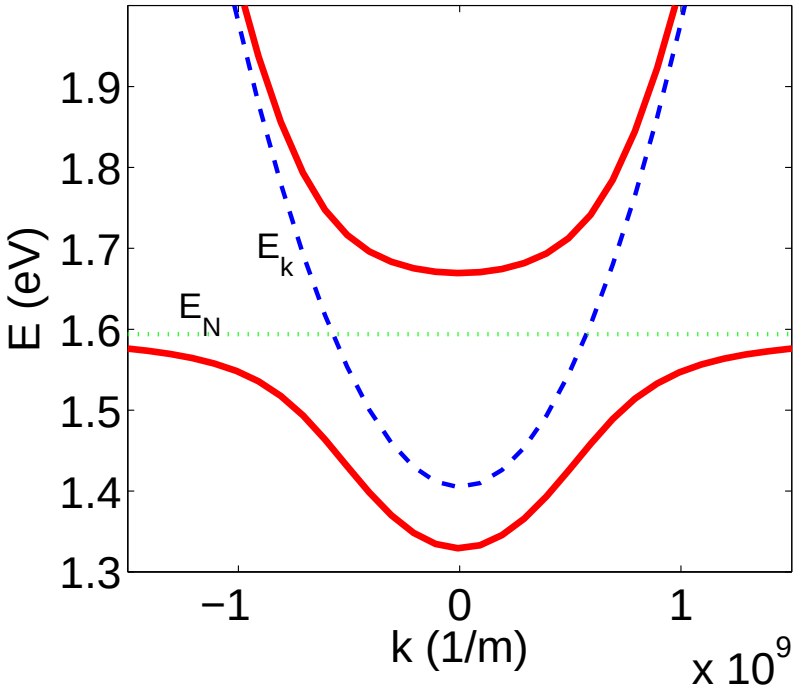

Figure 2.1: Dispersion relation for GaN_xAs_{1-x} with $x = 0.5\%$, calculated by BAC model of Eq. (2.1). E_k and E_N show the host semiconductor and nitrogen energies, respectively.

More details of the BAC model and how it can be modified to treat a range of different N defect states will be presented in chapter. 3.

2.2.2 LCINS model

O'Reilly, Lindsay and Fahy have previously used a tight-binding-based model to calculate the distribution of N states expected in random GaNAs alloys, treating explicitly the interactions between a **L**inear **C**ombination of **I**solated **N**itrogen **S**tates (LCINS) in this model [11, 17]. These interactions lead to a mixing between the different N states and a broadening of the N spectral energy (E_{Nj} no longer just equal to E_N) and of the interaction values V_{Nc}. In addition, the number of N pair and cluster states increases with N composition x. The pair states have energy close to E_{NN}, the energy of an isolated N pair, where a N pair is formed when two of a Ga atom's nearest neighbours are N atoms [21]. The density of localised N states calculated by the LCINS approach, weighted by $|V_j|^2/N_c$ (where N_c is the number of primitive cells in the system and V_j is the interaction matrix element of state j with the CBE), is shown in Fig. 2.2 for GaN_xAs_{1-x} several different values of nitrogen composition x.

It has been previously shown that use of this full distribution of N states can

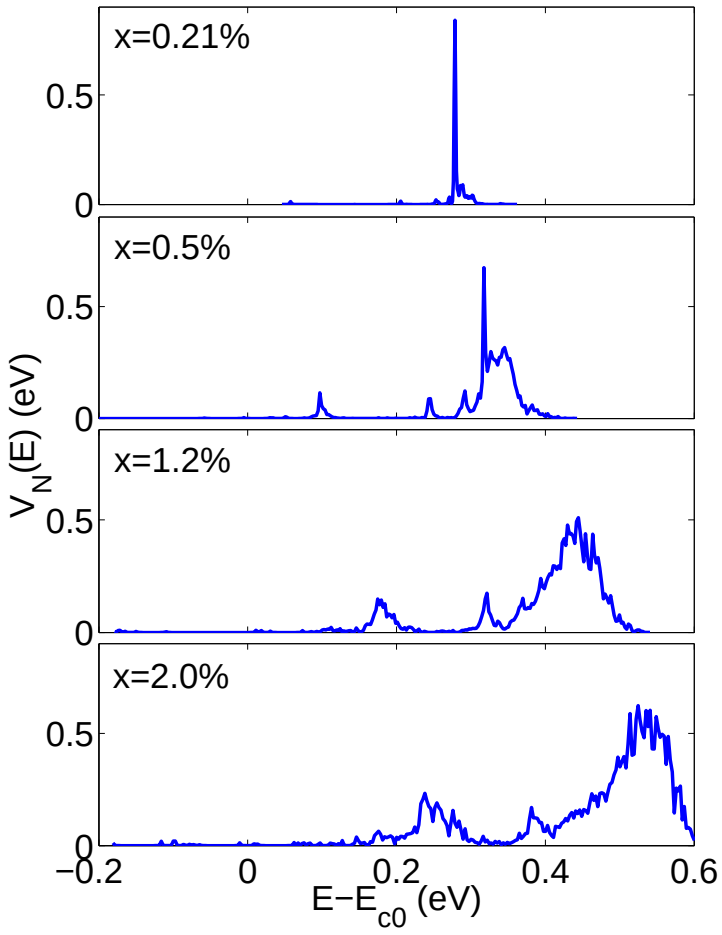

Figure 2.2: Calculated distribution of localised LCINS states, weighted by their interaction $|v_j|^2/N_c$ for each state, versus their energies respect to the conduction band edge of the host semiconductor, for GaN_xAs_{1-x} with $x = 0.21, 0.5, 1.2$ and 2.0%. Each energy level is broadened to a Gaussian of width 1 meV [13].

account very successfully for the non-monotonic variation of electron band edge mass with N composition x [25] and with hydrostatic pressure [26, 27], as well as the anomalous behaviour of the electron gyromagnetic ratio as a function of composition x [28] and the conduction band density of states projected onto the GaAs host matrix states [29]. It should therefore also provide a good description of the conduction band dispersion. In later chapters of this thesis we will employ the LCINS model, which includes a full distribution of N states, as well as the BAC model to investigate the density of states and transport properties for a range of dilute nitride alloys.

2.2.3 Green's function method

Because the "localised" N states in GaN_xAs_{1-x} are degenerate with the host CB matrix states, it should be expected that they behave as resonant states, with an associated resonant broadening. This broadening is omitted in the BAC model but can be considered by using the many impurity Anderson model.

In the many impurity Anderson model, the Hamiltonian for a set of localised N states interacting with the host matrix conduction band states can be written as

$$H = H_0 + V, \tag{2.2}$$

where H_0 is a sum of two terms describing the energies of extended and localised states, labeled by wave vector $|\mathbf{k}\rangle$ and position vector $|j\rangle$

$$H_0 = \sum_{\mathbf{k}} E_{\mathbf{k}} |\mathbf{k}\rangle\langle\mathbf{k}| + \sum_{j=1}^{M} E_j |j\rangle\langle j|, \tag{2.3}$$

where $E_{\mathbf{k}}$ and E_j are the energies of the host matrix CB states with wave vector $\mathbf{k}$, and of the j-th N state, respectively. The interaction between extended and localised states is given by

$$V = \sum_{\mathbf{k},j} \frac{1}{\sqrt{N_c}} \Big[V_{\mathbf{k}j} e^{i\mathbf{k}.\mathbf{R}_j} |\mathbf{k}\rangle\langle j| + V^*_{\mathbf{k}j} e^{-i\mathbf{k}.\mathbf{R}_j} |j\rangle\langle\mathbf{k}| \Big], \tag{2.4}$$

where N_c is the number of primitive cells in the system, $\mathbf{R}_j$ is the position of the j-th N atom, and $V_{\mathbf{k}j}$ is describing the interaction between the j-th N state and the k-h host matrix state. It can be assumed that the $\mathbf{k}$ dependence of the interaction term is weak, and so it can be written as V_j [30]. Assuming all the localised states have the same energy and using Anderson's many-impurity model in the coherent potential approximation [31], Wu *et al.* [18] derived the solutions of the Hamiltonian in Eq. (2.2) in terms of the Green's function

$$G_{kk} = \left\{ E - E_k - \frac{\beta^2 x}{E - E_N - i\Delta_N} \right\}^{-1}, \tag{2.5}$$

where $\Delta_N = \eta\pi\beta^2 D_0(E_N)$ is the broadening of E_N in the single-impurity Anderson model, and $D_0(E_N)$ is the unperturbed density of states at E_N. In this approximation, they used a prefactor η where value was chosen by comparison with absorption coefficient measurements to be $\eta = 0.22$. Including the broadening

Δ_N, Eq. (2.1) becomes

$$\begin{vmatrix} E_N(x) + i\Delta_N - E & V_{Nc} \\ V_{Nc} & E_k(x) - E \end{vmatrix} = 0. \tag{2.6}$$

When $\Delta_N = 0$, the eigenvalues of this equation are given by

$$E_{\pm}(k) = \frac{1}{2}\left[E_k + E_N \pm \sqrt{(E_k - E_N)^2 + 4V_{Nc}^2}\right], \tag{2.7}$$

where E_- and E_+ are the lower and upper conduction sub-bands, respectively. For nonzero broadening Δ_N, Eq. (2.6) has complex eigenvalues that can be written as $E_\pm + i\Gamma_\pm$, where $E_\pm$ and $\Gamma_\pm$ are the real and imaginary parts of the energy calculated by replacing E_N by $E_N + i\Delta_N$ in Eq. (2.7).

Vaughan and Ridley [32, 33] generalised this method to include additional nitrogen clusters such as N-N pairs sharing a nearest neighbour Ga ion, and derived the Green's function G_{kk} for the more general case as [30]

$$G_{kk} = \left\{ E - E_k - \frac{1}{N_c}\sum_j \frac{|V_j|^2}{E - E_j + i\Delta_j} \right\}^{-1}, \tag{2.8}$$

where E_k and E_j are the energies of the extended host semiconductor and localised nitrogen states, respectively, V_j is the host conduction band interaction energy with the impurity levels j, and N_c is the number of primitive cells in the system. Vaughan and Ridley [34] calculated the density of states of GaNAs from the imaginary part of the Green's function, assuming that the energy broadening Δ_j is constant and the same for all N levels E_j. Vogiatzis and Rorison [35, 36] have also studied the band structure and the density of states of bulk, quantum well and quantum wire GaInNAs, using Matsubara Green's function method.

In Chapter 4 of this thesis, we modify this method by calculating ΔE_N as the imaginary part of the energy shift using second order perturbation theory. We will also consider the real part of the energy shift as a shift in the localised state energies, dE_N. Then in Chapter 5 we further modify the Green's function (GF) method by introducing energy dependent broadening parameters, $\Delta E_j(E)$, calculated by a **S**elf-**C**onsistent **G**reen's **F**unction (SCGF) approach, where the real and imaginary parts indicate the shift in energy, and broadening, respectively, of localised states. We first calculate an energy-dependent broadening $\Delta E_j(E)$ using a self-consistent Green's function method and then investigate the effect of the energy dependent broadening on the calculated DOS of GaNAs.

2.3 Mobility and scattering

2.3.1 Carrier mobility

It has been observed that the introduction of small amount of N into III-V materials, not only perturbs the CB of the host semiconductor, but also significantly reduces the mobility of carriers [37–41]. Compared to the room temperature value of about 8000cm^2(Vs)$^{-1}$ expected for GaAs, Skierbiszewski *et al.* [41] measured the mobility of $GaN_{0.014}As_{0.986}$ to be 400cm^2(Vs)$^{-1}$ at 295 K. Young *et al.* [42] measured the mobility of GaN_xAs_{1-x} for several N concentrations from 0.01% up to 1.3% for carrier concentrations of $(5-7)\times10^{18}$ cm^{-3}. For $x = 0.4\%$ and $x = 1.3\%$, they reported $\mu = 187$ cm^2(Vs)$^{-1}$ and 165 cm^2(Vs)$^{-1}$, respectively. Ishikawa *et al.* [43] measured the mobility of GaN_xAs_{1-x} for x=0.8, 1.7 and 2.2% with several carrier concentrations. For x=0.8%, they measured μ=413, 208 and 89 cm^2(Vs)$^{-1}$ for n=(0.1, 1.0 and 5.1) $\times 10^{18}$ cm^{-3} , respectively. Their mobility for x=1.7% at n=5.3 $\times 10^{17}$ cm^{-3} was 185 cm^2(Vs)$^{-1}$. Reason *et al.* [44] have also measured mobility of Si-doped GaN_xAs_{1-x} for several N concentrations from 0.01% up to 2% (n=(0.3 − 1) $\times 10^{18}$). Their value for x=0.1%, is around 600 cm^2(Vs)$^{-1}$ and for x=0.5 and 1.2% they measured μ=300 and 200 cm^2(Vs)$^{-1}$ respectively. Fig. 2.3 shows the compilation of mobility values measured for GaN_xAs_{1-x} samples, along with theoretical estimation of the mobility which are discussed further below.

In a final estimate of the mobility in GaNAs, Fahy and O'Reilly [45, 46], using S-matrix theory, calculated the scattering cross-section for an isolated impurity as

$$\sigma = \frac{\pi}{4}\left(\frac{m^*}{2\pi\hbar^2}\right)^2\left[\frac{\mathrm{d}E_c}{\mathrm{d}x}\right]^2 a_0^6, \tag{2.9}$$

where a_0 is the GaAs lattice constant, m^* is the electron effective mass and $\mathrm{d}E_c/\mathrm{d}x$ is the derivative of the band edge energy with respect to the N concentration x. In the two-band model, assuming all localised states have the same energy, E_N, they estimated that the n-type carrier mobility is given by

$$\mu = \frac{\sqrt{3m^*k_BT}}{e}\pi\left(\frac{m^*}{2\pi\hbar^2}\right)^2\left[\frac{\mathrm{d}E_c}{\mathrm{d}x}\right]^2 a_0^3 x, \tag{2.10}$$

where e is the magnitude of the electron charge, k_B is Boltzmann's constant and T is the absolute temperature. For $x = 1\%$, Eq. (2.10) gives a mobility around 1000 cm^2(Vs)$^{-1}$, at room temperature. This value is comparable to the highest measured mobility in high-quality GaInNAs samples. This mobility is

substantially less than the ideal mobility of GaAs at room temperature.

Later, Fahy and O'Reilly [47] generalised Eq. (2.10) to include N-N pair and higher cluster of N distribution, in an independent scattering approximation, as

$$\mu = \frac{\sqrt{3m^* k_B T}}{e} \pi \left(\frac{m^*}{2\pi\hbar^2}\right)^2 \sum_j \left[\frac{\mathrm{d}E_c}{\mathrm{d}x_j}\right]^2 a_0^3 x_j, \tag{2.11}$$

where x_j is the concentration of the j-th environment. They concluded that including the N-N pair has a relatively small effect on the mobility, reducing the calculated values by less than 10%, compared to the two-band model, where all N atoms are treated independently. They proposed that the effects of nitrogen clusters on the mobility may in general be small when the clusters are distributed uniformly through the alloy. They [47] also suggested that the mobility has a very weak temperature dependence in the range $100-300$ K, due to the increase in the scattering cross-section at low temperature as the conduction band edge comes closer to the nitrogen resonance levels.

Vaughan and Ridley [34] also calculated the bulk mobility for GaN_xAs_{1-x} for the case of isolated N and N-N pair environments. In this work they ignored the details of the N distribution, and also did not consider polar optical, impurity and defect scattering, scattering mechanism that were included in their later work [49] for calculating the Hall mobility. These assumptions led to a higher mobility value compared with those calculated by Fahy *et al.* [47], and an order of magnitude higher than the highest measured values.

The dashed line in Fig. 2.3 shows the estimated variation of the room temperature electron mobility with x in GaN_xAs_{1-x}, calculated using the two-level band-anticrossing model for GaN_xAs_{1-x} [9, 45], which assumes all N resonant defect states to be at the same energy E_N. The electron mobility is estimated to be of order 1000 $\mathrm{cm}^2(\mathrm{Vs})^{-1}$ when x=1%, of similar magnitude to the highest values observed to date in dilute nitride alloys [50] but larger than that found in many samples, where $\mu \sim 100 - 300$ $\mathrm{cm}^2(\mathrm{Vs})^{-1}$, as shown by the data points in Fig. 2.3 (following [12, 44]). In practice, there is a wide distribution of N resonant state energies in GaN_xAs_{1-x}, associated with N-N nearest-neighbour pairs and clusters [24, 51], with a significant number of these defect levels calculated to be close to the conduction band edge. The lower lines in Fig. 2.3 shows the calculated mobility when scattering associated with the LCINS distribution of defect levels is included. It can be seen that inclusion of this full distribution can largely account for the low measured electron mobility in this alloy system.

The intrinsically low electron mobilities in dilute nitride alloys have significant

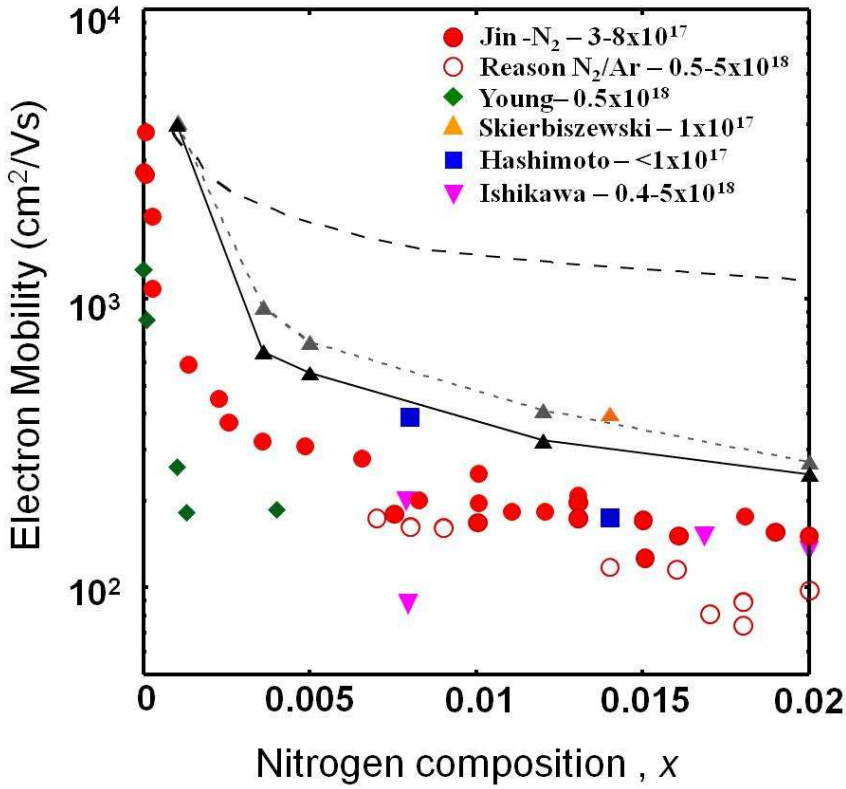

Figure 2.3: Data points: measured variation of electron mobility with N composition x in GaN_xAs_{1-x} (from [12]). The uppermost dashed line shows the calculated mobility, assuming scattering by isolated N atoms only (Eq. (2.10)) while the lower lines show the calculated mobility assuming a distribution of N states [13] and carrier density of 1×10^{17} cm^{-3} and 1×10^{18} cm^{-3} (grey and black triangles respectively), (following [48]).

consequences for potential device applications. The low electron mobility, combined with the short non-radiative lifetimes observed to date, limit the electron diffusion lengths and efficiency achievable in GaInNAs-based solar cells. Further efforts may lead to increased non-radiative lifetimes, but are unlikely to see significant further improvements in the alloy-scattering-limited mobility [50].

2.3.2 Resonant scattering

The rate of transition from an initial occupied state $|\psi_i\rangle$ to an empty final state $|\psi_f\rangle$ can be calculated from time-dependent perturbation theory, and is given by Fermi's Golden Rule as

$$R(i \to f) = \frac{2\pi}{\hbar} |\langle \psi_i | \Delta H | \psi_f \rangle|^2 D(E_f), \tag{2.12}$$

where ΔH in the matrix element is the perturbation to the Hamiltonian due to the scattering mechanism, $|\psi_i\rangle$ and $|\psi_f\rangle$ are both eigenstates of the unperturbed Hamiltonian H_0, the density of final states is $D(E_f)$ and $E_f = E_i$ for elastic scattering.

In a further work, Fahy *et al.* [13] developed a model based resonant scattering for LCINS nitrogen distribution and Fermi's golden rule. Within the Lorentzian approximation for the line shape for the weight of localised states the scattering rate for carriers at energy E due to a N resonant state at energy E_N is given by

$$R(E) = \frac{2\pi}{\hbar N_c} \frac{\beta^4}{(E - E_N)^2 + \Delta^2} \frac{D(E)}{N_c}, \tag{2.13}$$

where N_c is the number of group-V atoms in the system and β defines the interaction strength [13]. Here $\Delta = \pi\beta^2 D(E_N)/N_c$ is the imaginary part of the energy, and $D(E)$ is the density of states for the parabolic conduction band at energy E_N. Using an n-band Hamiltonian based on Anderson's many impurity model, Vaughan and Ridley [34] also derived an expression similar to Eq. (2.13) for the N scattering rate.

Using the LCINS distribution of N states, shown in Fig. 2.2, we can calculate the scattering rate due to this distribution of states. Fig. 2.4 shows the calculated energy dependence of the scattering rate for several different N compositions, with the zero of energy in each case is taken to be at the bottom of the GaNAs conduction band (equivalent to setting the lower eigenvalue of Eq. (3.1) as the zero of energy). Using the scattering rate given by Eq. (2.13) and the Boltzmann transport equation in the relaxation-time approximation, Fahy *et al.* [13] calculated the electron mobility for bulk and quantum well GaNAs alloys (shown by the lower lines in Fig. 2.3). Nitrogen cluster states are found to dominate the scattering near the conduction band edge and play a crucial role in limiting the electron mobility.

We will employ these resonant scattering rates in Chapter 6 to calculate the total scattering rate and drift velocity of carriers using the Boltzmann transport equation. However, in Chapter 7 we will modify the method of calculating resonant scattering rate using self-consistent Green's function method.

2.4 High field transport

The unusual band structure and strong scattering effects of N states led to a number of interesting proposals concerning high field transport in dilute nitride

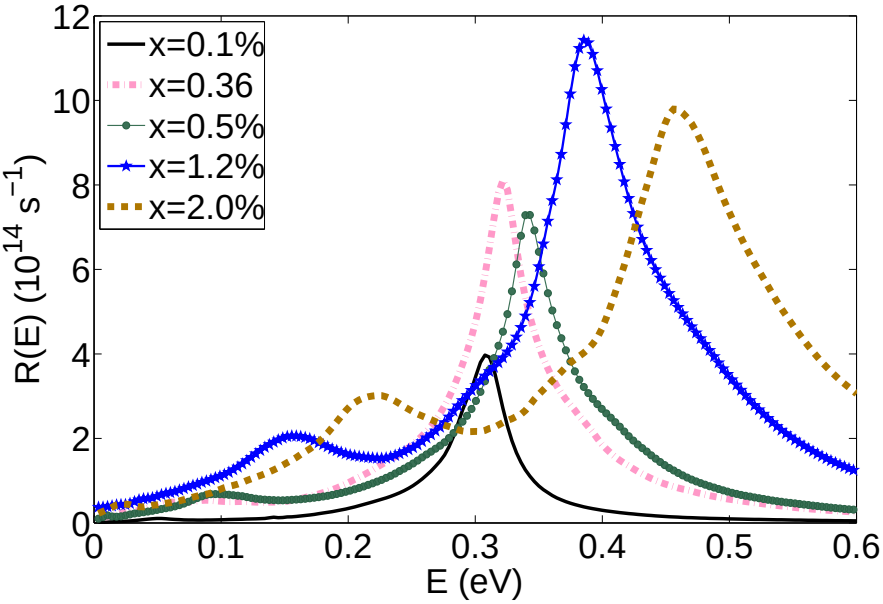

Figure 2.4: Scattering rate due to the distribution of N resonant states in GaN_xAs_{1-x} for selected values of x.

alloys. It was proposed by Adams [14], that the strong perturbation by N states, leading to a band gap above E_N in the BAC model, would limit the ability of electrons to gain higher energy from an applied electric field, and therefore the impact ionization coefficient could decrease for electrons. Because the valence band is largely unchanged, the hole impact ionization coefficient should not be affected by the addition of nitrogen and therefore the suppression of electron multiplication should allow the production of low-noise avalanche photodiodes (APDs) using these materials. This proposal motivated some of the work reported in Chapter 6 in this thesis.

Measurements to date have shown that there are differences in the behaviour of GaNAs and conventional APDs, but that there is no significant suppression of the electron multiplication rate [52]. This experimental result is consistent with Green's function calculations using the LCINS model, where including the full distribution of N levels tends to fill the gap observed in the BAC density of states.

Patanè *et al.* [15, 22, 53–55] predicted and observed a strong negative differential velocity (NDV) effect at high electric fields for $x = 0.1\%$ in GaN_xAs_{1-x}. They analysed theoretically the behaviour of carriers in high electric fields by solving dynamical balance equations [56]. This simple model neglects the energy distribution of electrons and energy dependence of resonant N scattering. In order to simplify the model, they also approximated the electron effective mass by an analytical expression that is fitted to the mass at the bottom of the GaAs CB.

The model predicted that NDV should persist and remain significant at higher N compositions, contrary to later experiments by Sun *et al.* [57] for GaInAsN quantum wells with $x = 1.0\%$ and $x = 1.5\%$. Our analysis in Chapter 6 shows that the NDV is indeed possible at very low N composition ($x \approx 0.1\%$), but does indeed become suppressed at higher N compositions, as N pair and cluster states start to have a significant impact on the low field mobility.

In order to develop a more sophisticated approach to calculate hot electron transport, we need to calculate scattering rates, carrier group velocity and density of states for all values of wave vector k. This limits the usefulness of the simple BAC model that predicts a gap in the CB, and is not well behaved near the N state energy E_N. Vaughan and Ridley [32] derived an analytical function for the DOS that remains well-behaved around the nitrogen complex energy level and that can be used in high field calculations.

Therefore, Sun *et al.* [57] performed a study of hot electron momentum relaxation in $Ga_{0.7}In_{0.3}As_{1-x}N_x$ quantum wells (with $x = 1.0\%$ and $x = 1.5\%$), and observed that the high field drift velocity saturates at 1×10^5 m/s with no evidence of NDV. Their simple model based on nondrifting hot phonons confirmed this behaviour. However in this model, they ignored the nonparabolicity of the CB of the host semiconductor and only included optical scattering and an elastic scattering mechanism, fitted to the low field mobility measurements.

Recent Monte Carlo calculations by Vogiatis and Rorison investigated the drift velocity variation with electric field in GaNAs samples with very low N composition ($x \leq 0.2\%$) [16, 58]. These calculations confirm a NDV at these low N compositions, but these authors did not undertake any detailed theoretical analysis of GaNAs samples with higher N composition ($x \sim 1 - 2\%$).

In Chapter 6 we will solve the steady-state Boltzmann transport equation in bulk GaN_xAs_{1-x}. Two different models of the conduction band structure will be studied to investigate the behaviour of electrons with increasing electric field in these alloys: (1) carriers in parabolic Γ and L bands are scattered by resonant nitrogen substitutional defect states, polar optic and acoustic phonons, and intervalley optical phonons; (2) carriers, constrained in the lower band of the band-anti-crossing (BAC) model, are scattered by phonons and by nitrogen states. We consider scattering both by isolated N atoms and also by a full distribution of N states presented by the LCINS approach (Fig. 2.4). For both models, we will calculate carrier distribution, mobility and drift velocity. Detailed motivation for the different models is given in Chapter 6.

2.5 Summary

In this chapter we presented an overview of the relevant background to the theory of the band structure, scattering and high field transport that we will study in this thesis. In the following chapters we begin in Chapter 3 by modifying and developing the BAC and Green's function models explained in § 2.2. Then we will compare the results of these models to supercell calculations in Chapter 4. In Chapter 5 we will study the band structure and the density of states using the self-consistent Green's function method. Following this investigation of the electronic structure, we will then examine scattering mechanisms and high field transport in GaNAs dilute nitride alloys in Chapter 6, where we also compare our results with the previous studies mentioned in sections 2.3 and 2.4. We then introduce in Chapter 7 a more sophisticated method to study the band structure, mobility and scattering by finding the poles of Green's function method. We compare the results of this method both with our methods presented in the chapters of this thesis, as well as the results of other authors. We conclude that this more sophisticated method addresses some of the issues in earlier works, but also raises interesting questions which we do not fully resolve regarding the carrier mean free path in dilute nitride alloys. We then return in chapter. 8 to use the BAC and LCINS models to investigate how optical absorption spectra should vary with N composition in different dilute nitride alloys. We conclude that the absorption spectra are well described using the LCINS model, but we note that the variation between different experimental measurements in similar samples make quantitative comparison difficult. Finally we summarise our conclusions and give an overview of possible future directions in Chapter 9.

Chapter 3

Band anti-crossing model

3.1 Introduction

As we saw in Chapter 2, the rapid reduction in energy gap in GaN_xAs_{1-x} with increasing x, is well explained in terms of a band-anticrossing (BAC) interaction between the GaAs host matrix conduction band (CB) edge and a set of N resonant defect levels above the CB edge [9]. The BAC model predicts an energy gap in the CB dispersion of GaNAs, above the N resonant state energy, which makes it difficult to investigate carrier transport in dilute nitride alloys such as GaNAs. However, the density of states (DOS), measured [29] and calculated using a Green's function method [34, 35], indicates a filling of this gap.

In this chapter, we give more detail of some modifications to the BAC model for GaNAs alloys. First in § 3.2 we include N broadening effects by considering a complex N energy. We also consider the shift in the N state due to the interaction with the host semiconductor CB. We show how this model can be used to calculate the fractional Γ character, the DOS and the band dispersion for this model, where the fractional Γ character of a given state describes the properties of the state which projects onto the host matrix extended states. In § 3.3 we will extend this model to include N-N pair states and to consider their consequences on the DOS and the band dispersion in GaN_xAs_{1-x}. Finally in § 3.4 we consider the full distribution of localised states given by the LCINS approach, and study their impact on the DOS and band structure of dilute nitride alloys in a modified BAC model.

3.2 Two-level BAC model

The band anticrossing model was introduced by Shan *et al.* [9] to explain the properties of III-V dilute nitrides and other mismatched alloys. The BAC model describes the electronic structure of dilute nitride material by considering the interaction between the de-localised states of the host semiconductor and localised impurity states. It is well known that an isolated N atom introduces a localised state with energy level E_N in conventional III-V materials [8].

Here we modify the BAC model, given by Eq. (2.1), to include both the broadening of nitrogen states and the shift in their energy due to their interaction with the CB states. We see that this modified BAC model is straightforward to implement and gives the same results to those previously obtained by Vaughan and Ridley [32, 33] and Vogiatzis and Rorison [35, 36] using the Green's function (GF) model. In order to implement this modification, the Hamiltonian of GaN_xAs_{1-x} can be written as

$$H = \begin{pmatrix} E_k & V_{Nc} \\ V_{Nc} & E'_N + i\Delta_N \end{pmatrix}, \tag{3.1}$$

where E_k=E_c+$\hbar^2k^2/(2m^*)$ is the GaAs conduction band energy, $E'_N = E_N+\Delta E_N$ is the shifted nitrogen state energy, Δ_N is the broadening of the nitrogen states, $\hbar$ and k are the reduced Planck constant and wavevector, respectively; m^*=$0.067m_0$ is the GaAs effective mass, and m_0 is the free electron mass. In this chapter, all energies are referenced to the GaAs conduction band (CB) edge energy E_c. The coupling matrix element V_{Nc} between the nitrogen and CB states depends on nitrogen concentration x, as V_{Nc}=$\beta x^{1/2}$ [6, 10], where we choose here β=2.0 eV as the interaction parameter [6].

The N energy, E'_N in Eq. (3.1) differs by ΔE_N from the original N energy E_N, that in this thesis we take $E_N = 0.23$ eV. This is because the interaction with the CB states shifts the mean N energy. This energy shift can be calculated from second order perturbation theory as [13, 59]

$$\Delta E_N = \int_0^{E_{max}} \frac{|\langle k|V|j\rangle|^2}{E - E_N} D(E)dE. \tag{3.2}$$

This shift is affected by the maximum energy, E_{max}, that is assumed for the conduction band dispersion.

Moreover, the magnitude of the imaginary part of the N energy, Δ_N, has been estimated using the Green's function method and second order perturbation

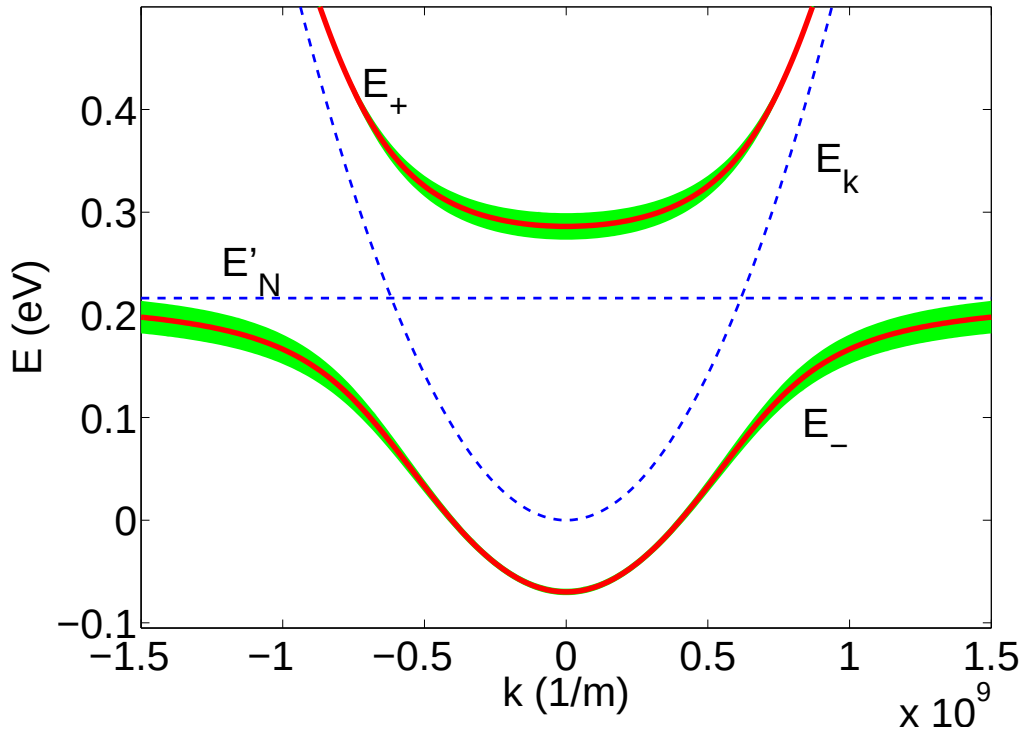

Figure 3.1: Energy-wavevector dispersion relation for E_- and E_+ for GaN_xAs_{1-x} with $x = 0.5\%$ (solid red line), calculated using Eq. (3.1). The broadening of the dispersion curves (green areas) illustrates the energy uncertainties. All the energies are referenced to E_c, the bottom of the conduction band of GaAs.

theory as [13]

$$\Delta_N = \pi\beta^2 D(E'_N)/N_c = \frac{(2m)^{3/2}a_0^3}{16\pi\hbar^3}\beta^2(E'_N)^{1/2}. \tag{3.3}$$

Here a_0, and N_c are the cubic lattice constant for GaAs, and number of group V atoms in the system respectively, while $D(E'_N)$ is the GaAs density of states at E'_N.

The energies of the upper and lower conduction subbands, denoted by E_+ and E_-, are given by the eigenvalue equation as

$$E_\pm = \frac{E'_N + i\Delta_N + E_k}{2} \pm \frac{\sqrt{(E'_N + i\Delta_N - E_k)^2 + 4V_{Nc}^2}}{2}. \tag{3.4}$$

The solid red lines in Fig. 3.1 exhibit the lower and upper bands in the absence of N broadening ($\Delta_N = 0$), for GaN_xAs_{1-x} with $x = 0.5\%$. In this plot, we have considered the shift in E_N due to the interaction with a conduction band with maximum energy $E_{max} = 0.86$ eV, that gives $\Delta E_N = -13.3$ meV. The energy

uncertainties can be obtained for non-zero Δ_N as $E_{R\pm} \pm E_{I\pm}$, where $E_{R\pm}$ and $E_{I\pm}$ are the real and imaginary parts of $E_{\pm}$, respectively. The green areas in Fig. 3.1, represent this broadening of the dispersion relations. It is seen that the energy broadening has its minimum value at the bottom of the lower band and increases towards its maximum value as it approaches the N state energy E_N. In the upper band this energy uncertainty starts with its maximum at the bottom of the band and decreases towards zero by distancing from E_N.

3.2.1 Fractional Γ character

It can be useful both for optical and transport analysis to know the fraction of each state, f_Γ, which has host matrix extended state character. Using the 2-level band anticrossing model, the Hamiltonian of the system can be written as

$$\begin{bmatrix} E_c(x) + \dfrac{\hbar^2 k^{*2}}{2m^*} & V_{Nc} \\ V_{Nc} & E'_N + i\Delta_N \end{bmatrix} \begin{bmatrix} \alpha_k \\ \alpha_N \end{bmatrix} = E \begin{pmatrix} \alpha_k \\ \alpha_N \end{pmatrix}, \tag{3.5}$$

and therefore we have

$$\left[E_c(x) + \frac{\hbar^2 k^{*2}}{2m^*}\right] \alpha_k + V_{Nc}\alpha_N = E\alpha_k, \tag{3.6}$$

and

$$V_{Nc}\alpha_k + \left[E'_N + i\Delta_N\right] \alpha_N = E\alpha_N. \tag{3.7}$$

Rearranging this equation we have:

$$\alpha_N = \alpha_k \frac{V_{Nc}}{E - E'_N - i\Delta_N}. \tag{3.8}$$

Multiplying Eq. (3.8) by its complex conjugate gives

$$|\alpha_N|^2 = |\alpha_k|^2 \frac{V_{Nc}^2}{\left|E - E'_N\right|^2 + \Delta_N^2}. \tag{3.9}$$

The normalisation condition implies

$$|\alpha_k|^2 + |\alpha_N|^2 = 1, \tag{3.10}$$

and therefore $|\alpha_k|^2$, which we define as the fractional Γ, f_Γ, character is given by

$$f_\Gamma = |\alpha_k|^2 = \left(1 + \frac{V_{Nc}^2}{\left|E - E'_N\right|^2 + \Delta_N^2}\right)^{-1}. \tag{3.11}$$

3.2.2 Density of states

We can define the nonparabolicity factor $\gamma(E)$ for a given band dispersion as

$$\gamma(E) = \frac{\hbar^2 k^2}{2m^*}, \tag{3.12}$$

where for the 2-band BAC model given by Eq. (3.1), $\gamma(E)$ is

$$\gamma(E) = E - E_c - \frac{V_{Nc}^2}{E - (E'_N + i\Delta_N)}. \tag{3.13}$$

We consider now the 3D density of states for a supercell of size L^3, which can be calculated for energy E in the BAC model as

$$D(E) = \frac{L^3}{2\pi^2}\frac{k^2}{dE/dk}. \tag{3.14}$$

The DOS projected onto the Γ valley (host CB) states, $D_{cb}(E)$, can be obtained by multiplying $D(E)$ by f_Γ for each $\mathbf{k}$ value, and is given by the real part of

$$\begin{aligned} D_{cb}(E) &= \frac{(2m^*)^{3/2}L^3}{4\pi^2\hbar^3}\left[E - E_c - \frac{V_{Nc}^2}{E - (E'_N + i\Delta_N)}\right]^{1/2} \\ &= \frac{(2m^*)^{3/2}L^3}{4\pi^2\hbar^3}\gamma^{1/2}(E). \end{aligned} \tag{3.15}$$

For $V_{Nc} = 0$, we recover the usual GaAs DOS

$$D_{GaAs}(E) = \frac{(2m^*)^{3/2}L^3}{4\pi^2\hbar^3}(E - E_c)^{1/2}. \tag{3.16}$$

If we denote the real and imaginary parts of $\gamma(E)$ by $\Theta(E)$ and $\Phi(E)$, respectively, Eq. (3.15) can then be written as

$$D_{cb}(E) = \frac{m^{*3/2}}{2\pi^2\hbar^3}\left[\Theta(E) + \left(\Theta^2(E) + \Phi^2(E)\right)^{1/2}\right]^{1/2}, \tag{3.17}$$

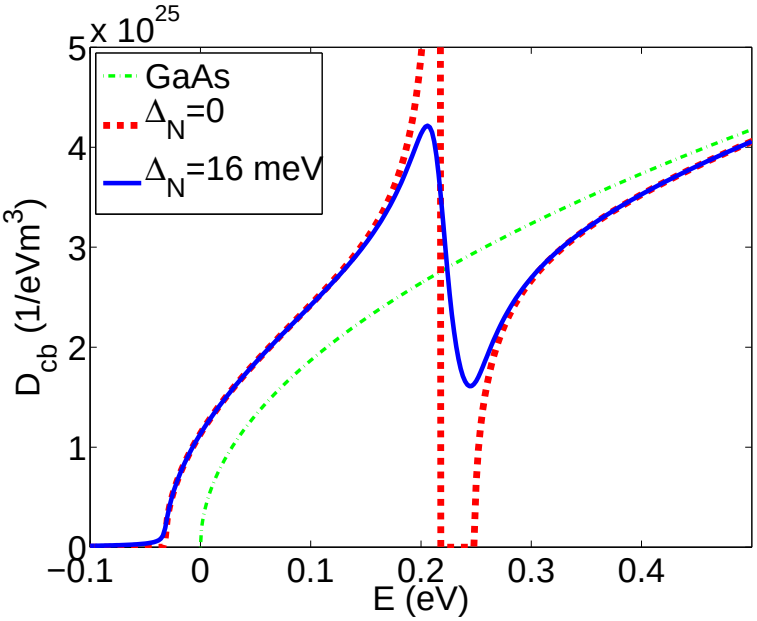

Figure 3.2: The density of states versus energy for GaN_xAs_{1-x}, with $x = 0.2\%$ calculated for the 2-level BAC model, with and without including the N broadening where shown by the solid blue and dashed red lines, respectively. The dash-dotted green line shows the DOS of GaAs ($x = 0$).

where the real part of $\gamma(E)$ is

$$\Theta(E) = E - E_c - \frac{V_{Nc}^2(E - E'_N)}{(E - E'_N)^2 + \Delta_N^2}, \tag{3.18}$$

and its imaginary part is given by

$$\Phi(E) = -\frac{V_{Nc}^2 \Delta_N}{(E - E'_N)^2 + \Delta_N^2}. \tag{3.19}$$

Eq. (3.17) is very similar to the DOS calculated by Vaughan and Ridley [34] using the Green's function method. In this method the DOS is given by

$$D_{cb} = -\frac{1}{\pi} \sum \Im[G_{kk}(E)], \tag{3.20}$$

where $G_{kk}(E)$ is the Green's function given for instance by Eq. (2.5). The Green's function in terms of $\Theta(E)$ and $\Phi(E)$ can be written as

$$G_{kk} = \Big[\Theta(E) - E_k - i\Phi(E)\Big]^{-1}, \tag{3.21}$$

with its imaginary part then given by

$$\Im[G_{kk}] = \frac{\Phi(E)}{\left(\Theta(E) - E_k\right)^2 + \Phi(E)^2}. \tag{3.22}$$

Figure 3.2 compares the DOS of $GaN_{0.002}As_{0.998}$, calculated by the simple BAC model ($\Delta_N = 0$) and the BAC model including the nitrogen states broadening calculated by Eq. (3.3) ($\Delta_N = 16$ meV). The dash-dotted green line in this plot displays the DOS of GaAs in the absence of N. It is clear that introducing N atoms in GaNAs pushes the conduction band edge (CBE) to lower energies. The usual BAC model predicts a gap in the DOS as shown by the dashed red line in this figure. However, including broadening of the localised states caused this gap to be filled in. Although this is in agreement with Green's function calculations [34] and experimental studies [29], we will see later in Chapter 5 using a self-consistent Green's function model that the gap should not be filled in a 2-level model, but is rather filled in experimental measurements due to the distribution of N states in actual samples.

3.2.3 The DOS projected to a single k state

In the BAC model the DOS projected onto a single **k** state, can be calculated as D_p=$d_- + d_+$ where

$$d_\pm = \frac{|\alpha_\pm|^2}{\pi} \frac{\Delta_\pm}{(E - E_{p_\pm})^2 + \Delta_\pm^2}, \tag{3.23}$$

where $E_{p\pm} = \Re[E_\pm]$ and $\Delta_\pm = \Im[E_\pm]$ are the real and imaginary parts of $E_\pm$ calculated from Eq. (3.4) and the fractional Γ character, $\alpha_\pm$, is given by the first coefficient of the corresponding normalized eigenvector. Eq. (3.23) is equivalent to $-(1/\pi)\Im[G_{kk}(E)]$ in the Green's function approach, where $\Im[G_{kk}(E)]$ is given by Eq. (3.22). Fig. 3.3 shows the DOS, D_p, projected onto single momentum states k, for all ranges of energy E and wavevector k. It is seen that the band is split strongly into two bands, so that for instance the DOS projected onto a state with $k = 0$ has a large peak below the GaAs CBE and another small peak about $E = 0.25$ eV. However between the two peaks the DOS has always a nonzero value, meaning that the lower and upper bands, in this model, are connected via the overlap of the DOS of individual states. By increasing the GaAs CB state energy, both peaks appear at higher energies, but the Γ character of lower one decreases while that of the upper one increases.

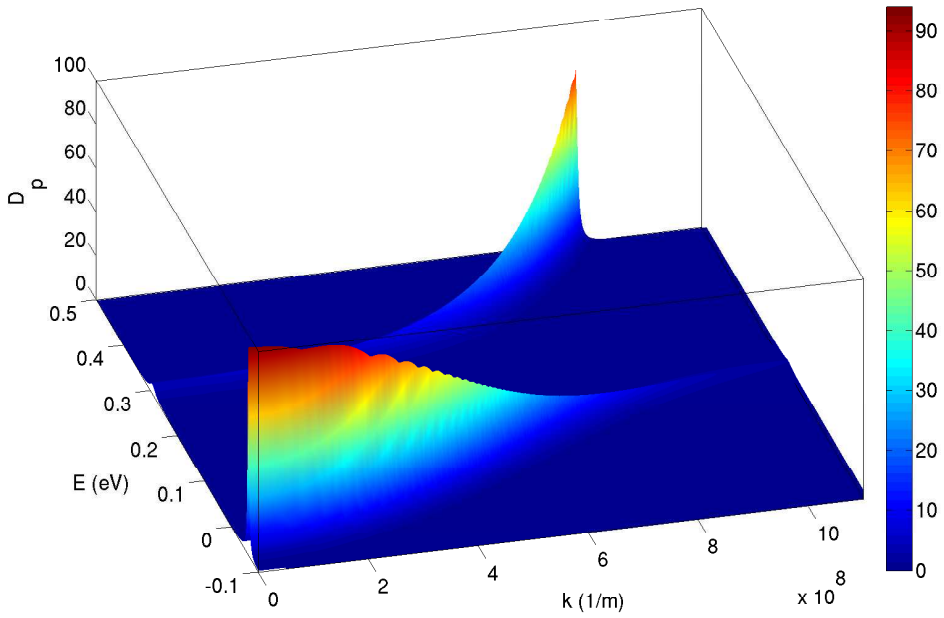

Figure 3.3: The Density of states projected onto selected GaAs $|k\rangle$ states, for all k-states calculated using the BAC model for GaN_xAs_{1-x} with $x = 0.5\%$.

3.2.4 The band dispersion

Figure 3.4 shows the conduction band dispersion for $GaN_{0.005}As_{0.995}$, calculated using Eq. (3.23). Actually this figure is a top view of Fig. 3.3. It can be seen that the band dispersion follows that of the BAC model of Eq. (3.1) (dashed white line in Fig.3.4), but with two notable differences. Firstly, the dispersion at each k point is broadened over a range of energy values, with the broadening increasing close to the nitrogen resonant state energy, E_N. Secondly, the k character of the states in the lower band decreases towards zero with increasing k value, as the band approaches E_N. (This also occurs but has generally been ignored in analyses based on the BAC model.)

The energy broadening in Fig. 3.4 in principle allows a means for electrons which are being accelerated in the lower band to scatter into the upper band. However, we will see later that such a distribution of states should not be expected in the 2-level BAC model when using a self-consistent Green's function approach [60].

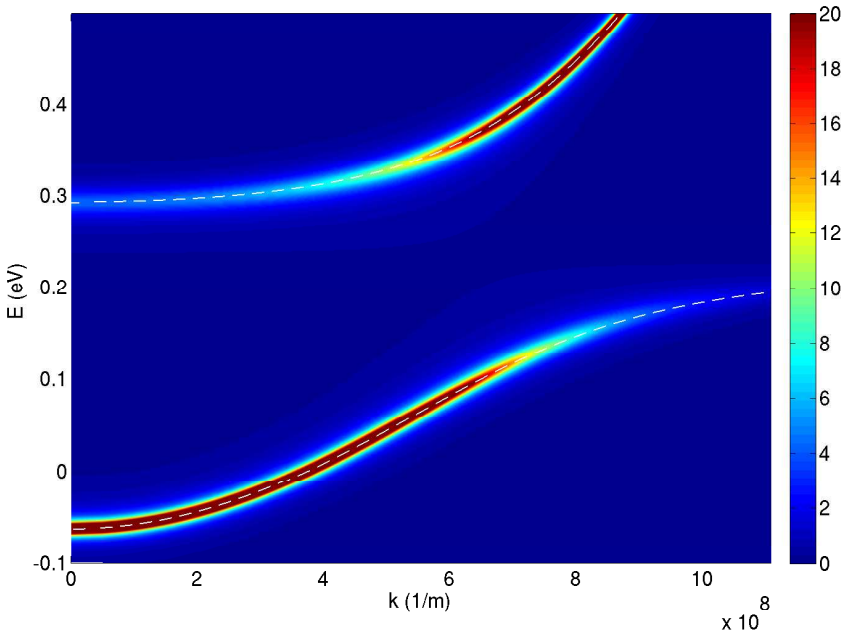

Figure 3.4: Energy-wavevector dispersion relation in the two-band BAC model for GaN_xAs_{1-x} with $x = 0.5$, while each k states is broadened by its DOS.

3.3 Three-level BAC model

The BAC model successfully describes many of the electronic properties of GaNAs alloys. However, as mentioned earlier in § 2.2, theoretical and experimental studies show a range of resonant defect levels close to the CBE in GaN_xAs_{1-x}, due to the formation of N complexes which are ignored in the conventional BAC model. Experimental studies of dilute nitride alloys with very low N concentrations, have shown a range of resonant defect levels above the CBE due to the formation of N complexes. These include, for instance, the pair N-N states, where a Ga atom has two N neighbours, that gives a resonant defect level close to the CBE of GaAs [7, 61, 62]. The empirical pseudopotential calculation by Kent *et al.* [51, 63] and tight-binding studied by Lindsay and O'Reilly [11] have found similar nitrogen resonant states.

Healy *et al.* [21] investigated the effect of N-N pairs by introducing a three-level BAC model, incorporating isolated and pair N states and their interactions with the host semiconductor CB level. In this model the Hamiltonian for GaN_xAs_{1-x} is given by

$$H = \begin{pmatrix} E_{NN}(x) & 0 & V_{NNc}(x) \\ 0 & E_N(x) & V_{Nc}(x) \\ V_{NNc}(x) & V_{Nc}(x) & E_c(x) \end{pmatrix}, \tag{3.24}$$

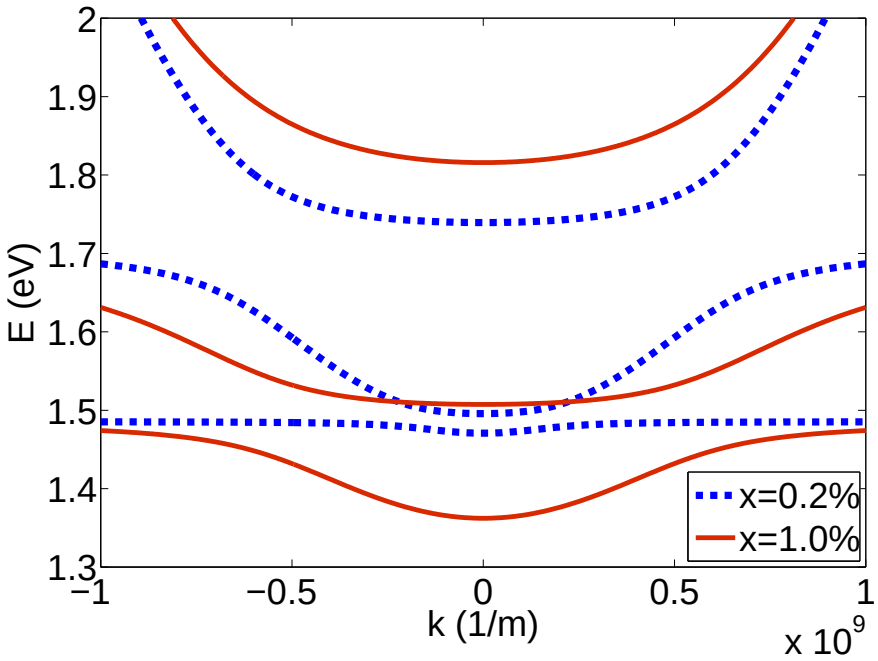

Figure 3.5: Energy-wavevector dispersion relation in 3-band BAC model for GaN_xAs_{1-x} for different values of x.

where the energies of the isolated N level E_N, N-N pair state E_{NN}, and the conduction band E_c, are obtained from

$$E_{NN}(x) = E_{NN0} - \alpha_N x, \tag{3.25}$$

$$E_N(x) = E_{N0} - \alpha_N x, \tag{3.26}$$

$$E_c(x) = E_{c0} - \alpha_c x + \frac{\hbar^2 k^2}{2m^*}, \tag{3.27}$$

where m^* is the effective mass of the host semiconductor, and the interaction parameters V_{Nc} and V_{NNc} also vary with composition x as

$$V_{NNc}(x) = \beta_{NN}\sqrt{x_{NN}}, \tag{3.28}$$

$$V_{Nc}(x) = \beta_N\sqrt{x_N}, \tag{3.29}$$

where x_N and x_{NN} are the concentrations of single and pair states of nitrogen, respectively, and are determined by

$$x_{NN} = 6x^2 \qquad \text{and} \qquad x_N = x - 2x_{NN}. \tag{3.30}$$

The parameters we have chosen are [21]: $E_{N0} = 1.706eV$, $E_{NN0} = 1.486eV$,

$Ec(GaAs) = 1.519eV$, $\beta_{NN} = 2.69eV$, $\beta_N = 1.97eV$, $\alpha_c = 2.1eV$ and $\alpha_N = 0.22eV$.

Figure 3.5 shows the calculated wavevector dependence of energy for GaN_xAs_{1-x} for $x = 0.2\%$ and 1.0%. We see that by increasing the nitrogen concentration x, the energy of the lowest conduction band shifts to lower values, the middle band width reduces slightly, and the upper band shifts to higher energies.

Healy *et al.* [21] showed that for low temperatures, at low N composition ($x = 0.1 - 1.0\%$) the band dispersion can be well described using a 3-level BAC model, while at higher concentrations the effects of longer-range N-N interactions need also to be considered [35].

However, the three-level BAC model given by Eq. (3.24) does not include the N state broadening and shift. In order to modify Eq. (3.24) we can replace E_N and E_{NN} by $E'_N + \Delta_N$ and $E'_{NN} + \Delta_{NN}$, respectively. Here, $E'_N = E_N + \Delta E_N$, where ΔE_N and Δ_N are given by Eqs. (3.2) and (3.3), respectively. In a similar way the shift, ΔE_{NN} for the pair N-N states is given by

$$\Delta E_{NN} = \int_0^{E_{max}} \frac{|\langle k|V|j\rangle|^2}{E - E_{NN}} D(E)dE, \tag{3.31}$$

and the broadening is given by

$$\Delta_{NN} = \pi\beta^2 D(E'_{NN})/N_c = \frac{(2m)^{3/2}a_0^3}{16\pi\hbar^3}\beta^2(E'_{NN})^{1/2}. \tag{3.32}$$

3.3.1 The DOS in the 3-level model

The density of state in the three-level BAC model, including the N broadening, can be calculated by Eq. (3.17) but we need to add terms corresponding to N-N pairs to Eq. (3.18) and Eq. (3.19) as

$$\Theta(E) = E - E_c - \frac{V_{Nc}^2(E - E'_N)}{(E - E'_N)^2 + \Delta_N^2} - \frac{V_{NNc}^2(E - E'_{NN})}{(E - E'_{NN})^2 + \Delta_{NN}^2}, \tag{3.33}$$

and

$$\Phi(E) = -\frac{V_{Nc}^2\Delta_N}{(E - E'_N)^2 + \Delta_N^2} - \frac{V_{NNc}^2\Delta_{NN}}{(E - E'_{NN})^2 + \Delta_{NN}^2}. \tag{3.34}$$

The red line in Fig. 3.6 displays the calculated DOS for GaN_xAs_{1-x} with $x = 0.5\%$ in the 3-band model, including localised state broadening. The energy shift and broadening of isolated N and pair N-N states are calculated using Eqs. (3.2), (3.3), (3.31) and (3.32), respectively, as: $\Delta_N = 15.6$ meV, $\Delta E_N = -12.8$meV,

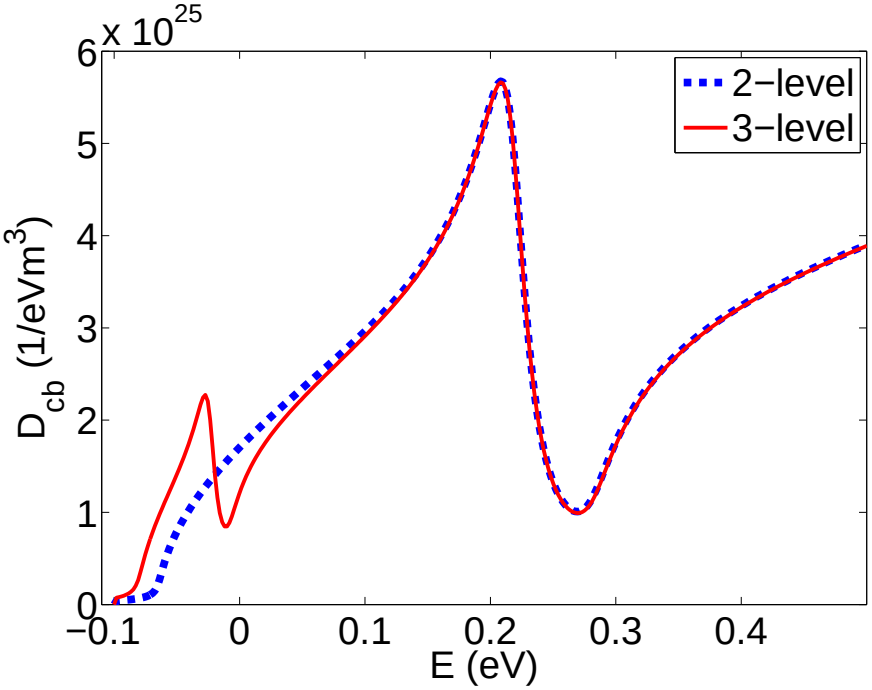

Figure 3.6: The comparison of the DOS for $GaN_{0.005}As_{0.995}$ in the 2-band and 3-band models.

$\Delta_{NN} = 6.5$ meV, $\Delta E_{NN} = -34.5$ meV.

The dashed blue line in this plot shows the DOS calculated in the 2-band model. We see that the inclusion of N-N pair shifts the CBE to slightly lower energy, and also around the N-N pair energy, E_{NN}, the DOS deviates from the DOS predicted by the 2-band model. As the N-N pair energy is close to the GaAs CBE, inclusion of such states can have a significant effect on carrier transport calculations, as we will discuss later in Chapter 6.

3.3.2 Band dispersion in the 3-level model

Moreover, the DOS projected onto each single momentum state can be given by Eqs. (3.23), (3.33) and (3.34). Having calculated this DOS for all k states we can plot the band dispersion. Fig. 3.7 shows the dispersion relation of $GaN_{0.005}As_{0.995}$ in the three level BAC model, when each k state in broadened by its DOS, given by Eq. (3.23). Overall the behaviour is similar to what we saw in the 2-band model, but here we have another gap related to N-N pair states.

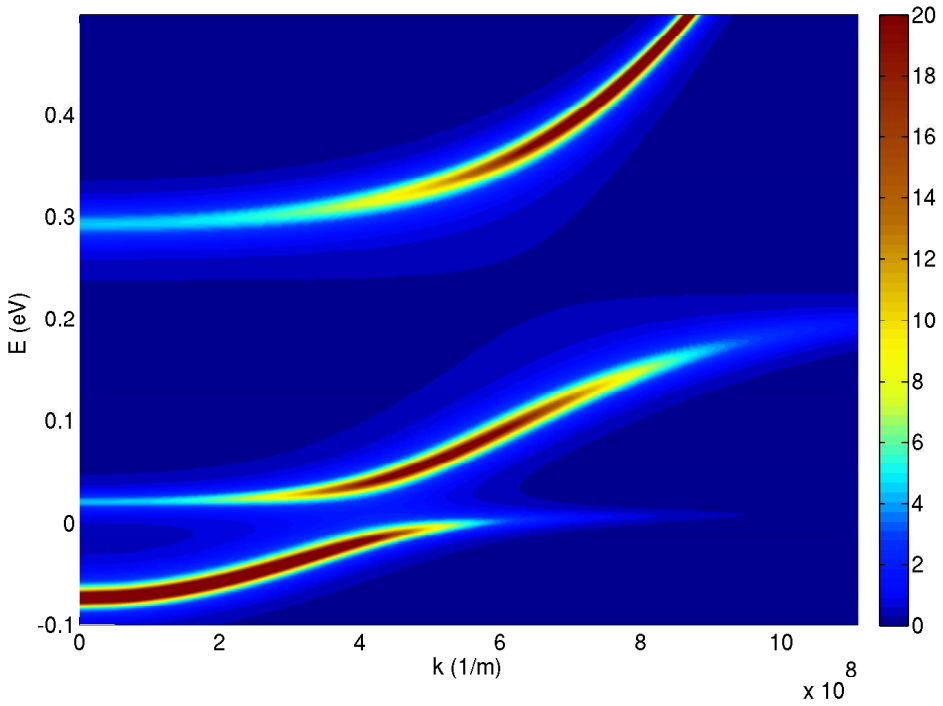

Figure 3.7: Energy-wavevector dispersion relation in the three-band BAC model for GaN_xAs_{1-x} with $x = 0.5\%$, while each k states is broadened by its DOS.

3.4 The LCINS model

The two and three level models are however oversimplified, because they omit the detail of the distribution of N states which are present in actual GaNAs samples. We can extend these models to consider a distribution of N states. In the LCINS model we consider n nitrogen states with energy E_j in a volume containing N_c group V atoms. The Hamiltonian for this (n+1)-state model can be written as

$$H = \begin{pmatrix} E_k(x) & V_1/\sqrt{N_c} & V_2/\sqrt{N_c} & \cdots & V_j/\sqrt{N_c} \\ V_1/\sqrt{N_c} & E_1' + \Delta_1 & 0 & \cdots & 0 \\ V_2/\sqrt{N_c} & 0 & E_2' + \Delta_2 & \cdots & 0 \\ \vdots & \vdots & \cdots & \ddots & \cdots \\ V_j/\sqrt{N_c} & 0 & 0 & \cdots & E_j' + \Delta_n \end{pmatrix} \tag{3.35}$$

where $V_j/\sqrt{N_c}$ is the interaction and $E_j' = E_j + \Delta E_j$ represents the energy of the jth localised state, with broadening Δ_j, that in a similar way to § 3.3 can be

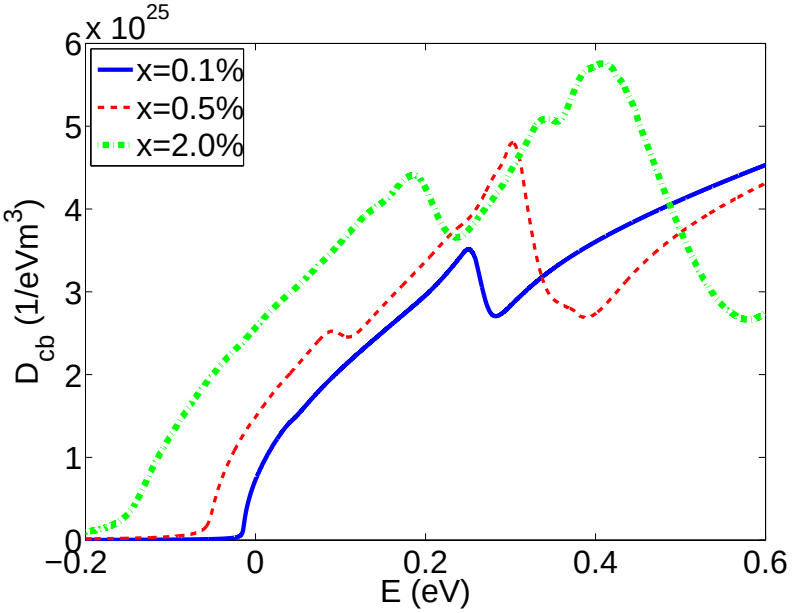

Figure 3.8: The density of states for GaN_xAs_{1-x} with $x = 0.1\%$, 0.5% and 2.0%, calculated using the Green's function and the full LCINS distribution of N state energies.

calculated from

$$\Delta_j = \pi\beta^2 D(E'_j)/N_c. \tag{3.36}$$

Also the shift in the localised state energy is given by

$$\Delta E_j = \int_0^{E_{max}} \frac{|\langle k|V|j\rangle|^2}{E - E_j} D(E)dE. \tag{3.37}$$

We can then solve the Hamiltonian of Eq. (3.35) including the distribution of N states in the LCINS approach [13], as discussed in § 2.2.2. In this thesis we use the LCINS distribution calculated by Lindsay, O'Reilly and Fahy [11, 17], as shown in Fig. 2.2 for selected N concentrations.

3.4.1 The DOS in the LCINS model

The DOS projected onto the host semiconductor CB states can be found using Eq. (3.17), or equivalently using Eq. (3.20), with $\Theta(E)$ given by

$$\Theta(E) = E - \frac{V_j^2}{N_c} \sum_j \frac{(E - E'_j)}{(E - E'_j)^2 + \Delta_j^2}, \tag{3.38}$$

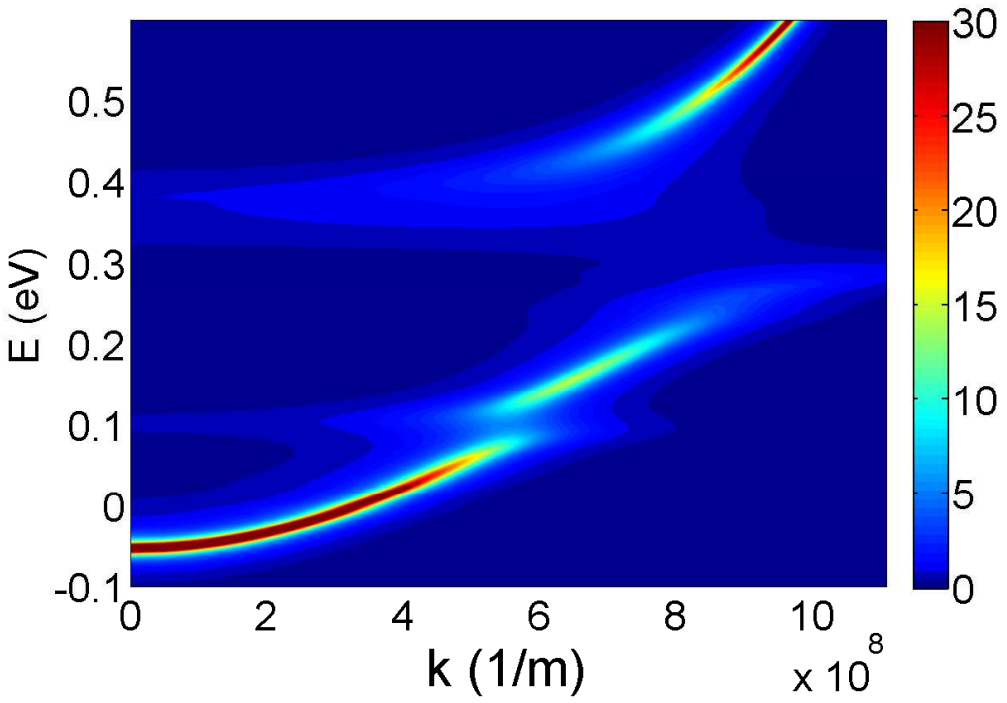

Figure 3.9: Dispersion relation for GaN_xAs_{1-x} with $x = 0.5\%$, calculated using the Green's function and the full distribution of N state energies.

and its imaginary part given by

$$\Phi(E) = -\frac{V_j^2}{N_c} \sum_j \frac{\Delta_j}{(E - E'_j)^2 + \Delta_j^2}. \tag{3.39}$$

Figure 3.8 shows the DOS calculated using the LCINS approach for GaN_xAs_{1-x} with $x = 0.1\%$, 0.5% and 2.0%. It is seen that the dips just above the isolated N state energies are smaller than in the 2 and 3-level models. Also, the higher N composition pushes the CB minimum to lower energies. In addition a shoulder can be observed in the DOS at lower energy, particularly in the 0.5% case, due to the increasing number of N pair states as the composition increases.

3.4.2 The band dispersion in the LCINS model

Having calculated the DOS projected onto all k states, we can plot the dispersion relation in the LCINS model. Fig. 3.9 displays the band dispersion of $GaN_{0.005}As_{0.995}$ calculated using the LCINS approach and the Green's function method, where each k state has a broadened projected DOS to that state. This plot is similar to the band dispersion calculated using the three-level model

(Fig. 3.7). However, the inhomogeneous broadening of the N state energies, E_j, leads to an increased energy broadening at each k point, while the BAC energy gap is clearly filled in by small contributions from a range of k points to the density of states at each energy.

3.5 Summary

In this chapter we provided a detailed overview of the BAC model, and of a number of the ways in which it can be adopted to provide a more detailed description of dilute nitride alloys. We first reviewed how the BAC model can be modified to include the N state broadening and energy shift, calculated respectively by the imaginary and real part of the energy change in second perturbation theory. We saw that including this broadening in N states leads to a filling the gap predicted by the usual BAC model. We also overviewed the effect of N-N pairs in § 3.3. Later in § 3.4 we included the full distribution of localised states presented by the LCINS approach, in an (n+1)-band model. In the next chapter we will examine in more detail the accuracy of the BAC model when solving the Anderson simple impurity model of Eq. (2.2) to describe the band structure of dilute nitride alloys.

Chapter 4

Supercell model

4.1 Introduction

We investigate here, the accuracy of the BAC model in describing the band structure of GaNAs, including the electronic structure both away from and close to the N resonant state energy. We directly solve a simplified random impurity model Hamiltonian for a very large supercell of GaNAs. We calculate the exact eigenstates of this Hamiltonian, and compare their behaviour with that predicted by the BAC model. We calculate the fractional Γ character, participation ratio and the density of states in the supercell, and compare these results with those calculated in BAC model to examine the validity of BAC model. Our results confirm the validity of the BAC model to describe states whose energy is well separated from the N resonant state energy. Our results also show that states with energy close to the N level energy are likely to be localised, implying a breakdown in the k selection assumed in the BAC model for such states. We discuss briefly the consequences of this state localisation for electron transport at high electric fields in dilute nitride alloys.

4.2 Supercell model

In order to test the BAC model, we consider a large supercell of side length L, with M randomly placed nitrogen states in the supercell. Using the many-impurity model [31, 34, 35], the Hamiltonian of this system can be written following Eqs. (2.2) to (2.4) as

$$H = \sum_{\mathbf{k}} E_{\mathbf{k}} |\mathbf{k}\rangle\langle\mathbf{k}| + \sum_{j=1}^{M} E_N |j\rangle\langle j| + \sum_{\mathbf{k},j} V_{Nc} \Big[e^{i\mathbf{k}.\mathbf{R}_j} |\mathbf{k}\rangle\langle j| + e^{-i\mathbf{k}.\mathbf{R}j} |j\rangle\langle\mathbf{k}| \Big], \quad (4.1)$$

where the first and second terms describe the energies of extended and localised states, labeled by wave vector $|\mathbf{k}\rangle$ and position vector $|j\rangle$, respectively. The last term represents the interaction between the extended and localised states, where $\mathbf{R}_j$ is the position of the j-th N atom, $\mathbf{k}$=(k_x, k_y, k_z) is the wavevector, and V_{Nc}=$\beta/N_c^{1/2}$ is the interaction parameter.

The first term in the Hamiltonian in Eq. (4.1) describes the host matrix CB states satisfying periodic boundary conditions in the supercell, given by

$$\psi_{n_x,n_y,n_z} = \frac{1}{(L_x L_y L_z)^{1/2}} \exp\left[i2\pi(\frac{n_x x}{L_x} + \frac{n_y y}{L_y} + \frac{n_z z}{L_z})\right], \tag{4.2}$$

with energy equal to

$$E_{n_x n_y n_z} = \frac{4\pi^2\hbar^2}{2m^*}\left[\left(\frac{n_x}{L_x}\right)^2 + \left(\frac{n_y}{L_y}\right)^2 + \left(\frac{n_z}{L_z}\right)^2\right] + E_c, \tag{4.3}$$

where n_x, n_y and n_z are quantum numbers in the x, y and z directions, respectively. We include in our calculations all host states with energy $E_{n_x n_y n_z} \leq E_{max}$, where E_{max}=$4\pi^2\hbar^2 l^2/(m^* L^2)$, and l is a positive integer.

The second term in Eq. (4.1) describes the M nitrogen states in the supercell, where M=xN_c. In each cubic unit cell volume a_0^3, we have 4 group V atoms. So for a supercell with side length L=$L_0 a_0$, we have N_c=$4L_0^3$ such atoms. Thus, for GaN_xAs_{1-x}, x=M/N_c=$M/4L_0^3$, and V_{Nc}=$\beta/(4L_0^3)^{1/2}$. For most calculations described below, we took a 4 million atom supercell (L_0=100), adding M=8000 N atoms, and choosing l=11, so that E_{max}=0.857 eV, with the zero of energy at the GaAs conduction band edge energy, E_c.

As mentioned in Chapter 3, the N energy, E_N in Eq. (4.1) differs by ΔE_N from the value E'_N in Eq. (3.1), because the interaction with the CB states shifts the mean N energy. From Eq. (3.2), ΔE_N=$-$13.3 meV when we choose E_N=0.23 eV and E_{max}=0.857 eV.

Using the Hamiltonian H we can then calculate directly different parameters for the chosen supercell. In the rest of this chapter, we calculate for supercell states their fractional Γ factor, the density of states, and wave function participation ratio for GaN_xAs_{1-x} with x=0.2%, and compare the results with the BAC model.

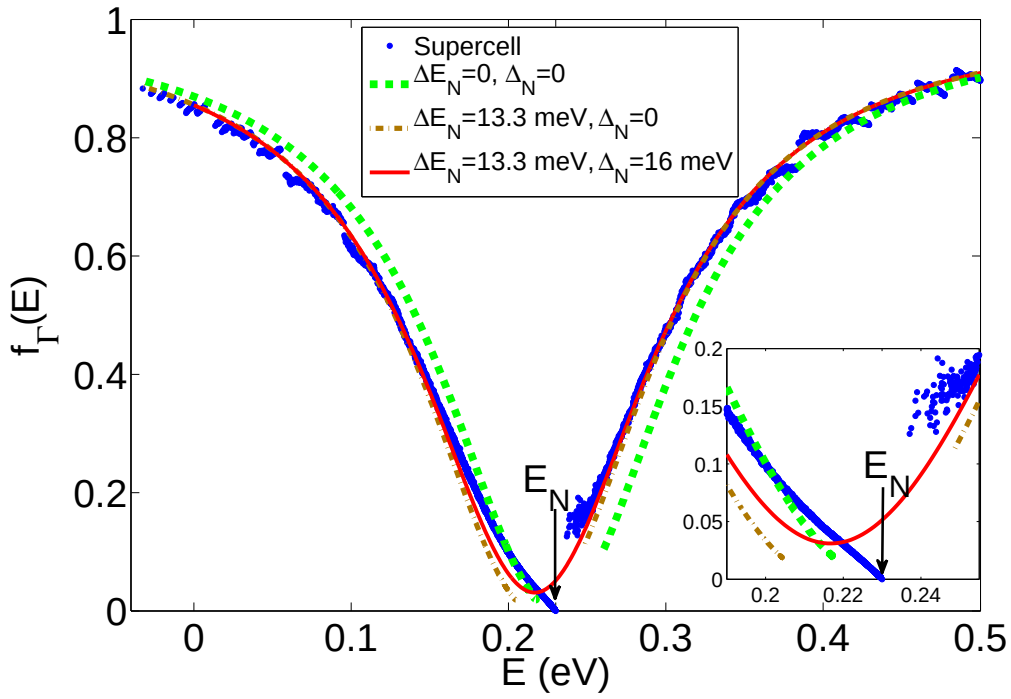

Figure 4.1: Fractional Γ character of the energy eigenstates in a x=0.2% calculation for cell size L=100a_0 (blue dots), compared with results from the BAC model when (i) ignoring the shift and broadening in N energy (dashed green line), (ii) including the shift in E_N (dash-dotted brown line), and (iii) considering the shift and broadening in E_N (solid red line). All energies are referenced to the GaAs CBE. The inset shows the details of the same plot around nitrogen energy E_N.

4.3 Fractional Γ character

The supercell conduction band states $|c_i\rangle$, are a linear combination of the original GaAs conduction band states $|\mathbf{k}\rangle$ and localised states $|j\rangle$. We can calculate the fractional Γ character f_Γ of a supercell eigenstate by summing the CB state weights, $|\langle\mathbf{k}|c_i\rangle|^2$ over all $\mathbf{k}$, where f_Γ provides a measure of the host matrix character of a given state. f_Γ is equal to the ratio of the GaAs to the alloy effective mass. The blue dots in Fig. 4.1 show the Γ character calculated for the large supercell of size L_0=100, with M=8000.

In the BAC model ignoring the N broadening ($\Delta_N = 0$), the conduction band weight at energy E for the upper (α_k^+) and lower band (α_k^-) can be calculated by

$$\alpha_k^\pm = \sqrt{(1 \pm \alpha_p)/2}, \tag{4.4}$$

where α_p is

$$\alpha_p = \frac{(E_k - E'_N)}{\sqrt{(E'_N - E_k)^2 + 4V_{Nc}^2}}. \tag{4.5}$$

The dashed green line in Fig. 4.1, shows the variation of $f_\Gamma = |\alpha_{\mathbf{k}}^{\pm}|^2$ calculated using the 2-band BAC model of Eq. (3.1) with ΔE_N=0 (E_N=0.23 eV) and Δ_N = 0, where $\alpha_{\mathbf{k}}^{\pm}$ is the amplitude for $E_\pm$ of the BAC eigenstate on the host $\mathbf{k}$ state given by Eq. (4.4). The dash-dotted (brown) line in Fig. 4.1 shows the 2-band f_Γ when we include this shift (E'_N=0.2167 eV). Very good agreement is obtained over a wide energy range between the supercell calculation and the BAC model with shifted N energy in Fig. 4.1. It can be seen however that for energies just below E_N the numerical results move toward the BAC model result with the original unshifted N energy.

In order to consider N broadening when calculating fractional Γ character, we can use Eq. (3.11), as obtained in Chapter 3

$$f_\Gamma = \left(1 + \frac{V_{Nc}^2}{\left(E - E'_N\right)^2 + \Delta_N^2}\right)^{-1}. \tag{4.6}$$

The red solid line in Fig. 4.1 shows f_Γ calculated using Eq. (4.6), and with ΔE_N, and Δ_N calculated using second perturbation theory, as discussed in Chapter 3. This result shows much better agreement with the supercell calculation, but for energies close to E_N, there are still some discrepancies between the supercell and BAC models.

4.4 Density of states

4.4.1 The DOS projected to a single state

The density of states projected onto a single CB momentum eigenstate (n_x, n_y, n_z) is given by

$$D_{n_x,n_y,n_z}(E) = \sum_i \delta(E - E_i)|a^i_{n_x,n_y,n_z}|^2, \tag{4.7}$$

where $a^i_{n_x,n_y,n_z}$ is the amplitude of the i^{th} wave function on the given CB state. We use a Gaussian function with broadening parameter ϵ=3 meV to represent the δ-function. The solid blue lines in Fig. 4.2.(a) show how the density of states projected onto the individual $\mathbf{k}$ states varies with increasing energy E_k of the $\mathbf{k}$ states. The dashed red lines in this figure display the results calculated by the BAC model. As we discussed in Chapter 3, the DOS projected onto a single $\mathbf{k}$

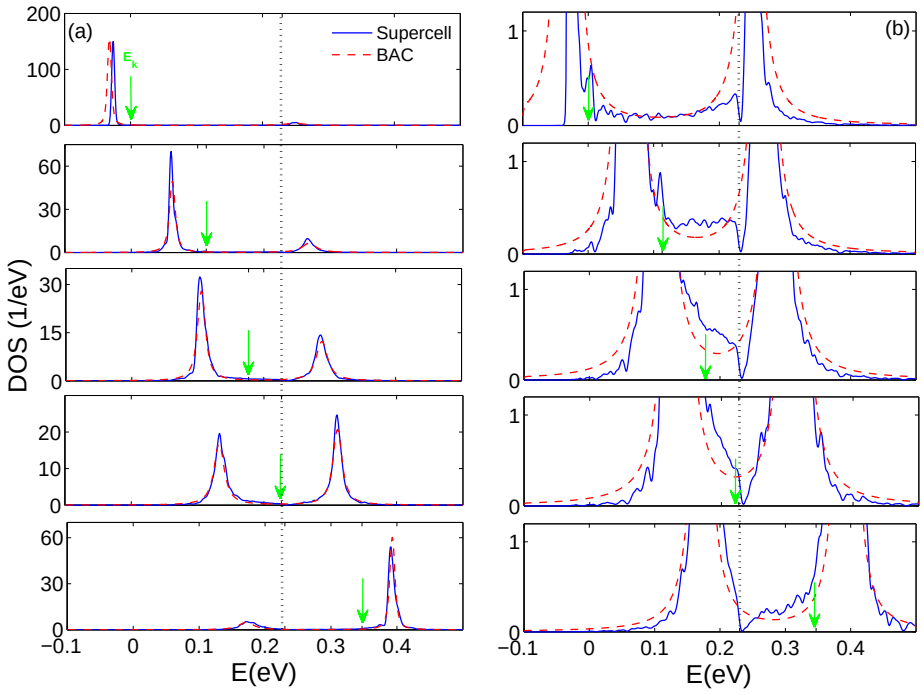

Figure 4.2: (a) The Density of states projected onto selected GaAs $|k\rangle$ states, calculated using the BAC model (dashed red lines) and using the numerical model for a box with L_0=100, l=11, M=8000, x=0.2% and ϵ=3 meV (solid blue lines), and the BAC model (dashed red lines). Arrows show the energy E_k of the original **k** state, and dotted line displays the N energy, E_N(=0.23 eV). (b) The same plot at very low DOS values.

state is given by Eq. (3.23). Overall we see a good agreement between the BAC model (with energy broadening and shifted N energy) and our supercell model eigenstates. Small differences are observed near the CB edge, E_k=0. However, for E_k near the N state energy, the results of the BAC model are very similar to the supercell calculations. A strong splitting of bands is seen especially near the N state energy.

However, the BAC model does not reproduce all the details of the DOS. Fig. 4.2.(b) (on the right hand side), shows the same plots but on a scale to highlight the regions with a low DOS, where the two models do not agree well. Despite the very good agreement between the BAC and supercell models at the peaks of the DOS, their details far from the peaks are different. In fact the supercell model predicts a small gap around E_N, while the BAC model incorrectly fills this gap. We shall return to discuss the details further following the introduction of a self-consistent Green's function method in the next chapter.

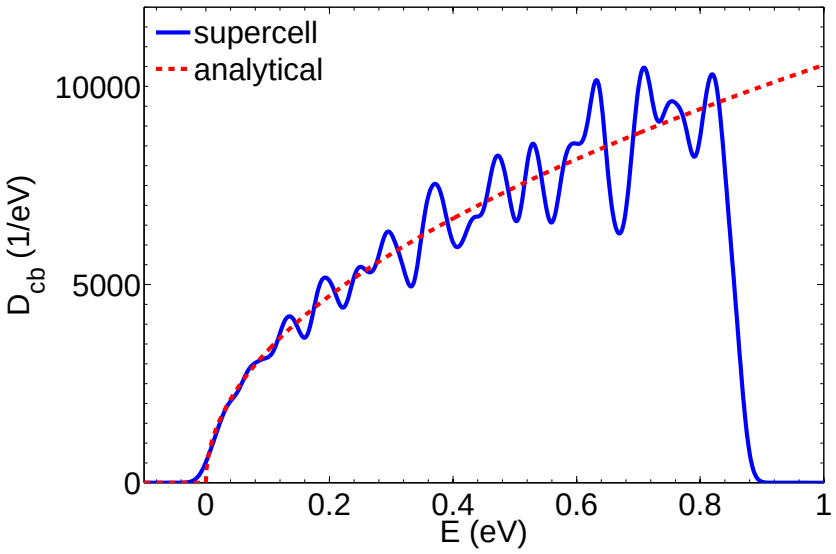

Figure 4.3: GaAs DOS calculated for a supercell with L=100a_0 (solid line) and analytically (dashed line).

4.4.2 Density of states projected to CB

We consider now the 3D density of states for a supercell of size L^3. We showed in Chapter 3 that this is given for the BAC model by Eq. (3.15). The DOS projected onto the GaAs CB states, in the supercell calculation, is

$$D_{cb}(E) = \sum_{i,\mathbf{k}} \delta(E - E_i)|a^i_{\mathbf{k}}|^2. \tag{4.8}$$

Figure 4.3 shows the DOS of GaAs in the absence of N, determined by the numerical calculation for the supercell with L=100a_0, l=11 (E_{max}=0.857 eV), and a Gaussian broadening ϵ=20 meV (solid line), compared to the DOS calculated analytically by Eq. (3.16) (dashed line). As expected very good agreement is observed in this figure, confirming the validity of our supercell calculation. The fluctuations in the numerical result arises because we only carry out calculations for superlattice wavevector $\vec{q} = 0$. The DOS could be further smoothed either by carrying out calculations over the full superlattice Brillouin zone ($|q_x|, |q_y|, |q_z| < \pi/(L_0 a_0)$), or else by further increasing the box size, L.

The solid red line in Fig. 4.4 shows the DOS projected onto the host CB states for a GaN_xAs_{1-x} supercell with x=0.2% and E_{max}=0.857 eV. This is compared with the projected DOS from the BAC model of Eq. (3.15) with E_{max}=∞, with (blue, dashed) and without (brown, dash-dotted) broadening. The unbroadened DOS in the BAC model has an (integrable) divergence as E approaches the N state energy, due to the infinite set of $\mathbf{k}$ values allowed for in Eq. (3.1). The DOS

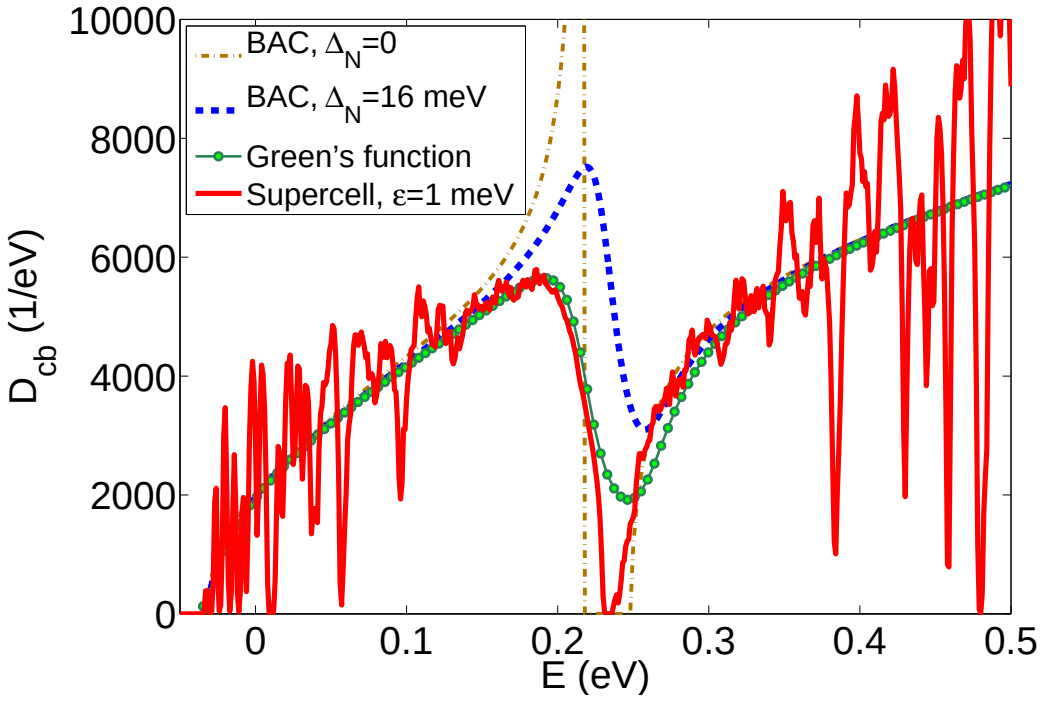

Figure 4.4: The DOS projected onto the GaAs CB states for GaN_xAs_{1-x} with x=0.2%; obtained from (i) the BAC model with and without N broadening, and assuming E_{max}=∞ (dashed red and dash-dotted brown lines, respectively), (ii) a supercell calculation including 8000 N (solid red line), and (iii) a Green's function method with E_{max}=0.857 eV (green dots). Energies are referenced to the bottom of the GaAs CB, and E_N is taken to be 0.23 eV.

calculated in the supercell model agree well with the BAC results for energies far from E_N. However, for energies around E_N the BAC model with an infinite CB predicts a much higher DOS than the supercell calculation. In order to confirm the effect of the infinite CB on the DOS calculated by Eq. (3.15), we also use the Green's function approach to calculate the DOS projected onto the host semiconductor CB states. The green circles in Fig. 4.4 show the DOS calculated using the Green's function method by Eq. (3.20), with a cut-off energy equal to that for the supercell calculation. A much better agreement is observed between the supercell and GF calculation with the same cut-off energy. However, contrary to the Green's function and BAC method, the supercell calculation shows a gap in the DOS of GaNAs alloys. But, this gap is much smaller than the one predicted by the original BAC model without N broadening (shown by the dash-dotted brown line in this figure). The DOS calculated in the supercell model in Fig. 4.4 confirms the gap already seen in the DOS projected onto single momentum states in Fig. 4.2, in disagreement with the Green's function approach (equivalent to

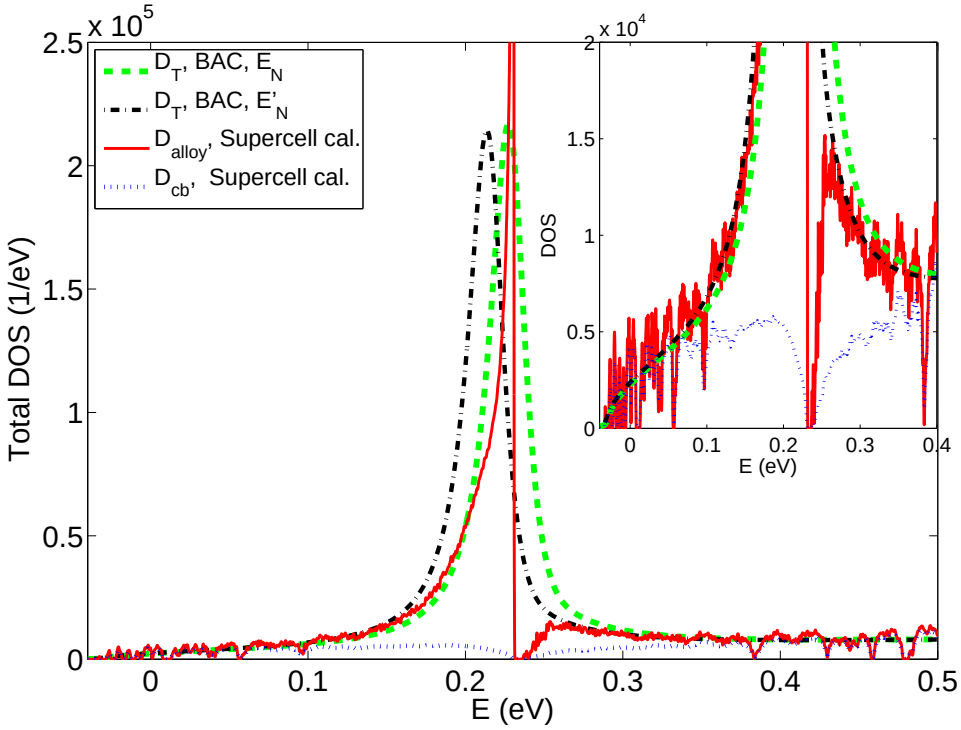

Figure 4.5: The total DOS calculated for $GaN_{0.002}As_{0.998}$ supercell for a box with $L = 100a_0$ and $\epsilon = 1$ meV (solid blue line), compared with the results of the BAC model with(dash-dotted line) and without (dashed green line) the shift in E_N. The dotted blue line shows the numerical DOS projected onto the host CB states. The inset shows the details of the same plot at lower values of DOS.

the BAC model with N broadening Δ_N and a maximum conduction band energy, $E_{max} = 0.857$ eV).

4.4.3 Total density of states

The total DOS in the supercell calculation is given by

$$D_{alloy}(E) = \sum_i \delta(E - E_i). \tag{4.9}$$

In the BAC model the total DOS can also be found by dividing the DOS projected onto the CB by the fractional Γ factor, $D_{alloy} = D_{cb}/f_\Gamma$. The red solid line in Fig. 4.5 shows the numerical results of total DOS calculated for a box with $L_0 = 100$, $l = 11$, and including 8000 N atoms ($x = 0.2\%$ and $E_{max} = 857$ meV). Near to the N energy, E_N, the DOS projected onto the N states is clearly much larger than the DOS projected onto the host CB states (dotted blue line). The dashed green line in this plot shows the total DOS calculated in the BAC model

ignoring the shift in E_N while the dash-dotted black line includes this shift, ΔE_N. We see that the BAC model with the shifted N energy predicts a correct total DOS for energies far from E_N. However, just below the N energy, in the low energy side of the peak in the total DOS, the BAC model with unshifted N energy gives better agreement with the numerical results. In addition, the BAC model with constant broadening Δ_N fills in the gap that is observed in the supercell model calculation.

4.5 Participation ratio

We investigate the degree of localisation of each state by calculating the participation ratio L for the CB part of each wave function, given by [64, 65]

$$L(E_i) = \frac{V \int_V d^3\mathbf{r} |\psi_i^{cb}(\mathbf{r})|^4}{\left(\int_V d^3\mathbf{r} |\psi_i^{cb}(\mathbf{r})|^2 \right)^2}, \tag{4.10}$$

where $\psi_i^{cb}(\mathbf{r}) = \sum_{\mathbf{k}} a_{\mathbf{k}}^i \exp(i\mathbf{k}.\mathbf{r})$, and $V = L_0^3 a_0^3$ is the supercell volume. Fig. 4.6 shows the calculated participation ratio for all states in a supercell with length L_0=50, containing M=1000 N, (x=0.2%) and with l=12. The stronger the localisation, the larger the participation ratio. To compare with the BAC model, the

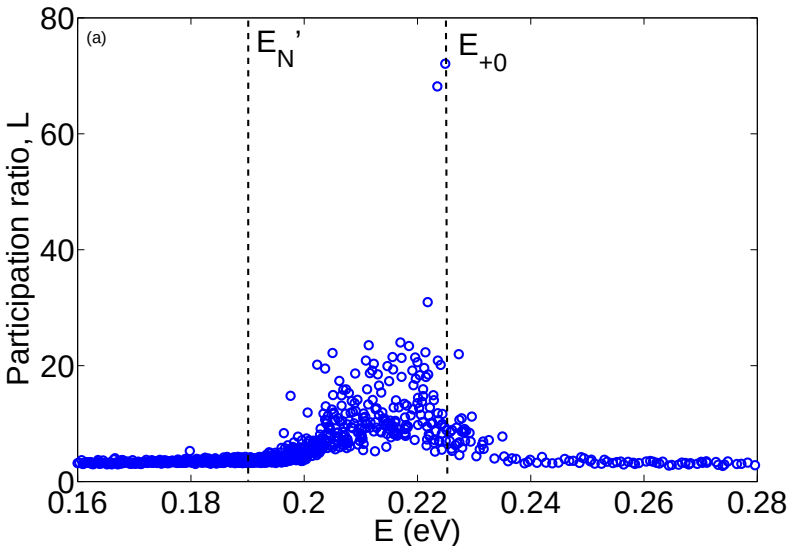

Figure 4.6: Participation ratio calculated from Eq. (4.10) for the supercell of size L_0=50, with M=1000 and l=12. Vertical lines display band edges predicted by the BAC model with E_{max}=4.08 eV.

maximum of the lower band E'_N, and minimum of the upper band E_{+0}, are indicated on the figure. The larger values of $L(E)$ in the BAC gap indicate that the states in this energy range (which have predominantly N character) are localised, in agreement with the experimental analysis of Patanè *et al.* [15, 22]. Note that in this figure the gap predicted in earlier calculations is filled because of a very high cut-off energy (E_{max} = 4.08 eV). We conclude, given the large density of N-related states near the N energy in Fig. 4.4(b) and the localised nature of these states from Fig. 4.6 that we may need to use a hopping transport model to describe conduction through such states when investigating high field transport in dilute nitride alloys.

4.6 Summary

We have shown by direct comparison with a supercell model Hamiltonian that the BAC model provides a good description of the electronic structure of dilute nitride alloys at energies which are well separated from the N state energy. For simplicity, we have neglected the effect of nitrogen pairs or larger clusters, that would provide further perturbation and localisation in conduction band of the host semiconductor [7, 24]. Our calculations show that the electronic structure deviates from that predicted using the BAC model close to the N resonant state energy, due to the finite density of N-related states, and carrier localisation effects (breakdown of $\mathbf{k}$ selection). We conclude that it may be necessary when modeling transport to consider hopping through the N states, at energies close to the N resonant state and BAC energy gap range.

Our results for the fractional Γ character and total DOS suggest that we need to consider the energy dependence of $\Delta E_N(E)$ and $\Delta_N(E)$ instead of a constant shift in the N energy, ΔE_N, and N broadening, Δ_N. We introduce in the next chapter a self-consistent Green's function method to do so.

Chapter 5

Self-consistent Green's function method

5.1 Introduction

In previous chapters we have seen that the BAC model gives a good explanation of many aspects of the electronic structure of dilute nitride alloys, such as the strong reduction in the energy gap with increasing nitrogen concentration [9]. Also, the dispersion relations calculated by the BAC model, close to and above the CBE is in good agreement with experiments in samples with very low x [22].

However as we saw in previous chapters, there is no maximum cut-off wavevector, k_c, in the BAC model, Eq. (3.1), which introduces errors in the density of states (DOS) and in high-field mobility calculations [66]. Furthermore, the BAC model considers only isolated N states, and ignores states associated with N pairs [7], where a Ga atom has two N neighbours, as well as ignoring states associated with larger clusters of N atoms [51, 63]. Such pair and cluster states have been shown to be very important for determining the band edge effective mass and transport properties of GaNAs alloys [13, 66].

Wu *et al.* [18] and then Vaughan and Ridley [32] developed the Green's function method to investigate the band dispersion and density of states in dilute nitride alloys, treating the N state energy broadening in terms of a constant imaginary energy shift ΔE_N, which arises due to the N states introduced being resonant with the host semiconductor conduction band. Vaughan and Ridley calculated the DOS of GaNAs in the two and three band models (including isolated N and pair, N-N, states), introducing a Lorentzian function to represent the N broadening. They assumed the same constant broadening energy for both N and N-N states [34]. Vogiatzis and Rorison [35, 36] have also studied the Anderson

model using Matsubara Green's function method and calculated the band structure and density of states of bulk and confined quantum well and quantum wire GaInNAs structures.

In chapters 3 and 4, the model of Vaughan and Ridley was modified by calculating both the real and imaginary parts of the nitrogen state energy shift, ΔE_N, using second order perturbation theory. This approach leads to a filling of the gap in the DOS of GaNAs, even in the 2-level BAC model, in agreement with measurements [29]. Although these results agree well with supercell calculations for energies far from the N energy level E_N, there are some disagreements close to E_N, indicating the need for a deeper investigation of the energy shift obtained in the Green's function calculations of the band structure of dilute nitride alloys. We show here that there are some aspects of the usual Green's function approach that introduce errors that can become significant, especially when treating high-field mobility.

Here we modify the Green's function (GF) method developed by Vaughan and Ridley [33, 34] by introducing an energy-dependent complex energy, $\Delta E_j(E)$, where the real and imaginary parts of ΔE_j indicate the shift in energy and broadening, respectively, of the localised states due to the energy dependence of the alloy density of states. In previous chapters we used constant values of $\Re[\Delta E_j]$ and $\Im[\Delta E_j]$ as the real and imaginary parts of the energy shift, calculated using second order perturbation theory. Here we first calculate an energy-dependent broadening $\Delta E_j(E)$ using a **S**elf-**C**onsistent **G**reen's **F**unction (SCGF) method, in which the energy shift of the nitrogen states and the conduction band density of states are calculated self-consistently. We then investigate the effect of the energy-dependent broadening on the calculated DOS of GaNAs.

In this chapter two models are considered; (1) the 2-band model (assuming all N states have the same energy) and (2) a **L**inear **C**ombination of **I**solated **N**itrogen **S**tates (LCINS) model [11, 17], which allows for interaction between N states on nearby sites as well as inhomogeneous broadening and produces a distribution of N state energies. We compare the SCGF results for the 2-band model with those calculated using the BAC model, and also with those calculated using the supercell approach of Chapter 4, where we solved the single particle Hamiltonian for a very large supercell containing randomly placed N states.

In the two-band model, the usual Green's function method (with constant nitrogen state broadening ΔE_N) predicts a continuous DOS in the CB with no gap, whereas the self-consistent Green's function method gives a gap in the CB, introduced above the N energy E_N, that increases in magnitude with increasing

N concentration x.

When the self-consistent approach is used with the full LCINS model, it can be used to calculate the energy shift $\Delta E_j(E)$ for each localised state j as a function of energy. This should lead to a more accurate treatment of the band structure in dilute nitride alloys, with the inhomogeneous broadening of the N states in the LCINS model then playing a critical role in determining the behaviour of the band dispersion at energies close to the N resonant state energies.

In the next section we introduce the self-consistent approach to treating the Green's function and show how to find the energy-dependent energy shift $\Delta E_j(E)$. We then present in § 5.3 the results for the DOS, projected onto extended and localised states, and the band structure for the two-level SCGF method. We benchmark our two-band model results by comparing them with supercell calculation results to confirm their validity. Afterward, in § 5.4 we include the full distribution of LCINS states and investigate the consequences of this broad distribution of localised states for the DOS of GaNAs alloys. We then in § 5.5 compare the band dispersion of the two-band and LCINS model, calculated by the SCGF method for GaN_xAs_{1-x}. Finally we discuss and summarise our conclusions in § 5.6.

5.2 Self-consistent Green's function method

In Chapter 2 we saw that in the many impurity Anderson model, the Hamiltonian for a set of localised N states interacting with the host matrix conduction band states using Eqs. (2.2)-(2.4) can be written as

$$H = \sum_{\mathbf{k}} E_{\mathbf{k}} |\mathbf{k}\rangle\langle\mathbf{k}| + \sum_{j=1}^{M} E_j |j\rangle\langle j| + \sum_{\mathbf{k},j} \frac{1}{\sqrt{N_c}} \Big[V_j e^{i\mathbf{k}.\mathbf{R}_j} |\mathbf{k}\rangle\langle j| + V_j^* e^{-i\mathbf{k}.\mathbf{R}_j} |j\rangle\langle\mathbf{k}| \Big]. \quad (5.1)$$

The exact solutions of the Hamiltonian in Eq. (5.1) can be obtained from the Green's function [30]

$$G_{kk}(E) = \left\{ E - E_k - \frac{1}{N_c} \sum_j \frac{|V_j|^2}{E - E_j - \Delta E_j(E)} \right\}^{-1}, \quad (5.2)$$

where the (complex) energy shift of each localised state j is given by

$$\Delta E_j(E) = \frac{|V_j|^2}{N_c} \sum_k G_{kk}(E). \quad (5.3)$$

The Green's function of localised states G_{jj} in addition is given by

$$G_{jj}(E) = \frac{1}{E - E_j - \Delta E_j(E)}. \tag{5.4}$$

When all the localised states have the same energy, $E_j = E_N$, the same interaction parameter value $V_j = \beta$, and have an atomic concentration x, Eq. (5.2) becomes

$$G_{kk}(E) = \left\{ E - E_k - \frac{V_{Nc}}{E - E_N - \Delta E_N(E)} \right\}^{-1}, \tag{5.5}$$

and Eq. (5.3) becomes

$$\Delta E_N(E) = \frac{\beta^2}{N_c} \sum_k G_{kk}(E). \tag{5.6}$$

where the coupling matrix element V_{Nc} between the nitrogen and CB states in Eq. (3.1) then depends explicitly on nitrogen concentration x, as V_{Nc}=$\beta x^{1/2}$ [6, 10].

Equations (5.2) and (5.3) do not in general admit an analytical solution. However, by assuming all the localised states have the same energy, and by assuming that $\Delta E_j(E)$ can be approximated by an imaginary constant broadening energy $i\Delta_j$, Wu *et al.* [18] solved the Green's function, using Anderson's many-impurity model in the coherent potential approximation [31]. Vaughan and Ridley [32, 33] generalised this method to include additional nitrogen clusters such as N-N pairs sharing a nearest neighbour Ga ion, with the Green's function G_{kk} given by [30]

$$G_{kk}(E) = \left\{ E - E_k - \frac{1}{N_c} \sum_j \frac{|V_j|^2}{E - E_j + i\Delta_j} \right\}^{-1}, \tag{5.7}$$

Vaughan and Ridley [34] then calculated the density of states of GaNAs from the imaginary part of the Green's function, assuming Δ_j is constant and the same for all N levels E_j. In Chapter 3 we extended this model by approximating $G_{kk}(E)$ in Eq. (5.3) by $G^0_{kk} = 1/[E - E_k]$, that still allowed an analytical solution.

Here, we go beyond these previous approaches and apply the Green's function method, taking fully into account the modification of the conduction band (CB) Green's function $G_{kk}(E)$ that is induced by its interaction with all localised states. This requires us to solve Eqs. (5.2) and (5.3) self-consistently.

5.2.1 The density of states

It can be shown that the density of states projected onto the host semiconductor momentum states is given by [34]

$$D_{cb}(E) = -\frac{1}{\pi}\sum_{k}\Im[G_{kk}(E)], \tag{5.8}$$

and the density of states projected onto the localised states is given by

$$D_{loc}(E) = -\frac{1}{\pi}\sum_{j}\Im[G_{jj}(E)], \tag{5.9}$$

where G_{kk} and G_{jj} are calculated by solving equations (5.2) to (5.4) self-consistently. Eq. (5.8) can be written, by replacing the sum over k with an integral over energy, as

$$D_{cb}(E) = -\frac{1}{\pi}\Im\int_{0}^{\infty} G_{kk}(E)D_0(E_k)dE_k, \tag{5.10}$$

where $D_0(E_k)$ is the host semiconductor density of states given by $(2m^*)^{3/2}E_k^{1/2}/(4\pi^2\hbar^3)$, and we have taken the zero of energy at the host matrix CBE. Defining $\gamma(E)$ as

$$\gamma(E) = E - \frac{1}{N_c}\sum_{j}\frac{|V_j|^2}{E - E_j - \Delta E_j(E)}. \tag{5.11}$$

G_{kk} can then be written as $G_{kk}(E) = [\gamma(E) - E_k]^{-1}$. Therefore, the DOS projected onto the extended states can be written as

$$D_{cb}(E) = -\frac{1}{\pi}\frac{(2m^*)^{3/2}}{4\pi^2\hbar^3}\Im\int_{0}^{E_{max}}\frac{E_k^{1/2}dE_k}{\gamma(E) - E_k}, \tag{5.12}$$

where E_{max} is the upper limit of the energy of the band states that couple with interaction matrix element V_j to the localised states. Because $\gamma(E)$ is independent of E_k, we can evaluate this integral as

$$\int_{0}^{E_{max}}\frac{E_k^{1/2}dE_k}{\gamma - E_k} = -2E_{max}^{1/2} + \sqrt{\gamma}\ln\left(\frac{1+\sqrt{E_{max}/\gamma}}{1-\sqrt{E_{max}/\gamma}}\right). \tag{5.13}$$

We note that the real part of this integral (and, hence, the real part of the energy shift ΔE_j) is not well-defined as $E_{max} \to \infty$. However, for $E_{max} >> |\gamma|$, the

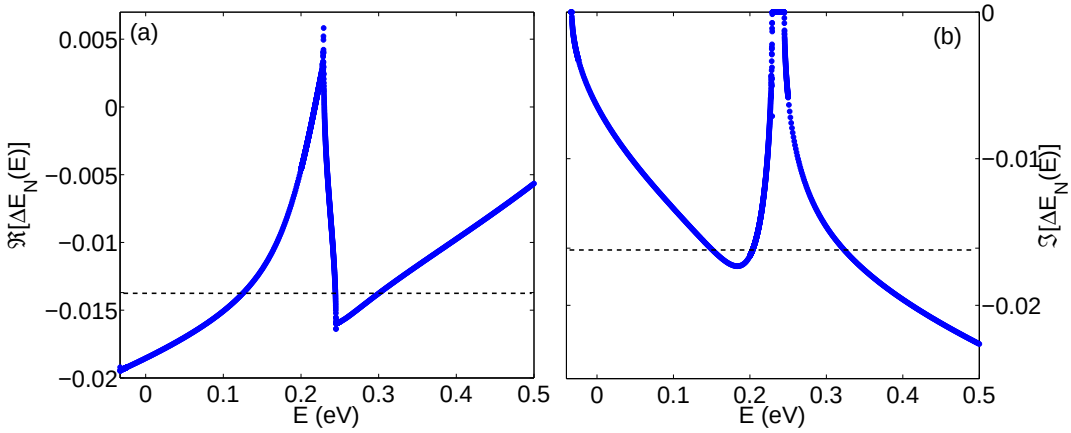

Figure 5.1: (a) The real and (b) the imaginary parts of the energy shift $\Delta E_N(E)$ for the two-band model of GaN_xAs_{1-x} with $x = 0.2\%$. The horizontal dashed lines display the values obtained in second order perturbation theory.

logarithmic factor tends to $\ln(-1) = -i\pi$ and the imaginary part of this integral is given by

$$\Im\Big(- i\pi\gamma^{1/2} - \Big[2E_k^{1/2}\Big]_0^{\infty}\Big) = -\pi\Re\big(\gamma(E)^{1/2}\big), \tag{5.14}$$

from which we can find the projected DOS

$$D_{cb}(E) = \frac{(2m^*)^{3/2}}{4\pi^2\hbar^3}\Re\big[(\gamma(E))^{1/2}\big]. \tag{5.15}$$

If we denote the real and imaginary parts of $\gamma(E)$ by $\Gamma(E)$ and $\Phi(E)$, respectively, Eq. (5.15) can then be written as

$$D_{cb}(E) = \frac{m^{*3/2}}{2\pi^2\hbar^3}\left[\Gamma(E) + \Big(\Gamma^2(E) + \Phi^2(E)\Big)^{1/2}\right]^{1/2}. \tag{5.16}$$

Having calculated ΔE_j and $\gamma(E)$ self-consistently, using a finite value of E_{max}, we may then take the limit of $E_{max} \to \infty$ in examining the density of states, as given by Eqs. (5.15) and (5.16). Note, however, that the real part of ΔE_j is not well-defined.

5.3 The two-level SCGF

In the two-band model we assume all the N states lie at the same energy, $E_N = 0.23$ eV, with interaction strength $\beta = 2.0$ eV [13], the host matrix conduction band energy at $E_c = 0$ eV, and electron effective mass $m^* = 0.067m_0$ where m_0 is

the free electron mass. To calculate the DOS we consider real energies E, while allowing that $\Delta E_N(E)$ is a complex quantity. In order to solve Eqs. (5.5) and (5.6) self-consistently, the initial value of $\Delta E_N(E)$ in Eq. (5.5) is found using second order perturbation theory. In the calculations presented here, the upper limit of the band energy is taken to be $E_{max} = 856$ meV. $G_{kk}(E)$, given by Eq. (5.5), is then used in Eq. (5.6) to calculate a new value of $\Delta E_N(E)$. We continue in this way until we reach a converged value for $\Delta E_N(E)$. We find that 40 iterations are sufficient to reach a converged value of $\Delta E_N(E)$ for all real E, and that as few as 2 iterations give a good estimate of the DOS for energies away from the energy gap in this case.

Figure 5.1 shows the real and imaginary parts of (converged) $\Delta E_N(E)$ calculated by the SCGF method. This figure presents the main result of our SCGF method. In previous work we used constant values for $\Im(\Delta E_N)$ and $\Re(\Delta E_N)$ shown by the horizontal dashed lines in Fig. 5.1. From Eqs. (5.6) and (5.8) it is clear that $-\Im(\Delta E_N(E))$ is proportional to the density of states in the 2-level BAC model. $\Re(\Delta E_N(E))$ monotonically increases from -20 meV at the bottom of the lower band to +5 meV at the top of the band, decreases sharply with E in the band gap, and again monotonically increases in the upper band.

5.3.1 The DOS for the two-level SCGF model

Figure 5.2 shows the evolution of the density of states for different numbers of iterations, s, for $GaN_{0.002}As_{0.998}$. The red dashed line in this figure displays the DOS calculated by the ordinary (non-self-consistent) Green's function calculation ($s = 1$), that predicts a continuous and finite CB DOS at all E in the two-band model. However after a sufficient number of iterations a gap appears in the DOS, as shown by the blue solid line in Fig. 5.2.

We presented in Chapter 4 a supercell model to calculate the density of states of GaNAs alloys. We used the Hamiltonian given by Eqs. (5.1)-(2.4), assuming that all N states have the same energy E_N, the interaction parameter is given by $V_{Nc} = \beta/N_c^{1/2}$, and including all host states with energy less than $E_{max} = 4\pi^2\hbar^2 l^2/(mL^2)$. ($l$ is a positive integer.) In this model the DOS projected onto the GaAs CB states is given by

$$D_{cb}(E) = \sum_{i,k} \delta(E - E_i)|a_k^i|^2, \tag{5.17}$$

where a_k^i is the amplitude of conduction band state k in the i^{th} wave function. We use a Gaussian function below with broadening parameter ϵ to represent the

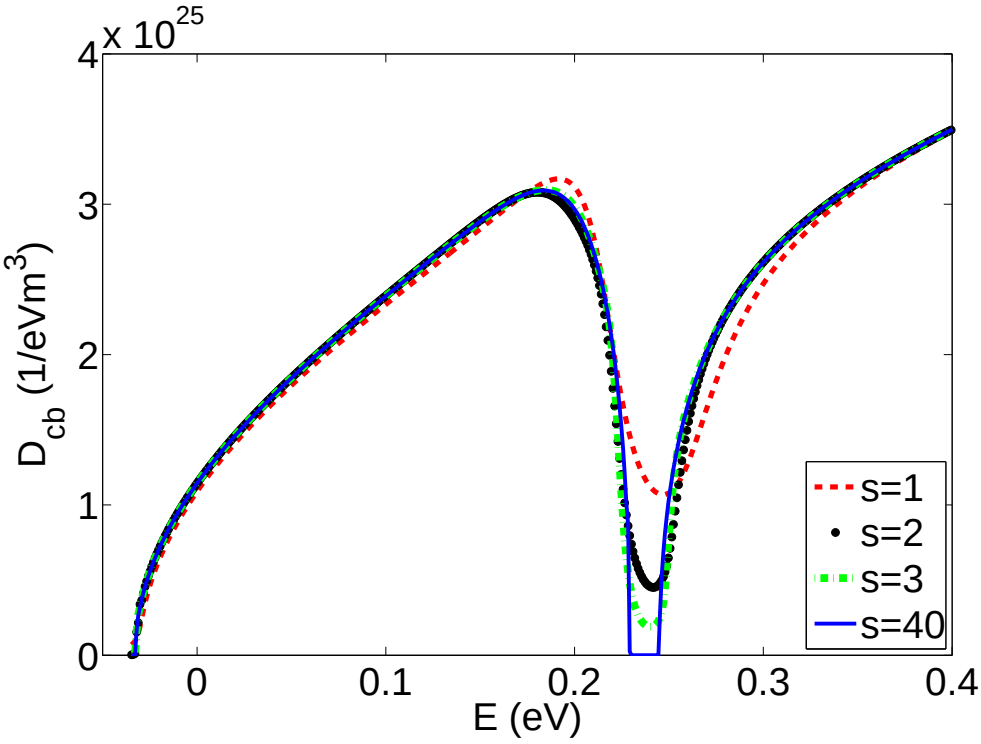

Figure 5.2: The density of states for GaN_xAs_{1-x} with $x = 0.2\%$, for different number of iterations s, of the two-band SCGF method, assuming all N states have the same energy.

δ-function.

Figure 5.3 compares the density of states obtained by the self-consistent Green's function method, with the result of the supercell calculation, with superlattice wavevector $\mathbf{q} = 0$, for GaN_xAs_{1-x} with $x = 0.2\%$ for a box of side length $L = 100a_0$, with $M = 8000$ randomly placed nitrogen states, $E_{max} = 856$ meV, and Gaussian broadening $\epsilon = 1$ meV and $\epsilon = 10$ meV. In our earlier work [60], we chose $\epsilon = 20$ meV, that showed a very good agreement with the results of the (ordinary) Green's function method with constant ΔE_N, predicting a continuous CB with no gap in the DOS. However, our current calculations (by considering the SCGF approach) do not confirm this assumption. Considering higher values for Gaussian broadening in the supercell calculation makes the density of states much smoother, but it obscures the presence of an energy gap. The DOS calculated with $\epsilon = 1$ meV (solid red line) shows very good agreement with the one calculated by the SCGF method, confirming the presence of the gap in the two-level model. The noisy behaviour in this spectrum arises because we only carry out our calculations for superlattice wavevector $\mathbf{q} = 0$. The DOS could be further smoothed either by carrying out calculations over the full superlattice Brillouin

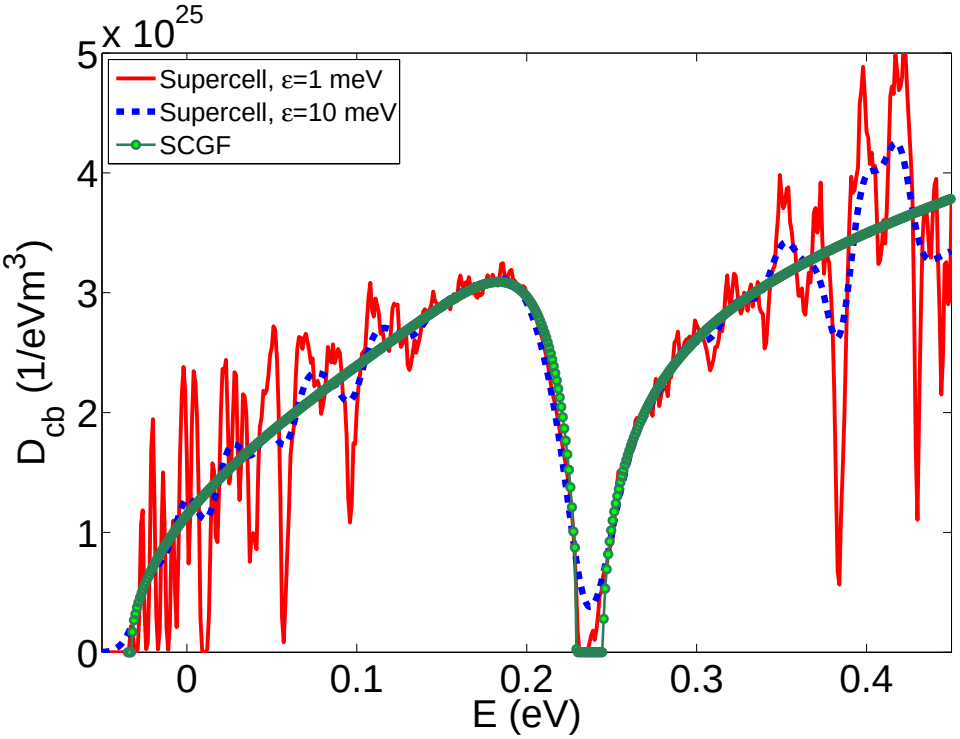

Figure 5.3: The density of states for GaN_xAs_{1-x} with $x = 0.2\%$, calculated by the SCGF approach (green circles), compared with the result of the supercell calculation for a box with $L = 100a_0$, $M = 8000$ and $E_{max} = 856$ meV, with broadening parameter $\epsilon = 1$ meV (solid red line), and $\epsilon = 10$ meV (dashed blue line).

zone ($|q_x|$,$|q_y|$,$|q_z| < \pi/L$), or else by further increasing the box size, L. We chose the same cut-off energies in both the SCGF and the supercell calculations, as using a higher cut-off energy shifts the gap to lower energy, and makes it smaller.

Figure 5.4 shows the density of momentum states for GaN_xAs_{1-x} with x=1%, calculated by the SCGF method and using the supercell approach. Very good agreement is observed between the SCGF and the supercell calculations with $\epsilon = 1$ meV for the whole range of nitrogen concentration x. The gap between the lower and upper bands increases with increasing x. For higher concentrations we find that even larger values of the broadening parameter ϵ do not obscure the gap.

In the SCGF calculations shown in Fig. 5.3, we have assumed that the CB energy is cut-off at $E_{max} = 856$ meV, in Eqs. (5.6) and (5.8). We note however that the DOS for an infinite CB can be obtained using Eq. (5.16). The red solid line in Fig. 5.5 shows the DOS calculated by Eq. (5.16) with $E_{max} = \infty$, in comparison with the DOS calculated by Eq. (5.8) with $E_{max} = 856$ meV,

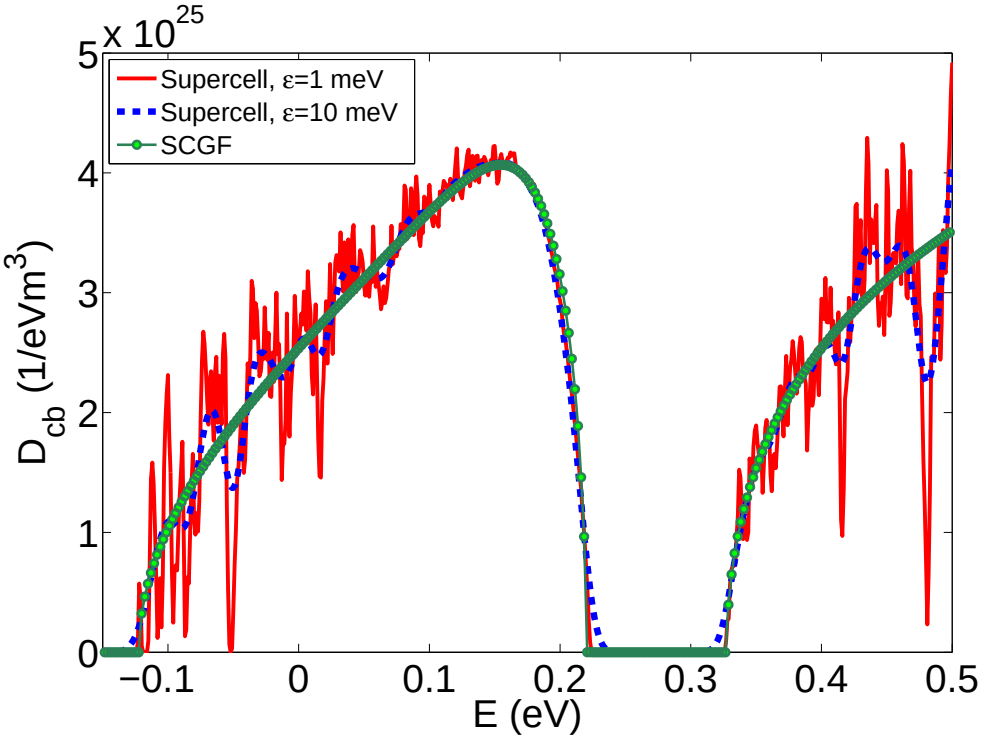

Figure 5.4: The density of states for GaN_xAs_{1-x} with $x = 1.0\%$, calculated by the SCGF approach (green circles), compared with the result of the supercell calculation with broadening parameter $\epsilon = 1$ meV (solid red line), and $\epsilon = 10$ meV (dashed blue line), for GaN_xAs_{1-x} with $x = 1.0\%$, $L = 70a_0$, $M = 13720$ and $E_{max} = 1.45$ eV.

equivalent to $k_{max} = 1.23 \times 10^9$ m^{-1} (shown by the blue dashed line). Note that in both plots, $\Delta E_N(E)$ has been calculated for a finite CB in Eq. (5.6). It is seen that, due to the contribution of higher momentum states in the infinite CB, the DOS calculated by Eq. (5.16) has a singularity at the localised state energy, E_N.

This difference is very similar to what we observed in our previous non-self-consistent GF calculations (in agreement with calculations using a modified BAC model). In order to illustrate the effect of the energy dependent $\Delta E_N(E)$ (that includes both real and imaginary parts), the results of the previous GF model are also shown in this figure. The green dots and the dash-dotted brown line in Fig. 5.5 display the DOS calculated by the ordinary GF method assuming a finite ($E_{max} = 856$ meV) and an infinite CB, respectively. In this model, as discussed in chapter 3 we assume that the N broadening is given by second order perturbation theory as $\Im[\Delta E_N(E)] = 16$ meV for all values of energies. Comparison of the dashed blue line and the green dots in this figure clarifies the importance of the energy-dependent broadening $\Delta E_N(E)$ used in the self-consistent calculations. It can be seen that the self-consistent approach predicts a gap between the lower

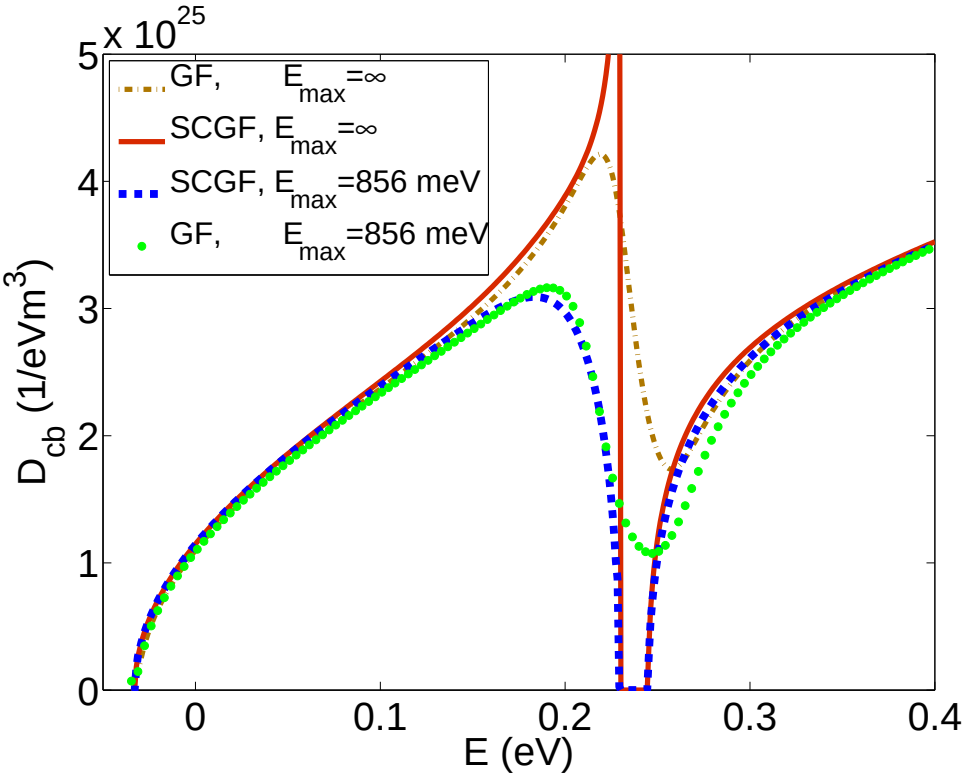

Figure 5.5: The DOS projected onto GaAs CB states for GaN_xAs_{1-x} with $x = 0.2\%$ calculated by the SCGF approach of Eq. (5.12) (blue dashed line: CB cut off at 856 meV), and Eq. (5.15) (solid red line: infinite CB), compared with the results of similar calculations but with constant $\Delta E_N(E) = 16i$ meV, for the CB with $E_{max} = 856$ meV (green dots), and for infinite CB (dash-dotted brown line).

and upper mini-bands in GaNAs, in contrast with our earlier calculations in Chapter 3.

The DOS calculated by the SCGF method, for an infinite band, is similar but not identical to the results obtained using the simple BAC model (without N broadening). For example, in the usual BAC model the maximum of the lower band is constant and equal to $E_N = 0.23$ eV. By contrast, the energy of the highest state in the lower band decreases with increasing x in the SCGF method.

The DOS calculated by SCGF method, for infinite band, is similar to the result of the simple BAC model (without N broadening). However, our calculations show that the gap calculated by the SCGF and the supercell calculations are smaller than the gap predicted by the usual BAC model.

In the usual BAC model the maximum of the lower band is equal to $E_N = 0.23$ eV. However, we have assumed that each N state can interact with only one supercell host matrix state, and therefore the volume of k-space included should be equal to the volume of the full Brillouin zone times the N concentration, x,

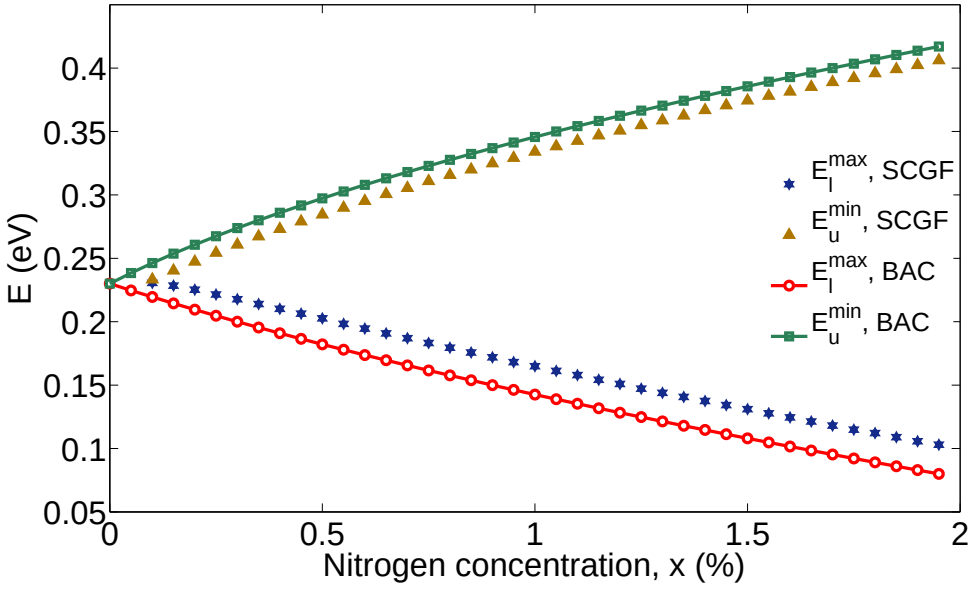

Figure 5.6: The maximum of the lower band, E_l^{max}, and the minimum of the upper band E_u^{min} for GaN_xAs_{1-x} versus nitrogen concentration x, calculated by the self-consistent Green's function and the BAC model, with $E_{max} = 0.6$ eV.

and the maximum allowed wave vector is given by $k_{max} = x^{1/3}2\pi/a_0$, where a_0 is the GaAs lattice constant [1]. Fig. 5.6 compares the concentration dependence of the energy of the top of the lower band and the bottom of the upper band, calculated by the BAC model (with k_{max}) and the SCGF approach , for the range of x in GaN_xAs_{1-x}. In both cases the band-edges are linear with respect to x. In the BAC model the gap between the lower and upper bands is larger than that in the SCGF approach. In SCGF method, in contrast with the BAC model, no gap is observed for very low N concentrations ($x < 0.08\%$).

In the BAC model in chapters 3 and 4 we included the real part of the energy shift of localised state energies, given by Eq. (3.2), which has not been considered in Fig. 5.6. Including this shift, pushes the minimum of the upper band of BAC model E_u^{min} to higher energies and gives similar results as SCGF method.

We previously calculated the projected DOS onto single momentum states in the supercell and BAC models (including complex N energy, $E_N - i\Delta$) and found quite good agreement between the two approaches in chapter 3.

The DOS projected onto a single CB state with momentum k is given by $-\Im[G_{kk}(E)]/\pi$, where $G_{kk}(E)$ can be calculated from Eq. (5.5) once $\Delta E_N(E)$ has been determined. In § 4.4 we calculated this projected DOS onto single momentum states in the supercell and BAC models (including complex N energy,

[1] See Sec. 6.2 for more more details.

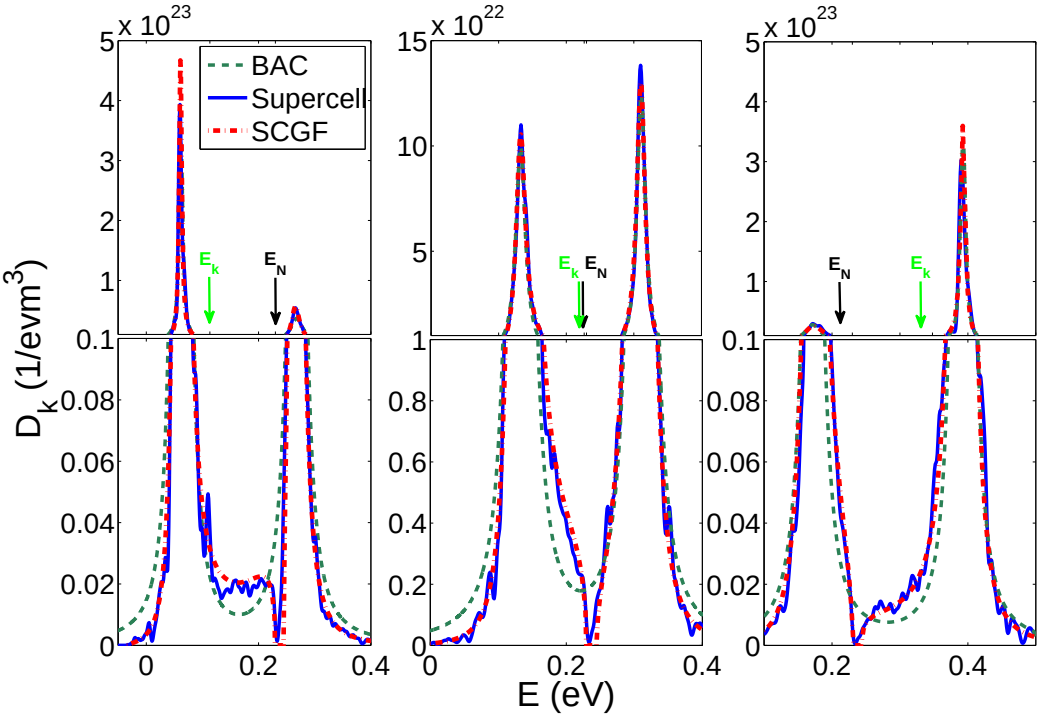

Figure 5.7: The DOS projected onto selected GaAs momentum states, calculated using the BAC model (dash-dotted green lines), the supercell calculation for a box with $L = 100a_0$, and 8000 N states (solid blue lines), and the SCGF model (dashed red lines) for $GaN_{0.002}As_{0.998}$. Green and black arrows show the energy E_k of the original k state ($E_k = 113.3, 226.6$, and 347.9 meV), and the N energy E_N, respectively. Note the different scale in the lower part of y-axes.

$E_N - i\Delta$) and found quite good agreement between the two approaches. Fig. 5.7 shows how the DOS projected onto the individual k states varies with increasing energy E_k, in the BAC, supercell, and the SCGF approach, where the green arrow E_k indicates the energy of the host matrix state in each of the 3 cases considered. The dashed green lines in Fig. 5.7 show the result predicted by the BAC model for $GaN_{0.002}As_{0.998}$, while the solid blue curves display the numerical results for a supercell with length $L = 100a_0$, containing 8000 N ($x = 0.2\%$), and Gaussian broadening $\epsilon = 3$ meV. Note the change in scale in Fig. 5.7 in the middle of each figure. Despite the very good agreement between the BAC and the supercell models in the peaks of the DOS (upper panels), the details of the DOS far from the peaks differ (lower panels). However, the DOS calculated by the SCGF method (shown by dashed red lines), is in a very good agreement with the supercell calculations both in the peaks of the DOS and in the details far from the peaks. The BAC (usual Green's function) model does not predict a gap in DOS, while the SCGF method in agreement with supercell calculations confirms

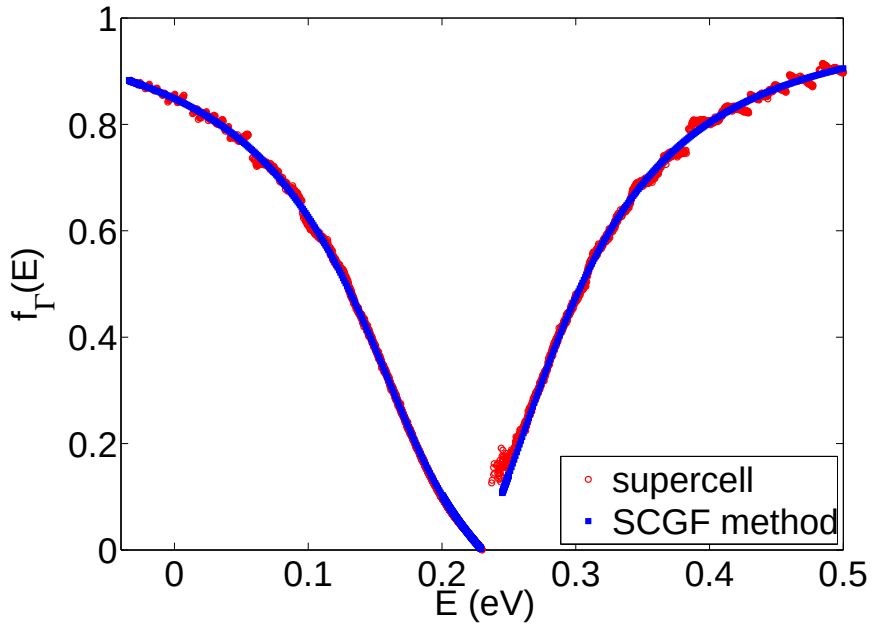

Figure 5.8: The fractional Γ character for $GaN_{0.002}As_{0.998}$ predicted by the 2-level SCGF method by Eq. (7.14) (blue dots), compared with the supercell calculations for a box with length $L = 100a_0$ containing 8000 N ($x = 0.2\%$).

the existence of a gap in DOS. These results again confirm the presence of a gap in the two-band model, and demonstrate that the SCGF method provides an accurate description of the DOS for individual k values.

5.3.2 Fractional Γ character

In analysing the band structure of dilute nitride alloys, it can be very useful both for transport and optical properties to determine the fractional Γ character, f_Γ, of a given state, where f_Γ equals the fraction of the state which projects onto the host matrix extended states $|\mathbf{k}\rangle$.

As we have shown in Appendix A, the Hamiltonian of the system can be written by Eq. (A.1), where α_M and α_j are the weights of CB and j-th localised state, respectively. The fractional Γ character f_Γ, that is given by $|\alpha_M|^2$, measures the host matrix character of a given state. For the two-band model Eq. (A.6) becomes

$$f_\Gamma = \left[1 - \frac{V_{Nc}^2}{\left|E - E_N - \Delta E_N(E)\right|^2}\right]^{-1}. \tag{5.18}$$

Figure 5.8 compares the fractional Γ character calculated by Eq. (5.18) with the results of supercell calculations, for $GaN_{0.002}As_{0.998}$. We observe excellent agreement, over the full energy range, between the SCGF result obtained from

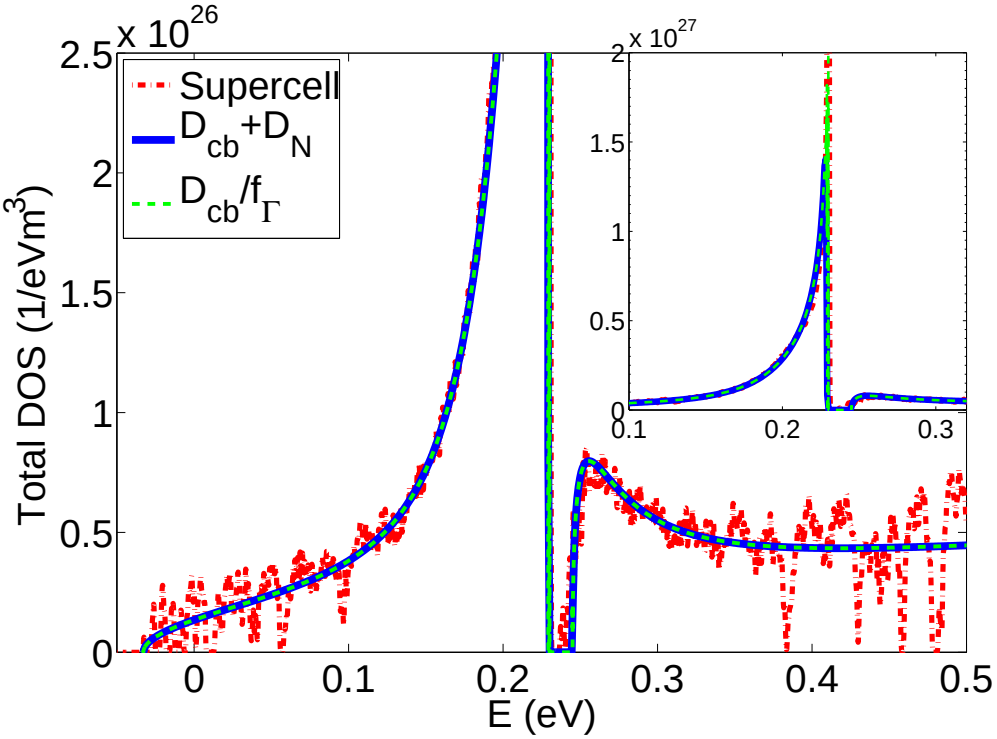

Figure 5.9: The total DOS for $GaN_{0.002}As_{0.998}$ obtained from; (i) a supercell with $L = 100a_0$, containing 8000 N, and $E_{max} = 856$ meV, with broadening parameter $\epsilon = 1$ meV (dash dotted red line), (ii) the SCGF as a summation of DOS projected onto extended and localised states (solid blue line), and (iii) the SCGF as D_{cb}/f_Γ (dashed green line). The inset displays the results around the peak of the total DOS.

Eq. (5.18) and the numerical results obtained for a supercell with size $L = 100a_0$ including 8000 N atoms. In our earlier work, presented in Chapter 3, the results of the GF calculation, with ΔE_N calculated by second order perturbation theory, did not agree with the supercell calculation results in particular for energies close to the N state energy, E_N, as we neglected the energy dependence of ΔE_N in that study.

5.3.3 Total density of states

The Green's function for the N states, for the 2 band model, is given by

$$G_{jj}(E) = \frac{1}{E - E_N - \Delta E_N(E)}, \tag{5.19}$$

and the density of states projected onto the localised states, $D_{loc}(E)$ can then be calculated by Eq. (5.9). The total DOS shown by the solid blue line in Fig. 5.9, can be obtained by adding the DOS projected onto the host matrix CB states to

the result of Eq. (5.9). Excellent agreement, over the full range of energies, is seen between this result and the supercell calculation obtained in Chapter 4, shown by the dash-dotted red line in Fig. 5.9. The DOS projected onto the N states is clearly much larger than the DOS projected onto the host CB states for energies close to the N state energy, E_N. The total density of states can also be obtained from $D_{cb}(E)/f_\Gamma$. The DOS calculated in this way (dashed green line) is in very good agreement with the solid blue line in Fig. 5.9. Again the agreement between the SCGF and the supercell method is much better than what we observed in Chapter 4 for GF calculations with constant ΔE_N, including that the peak of the total DOS calculated by the previous GF model showed a shift with respect to the supercell calculation result, which is now removed when including the energy-dependent shift in the real part of $\Delta E_N(E)$.

5.4 The LCINS model

The two-band model is oversimplified, because it omits the direct interactions between N states, which are present in actual GaNAs samples. Lindsay and O'Reilly have previously used a tight-binding-based model to calculate the distribution of N states expected in random GaNAs alloys, treating explicitly the interactions between a Linear Combination of Isolated Nitrogen States (LCINS) in this model [11, 17, 24]. This approach takes account of the formation of N pair and cluster states with increasing N composition, x, where a N pair is formed when a Ga atom has 2 N nearest neighbours, and a cluster consists of 3 or more N atoms linked to each other through shared Ga neighbour sites. The LCINS model also takes into account that interactions between isolated N atoms which are close to each other in the alloy contributes to a broadening of the N spectral energy. These interactions lead to mixing between the N states on different sites and a broadening of the N spectral energy (E_j no longer just equal to E_N), and of the interaction values V_j. The inclusion of this distribution of N states has previously been shown to be critical both to obtain good quantitative agreement between the theoretical and experimental variation with N composition x of the conduction band edge effective mass and electron gyromagnetic ratio [25, 28] and also to explain the conduction band density of states measured experimentally using scanning tunnelling spectroscopy [29].

The density of localised N states calculated by the LCINS approach, with each state weighted by V_j^2/N_c (the square of its interaction matrix element with the CBE), is shown in Fig. 5.10. We investigate below how the inclusion of

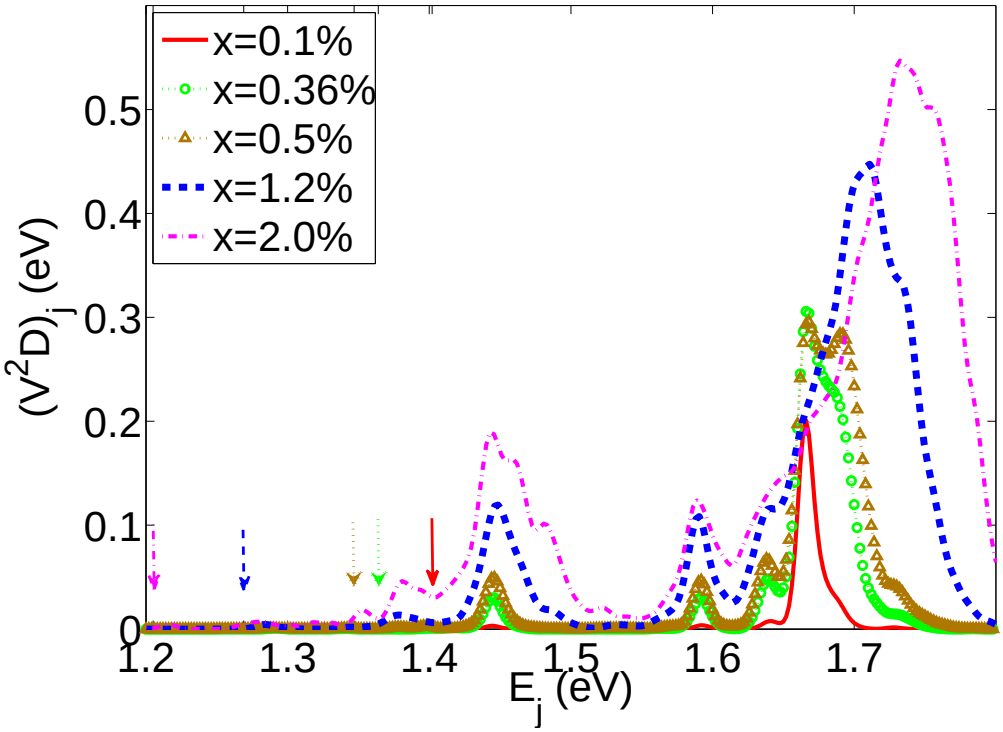

Figure 5.10: The density of localised LCINS states, weighted by $|V_j|^2/N_c$ for each state, versus their energies, for GaN_xAs_{1-x} with different values of x. Each energy level is broadened by a Gaussian of width 5 meV. The vertical arrows display the calculated CBE energies at room temperature, with respect to the top of the valence band, given in Ref. [13]. Zero of energy is taken at top of GaAs valence band.

this distribution of N states modifies the band dispersion and density of states calculated using the SCGF method with Eqs. (5.2) and (5.3).

5.4.1 The DOS for the LCINS model

The dashed blue line in Fig. 5.11 displays the DOS of $GaN_{0.0036}As_{0.9964}$ with the full LCINS distributions, calculated by solving Eqs. (5.2) and (5.3). The zero of energy for these calculations is taken at the top of the GaAs valence band and we use room temperature values for the GaAs energy gap and N state energies [6]. The solid red and dash-dotted green lines in this figure show the results of the ordinary GF model (Eq. (5.7); without iteration) with constant N broadening $\Delta_j = 16$ and 1 meV, respectively [2], where the $\Delta_j = 1$ meV results allow to see the calculated DOS with minimal broadening included. It can be seen

[2]Using $\Delta_j = 1$ in Eq. (5.7) is equivalent to taking $\Delta E_j(E) = 0 + 1i$ in Eqs. (5.3) and (5.2), where $i = \sqrt{-1}$.

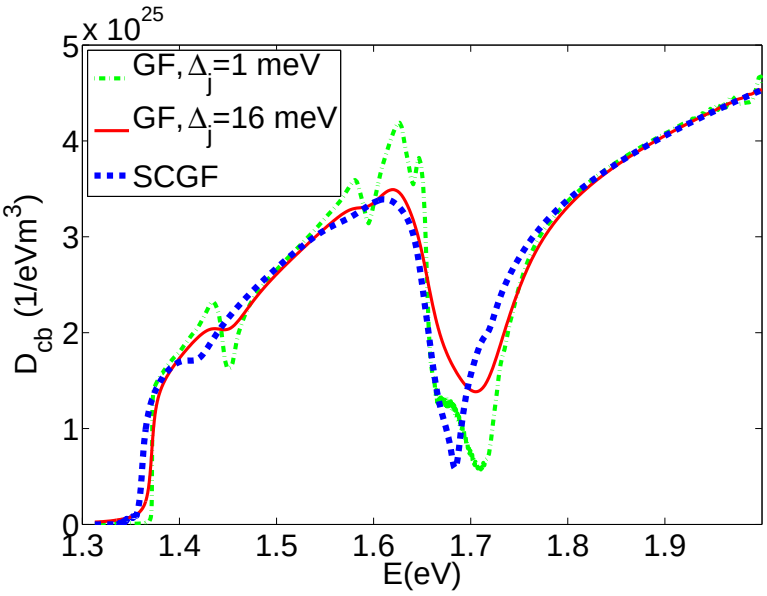

Figure 5.11: The density of states for $GaN_{0.0036}As_{0.9964}$ calculated by the ordinary Green's function method, with constant energy shifts $\Im[\Delta E_j(E)] = 16$ meV (the solid red line) and $\Im[\Delta E_j(E)] = 1$ meV (the dash-dotted green line) compared with the SCGF method result with 10 iterations (the dashed blue line).

that including the full distribution of N states causes the gap in the conduction band to disappear, even for $\Delta = 1$ meV, in agreement with experiments [29]. Several features can be seen in the unbroadened spectrum ($\Delta = 1$ meV) associated with the N states, including a dip just around 1.45 eV associated with N pair states (close to the same energy in Fig. 5.10), as well as several further features associated with different N environments between 1.55 and 1.65 eV. Most of these features get washed out for the spectrum with $\Delta_j = 16$ meV. We saw earlier that the broadening in the SCGF calculations is proportional to the DOS, $D_{cb}(E)$ in the 2-band model (where E_j and V_j are constant). Similar behaviour can be expected when using the LCINS approach. The SCGF broadening then smears out most of the features observed in the $\Delta = 1$ meV spectrum, although the dip in the spectrum remains clear just above 1.65 eV, and a shoulder is also observed in the DOS below 1.45 eV due to the N pair states. The dip in the SCGF DOS is shifted to lower energy compared to the $\Delta_j = 1$ meV case, due to the energy dependence of the real part of $\Delta E_N(E)$ in the SCGF case.

Figure 5.12 shows the CB density of states for GaN_xAs_{1-x} for $x = 0.1, 0.5, 1.2$ and 2.0%, calculated using Eq. (5.8) where G_{kk} is calculated by Eqs. (5.2) and (5.3), including the full distribution of N state energies and interactions from Refs. [11, 67] as shown in Fig. 5.10. Increasing the N concentration pushes the bottom of the CB to lower energy and makes the peak around the isolated N

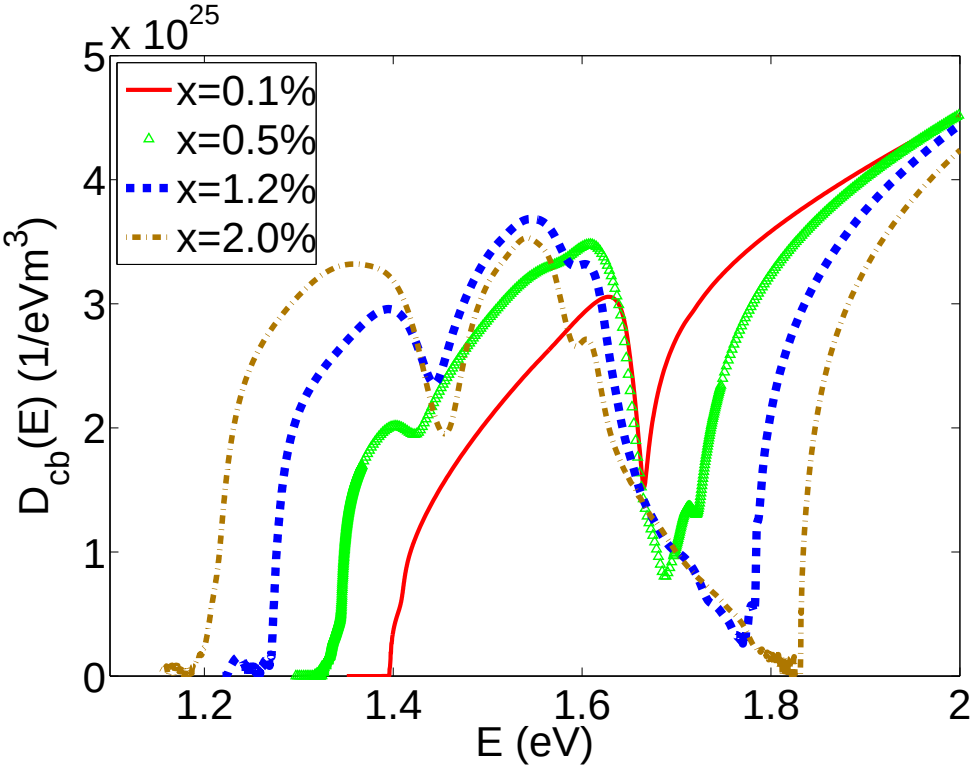

Figure 5.12: The density of states for different values of x in GaN_xAs_{1-x}, calculated using the SCGF method and the full LCINS distribution of N states.

states wider.

5.4.2 Total density of states

In the LCINS model, as shown in Appendix A, f_Γ can be calculated by generalising Eq. (5.18) to take account of the distribution of N states, using

$$f_\Gamma = \left(1 + \frac{1}{N_c}\sum_j \frac{|V_j|^2}{|E - E_j - \Delta E_j(E)|^2}\right)^{-1}. \tag{5.20}$$

The fractional Γ character calculated by the LCINS approach, for $GaN_{0.0036}As_{0.9964}$, is given in the inset of Fig. 5.13. As is seen in the figure, the overall behaviour is similar to the 2-level calculations.

However, the inclusion of the full LCINS distributions leads to a sharp reduction in f_Γ at energies close to the N pair state energy (close to the CBE), thereby leading to an increased electron mass near the CB minimum compared to that which would be predicted using the 2-level BAC model of Eq. (3.1). There is in addition another small shoulder in the value of f_Γ just below $E = 0.2$ eV,

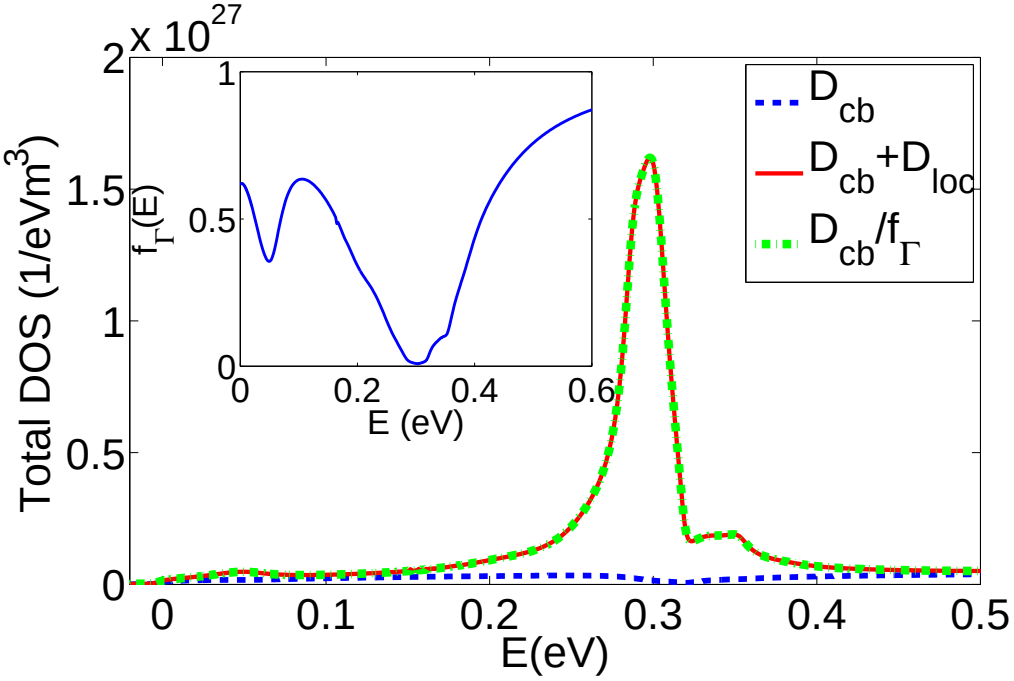

Figure 5.13: The total density of states in comparison with the DOS projected onto the host CB states for $GaN_{0.0036}As_{0.9964}$ (dashed blue line), predicted by the SCGF method and the full distribution of LCINS approach. The red line shows the result of $D_{cb} + D_{loc}$, and the dash dotted green line displays the total DOS given by D_{cb}/f_Γ. The inset shows the fractional Γ character calculated by Eq. (5.20) for $GaN_{0.0036}As_{0.9964}$. The zero of energy is taken to be at the CBE of $GaN_{0.0036}As_{0.9964}$.

associated with the N levels just below the isolated N state peak at 1.6 eV in Fig. 5.10.

The total DOS for the LCINS model can again be calculated by summation of the DOS projected onto the GaAS CB states, D_{cb}, and the density of localised states, D_{loc}. This total DOS is shown by the solid red line in Fig. 5.13, in comparison with D_{cb} for $GaN_{0.0036}As_{0.9964}$. The DOS projected onto the localised N states is now clearly much larger than the DOS projected onto the host CB states over a wide energy range. The dash dotted green line in this figure presents the total DOS calculated by D_{cb}/f_Γ, which again shows excellent agreement with the summation of $D_{cb} + D_{loc}$.

5.5 Band structure

The DOS projected onto selected momentum states was presented in Fig. 5.7. By calculating the DOS projected onto momentum states for all k values, we are able to plot the band dispersion for GaNAs. Fig. 5.14 shows the conduction band

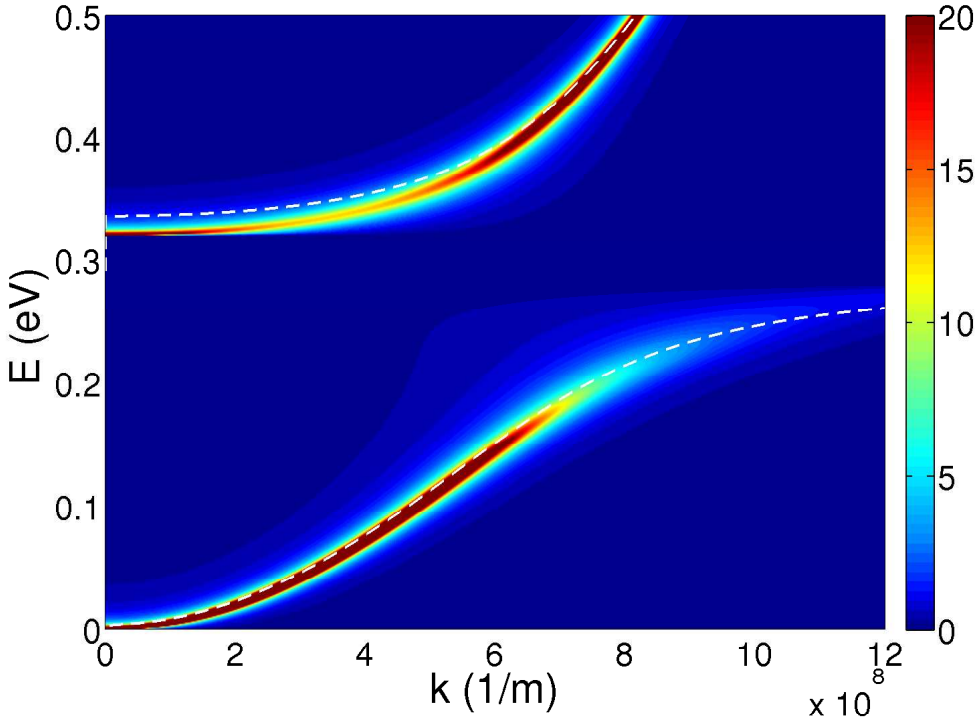

Figure 5.14: Energy- and momentum-projected density of states for GaN_xAs_{1-x} with $x = 0.36\%$ calculated with the two-level SCGF method. The dashed white lines show the band dispersion calculated using the BAC model [Eq. (3.1)] with the zero of energy taken at the bottom of the BAC CBE at room temperature.

dispersion for $GaN_{0.0036}As_{0.9964}$, calculated by the two-level SCGF method, where the energy spectrum for each k state is given by $-\Im[G_{kk}(E_k)]/\pi$. It can be seen that overall the band dispersion is similar to the results of the BAC model of Eq. (3.1) (shown by the white dashed line in this figure). The peaks at each k point are broadened in the SCGF method, with this broadening increasing close to the nitrogen resonant energy, E_N. Similar behaviour was previously observed using the Anderson single impurity approach [18], although the broadening Δ_j was taken to be independent of energy in that approach. The conduction band character of the states also decreases towards zero when E_k approaches E_N. However, in contrast to the GF calculations with constant ΔE_N presented in Fig. 3.4, this figure, in agreement with Figs. 5.3 and 5.7, confirms that the energy broadening in the two-level SCGF model does not provide a continuous spectrum of states for electrons in the lower band to scatter into the upper band. The two-level model, however, is not complete, as it ignores the detail of the N distribution in actual GaNAs samples.

Fig. 5.15 shows the conduction band dispersion for $GaN_{0.0036}As_{0.9964}$, calculated by the SCGF method in the framework of the LCINS approach to include

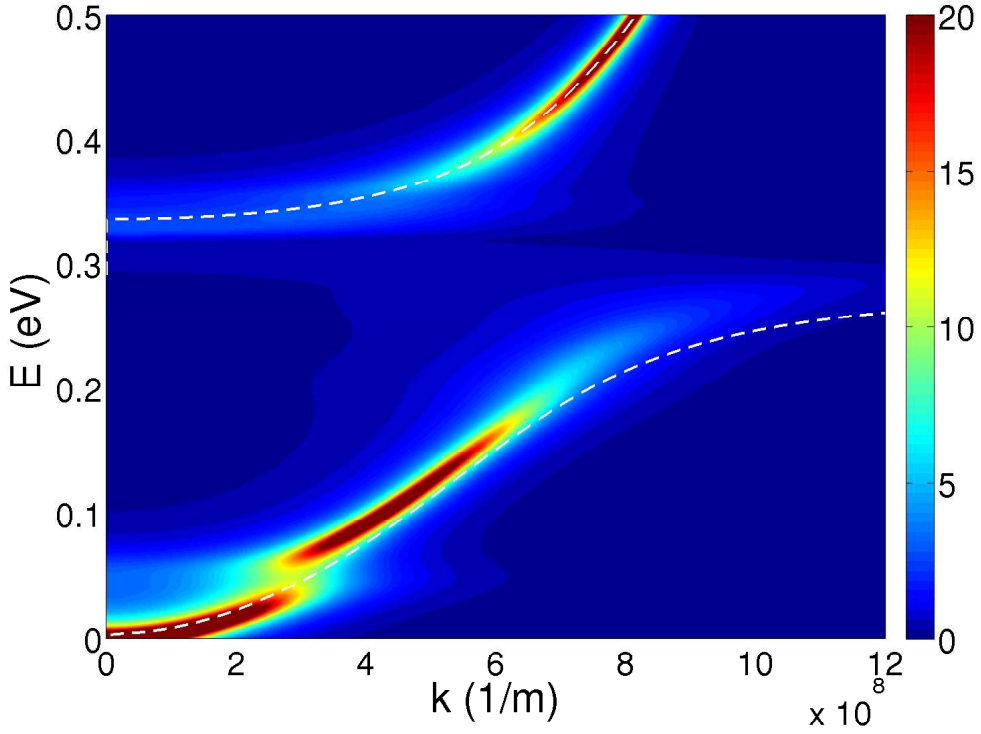

Figure 5.15: The k-projected density of states for GaN_xAs_{1-x} with $x = 0.36\%$, calculated by the SCGF method and including the full distribution of localised states, showing the band dispersion and broadening. The dashed white lines show the BAC band dispersion calculated by the BAC model of Eq. (3.1).

the full N distribution. It can be seen that the overall behaviour is similar to what we saw in Fig. 5.14, but with two notable differences. First, the band dispersion and broadening show clear features related to N pair states. Also, the energy broadening at each k point has been increased by the inhomogeneous broadening of the N states, leading to a filling of the gap predicted by the BAC model. This result, in agreement with the DOS shown in Fig. 5.11, shows that there is a route by which carriers, which are being accelerated in the lower sub-band, can scatter to the higher sub-band.

5.6 Discussion and conclusions

We have implemented a self-consistent Green's function method to calculate the density of states in dilute nitride alloys. Our results show that the SCGF method provides an excellent description of the electronic structure in GaNAs alloys. In this model, the nitrogen energy shift, $\Delta E_j(E)$, due to interaction with the continuum states, was taken as a complex energy dependent parameter, calculated self-

consistently. In Chapter 3 we calculated this parameter using second order perturbation theory, with the real and imaginary parts representing a constant shift in the nitrogen energy, and a constant energy broadening of the localised states, respectively. We considered two different models, namely the 2-band model (assuming all N states located at the same energy), and the LCINS model, which includes a full distribution of N states. We compared the results of the 2-band model with those calculated by the supercell and the BAC models.

In the 2-band model, the DOS calculated by the SCGF approach is in very good agreement with the results of calculations of supercells with a random spatial distribution of N states. Both models predict a gap in the conduction band DOS, in contrast with the DOS calculated by the usual Green's function model (or equivalently the BAC model with constant N broadening). Overall the BAC model gives a good qualitative description of the calculated band structure but with a number of minor differences between the calculated results, including that the BAC model without N broadening also predicts a gap that is wider than the one given in the SCGF method. Turning to the band dispersion, the density of states projected onto the individual k states calculated by the 2-level SCGF method is in excellent agreement with that calculated by the supercell model. In addition the fractional Γ character and the total DOS calculated by the two-level SCGF method show excellent agreement with the supercell calculation in all energy ranges, confirming the accuracy of this method. The non-self-consistent Green's function method, which assumed that ΔE_N was energy-independent, did not show the same level of agreement.

Including the full distribution of N states, using the LCINS model [11, 17], has a number of important effects on the calculated band structure and density of states. Firstly, it inhibits the gap in the density of states of GaN_xAs_{1-x} for all x values considered. Secondly, it leads to an increased mixing between N and conduction states across a wider energy range, causing a reduction in the host matrix Γ character of many of the states, consistent with the increased band edge mass observed in many GaN_xAs_{1-x} samples [10, 17]. Finally, it can also lead to the observation of additional features in the conduction band density of states, such as the shoulder observed in Fig. 5.11 and in the scanning tunnelling spectroscopy measurements of [29].

In summary, we have presented a self-consistent Green's function approach to study the band structure and density of states of dilute nitride alloys. The results of the model are in excellent agreement with supercell calculations that we have undertaken. Although in this paper we investigated GaN_xAs_{1-x}, this method can

be easily applied to other highly mismatched semiconductors, including different dilute nitride alloys and dilute bismide semiconductors, containing bismuth (Bi). We conclude that the SCGF approach, in conjunction with the use of a realistic distribution of localised N states provides a very powerful tool to examine the details of electronic structure of GaNAs and related materials.

We turn in the next two chapters to consider consequences of N incorporation on carrier scattering and electron mobility. We will first in Chapter 6 investigate the mobility assuming that the band dispersion is either parabolic or gives by the 2-level BAC model. We then in Chapter 7 extend the work presented in this chapter to use the SCGF method to calculate the band dispersion, scattering rate and mobility of carriers in GaNAs alloys, where the carrier energies and decay rates are taken to correspond to the complex poles of the self-consistent Green's function.

Chapter 6

Intermediate and high field mobility

6.1 Introduction

The quantitative analysis of electron transport and mobility in dilute nitride alloys is a difficult problem. It is well established that replacing a fraction x of the arsenic atoms in GaAs by nitrogen atoms to form GaN_xAs_{1-x} strongly perturbs the conduction band structure. In previous chapters we have seen that the introduction of a single N atom in place of an As atom introduces a N resonant defect level, about 230 meV above the conduction band edge (CBE) at room temperature. Such a state can act as a resonant scattering centre [68], leading to strong elastic scattering of electrons with energy close to the resonant state energy [13]. The introduction of a N pair into GaAs, where two of a given Ga atom's neighbours are N, leads to a resonant defect level which is closer to the CBE [7], and therefore strongly scatters electrons whose energy lies close to the band edge [13].

Models for electron transport and mobility need to include the scattering due to such a distribution of N states above the CBE in GaN_xAs_{1-x}. However, in addition to acting as scattering centres, the N-related states also strongly perturb the conduction band dispersion. It is possible to treat this change in band dispersion in a reasonably straightforward way for low-field transport and mobility calculations [13], but we describe below how it is considerably more difficult to do so in the intermediate and high-field case.

There are two aspects of the BAC model which introduce errors that become significant when treating high-field mobility. Firstly, the BAC model in Eq. (3.1) implicitly assumes an infinite density of N atoms. Because there is no maximum

cut-off wavevector, k_c, Eq. (3.1) requires an infinite density of N levels interacting with the host matrix extended conduction states. Secondly, application of Eq. (3.1) leads to an energy gap in the conduction band, just above the N resonant state energy, E_N. The presence of this energy gap confines carriers to the lower of the two energy bands given by Eq. (3.1), placing an absolute upper limit on the energy to which carriers can be accelerated in the BAC model.

More detailed analysis [34, 35, 60] and measurement [29] shows that this energy gap does not occur in actual Ga(In)AsN samples. Instead, as shown in earlier chapters, the gap is washed out because of disorder effects and the distribution of N levels. We calculate that the disorder due to the predominantly N-related states which fill the BAC energy gap leads to the states in the gap being localised [60], in agreement with the conclusions of low temperature high-field electron transport measurements [15, 53–55].

A full model for high-field transport in dilute nitride alloys would therefore need to treat a conduction band structure which has extended states at energies away from the N resonant levels, and bands of localised states at energies close to the N resonant levels. It is very difficult to treat such a continuous band of states in conventional transport models, and we do not attempt to do so. Instead we use and compare the results of two approaches, one of which is likely to provide a lower bound on the effects of N incorporation, while the second approach clearly overestimates the effects of N on the band structure.

For the first approach, we ignore the effect which N has on the conduction band dispersion in GaN_xAs_{1-x}. We assume that the conduction band retains a parabolic dispersion, but includes explicitly the strong resonant scattering associated both with isolated N atoms and also with a full distribution of N states. Our previous calculations have shown that the N resonant scattering leads to a very short mean free path close to E_N in GaN_xAs_{1-x} [13]. The consequences of this short mean free path should be equivalent to those of carrier localisation. The parabolic band dispersion allows carriers in this case to be accelerated at sufficiently high field through the distribution of N levels up to higher energies where the drift velocity is then limited by scattering from the Γ valley into the L valleys [69, 70].

For the second approach, we calculate the intermediate and high-field electron transport properties of GaN_xAs_{1-x} using the BAC model to describe the band structure. As noted above, this approach must fail at high fields, because it limits the maximum energy to which carriers can be accelerated.

We present in the next section an overview of the band dispersion in GaNAs,

based on using a Green's function method to analyse the interaction between N states and the GaAs host matrix conduction band states. We show how the calculated band dispersion displays aspects of the two band structure models which we use, supporting their use in transport calculations. We then present in § 6.3 a description of the Boltzmann transport equation method which we use to calculate the electron mobility and velocity-field characteristics in GaN_xAs_{1-x}. We follow a method similar to that used by Conwell and Vassell [71, 72], solving the Boltzmann equation using an orthogonal polynomial expansion of the angular distribution of momenta to investigate the carrier transport with increasing electric field. The comparison of the results calculated by this asymptotic solution with the Monte Carlo method, for silicon, has already confirmed the validity of this method [73]. Moreover, we will show that this method, by the modifications that we made, leads to a very similar results to those calculated by the Monte Carlo method in the case of GaAs [74]. The earlier works approximated polar optical relaxation by a simple Taylor series expression that causes inaccuracy in the results [71]. In addition it solved the Boltzmann equation by expanding the energy distribution function in a Taylor expansion. We use a more accurate approach here that avoids both these approximations, as described in § 6.3. We also include in § 6.3 a description of the different scattering processes included in the calculation. These are all included completely in our formalism, avoiding unphysical low-field approximations used in the original application of the method [71]. We present our main results in § 6.4, analysing the influence both of N composition and of applied field on the carrier transport characteristics. We consider scattering both by isolated N atoms and also by a full distribution of N states. We find that it is necessary to include the full distribution of levels in order to account for the small low-field mobility and the absence of a negative differential velocity regime observed experimentally with increasing N composition x. The model using the BAC model breaks down at intermediate and high field, due to the unphysical constraint of limiting carriers to the lower BAC band. We find for the parabolic band model that carrier scattering into the L bands is reduced at intermediate electric fields but is comparable at high fields to that observed in GaAs, with the calculated high-field mobility and carrier distribution then also being comparable to GaAs. Overall the results account well for a wide range of experimental data. Finally we summarise our conclusions in § 6.5.

6.2 Band structure of GaN_xAs_{1-x}

It has been shown in Chapter 5 that the conduction band structure of GaNAs can be well described using the Green's function method. We observed that the energy broadening in Fig. 5.15 allows a means for electrons which are being accelerated in the lower band to scatter into the upper band, consistent also with there being a distribution of localised N-related states within this energy gap region [60]. It can be seen that the band dispersion of Fig. 5.15 is intermediate between the two models that we use. The first model assumes a parabolic band dispersion, with strong resonant scattering by N states. The E-k relation is given in this case by

$$\frac{\hbar^2 k^2}{2m^*} = \gamma(E), \tag{6.1}$$

where

$$\gamma(E) = E - E_c. \tag{6.2}$$

This model underestimates the effect of N on the band dispersion, but should give a good description of the strong N scattering.

In the second approach, the E-k relation in Eq. (6.2) is given for the BAC model by

$$\gamma(E) = E - E_c - \frac{V_{Nc}^2}{E - E_N}, \tag{6.3}$$

with the density of states $D(E)$ given in terms of γ by

$$D(E) = \frac{m^{*3/2}}{\sqrt{2}\pi^2\hbar^3}\gamma^{1/2}(E)\frac{d\gamma(E)}{dE}. \tag{6.4}$$

This relation overestimates the effects of N on the band structure near E_N. Ideally, one should use the smeared band dispersion of Fig.5.15 with the Boltzmann transport equation to describe the transport properties, but this is beyond the scope of the present chapter. Instead, the Hamiltonian of Eq. (2.1) is very useful, because it allows the analytical solution of the Green's function model.

Determining the cut-off energy, E_{max}, in the BAC model is very critical [60]. As E_{max} approaches the nitrogen state energy the density of conduction states and the integrated density of conduction states both diverge. We assumed that each N state can interact with only one supercell host matrix state. As a result, the volume of k-space included should be equal to the volume of the full Brillouin zone times the N concentration, x. The maximum allowed wave vector is then given by $k_{max} = x^{1/3}2\pi/a_0$, where a_0 is the GaAs lattice constant. Therefore, the maximum energy of the lower band in the BAC model depends on N concentration

as

$$E_{max} = \frac{1}{2}\left\{E_N + E_{c,max} - \sqrt{(E_N - E_{c,max})^2 + 4V_{Nc}^2}\right\}, \tag{6.5}$$

where $E_{c,max} = E_c + \hbar^2 k_{max}^2 / 2m^*$.

6.3 Transport calculation method

6.3.1 Boltzmann equation

We solve the Boltzmann transport equation to determine the response of the electron distribution to an applied electric field. The distribution function $f(k)$ gives the probability that a band state at energy E_k will be occupied by a carrier. We assume that, in the absence of an external field the carriers are in thermal equilibrium, so that $f(k)$ is then given by the Fermi-Dirac distribution function. The application of an external field perturbs the distribution, with the distribution evolving in time as

$$\frac{\partial f(\mathbf{k})}{\partial t} = \left(\frac{\partial f(\mathbf{k})}{\partial t}\right)_{scatt} + \left(\frac{\partial f(\mathbf{k})}{\partial t}\right)_{F}, \tag{6.6}$$

where the first term on the left describes the effects of carrier scattering, while the second term describes the evolution of the distribution due to the applied electric field, which is related to the applied field $\mathbf{F}$ as

$$\left(\frac{\partial f(\mathbf{k})}{\partial t}\right)_{F} = -\frac{e\mathbf{F}}{\hbar}.\nabla_{\mathbf{k}} f(\mathbf{k}). \tag{6.7}$$

The scattering term in Eq. (6.6) is given by [56]

$$\begin{aligned}\left(\frac{\partial f(\mathbf{k})}{\partial t}\right)_{scatt} = \int \Big\{ & S(\mathbf{k}_0, \mathbf{k}) f(\mathbf{k}_0)[1 - f(\mathbf{k})] \\ & - S(\mathbf{k}, \mathbf{k}_0) f(\mathbf{k})[1 - f(\mathbf{k}_0)] \Big\} d^3\mathbf{k}_0,\end{aligned} \tag{6.8}$$

where $S(\mathbf{k}, \mathbf{k}_0)$ and $S(\mathbf{k}_0, \mathbf{k})$ are the scattering rates $\mathbf{k}$ to $\mathbf{k}_0$ and vice versa. $f(\mathbf{k})$ is the probability that the state $\mathbf{k}$ is occupied and $(1 - f(\mathbf{k}_0))$ is the probability that $\mathbf{k}_0$ is not occupied. For the steady state, the rate at which electrons gain energy from the field must be equal to the rate at which they lose it to the lattice.

In order to solve the Boltzmann equation, Eq. (6.6), we assume that it is

possible at each arbitrary field $\mathbf{F}$ to expand the distribution function f in a series of Legendre polynomials

$$f(\mathbf{k}) = \sum_{j=0}^{\infty} f_j(E) P_j(\cos\theta), \tag{6.9}$$

where $P_j(x)$ is the Legendre polynomial of order j and θ is the angle between wavevector $\mathbf{k}$ and electric field $\mathbf{F}$. The unknown functions f_j can then be obtained by solving the equations resulting from substituting for f in the above series. Following the approach of Baraff [75] and of Conwell and Vassell [71], we assume that it is possible to drop all terms beyond $j = 1$ in this expansion, so that the distribution function $f(k)$ is then given by

$$f(\mathbf{k}) = f_0(E) + k_F g(E), \tag{6.10}$$

where k_F is the component of $\mathbf{k}$ along the direction of the field $\mathbf{F}$. From Eq. (6.7) and by replacing $\hbar^2 k_F^2/m^*$ by its average $2\gamma/3$, the rate of change of the distribution due to the electric field can be written as

$$\left(\frac{\partial f(\mathbf{k})}{\partial t}\right)_F = -\frac{eF}{\hbar}\left\{g + \frac{2}{3}\frac{\gamma}{(d\gamma/dE)}g' + \frac{\hbar^2 k_E}{m^*(d\gamma/dE)}f_0'\right\}, \tag{6.11}$$

where g' and f_0' are the energy derivatives of g and f_0 respectively. Within the relaxation time approximation, we assume that the net effect of the collision processes is to cause $g(E)$ to relax with a time constant τ

$$\left(\frac{\partial f(\mathbf{k})}{\partial t}\right)_{scatt} = \left(\frac{\partial f_0}{\partial t}\right)_{scatt} - \left(\frac{k_F g}{\tau}\right). \tag{6.12}$$

Therefore the asymmetric part of the distribution function can be calculated from

$$g = -\frac{\hbar eF}{m^*}\frac{\tau}{(d\gamma/dE)}f_0'. \tag{6.13}$$

Hence the rate of change of the symmetric part of the distribution function is given by

$$\left(\frac{\partial f_0}{\partial t}\right)_F = \frac{2e^2F^2}{3m^*(d\gamma/dE)\gamma(E)^{1/2}}\frac{d}{dE}\left(\frac{\gamma(E)^{3/2}\tau}{(d\gamma/dE)}f_0'\right), \tag{6.14}$$

and where τ is the net relaxation time

$$1/\tau = \sum 1/\tau_i, \tag{6.15}$$

where τ_i is the relaxation time associated with the i^{th} scattering process considered. We note that although we refer to relaxation times in Eq. (6.15) and elsewhere in this chapter, these are all energy dependent relaxation times, defined as the inverse of a scattering rate and including (for polar optic phonons below) inelastic scattering between initial and final states at different energies.

6.3.2 Scattering processes

We consider four different scattering processes when modeling electron transport in GaNAs, namely scattering by (i) N resonant states, (ii) polar optical phonons, (iii) acoustic phonons, and (iv) intervalley scattering between the Γ valley and the four L valleys. Previous work [13] has shown that scattering by localised N states plays a significant role in carrier transport in GaNAs. Also, similar to GaAs, phonon scattering, especially longitudinal optical (LO), scattering must be considered as an important collision process [33, 34]. We additionally consider intervalley scattering between the Γ valley and the four L valleys, which becomes increasingly important at higher fields. Finally, we also include scattering by acoustic phonons (AP), which is important particularly in the L valley of GaAs, and also important in the BAC model.

6.3.2.1 Nitrogen scattering

We saw in § 6.2 that N strongly perturbs the conduction band of GaAs, introducing a distribution of resonant N states above the conduction band edge. These N states act as resonant scattering centres. Using Fermi's golden rule, the scattering rate for carriers at energy E due to a N resonant state at energy E'_N is given by Eq. (2.13). We use two different models for N scattering in our calculations. Firstly, we presume that all N states are at the same energy, so that the scattering strength due to M nitrogen atoms is then just M times the rate for a single N atom, as given in Eq. (2.13). Secondly, we use the distribution of N states, determined from tight-binding calculations [13] to calculate the scattering rate due to this distribution of states. Fig. 2.4 shows the calculated energy dependence of the scattering rate for several different N compositions, with the zero of energy in each case taken to be at the bottom of the GaNAs conduction band (equivalent to setting the lower eigenvalue of Eq. (3.1) as the zero of energy).

6.3.2.2 Polar optical scattering

Using Eqs. (6.8) and (6.12), the polar optical scattering operator of the symmetric part of the distribution function is given by [71]

$$\begin{aligned}\left(\frac{\partial f_0}{\partial t}\right)_{po} =& \frac{(2m^*)^{1/2}\omega e^2}{4\pi\epsilon_p\hbar\gamma^{1/2}(E)}\left[\left\{\left(n(\omega)+1\right)f_0(E+\hbar\omega)\right.\right.\\ &\left.-n(\omega)f_0(E)\right\}\coth^{-1}\left(\frac{\gamma(E+\hbar\omega)}{\gamma(E)}\right)^{1/2}\left(\frac{d\gamma}{dE}\right)_{E+\hbar\omega}\\ &+\theta\left(E-\hbar\omega\right)\left\{n(\omega)f_0(E-\hbar\omega)-\left(n(\omega)+1\right)f_0(E)\right\}\\ &\left.\tanh^{-1}\left(\frac{\gamma(E-\hbar\omega)}{\gamma(E)}\right)^{1/2}\left(\frac{d\gamma}{dE}\right)_{E-\hbar\omega}\right],\end{aligned} \tag{6.16}$$

and the general form of the momentum relaxation rate, neglecting the wavevector dependence of the cell periodic part of the Bloch function, is given by calculating the rate of change of the asymmetric part of the distribution function, as [71]

$$\begin{aligned}\frac{1}{\tau_{po}} =& \frac{e^2\omega^2(2m^*)^{1/2}}{8\pi\epsilon_p\gamma^{1/2}(E)}\left[n(\omega)\left(\frac{d\gamma}{dE}\right)_{E+\hbar\omega}\left\{\left(\frac{\gamma(E+\hbar\omega)}{\gamma(E)}\right)^{1/2}\right.\right.\\ &-\left(\frac{\gamma(E+\hbar\omega)-\gamma(E)}{\gamma(E)}\right)\coth^{-1}\left(\frac{\gamma(E+\hbar\omega)}{\gamma(E)}\right)^{1/2}\Bigg\}\\ &+\theta\left(E-\hbar\omega\right)\left\{n(\omega)+1\right\}\left(\frac{d\gamma}{dE}\right)_{E-\hbar\omega}\left\{\left(\frac{\gamma(E-\hbar\omega)}{\gamma(E)}\right)^{1/2}\right.\\ &\left.\left.-\left(\frac{\gamma(E-\hbar\omega)-\gamma(E)}{\gamma(E)}\right)\tanh^{-1}\left(\frac{\gamma(E-\hbar\omega)}{\gamma(E)}\right)^{1/2}\right\}\right],\end{aligned} \tag{6.17}$$

where $\theta\left(E-\hbar\omega\right)$ is the step function, $\hbar\omega$ is the optical phonon energy, and the phonon mode occupation number $n(\omega)$ is given by the Bose factor $n(\omega) = 1/[\exp(\hbar\omega/k_BT_L) - 1]$ where k_B is Boltzmann's constant and T_L is the absolute temperature of the lattice, and ϵ_p is given by

$$\frac{1}{\epsilon_p} = \frac{1}{\epsilon_0}\left(\frac{1}{\kappa_\infty} - \frac{1}{\kappa_0}\right). \tag{6.18}$$

Here ϵ_0 is the permittivity of free space and κ_0 and κ_∞ are the low and high frequency dielectric constants respectively. Conwell and Vassell had to approximate

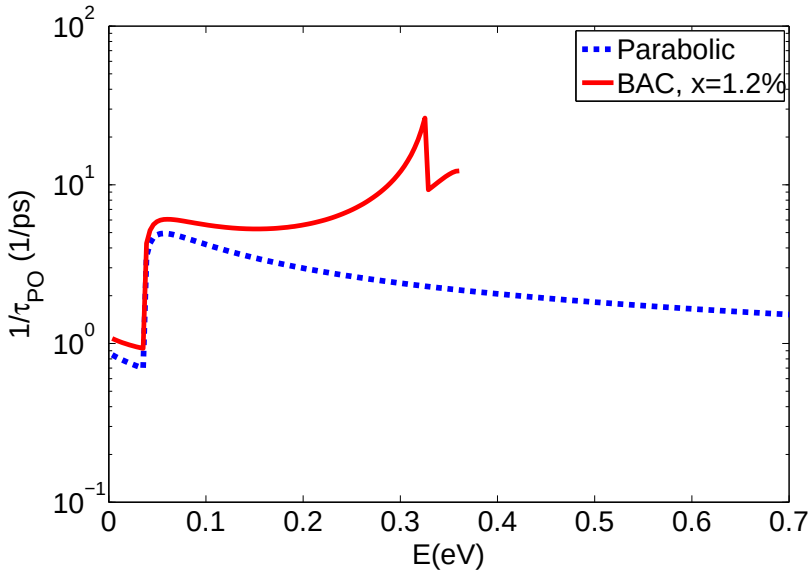

Figure 6.1: Polar optical scattering rate calculated for parabolic central valley of GaAs and lower BAC band of GaN_xAs_{1-x} with $x = 1.2\%$.

Eq. (6.17) by including terms just to lowest order of $(E \pm \hbar\omega)$ in the Boltzmann equation. Later Monte-Carlo calculations [74] showed that this is not a good approximation, so we use Eq. (6.17) with no approximation in our calculations. The dashed blue line in Fig. 6.1 shows the polar optical scattering rate for a parabolic band ($\gamma(E) = E$ and $d\gamma/dE = 1$), while the solid red curve shows this scattering rate when using the nonparabolic band dispersion from the BAC model of Eq. (6.3) for a N composition $x = 1.2\%$.

6.3.2.3 Intervalley scattering

In GaAs the four degenerate L valleys are located about 0.3 eV above the central, Γ, valley. In high electric field, carriers are accelerated to high energies in the Γ valley. When the carriers are above the L valley minimum energy, then intervalley scattering becomes possible, including both Γ-L and L-L scattering. For scattering from the initial valley i to the final valley f, the intervalley phonon energy, $\hbar\omega_{if}$, can be assumed to be constant and its value is given in Table 6.1, with the intervalley scattering rate given by [71, 76]

$$\frac{1}{\tau_{if}} = \frac{\pi D_{if}^2 Z_f}{2\rho\omega_{if}}\left(n(\omega_{if}) + \frac{1}{2} \mp \frac{1}{2}\right) D_f\Big(E - \Delta E_{fi} \pm \hbar\omega_{if}\Big), \tag{6.19}$$

where D_f is the density of states in the final valley, Z_f is the number of final valleys available for scattering, $n(\omega_{if})$ is the number of intervalley phonons (given by the Bose-Einstein factor), and ΔE_{fi} is the energy separation between the final valley

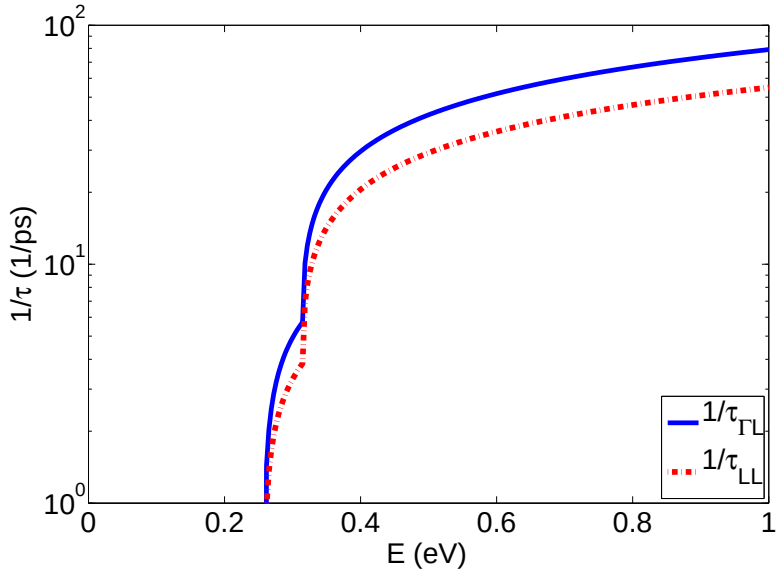

Figure 6.2: Equivalent, L − L, and non-equivalent, $\Gamma - L$, intervalley scattering rates for parabolic Γ and L valleys in GaAs

f and initial valley i band edges. (ΔE_{fi} is zero for intervalley scattering between equivalent valleys.) Fig. 6.2 shows the calculated intervalley scattering rates for parabolic bands in GaAs.

Also using Eq. (6.8), the term due to intervalley scattering from initial valley, i to final valley, f is given by [71]

$$\begin{aligned}\left(\frac{\partial f_i}{\partial t}\right)_{i\rightleftarrows f} = \frac{\pi D_{if}^2 Z_f}{2\rho\omega_{if}}\Bigg\{ & D_f\Big(E - \Delta E_{fi} + \hbar\omega_{if}\Big)\Big[\Big(n(\omega_{if})+1\Big) \\ & \times f_f(E+\hbar\omega_{if}) - n(\omega_{if}) f_i(E)\Big] + D_f\Big(E - \Delta E_{fi} - \hbar\omega_{if}\Big) \\ & \times\Big[n(\omega_{if}) f_f(E-\hbar\omega_{if}) - \Big(n(\omega_{if})+1\Big) f_i(E)\Big]\Bigg\}.\end{aligned} \tag{6.20}$$

6.3.2.4 Acoustic phonon scattering

We can reasonably assume that the acoustic phonon (AP) scattering is elastic near room temperature, with the AP scattering rate given by [49, 76]

$$\frac{1}{\tau_{AP}} = \frac{\pi D_A^2 k_B T_L}{\hbar c_l} D(E), \tag{6.21}$$

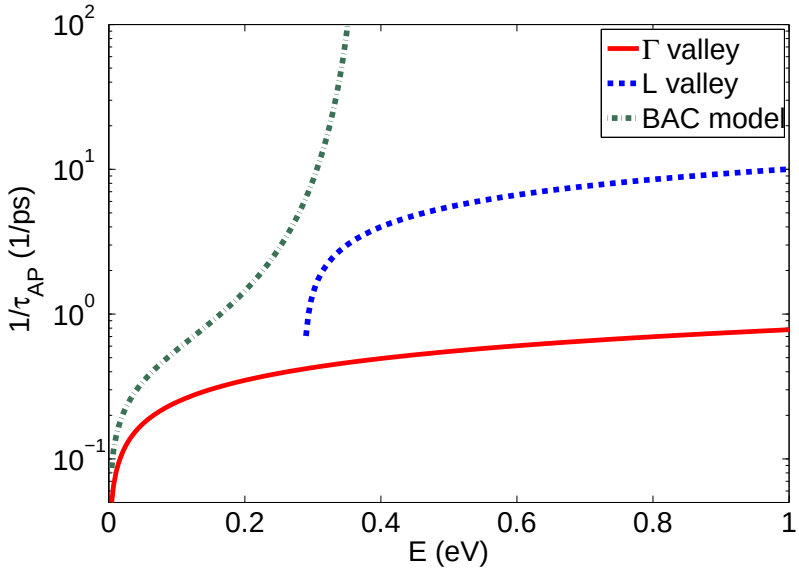

Figure 6.3: Acoustic phonon scattering rates for Γ and L parabolic bands in GaAs, and lowest BAC band for GaN_xAs_{1-x} with $x = 1.2\%$.

where D_A is the electron acoustic deformation potential, and $D(E)$ is the density of states defined in Eq. (6.4). The elastic constant, c_l, is related to the sound velocity, v_s, and mass density, ρ by: $c_l = \rho \times v_s^2$. Fig. 6.3 shows calculated acoustic phonon scattering rates, using parameters given in Table 6.1, in parabolic Γ (solid red curve), and L (dashed blue line) valleys. As we see in the figure, because of the heavier effective mass in the L valley, the relaxation time associated with AP scattering is much smaller there than in the Γ valley. Finally, the green dotted dashed line in Fig. 6.3 shows the calculated AP scattering rate in the lower band of the BAC model for $x = 1.2\%$. The strong increase in scattering rate seen at all energies arises because of the increased density of states in the BAC model compared to the parabolic band model.

6.3.3 Transport calculation method

We describe here the calculation method which we use, taking as an example the case of GaAs with parabolic Γ and L bands. The Boltzmann equation for the Γ valley can be written as

$$\left(\frac{\partial f_\Gamma}{\partial t}\right) = \left(\frac{\partial f_\Gamma}{\partial t}\right)_F + \left(\frac{\partial f_\Gamma}{\partial t}\right)_{PO} + \left(\frac{\partial f_\Gamma}{\partial t}\right)_{\Gamma \rightleftarrows L}, \tag{6.22}$$

where f_Γ is the symmetric part of the distribution functions in the central (Γ) valley of GaAs. The rate of change of the distribution function due to the electric

field is given by Eq. (6.14), while the change due to the polar optical and intervalley scattering terms are given by Eqs. (6.16) and (6.20) respectively. Because we assume a parabolic Γ valley for GaAs, $\gamma(E) = E$, and $d\gamma/dE = 1$.

The relaxation time in Eq. (6.11) is then given in its most general form by

$$\frac{1}{\tau^{\Gamma}} = \frac{1}{\tau_{PO}} + \frac{1}{\tau_{\Gamma L}} + \frac{1}{\tau_{AP}} + \frac{1}{\tau_{N}}, \tag{6.23}$$

with the last term on the right hand equal to zero for GaAs.

The Boltzmann equation for the symmetric part of the distribution function in the L valley can likewise be written as

$$\left(\frac{\partial f_L}{\partial t}\right) = \left(\frac{\partial f_L}{\partial t}\right)_F + \left(\frac{\partial f_L}{\partial t}\right)_{scatt}, \tag{6.24}$$

where

$$\left(\frac{\partial f_L}{\partial t}\right)_F = \frac{2e^2F^2}{3m_L^*(E-E_{L0})^{1/2}}\frac{d}{dE}\left((E-E_{L0})^{3/2}\tau^L f_L'\right), \tag{6.25}$$

and where the collision operator is found by summing over the different scattering

Table 6.1: transport parameters in GaAs

Parameter	*Symbol*	*Value*
Mass density [77]	ρ	5.36 (g/cm^3)
Lattice constant [77]	a_0	5.462 (Å)
Dielectric constant [77]		
High frequency	κ_∞	10.92
Low frequency	κ_0	12.90
Sound velocity [77]	v_s	5.24×10^5 (cm/s)
Electron effective mass [78]		
Γ valley	m^*	$0.067(m_0)$
L valley	m_L^*	$0.286(m_0)$
Acoustic deformation potential [76]		
Γ valley	$D_{A,\Gamma}$	7.01 (eV)
L valley	$D_{A,L}$	9.2 (eV)
Optical deformation potential [76]		
$\Gamma - L$	$D_{\Gamma-L}$	1.0×10^{11} (eV/m)
$L - L$	D_{L-L}	1.0×10^{11} (eV/m)
LO phonon energy [76]	$\hbar\omega$	35.36 (meV)
Intervalley phonon energy [76]		
$\Gamma - L$	$\hbar\omega_{\Gamma L}$	27.8 (meV)
$L - L$	$\hbar\omega_{LL}$	29.0 (meV)
Energy separation between		
Γ and L valleys [79]	$\Delta E_{\Gamma L}$	284 (meV)

processes as

$$\left(\frac{\partial f_L}{\partial t}\right)_{scatt} = \left(\frac{\partial f_L}{\partial t}\right)_{PO} + \left(\frac{\partial f_L}{\partial t}\right)_{L\rightleftarrows\Gamma} + \left(\frac{\partial f_L}{\partial t}\right)_{L\rightleftarrows L}, \tag{6.26}$$

with the relaxation time then given by

$$\frac{1}{\tau^L} = \frac{1}{\tau_{AP}} + \frac{1}{\tau_{\Gamma L}} + \frac{1}{\tau_{LL}}, \tag{6.27}$$

To calculate the distribution functions in the Γ and L valleys, we have solved the time dependent coupled differential equations, Eqs. (6.22) and (6.24) using the finite difference method. We assume a Maxwell-Boltzmann distribution, $\exp(-E/k_BT)$, for the distribution functions $f_\Gamma(E)$ and $f_L(E)$, in zero electric field, $F = 0$. We then calculate how the distribution evolves with increasing field, using the calculated distribution at the ith field value, $F = F_i$ as the starting distribution for field $F_{i+1} = F + \Delta F$, and then integrating the coupled equations until we reach the steady state distribution at field F_{i+1}. We use an energy step size $\delta E = 0.1\hbar\omega$, and set $E_{max} = 1.06$ eV. i.e. for energies higher than that, $f_\Gamma(E) = f_L(E) = 0$. The time step size and the number of time loops varies with the shape of the band, the electric field strength, and the scattering processes included.

Figure 6.4 shows the calculated distribution functions in the parabolic Γ and L valleys in GaAs at different values of electric field strength, from zero up to $F = 70$ kV/cm. All distributions are normalized to $f_\Gamma(0)$, and we have used the transport parameters given in Table 6.1. The lowest (red) lines show the distribution functions in the Γ band (dashed red line), and L band (solid red line) at zero field. For fields up to about 20 kV/cm, $f(E)$ remains parallel to that for $F = 0$ above the bottom of the L valley, indicating that fields up to this value do not cause any significant acceleration of higher-energy electrons. Despite ignoring the band nonparabolicity in GaAs and minor differences in the transport parameters that we use, the results in Fig. 6.4 are very similar to those previously calculated using the Boltzmann equation [71, 80], and the Monte Carlo method [74, 81], confirming that our method therefore provides a good basis to investigate the effects of N on intermediate and high field transport in GaN_xAs_{1-x}.

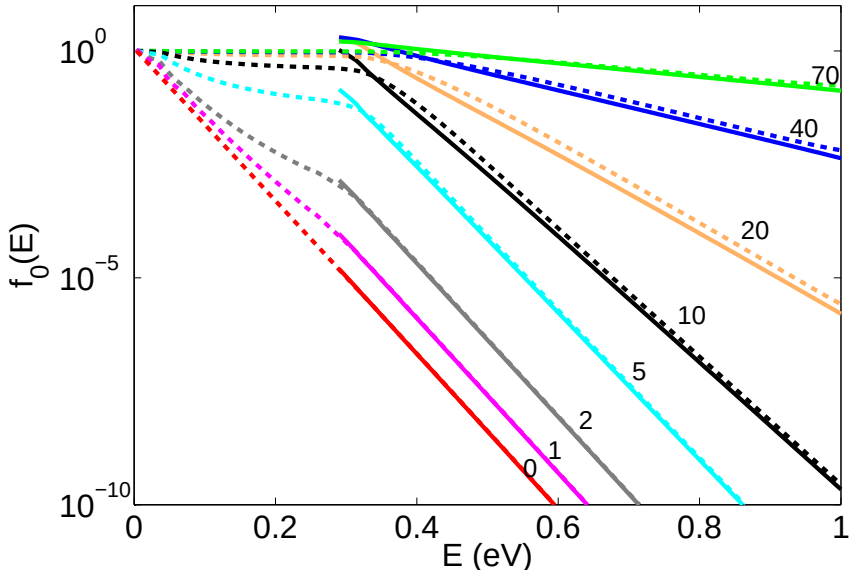

Figure 6.4: Distribution functions in Γ (dashed lines), and L valley (solid lines) of GaAs for increasing values of electric field. The numbers on each curve denote the electric field strength in kV/cm.

6.4 Transport results

We investigate in this section the influence of N scattering on the overall room temperature transport characteristics of GaN_xAs_{1-x} alloys for a range of N compositions, from $x = 0.1\%$ to $x = 2.0\%$. We first use the parabolic band model, described in § 6.2, to analyse the influence of N scattering, including its effect on the carrier distribution functions, carrier mobility as a function of applied field, and variation of drift velocity with applied field up to high electric fields ($F = 70$ kV/cm). We then repeat the analysis using the BAC model, in order to see whether there are any significant differences between the two approaches. Although the overall energy distribution of carriers is clearly very different at high field in the two models, we find very similar overall conclusions regarding carrier mobility and drift velocity as a function of field using the two approaches.

6.4.1 Carrier energy distribution

Figure 6.5 shows the calculated distribution functions in the parabolic Γ and L valleys at $F = 20$ kV/cm, and including various scattering processes. This field was chosen because, in the absence of N scattering, it gives an almost constant electron distribution function in the Γ valley, as shown by the highest (dashed red) line in Fig. 6.5. The middle (blue) lines show the calculated distribution functions when scattering by isolated N states is included (all N resonant states

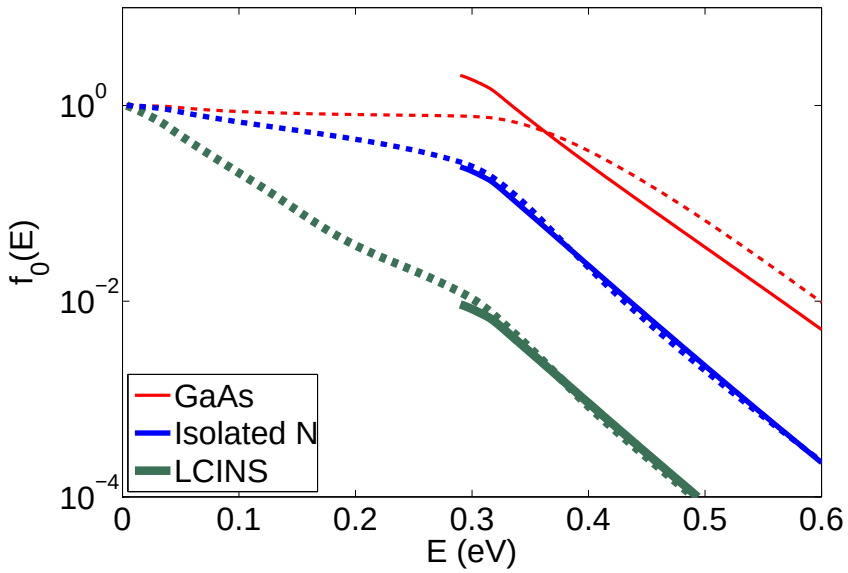

Figure 6.5: (color online) Distribution functions in Γ (dashed lines), and L valley (solid line) in GaN_xAs_{1-x} (x=1.2%), at $F = 20$ kV/cm without N scattering (thin red lines), including only isolated N scattering (blue lines), and scattering by the full distribution of N states (thick green lines).

assumed to be at the same energy, E_N). The lowest (green) lines show the Γ and L distribution functions, including scattering by the full (LCINS) distribution of N states shown in Fig. 2.4. These results confirm that the inclusion of elastic scattering by N states can, at intermediate electric fields, strongly suppress the acceleration of electrons to higher energies in GaN_xAs_{1-x}, with the proportion of carriers in the L valley down by over two orders of magnitude in this case.

This conclusion is confirmed by Fig. 6.6, which shows the calculated average energy of electrons in the Γ band in GaN_xAs_{1-x} as a function of electric field strength up to $F = 30$ kV/cm, for different values of x, and including resonant scattering by the full LCINS distribution of N states. It can be seen for $x = 0$ (GaAs) that the average energy initially increases much more rapidly with F than is the case for $x > 0$, and remains consistently higher at all fields. Using these distribution functions, we can calculate the ratio of the number of carriers, n_Γ in the Γ valley to the total number of carriers, $n_\Gamma + n_L$ as a function of applied field. Fig. 6.7 shows the evolution of this ratio as a function of field for the different values of x considered, again including resonant scattering by the full LCINS distribution of N states. It can be seen that the calculated onset of scattering into the L valley occurs at a higher field in GaN_xAs_{1-x} (~ 6 kV/cm) compared to GaAs (~ 2 kV/cm) and also that the transfer occurs over a much wider field range in GaN_xAs_{1-x}, with 50% of the carriers estimated to be still in

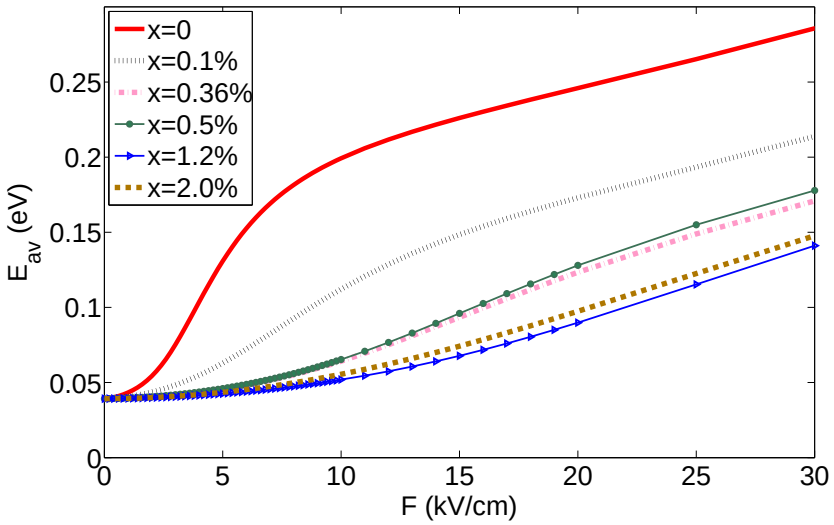

Figure 6.6: Average energy versus electric field in the central band of GaN_xAs_{1-x} for different value of x, in parabolic band model with scattering by full distribution of N states.

the Γ valley at ~ 25 kV/cm, compared to 50% having transferred by ~ 5 kV/cm in GaAs. This confirms the initial suggestion by Adams [14] that the presence of N should suppress carrier acceleration to higher energy in GaNAs compared to GaAs. However, the threshold field for significant impact ionization in GaAs is estimated to be of order 100 kV/cm, and it can be seen from Fig. 6.7 that the majority of electrons are calculated to have been transferred into the L valley by this field in GaN_xAs_{1-x}. This is consistent with the experimental observation that the electron multiplication rate is not strongly modified in GaNAs compared to GaAs [52].

6.4.2 Electron mobility and drift velocity: parabolic band model

Given the carrier distribution function, the current density associated with valley i can then be calculated as

$$j_i = -\frac{2}{3}e^2F\int \frac{\gamma_i(E)\tau^i}{m_i^*(d\gamma_i/dE)^2}\frac{df_i(E)}{dE}N^i(E)dE, \tag{6.28}$$

where m_i^* and τ^i are respectively the effective mass and total relaxation time in the band. Given the current density, we can then calculate the mobility μ as a function of field F as $\mu = j_{tot}/n_{tot}eF$, where j_{tot} is the current density and n_{tot} the carrier density summed over all valleys.

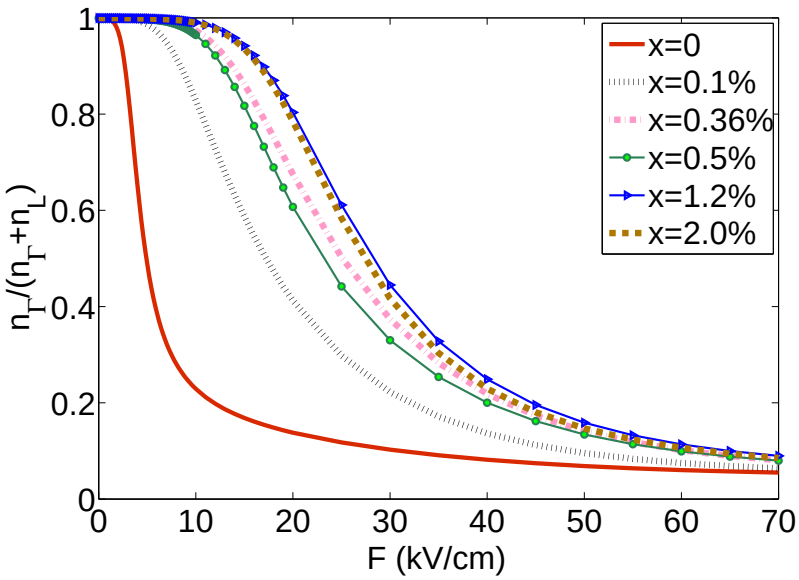

Figure 6.7: Fraction of carriers in the Γ valleys, for different values of x in GaN_xAs_{1-x}, and parabolic Γ and L bands.

Figure 6.8 (a) shows the calculated variation of mobility with applied field F for several values of x, assuming scattering by isolated N states only, while Fig. 6.8 (b) shows the calculated variation when scattering by a full distribution of N states is included. In the absence of N scattering, the low field mobility, around 12000 cm^2/Vs, is higher than the accepted value for GaAs carrier mobility ($\sim$ 8000 cm^2/Vs). This overestimate of the mobility has a number of causes, including our ignoring the nonparabolically of the bands. It can be seen that inclusion of even a small amount of nitrogen causes a drastic reduction in the low field electron mobility. Although the calculated mobility values for GaN_xAs_{1-x} remain larger than those calculated by Fahy *et al.* for the case of scattering by isolated N states [46, 47] they are in very good agreement for the case of scattering by the full LCINS distribution of N states [13]. It can be seen that the calculated mobility decreases with increasing field for all N concentrations, x, both due to the strong effects of N scattering at higher energies in the Γ valley, and also due to increased electron scattering into the lower mobility L valleys. There is no evidence whether N-related resonant scattering is of importance in the L valley, so we therefore do not include any such scattering in the calculations here. Inclusion of N scattering in the L valley could lead to a further reduction in the overall mobility, but this effect is unlikely to be significant, given the strong effect of other scattering mechanisms in the L valley. However, we note that the proximity of the N resonance to the L-valley minimum, along with the relatively large effective mass and density of states there, would give rise to a substantially

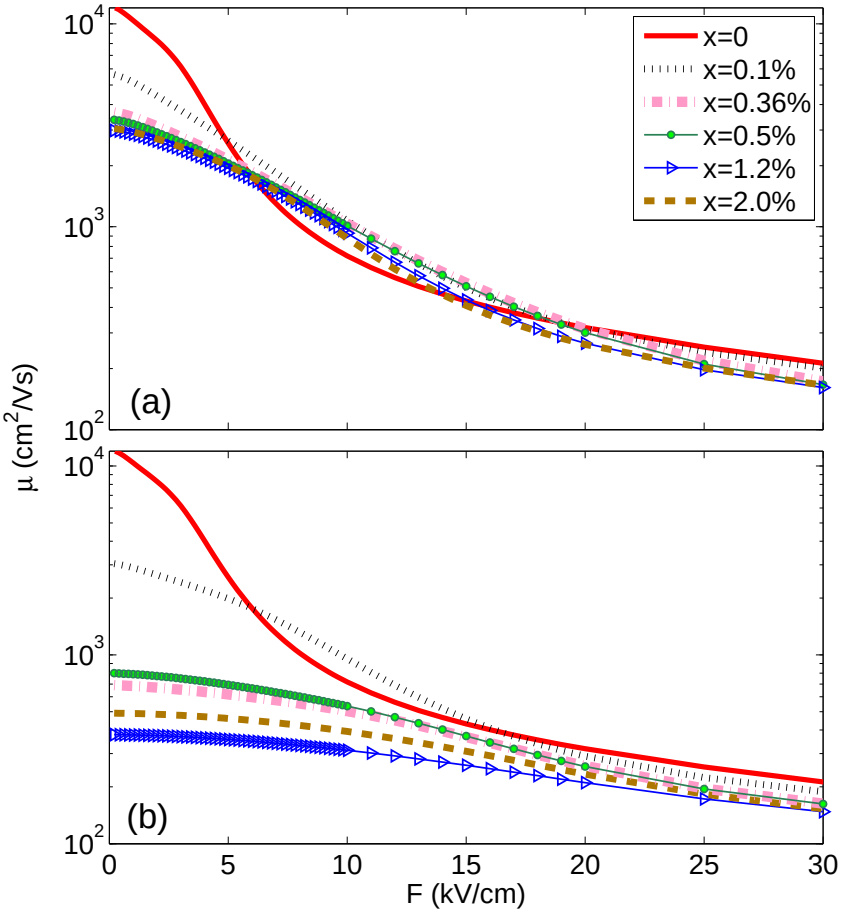

Figure 6.8: Electron mobility, for different values of x in GaN_xAs_{1-x} in parabolic band model including; (a) scattering by isolated N states, and (b) scattering by a full LCINS distribution of N states.

larger N-related scattering rate for carriers in the bottom of this valley, compared to the Γ-valley. There is considerable interest in the variation of the drift velocity v_d with applied electric field in GaAs and in GaN_xAs_{1-x}, and in particular the extent to which a negative differential drift velocity may be possible in the latter case [15, 22, 55]. The total drift velocity can be calculated as

$$v_d = \frac{j_\Gamma + j_L}{e(n_\Gamma + n_L)}, \tag{6.29}$$

Figure 6.9 shows the calculated field dependence of the drift velocity in GaN_xAs_{1-x} with $x = 1.2\%$, for parabolic Γ and L valleys, without and with N scattering.

The dot-dashed red line in this figure shows the calculated variation of v_d for GaAs, assuming a parabolic Γ band and no N scattering. This curve shows a very similar behaviour to that previously calculated [71, 74] and measured [82] for

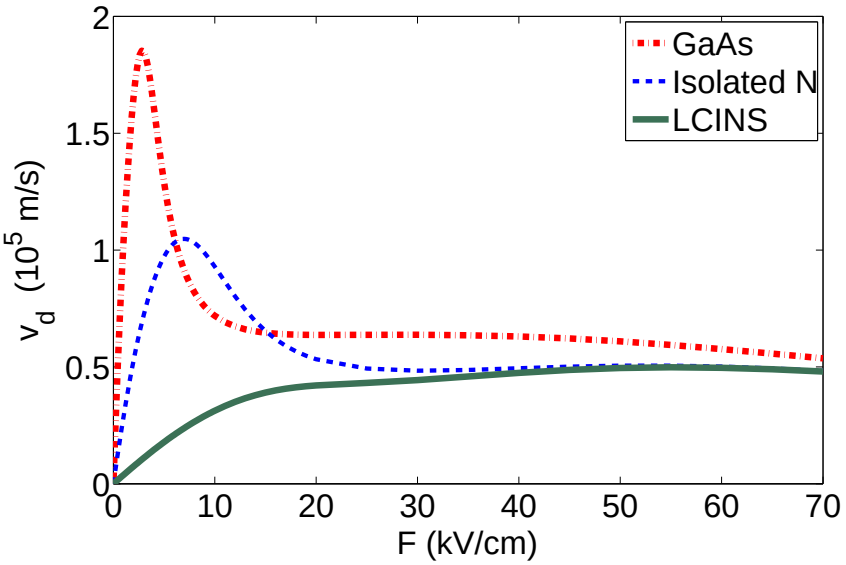

Figure 6.9: Calculated variation of drift velocity with electric field for GaAs in comparison with $GaN_{0.012}As_{0.988}$ with scattering by isolated N, and full LCINS distribution of N states in parabolic band model.

GaAs, with the drift velocity showing a rapid linear increase at low fields, before it reaches a peak value and then decreases rapidly, to less than 40% of its peak value, as scattering into the L valley becomes important close to $F = 5$ kV/cm. When we include scattering due to isolated N atoms (dashed blue line), the peak in the drift velocity occurs at a lower velocity and higher field value. Including scattering by a full distribution of N states suppresses the negative differential velocity. There is still a small calculated decrease in velocity at higher field, but the maximum magnitude of this calculated decrease, $|dv_d/dF|$, is down by over an order of magnitude compared to the N-free case. Given that the model we are using overestimates the low field mobility compared to previous calculations, we conclude that a field region with negative differential velocity is then highly unlikely for $x = 1.2\%$, in agreement with experimental analysis [57].

Figure 6.10 presents the calculated variation of drift velocity with field for several nitrogen concentrations, x, where we include in this case scattering by the full distribution of N states. It can be seen that the inclusion of even just 0.1% of N causes a reduction in the peak value, and shifts it to higher field, with an even stronger reduction and complete elimination of the negative differential field region at higher compositions, as we see no NDV for 1.2 and 2.0%.

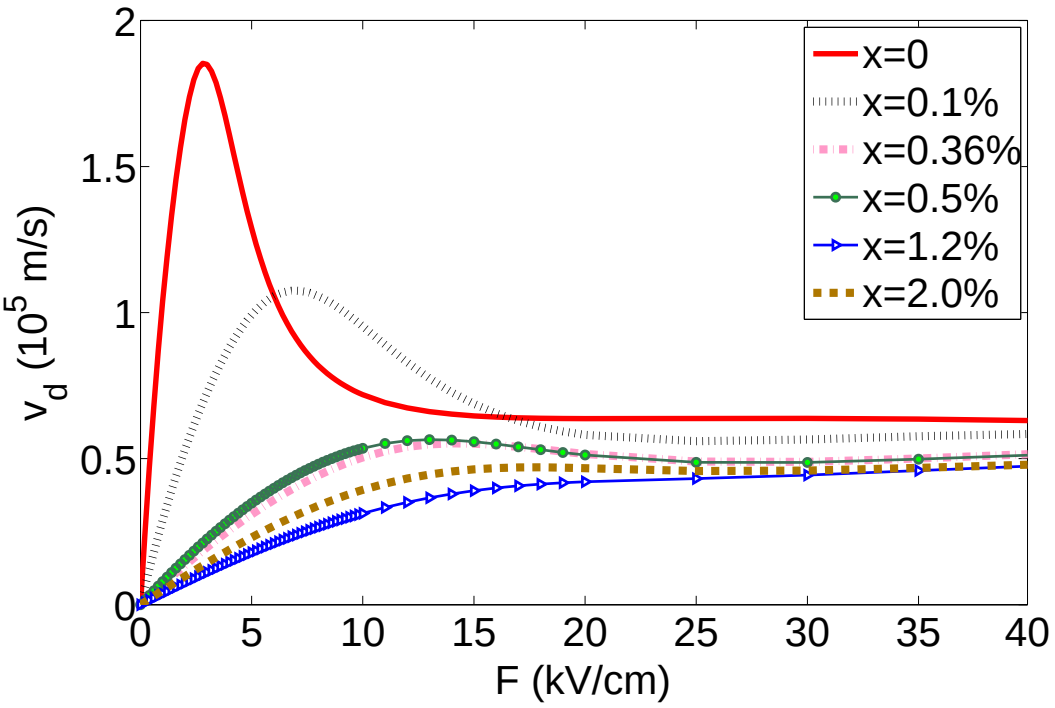

Figure 6.10: Drift velocity versus electric field in GaN_xAs_{1-x} for different values of x in parabolic band model, including scattering by the full distribution of nitrogen states.

6.4.3 Electron mobility and drift velocity: BAC model

The parabolic band model used to this point correctly allows electron acceleration to higher energies, but ignores the conduction band non-parabolicity expected in dilute nitride alloys. To investigate the effects of band non-parabolicity, we now use the BAC model to calculate the field dependence of the carrier distribution function, mobility and drift velocity.

The distribution function for electrons confined in the lower band of the BAC model can be calculated by solving the Boltzmann equation as

$$\left(\frac{\partial f_0}{\partial t}\right)_{BAC} = \left(\frac{\partial f_0}{\partial t}\right)_{F,BAC} + \left(\frac{\partial f_0}{\partial t}\right)_{PO,BAC}, \tag{6.30}$$

where the electric field and scattering terms are given by Eqs. (6.14) and (6.16), respectively. The nonparabolicity factor, $\gamma(E)$, is given in this case by Eq. (6.3), and the relaxation time can be obtained as

$$\frac{1}{\tau_{BAC}} = \frac{1}{\tau_{PO}} + \frac{1}{\tau_{AP}} + \frac{1}{\tau_N}. \tag{6.31}$$

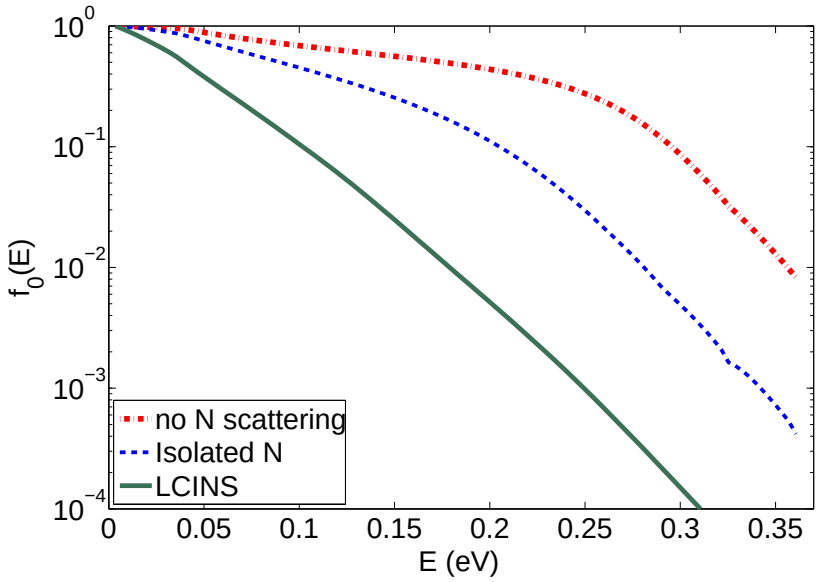

Figure 6.11: Distribution function in the lower band of BAC model in $GaN_{0.012}As_{0.998}$ at $F = 20$ kV/cm, in the absence of N scattering (dashed-dotted red line), including scattering by isolated N (dashed blue line), and full distribution of N states (solid green line).

The polar optical and acoustic phonon scattering rates are given by Eqs. (6.17) and (6.21), respectively. Also, $1/\tau_N = R(E)$ represents the assumed N scattering rate, which varies depending on whether we just include scattering by isolated nitrogen levels, or treat the full distribution of N levels, as presented in Fig. 2.4.

We solve the time dependent equation for the distribution function, Eq. (6.30), in a similar way to that done for the parabolic band model, with the maximum (cut-off) energy of the band E_{max}, given by Eq. (6.5), e.g. $E_{max} = 361$ meV for $x = 1.2\%$.

The dashed-dotted red line in Fig. 6.11 shows the symmetric part of the distribution function calculated using the BAC band structure for GaN_xAs_{1-x} with $x = 1.2\%$ and $F = 20$ kV/cm, with no N scattering included. The middle (dashed blue) line shows the calculated distribution function including scattering by isolated N states, while the lowest (solid green) line shows the distribution function calculated assuming scattering by the full distribution of N states. These results show a greater suppression of electron acceleration, compared to the results calculated using the parabolic band model (see Fig. 6.5).

Figure 6.12 shows the mobility calculated for different nitrogen concentrations, x, using the BAC band structure model, including resonant scattering by a distribution of N states. It can be seen that the calculated low-field mobility is reduced here, in most cases by about 40%, compared to the values in Fig. 6.8 (b).

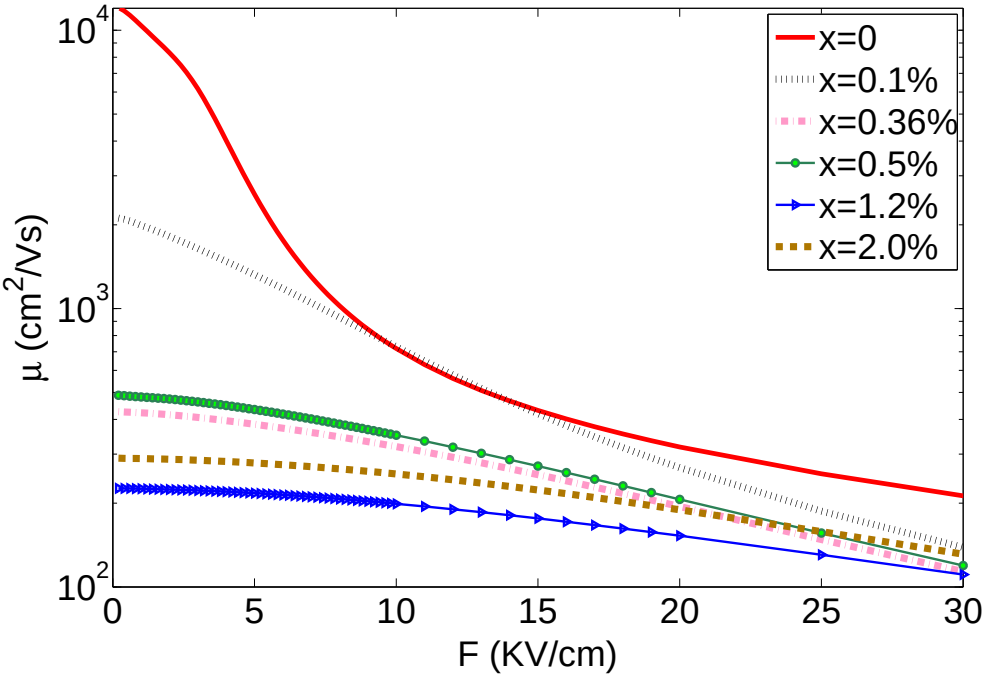

Figure 6.12: Electron mobility in the lower Band of BAC model, including scattering by full distribution of N states, for different values of x in GaN_xAs_{1-x}.

This reduction arises due both to the band nonparabolicity in the BAC model, and also due to the increased band edge mass in the BAC model compared to the parabolic band model used in Fig. 6.8 (b), which assumed an electron mass equal to that in GaAs. These low-field mobilities are very similar to those calculated by Fahy *et al.* [13] using the full distribution of N states and a parabolic band model with the BAC band edge effective mass. The mobility again decreases with increasing field in the BAC model, associated in this case with electrons approaching the flat band dispersion at the top of the BAC band. Since the localised state spectrum and the position of the conduction band edge change substantially with nitrogen concentration, the observed trends in the variation of mobility is not monotonic, i.e. the mobility may not necessarily increase when the nitrogen concentration decreases, as seen in Figs. 6.8 and 6.12.

Figure 6.13 shows the electric field dependence of the drift velocity in GaN_xAs_{1-x} for $x = 1.2\%$, calculated using the BAC model. The dashed-dotted red line shows the drift velocity calculated in the BAC model, omitting the effects of N scattering. It can be seen that the BAC band nonparabolicity, and finite cut-off energy, E_{max}, lead in this case to a negative differential velocity above a field $F = 7$ kV/cm. This behaviour is similar to that calculated previously us-

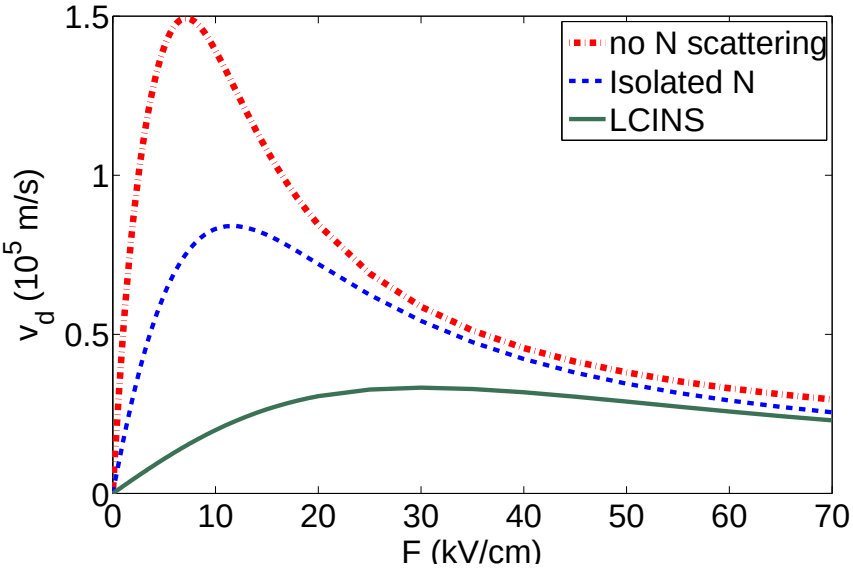

Figure 6.13: Electric field dependence of drift velocity in the lower band of BAC model in $GaN_{0.012}As_{0.998}$, in the absence of N scattering (dashed-dotted red line), including scattering by isolated N (dashed blue line), and full distribution of N states (solid green line).

ing detailed balance equations [15] and assuming energy-independent scattering times. The blue dashed line shows the calculated drift velocity including scattering by isolated N levels, while the solid green line shows the effect of including scattering due to the full LCINS distribution of N levels. It can be seen that both of these reduce the calculated peak velocity value, shifting it also to a slightly higher field, and leading to a substantial reduction in the velocity-field slope value in the negative differential velocity region.

Figure 6.14 shows the drift velocity versus electric field calculated for various values of x in GaN_xAs_{1-x} using the BAC model, and including scattering due to the LCINS distribution of N states. For comparison, the solid red line shows the drift velocity of GaAs, calculated using the parabolic band model. It can be seen that using the BAC model and including nitrogen scattering leads to a much reduced peak velocity for all N compositions. It can be noted that, whereas the calculated drift velocity begins to increase again with increasing field in GaAs, it continues to decrease to higher field in the N-containing samples. This continued reduction occurs because the BAC model used in Fig. 6.14 includes the unphysical assumption that carriers cannot be accelerated to energies above E_{max}. An increasing proportion of carriers are then found near to the top of the BAC band with increasing field, where the large mass and strong N scattering then limit the calculated drift velocity value.

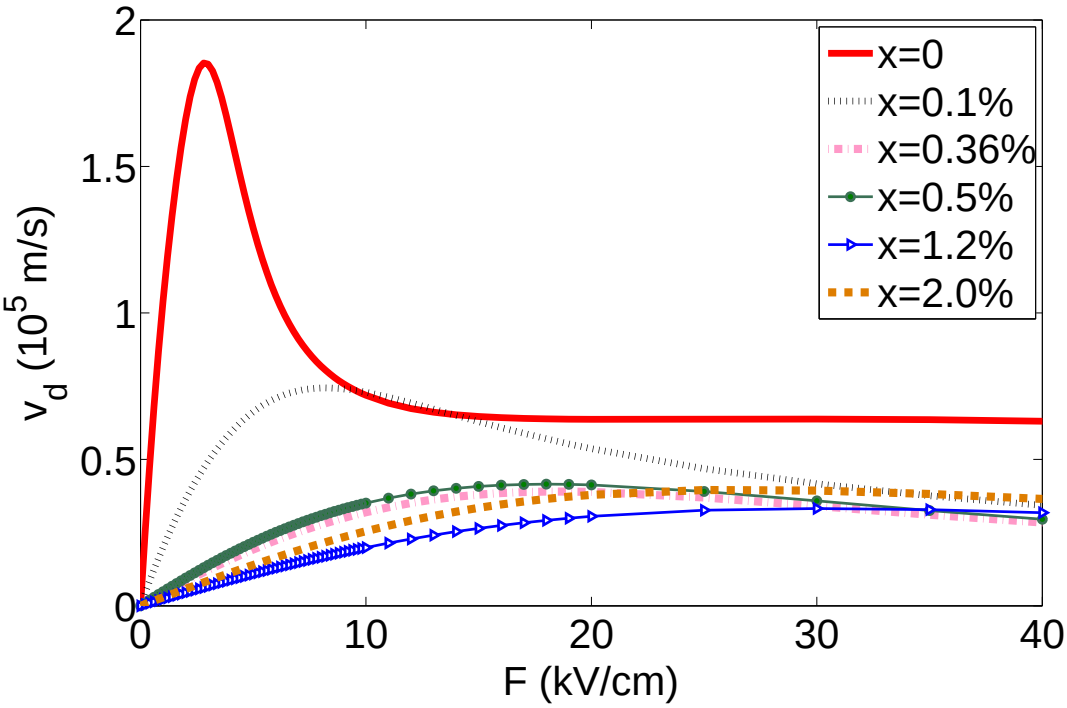

Figure 6.14: Electric field dependence of drift velocity in BAC model, including scattering by full distribution of N states, in GaN_xAs_{1-x} with different values of N concentration x.

6.5 Discussion and conclusions

It is well recognized that modeling of electron transport properties in dilute nitride alloys is difficult [83], because N introduces such a strong perturbation to the conduction band dispersion, with the influence of N often described using the band-anticrossing model [9]. The low-field mobility of GaNAs has previously been calculated using both parabolic band [13, 16] and BAC [16, 34, 35] approaches. Both methods predict a strongly reduced electron mobility in GaNAs compared to GaAs, in good agreement with experiment, for which typical mobility values are in the range $\sim 100 - 200$ cm^2/Vs.

There is also interest in the intermediate and high-field transport properties of dilute nitride alloys, both for potential negative differential (NDV) devices [15], and also for suppression of electron multiplication in avalanche photodiodes [14]. Theoretical analysis of such structures requires an understanding of the behaviour of higher energy electrons in GaNAs alloys.

In order to address this problem, we therefore first considered here the band structure of dilute nitride alloys, using a Green's function model in § 6.2 to address the conduction band dispersion in random alloys. We showed that the BAC model

describes well the band dispersion away from N resonant state energies, but that the energy gap predicted by the BAC model does not occur in actual Ga(In)AsN samples. Instead, the gap is washed out both because of disorder effects and also because the N levels are broadened, due to their being resonant with the host matrix conduction band levels.

It is very difficult to treat the Green's function band structure exactly in conventional transport models, and we did not attempt to do so. Instead we use and compare the results of two approaches, one of which is likely to provide a lower bound on the effects of N incorporation, while the second approach clearly overestimates the effects of N on the band structure.

For the first approach, we assumed that the conduction band retains a parabolic dispersion, but included explicitly the strong resonant scattering associated both with isolated N atoms and also with a full distribution of N states, calculated using a tight-binding approach. We showed that the N-related elastic scattering strongly limits the mobility and the acceleration of electrons to higher energy, with the initial transfer of carriers to the L bands occurring at higher field than for GaAs, and with a much higher field also being required to achieve close to total carrier transfer to the L bands.

This reduction in low-field mobility and slower rate of carrier transfer to the L bands leads to a suppression of the strong negative differential velocity (NDV) effects observed in GaAs, consistent with NDV only being observed to date in GaNAs at very low N composition ($x \sim 0.2\%$) and temperature.

We nevertheless find at the high fields required for avalanche multiplication that the calculated fraction of carriers in the L bands is comparable in GaNAs and in GaAs, consistent with the experimental observation that electron multiplication in GaNAs samples shows similar behaviour to that observed in GaAs [52].

The results of this parabolic band model were then compared with calculations using the highly non-parabolic band dispersion given by the BAC model, where the carriers are constrained to remain in the lower BAC band, at energies below the normal N resonant state energy. These calculations show that the inclusion of a strongly non-parabolic band dispersion with N resonant scattering further reduces the low-field mobility compared to the parabolic band case. The results of the BAC-based calculations are not however expected to be relevant at high fields, because of the unphysical constraint of limiting the electron acceleration to a maximum cut-off energy.

We conclude for lower N concentration, in agreement with previous Monte-Carlo calculation [16, 58] and experimental results [15], that NDV can still be

present, but at higher electric fields than those where NDV occurs in GaAs. However, for higher N concentration NDV disappears, in agreement with experimental measurement [57].

Overall, we conclude that it remains a challenging problem to describe exactly intermediate- and high-field carrier transport in dilute nitride alloys, including details of the conduction band dispersion such as we presented in § 6.2. Nevertheless, the combination of information from the two models which we use here provides a clear analysis of the strong influence of N scattering on electron transport in dilute nitride alloys, consistent with the observed experimental behaviour across the complete range of electric fields considered. In Chapter 7 we will further investigate the band structure of GaNAs by finding the complex poles of the SCGF method presented in Chapter 5. We then calculate the band dispersion, scattering rate and mobility of carriers using this method.

Chapter 7

Band dispersion, scattering rate and carrier mobility using the poles of the Green's function

7.1 Introduction

In Chapter 6, we calculated electron mobilities using two approximate models of the carrier band dispersion and scattering: the parabolic band model and the BAC model. In the parabolic band model, we ignored the effects of the localised states on the band dispersion and included only their effect on the carrier scattering rate. In the BAC model, we included principally the effect on the band dispersion, while calculating the nitrogen scattering rate approximately from second order perturbation theory. In this chapter we calculate the carrier band dispersions and scattering rates in a self-consistent manner from the (complex) poles of the Green's function G_{kk} discussed in Chapter 5. This allows us to take into account the effects of nitrogen-induced states on both the band dispersion and carrier scattering. We find poles of G_{kk} at complex energies $\varepsilon_p(k)$. We interpret the real part of $\varepsilon_p(k)$ as the physical (average) energy of a carrier state of momentum k and the imaginary part (multiplied by $-2/\hbar$) as the scattering rate due to disorder.

We then use these band dispersions and scattering rates in a semiclassical calculation of the carrier mobility, obtained from the Boltzmann Transport Equation in the relaxation time approximation, in an approach formally similar to that used in Ref. [13], where a parabolic model of the band dispersion was used. Our results show a shorter carrier mean free path and lower carrier mobility for GaNAs, compared with those obtained in Ref. [13], agreeing more closely with experimental

measurements of the carrier mobility.

To find the poles $\varepsilon_p(k)$, where $G_{kk}^{-1}(\varepsilon_p(k)) = 0$, we need to solve for the self-consistent Green's function (SCGF) at complex energies. In finding the density of states in Chapter 5, we determined the self-consistent Green's function for real values of the energy using an iterative search method to solve the self-consistent equations (Eqs. (5.2) and (5.3)) involved. We found that this iterative search method converged well for the range of energies of interest. However, there is no general guarantee that such a method will converge for arbitrary complex energies. (Indeed, there was no guarantee in advance that it would converge for real energies, but we found empirically that it did.) In finding the complex poles, it turns out that we can simplify the problem, making use of a particular property of the integrated Green's function, $G_{cb}(E) = \int G_{kk}(E)\mathrm{d}^3\mathbf{k}$, namely that it depends on the E only through the quantity $\gamma = G_{kk}^{-1} + E_k$, where $E_k = \hbar^2k^2/2m^*$. Thus, for each k, since $G_{kk}^{-1} = 0$ at the pole, the (self-consistent) value of γ that we require at the pole energy is simply E_k. (We note that this approach is valid only at the poles and does not allow determination of the Green's function at other values of the complex energy.) This substantially simplifies the numerical problem of determining the pole energies, $\varepsilon_p(k)$, as discussed in § 7.3.1, below.

The object of this chapter is to calculate charge transport properties taking into account the scattering rates and energy shifts of the carrier bands, calculated in a self-consistent manner. Band dispersions and scattering rates are obtained from the poles of the Green's functions, and compared with simple parabolic and BAC models of the bands.

We present in the next section the SCGF method with complex energy, and then in § 7.3 and § 7.4 we calculate the poles of Green's function, for two-level and LCINS models, respectively. Thereafter in § 7.5, we calculate the rates for electron scattering by N states, and derive the n-type carrier mobility and mean free path for GaN_x As_{1-x}alloys in § 7.6. Finally we summarize and conclude in § 7.7.

7.2 The poles of the SCGF

7.2.1 The self-consistent Green's function method

We have already shown in § 5.2 that the Green's function for extended states k and localised states j are given by Eqs. (5.2) and (5.4), respectively. Also the (complex) energy shift of each localised state j is given by Eq. (5.3).

We solved equations (5.2) and (5.3) self-consistently by an iterative search

numerical procedure, as they do not in general admit an analytical solution. Having calculated $\Delta E_j(E)$, the density of states projected onto extended and localised states can be calculated by Eqs. (5.8) and (5.9), respectively. The results in Chapter 5 for the DOS, calculated in the two-level SCGF method, showed excellent agreement with the DOS, calculated by numerical diagonalisation of the Hamiltonian of random supercells, and confirms the validity of this method.

Once we have the Green's function, we can calculate a variety of physical properties of our system. Of particular importance in transport calculations are the poles of the Green's function, where $G_{kk}^{-1}(\varepsilon_p) = 0$, in the lower-half complex plane: the real part of ε_p equals the energy of the state with momentum k and the (negative) imaginary part is $-\hbar/(2\tau_k)$, where τ_k is the lifetime [84, p. 275]. Having these poles ε_k of the Green's function, we are then able to determine the group velocity and decay rate of carrier states and, using these in a semi-classical Boltzmann transport equation, we can calculate the carrier mobility.

To calculate the poles of the GF, we consider a complex energy, $\varepsilon = E + i\delta$, instead of real energy E in Eqs.(5.2) and (5.3), where $E = \Re[\varepsilon]$ and $\delta = \Im[\varepsilon]$. We then have the self-consistent equations for complex ε

$$G_{kk}(\varepsilon) = \left\{ \varepsilon - E_k - \frac{1}{N_c} \sum_j \frac{|V_j|^2}{\varepsilon - E_j - \Delta E_j(\varepsilon)} \right\}^{-1}. \tag{7.1}$$

and

$$\Delta E_j(\varepsilon) = \frac{|V_j|^2}{N_c} \sum_k G_{kk}(\varepsilon), \tag{7.2}$$

We have considered two different methods of finding the poles of Green's function. In the first method, we find ε_p using a *complex eigenvalue method* which is explained in the next section. We present an alternative *iterative search method* (analogous to that used in Chapter 5) of finding the poles in Appendix B. In this method we search numerically for zeros of G_{kk}^{-1}, by finding $\Delta E_j(\varepsilon)$ for all values of real and imaginary part of the complex energy ε by an iterative search method. Where both methods converge their results agree well, but the convergence of the second method tends to fail near band edges.

7.3 The two-band model

Here we first consider the two-level model, assuming all localised states have the same energy E_N. This model provides a good understanding of the effect of the isolated N states in GaNAs alloys. We are also able to compare the results of the

SCGF approach calculated for the two-band model with the BAC and supercell models.

7.3.1 Complex eigenvalue method of finding the poles in the 2-band model

The broadening $\Delta E_N(\varepsilon)$ in the two-level model, using Eq. (5.3), is given by

$$\Delta E_N(\varepsilon) = \frac{\beta^2}{N_c}\int_0^{E_{max}} G_{kk}(\varepsilon)D_0(E_k)\mathrm{d}E_k. \tag{7.3}$$

Employing Eqs. (5.12) and (5.13), this can be written as

$$\Delta E_N(\varepsilon) = \beta^2\frac{(2m^*)^{3/2}a_0^3}{16\pi^2\hbar^3}\left\{\sqrt{\gamma(\varepsilon)}\ln\left[\frac{\sqrt{\gamma(\varepsilon)}+\sqrt{E_{max}}}{\sqrt{\gamma(\varepsilon)}-\sqrt{E_{max}}}\right]-2E_{max}^{1/2}\right\}, \tag{7.4}$$

where E_{max} is the maximum energy of band states coupling to the localised states and γ is defined in Chapter 5. The condition for the pole ε_p of the Green's function is

$$\varepsilon_p - \frac{V_{Nc}^2}{\varepsilon_p - E_N - \Delta E_N(\varepsilon_p)} = \gamma(\varepsilon_p) = E_k. \tag{7.5}$$

Thus, substituting E_k for $\gamma(\varepsilon_p)$ in Eq. (7.4) gives a single value of the localised state energy shift for each momentum k as

$$\Delta E_N(\varepsilon_p) = \beta^2\frac{(2m^*)^{3/2}a_0^3}{16\pi^2\hbar^3}\left\{\sqrt{E_k}\ln\left[\frac{\sqrt{E_k}+\sqrt{E_{max}}}{\sqrt{E_{max}}-\sqrt{E_k}}\right]-2E_{max}^{1/2}-i\pi\sqrt{E_k}\right\}, \quad \text{for } 0\le E_k\le E_{max} \tag{7.6}$$

and there is no need to determine ΔE_N by an iterative search. Solving Eq. (7.5) and using the value of $\Delta E_N(\varepsilon_p)$ in Eq. (7.6) the complex band energies for the 2-level system are then given by the closed formula

$$\varepsilon_p = \frac{E_k + E_N + \Delta E_N(\varepsilon_p)}{2} \pm \sqrt{\frac{\left(E_k - E_N - \Delta E_N(\varepsilon_p)\right)^2}{4} + V_{Nc}^2}. \tag{7.7}$$

This is very similar to Eq. (3.4) that we used in the modified BAC, in Chapter 3. The only difference is that here the (complex) broadening parameter is given explicitly by Eq. (7.6).

In Appendix B we present an iterative search method as an alternative way of finding the poles of the Green's function. The iterative search method of finding

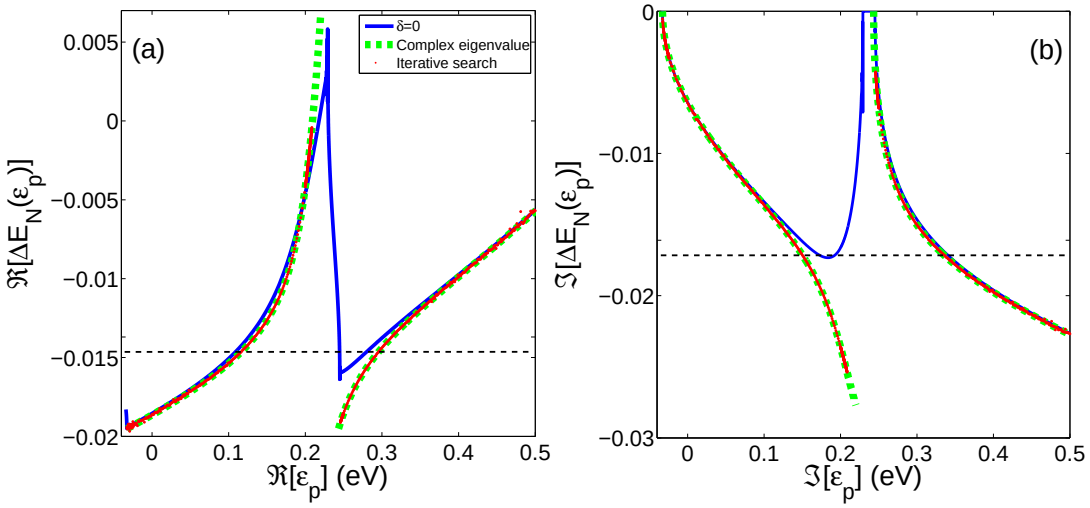

Figure 7.1: The real and imaginary parts of the broadening parameter $\Delta E_N(\varepsilon)$ for the two-band model of GaN_x $As_{1-x}$with $x = 0.2\%$. The green dashed lines, and red dots show $\Delta E_N(\varepsilon_p)$ calculated by complex eigenvalue approach and iterative search method, respectively. The blue line shows the value of $\Delta E_N(E)$ for the corresponding real values of $E = \Re(\varepsilon_p)$. The horizontal lines display the values obtained using the second order perturbation theory.

the poles fails to find $\Delta E_N(\varepsilon_p)$ for energies E very close to band edges. In contrast to the complex eigenvalue method, which calculates $\Delta E_N(\varepsilon_p)$ only at poles of the Green's function, the iterative search approach calculates $\Delta E_N(E + i\delta)$ for all values of real, E, and imaginary, δ, parts of the complex energy surface.

Figure 7.1 displays the imaginary and real parts of $\Delta E_N(\varepsilon)$ at poles, ε_p, and at the real energy E. Dashed green lines in this figure show the imaginary and real parts of $\Delta E_N(\varepsilon_p)$ calculated by Eq. (7.6) assuming $E_{max} = 0.857$ eV and varying CB energy from 0 to 0.7 eV. The red dots in this figure show the same quantities calculated using the iterative search method. Very good agreement is observed between the results of $\Delta E_N(\varepsilon_p)$ in two methods. However, we see that the iterative search method does not converge and is unable find any value of $\Delta E_N(\varepsilon_p)$ for energies close to E_N, whereas the complex eigenvalue method does not have this problem. In contrast to the iterative search method, in the complex eigenvalue method the upper sub-band starts from $k = 0$.

The real and imaginary parts of $\Delta E_N(E)$ at real axis of energy ($\delta = 0$) are shown by the blue solid line in Fig. 7.1. Within the bands, for the energies far from localised N states, $\Delta E_N(\varepsilon_p)$ is apparently equal to $\Delta E_N(E)$ (at real axis), but this is not the case close to E_N.

The results calculated at the poles deviate from those calculated at the real

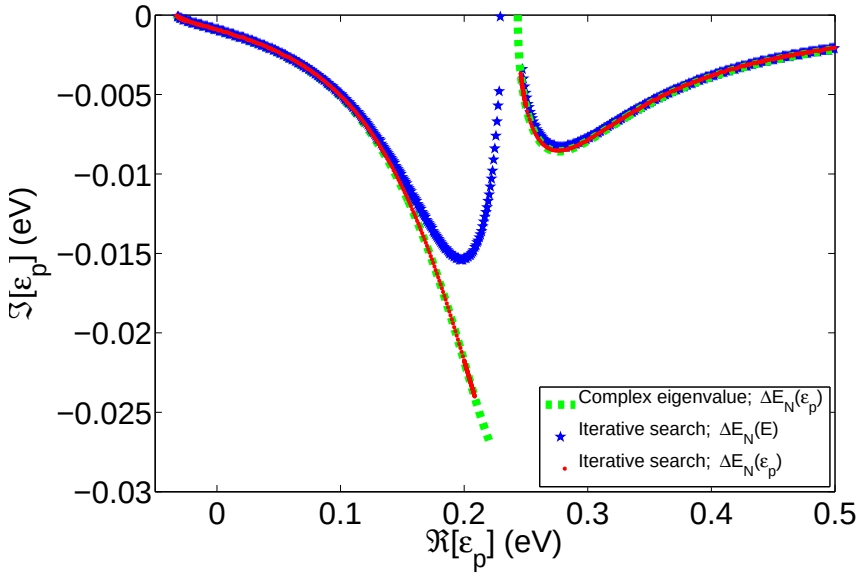

Figure 7.2: The imaginary part of poles of the Green's function G_{kk} calculated for 2-band model in $GaN_x As_{1-x}$with $x = 0.2\%$, using iterative search method by $\Delta E_N(\varepsilon_p)$ (red dots) and $\Delta E_N(E)$ for real E (blue stars), and complex eigenvalue method (green dashed line) for $E_{max} = 857$ meV and varying CB energy E_k from 0 to 0.7 eV.

axis, both at the bottom of upper and top of the lower band. From Eqs. (5.6) and (5.8) the density of states can be obtained by

$$D_{cb} = -(N_c/\pi\beta^2)\Im[\Delta E_N(E)]. \tag{7.8}$$

So the blue solid line in Fig. 7.1.(b) is proportional to D_{cb} (green circles in Fig. 5.3). Later in this chapter we will compare some results of considering ΔE_j at real axis, $\Delta E_j(E)$, and on the complex surface, $\Delta E_j(\varepsilon)$.

In Fig. 7.2 the dashed green line displays the imaginary part of the poles, ε_p versus its real value, calculated using complex eigenvalue method. The blue stars and red dots in this figure show the poles, ε_p, of Green's function calculated in iterative search method using ΔE_N given on the complex surface (the green dashed lines in Fig. 7.1), and at the real axis (the blue solid lines in Fig. 7.1), respectively. As we see, ignoring the δ dependence of ΔE_N (assuming $\Delta E_N(\varepsilon_p) = \Delta E_N(E)$), pushes $\Im[\varepsilon_p]$ to zero for the energies just below the N energy, E_N.

This plot again confirms the agreement between the two methods of finding the poles. The complex eigenvalue method not only finds poles for all energy ranges, but also it is much faster than the iterative search method, as we do not need any iteration to find ΔE_N at the poles of Green's function. However, we note that if the maximum of CB energy E_k approaches to E_{max} the logarithmic

term in the bracket in Eq. (7.6) tends to infinity. This arises due to abrupt change of coupling (from β to zero) to states with energy greater than E_{max}. That is why we avoid E_k very close to E_{max} in calculating $\Delta E_N(\varepsilon_p)$ using Eq. (7.6).

7.3.1.1 Exact solution for localised state with Lorentzian inhomogeneous broadening

We can extend this 2-band solution given in Eq. (7.7) to the case of an inhomogeneously broadened level if we assume that the inhomogeneous broadening is given by a Lorentzian distribution, centered at energy E_N with energy width ζ. In this case $\Delta E_N(\varepsilon_p)$ in the previous formula for ε_p is replaced by $\Delta E_N(\varepsilon_p) - i\zeta$, to give

$$\varepsilon_p = \frac{E_k + E_N + \Delta E_N(\varepsilon_p) - i\zeta}{2} \pm \sqrt{\frac{\left(E_k - E_N - \Delta E_N(\varepsilon_p) + i\zeta\right)^2}{4} + V_{Nc}^2}. \quad (7.9)$$

Note that, unlike the case for the localised level without broadening, the imaginary part of ε_p does not tend to zero as $k \longrightarrow 0$. If the momentum band collides with a continuous distribution of localised states, the lifetime of the band state is finite at $k = 0$.

As the momentum k is varied, the lower energy band at small k will connect continuously, either with the lower energy band or with the upper energy band at large k. Which band topology occurs depends on the behaviour of the square root in Eq. (7.9): if the localised state concentration x is very small or the broadening ζ is large, then the (complex) argument of the square root winds once around the origin in the complex plane as k goes from 0 to ∞ and the lower band (for small k) connects continuously with the upper band (for large k). An approximate condition for this is

$$\left\{\frac{-\Im[\Delta E_N] + \zeta}{2}\right\}^2 > V_{Nc}^2, \quad (7.10)$$

when $E_k = E_N + \Re[\Delta E_N]$. This then gives that

$$\beta^2 \frac{(2m^*)^{3/2} a_0^3}{16\pi\hbar^3} \sqrt{E_k} + \zeta > 2\beta\sqrt{x}. \quad (7.11)$$

Thus, localised states of very low concentration x distort the band dispersion of the original parabolic band but do not alter its topology, leaving the upper and lower sections of the original parabolic band connected to each other. For higher concentrations, the lower band does not connect continuously to the upper band, giving an anti-crossing type of band topology.

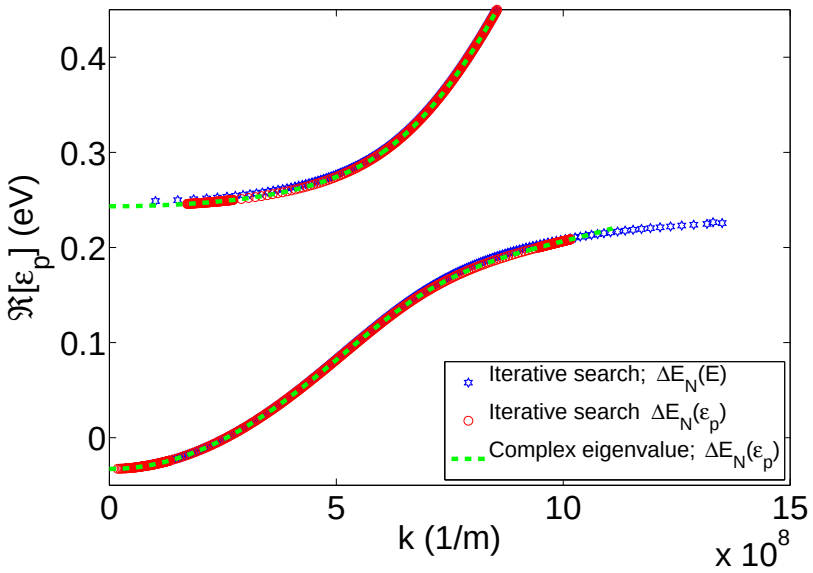

Figure 7.3: Energy versus wavevector for $GaN_x As_{1-x}$with $x = 0.2\%$ predicted by the 2-level SCGF method. The blue stars display the result assuming $\Delta E_N(E + i\delta) = \Delta E_N(E)$, while the red circles show the result with $\Delta E_N(\varepsilon_p)$ using the iterative search method. The green line shows the band dispersion calculated by complex eigenvalue method.

7.3.2 The dispersion relation

The dashed green line in Fig. 7.3 shows the band dispersion for GaN_xAs_{1-x} with $x = 0.2\%$ calculated by Eqs. (7.6) and (7.7). Here $E_{max} = 857$ meV and and E_k is varied from 0 to 0.7 eV. The blue stars show the result of estimating $\Delta E_N(\varepsilon_p)$ by $\Delta E_N(E)$ (given by blue solid lines in Fig. 7.1). The dispersion relation calculated at the real axis of energy is similar to the one calculated by the BAC model.

The band dispersion calculated using the iterative search method is very similar to the result of the complex eigenvalue approach. But due to the problem with the stability of iterative search method of determining $\Delta E_N(\varepsilon_p)$, the upper band in this method does not start from zero, whereas the complex eigenvalue method does not have this problem.

7.3.3 Fractional Γ character

As we have shown in Appendix A, the fractional Γ character of band states is given by

$$f_\Gamma = |\alpha_M|^2 = \left(1 + \frac{1}{N_c}\sum_j \frac{|V_j|^2}{|\varepsilon_p - E_j - \Delta E_j(\varepsilon_p)|^2}\right)^{-1}. \tag{7.12}$$

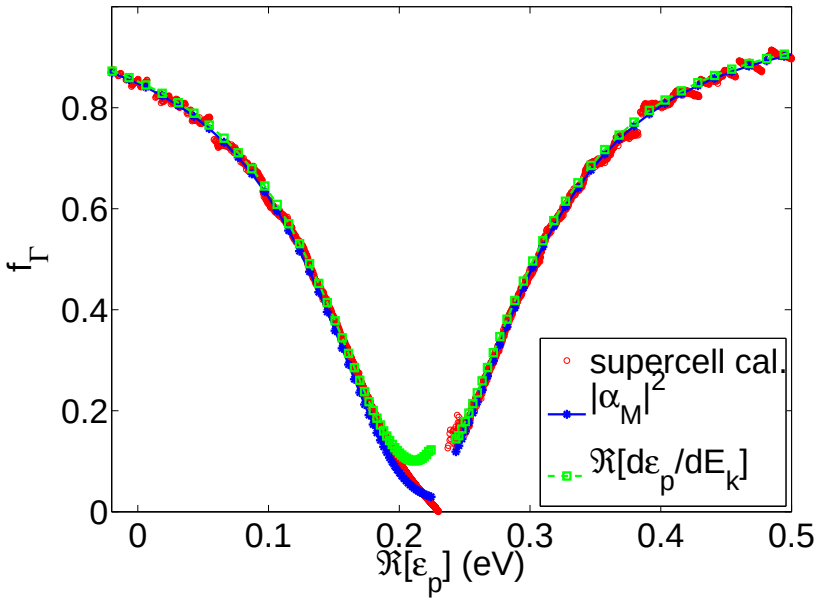

Figure 7.4: The fractional Γ character for $GaN_{0.002}As_{0.998}$ predicted by the 2-level SCGF method by Eq. (7.14) (blue stars), and by Eq. (7.13) green squares, compared with the supercell calculations for a box with length $L = 100a_0$ containing 8000 N (red circles). $E_{max} = 0.857$ eV in both calculations and E_k is varied from 0 to 0.75 eV.

By analogy with the corresponding result for exact eigenstate, we might expect to obtain f_Γ from $\Re[\mathrm{d}\varepsilon_p/\mathrm{d}E_k]$, that as shown in Appendix C to be given by

$$\Re\left[\frac{\mathrm{d}\varepsilon_p}{\mathrm{d}E_k}\right] = \Re\left[\left\{1 - \frac{1}{N_c}\sum_j \frac{|V_j|^2}{[\varepsilon_p - E_j - \Delta E_j(\varepsilon_p)]^2} \times\left(1 - \frac{\mathrm{d}\Delta E_j(\varepsilon_p)}{d\varepsilon_p}\right)\right\}^{-1}\right]. \tag{7.13}$$

In the next section we will see that the results of Eq. (7.12) and (7.13) are very similar for energies far from N state energies. However, although $\Re[\mathrm{d}\varepsilon_p/\mathrm{d}E_k]$ is a good approximation for f_Γ, the two quantities are not strictly identical for states with complex energies.

In the two-band model Eq. (7.12) becomes

$$f_\Gamma = \left[1 + \frac{V_{Nc}^2}{\left|\varepsilon_p - E_N - \Delta E_N(\varepsilon_p)\right|^2}\right]^{-1}. \tag{7.14}$$

Figure 7.4 compares the fractional Γ character calculated by the two-level SCGF and the supercell calculations presented in Chapter 4, for $GaN_{0.002}As_{0.998}$. Here

blue dots and green diamonds show the result calculated by Eqs. (7.14) and (7.13), respectively, while the poles of Green's function are calculated by complex eigenvalue approach.

We observe that the self-consistent result calculated by Eq. (7.14) agrees very well with the numerical results obtained for a supercell with size $L = 100a_0$ including 8000 N atoms. It is seen that the result of $\Re[d\varepsilon_p/dE_k]$ is in very good agreement with f_Γ calculated by SCGF and supercell models, for energies far from E_N. But just before N energy $\Re[d\varepsilon_p/dE_k]$ deviates from f_Γ calculated by Eq. (7.14). Therefore, we again emphasize that, in contrast to the calculation at the real axis, $\Re[d\varepsilon_p/dE_k]$ (at the poles) does not always give the correct fractional Γ character. However, we will use $\Re[d\varepsilon_p/dE_k]$ in calculating group velocity, as discussed in the following section.

7.3.4 Group velocity

The group velocity is proportional to the derivative of energy with respect to wave vector and can be written as

$$v_g = \frac{1}{\hbar}\Re\left[\frac{\mathrm{d}\varepsilon_p}{\mathrm{d}k}\right] = \frac{1}{\hbar}\Re\left[\frac{\mathrm{d}\varepsilon_p}{\mathrm{d}E_k}\right]\frac{\mathrm{d}E_k}{\mathrm{d}k} = \left(\frac{2E_k}{m^*}\right)^{1/2}\Re\left[\frac{\mathrm{d}\varepsilon_p}{\mathrm{d}E_k}\right], \tag{7.15}$$

where $\Re[\mathrm{d}\varepsilon_p/\mathrm{d}E_k]$ is given by Eq. (7.13). In the BAC model the energies of the BAC upper and lower conduction subbands, denoted by E_+ and E_-, are given by

$$E_\pm = \frac{1}{2}\left\{E_N + \gamma_{bac}(E) \pm \sqrt{(E_N - \gamma_{bac}(E))^2 + 4V_{Nc}^2}\right\}, \tag{7.16}$$

where $\gamma_{bac}(E) = E_k = \hbar^2k^2/2m^*$. Using the chain rule with the general definition of group velocity, Eq. (7.15) can be written as

$$v_g(E) = \frac{1}{\hbar}\frac{\mathrm{d}E}{\mathrm{d}\gamma_{bac}}\frac{\mathrm{d}\gamma_{bac}}{\mathrm{d}k}, \tag{7.17}$$

where $\mathrm{d}\gamma_{bac}/\mathrm{d}k = \hbar(2\gamma_{bac}/m^*)^{1/2}$. Therefore

$$v_g(E) = \left(\frac{2}{m^*}\right)^{1/2}\frac{\gamma_{bac}^{1/2}(E)}{\mathrm{d}\gamma_{bac}(E)/\mathrm{d}E}, \tag{7.18}$$

where in the BAC model

$$\gamma_{bac}(E) = E - \frac{V_{Nc}^2}{E - E_N}. \tag{7.19}$$

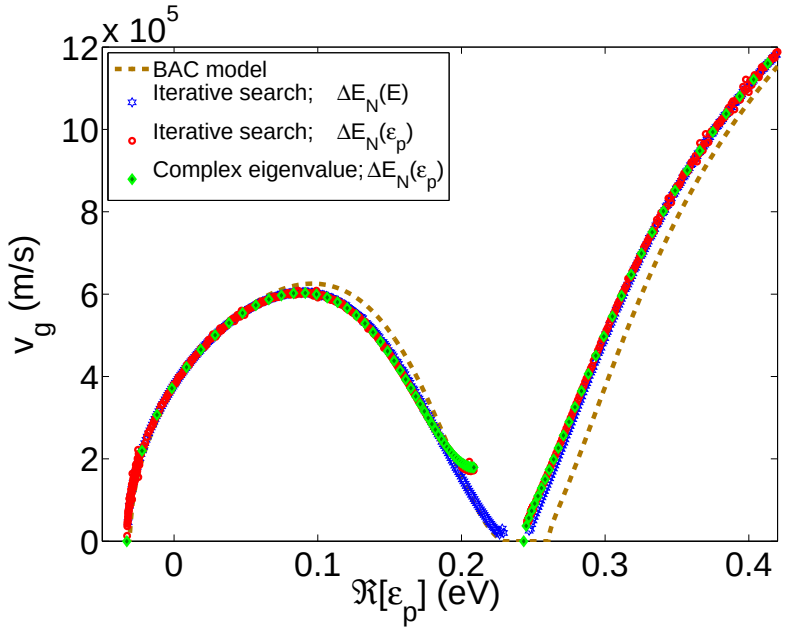

Figure 7.5: The group velocity of $GaN_{0.002}As_{0.998}$, calculated by the ordinary BAC model (brown dashed line) in comparison with results of the 2-level SCGF method with $\Delta E_N(E)$ (blue stars) and $\Delta E_N(\varepsilon_p)$ using iterative search (red circles) and complex eigenvalue (green diamonds) methods. E_k is varied from 0 to 0.6 eV and E_{max} is taken to be 0.857 eV.

Actually Eq. (7.18) could be given by substituting E_k and $(\mathrm{d}\varepsilon_p/\mathrm{d}E_k)$ in Eq. (7.15) by γ_{bac} and $(\mathrm{d}\gamma_{bac}(E)/\mathrm{d}E)$, respectively. Fig. 7.5 compares the group velocity calculated in the BAC and the two-band SCGF methods. The brown dashed line in this figure shows the v_g calculated by Eq. (7.18) (BAC model), while the blue stars represent the group velocity calculated by SCGF method (by Eq. (7.15)) using $\Delta E_N(E)$ at the real axis (the blue stars in Fig. 7.2). It is seen that the two-level SCGF at the real axis of energy gives a narrower gap, compared to the BAC model. However, as we have already seen, the SCGF method at the poles ε_p of Green's function calculated by either complex eigenvalue (green diamonds) or iterative search (red circles) methods gives a wider gap than the SCGF method at the real axis of energy. In this case, we see that the lower band disappears before the group velocity vanishes. This is physically acceptable, bearing in mind that in this region large imaginary energy (Fig. 7.2) implies very strong scattering.

The excellent agreement between the two-level SCGF approach and the supercell calculations confirms the validity of using the SCGF to study the band structure of dilute nitride alloys. However, the complete model should include the full distribution of localised states, as we will consider in the next section.

7.4 The LCINS model

In the previous section we assumed all localised states were located at the same energy E_N. This provided insight into the effect of N states on the CB and we could compare the model with the supercell calculation results. However, a more accurate model is required to consider the full distribution of nitrogen-induced localised states, which arise when we consider the direct interaction between localised states.

7.4.1 The complex eigenvalue method

If we represent the full distribution of localised states as a sum of N Lorentzians, each centred at (real) energy E_j with weight x_j and width ζ_j, so that for real E,

$$D_{loc} = \frac{1}{\pi}\sum_{j=1}^{N}\frac{x_j\zeta_j}{(E-E_j)^2+\zeta_j^2}, \tag{7.20}$$

and assuming that the states of type j have an interaction parameter β_j with the conduction band, then using the integrated conduction band Green's function for each momentum k

$$G_{cb}(k) = \frac{(2m^*)^{3/2}a_0^3}{16\pi^2\hbar^3}\left\{\sqrt{E_k}\ln\left[\frac{\sqrt{E_k}+\sqrt{E_{max}}}{\sqrt{E_k}-\sqrt{E_{max}}}\right] - 2E_{max}^{1/2}\right\}, \tag{7.21}$$

we obtain $N+1$ band energies at the complex roots of the $N+1$ order polynomial equation obtained from

$$\varepsilon_p - \sum_{j=1}^{N}\frac{x_j\beta_j^2}{\varepsilon_p - E_j - \beta_j^2 G_{cb}(k) + i\zeta_j} = E_k. \tag{7.22}$$

In order to solve the roots of these equations we map the problem onto the corresponding (complex) eigenvalue problem

$$\mathbf{Hn} = \varepsilon_{p,n}\mathbf{n}, \tag{7.23}$$

where $\mathbf{n}$ is the eigenvector of $\mathbf{H}$ corresponding to the eigenvalue, $\varepsilon_{p,n}$, $H_{00} = E_k$, $H_{jj} = E_j + \beta_j^2 G_{cb}(k) - i\zeta_j$ and $H_{0j} = H_{j0} = \sqrt{x_j}\beta_j$, and $H_{ij} = 0$ for $i \neq j$. By varying E_k from zero to its maximum value we are able to calculate the poles $\varepsilon_{p,n}(E_k)$ for each sub-band n.

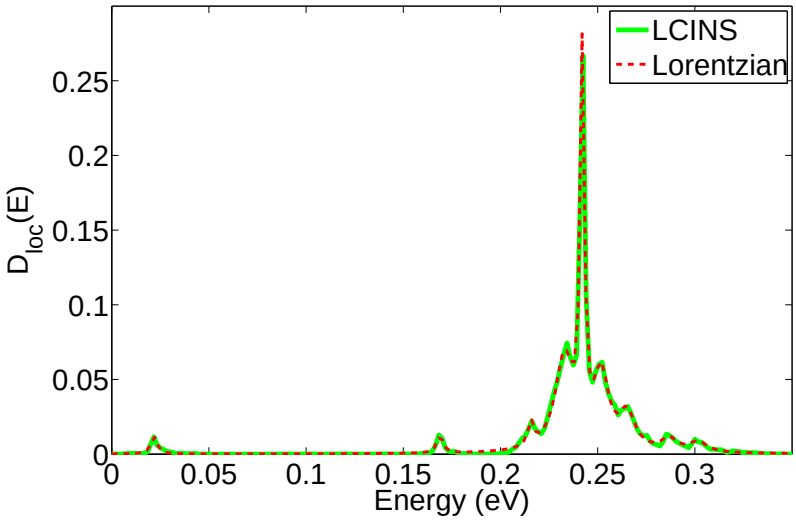

Figure 7.6: Calculated density of localised LCINS states for $GaN_{0.0036}As_{0.9964}$ versus their energies with respect to the CBE of GaAs, while each energy level is broadened to a Gaussian of width 1 meV (solid green line). The dashed red line shows the summation of 9 Lorentzians fitted to this distribution. The Lorentzian parameters are given in Table 7.1.

7.4.2 The band dispersion calculated using the complex eigenvalue method

The solid green line in Fig. 7.6 represents the distribution of localised LCINS states calculated for GaN_xAs_{1-x} with $x = 0.36\%$ [11]. Our analysis shows that the summation over 9 Lorentzians, given by the dashed red line in Fig. 7.6 is sufficient to provide a distribution very close to the LCINS distribution. The energy peak E_j, weight x_j, width ζ_j and interaction parameter β_j for each Lorentzian is given in Table 7.1. β_j's are calculated by averaging $V_j/\sqrt{N_c}$ for each given Lorentzian. Having these Lorentzian parameters we can build the Hamiltonian of Eq. (7.23) and calculate the eigenvalues of this equation, which are the poles of Green's function.

In Appendix B the details of finding the poles for the LCINS approach is

Table 7.1: Lorentzian fitting parameters (Eq. (7.20)) of the LCINS distribution for $GaN_{0.0036}As_{0.9964}$.

j	1	2	3	4	5	6	7	8	9
E_j (meV)	21.9	168.9	215.6	232.8	242.1	251.8	265.1	286.8	301.7
$x_j(\times 10^{-4})$	0.7	0.7	0.9	11.0	10.2	7.1	3.7	1.3	1.3
$\zeta_j(meV)$	2.00	1.84	1.77	5.64	1.26	4.55	4.96	4.70	5.39
$\beta_j(eV)$	2.66	2.43	1.94	1.17	1.75	2.26	3.01	2.49	1.83

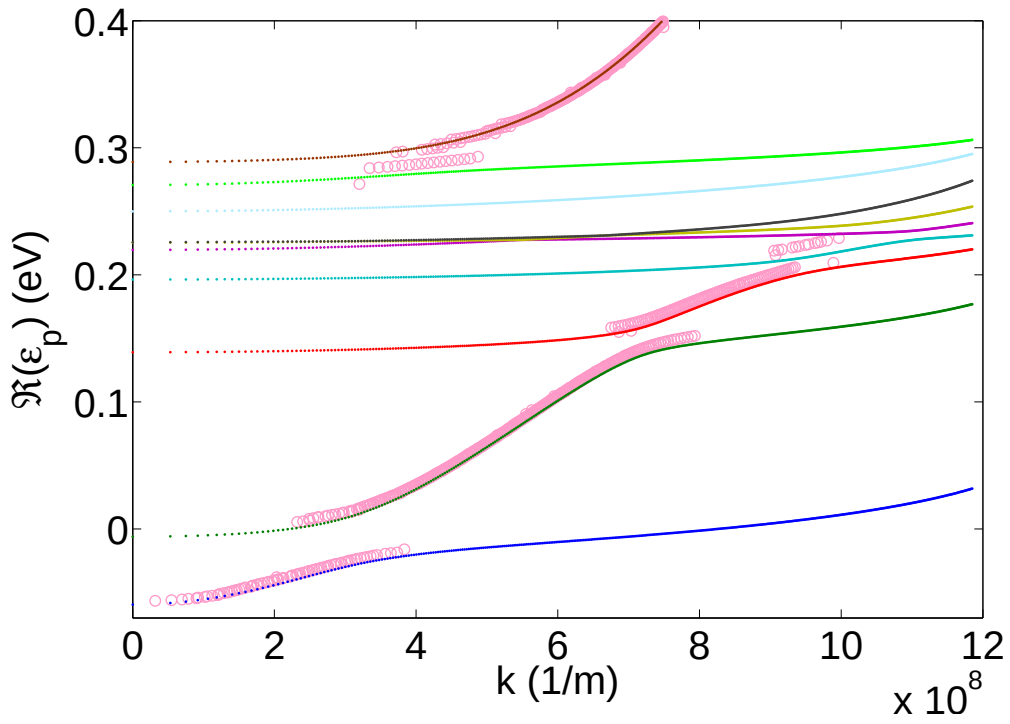

Figure 7.7: The dispersion relation of $GaN_{0.0036}As_{0.9964}$ calculated by the SCGF approach using the full distribution of nitrogen localised states from the LCINS method. The pink circles show the band dispersion when the poles ε_p are calculated using the iterative search method while the dotted lines display the results when the poles of Green's function, ε_p, are calculated by Eq. (7.23).

presented for the iterative search method. Fig. 7.7 compares the band dispersion of $GaN_{0.0036}As_{0.9964}$ using the SCGF method and using the iterative search and complex eigenvalue approaches. The dotted lines in this plot show the disper-

Table 7.2: Lorentzian fitting parameters (Eq. (7.20)) of the LCINS distribution for $GaN_{0.001}As_{0.999}$.

j	1	2	3	4	5	6	7	8	9	10	11	12	13
E_j (meV)	22	169	217	229	235	243	252	259	263	267	286	300	305
$x_j(\times 10^{-4})$	0.06	0.07	0.10	0.30	1.01	7.10	0.81	0.18	0.10	0.15	0.10	0.05	0.04
$\zeta_j(meV)$	1	1	1	2	2	1	2	1.5	1	1	1	0.4	3
$\beta_j(eV)$	2.7	2.6	2.5	0.6	0.9	1.9	2.5	2.7	2.9	2.9	0.6	0.2	1.8

Table 7.3: Lorentzian fitting parameters (Eq. (7.20)) of the LCINS distribution for $GaN_{0.012}As_{0.988}$.

j	1	2	3	4	5	6	7	8	9	10	11	12	13	14	15
E_j (meV)	-74	-50	-41	22	27	41	168	210	229	241	253	270	291	308	335
$x_j(\times 10^{-4})$	0.1	0.1	0.3	2.3	2.3	1.5	4.6	7.6	18.2	21.3	12.1	19.7	10.6	9.1	1.8
$\zeta_j(meV)$	3	3	3	5	5	5	5	5	7	6	7	10	10	10	5
$\beta_j(eV)$	3.6	3.0	2.9	2.4	2.4	2.8	2.0	1.3	1.1	1.3	1.5	2.3	2.8	2.9	2.7

sion relation calculated by Eq. (7.23). As we have considered 9 Lorentzians to fit with LCINS distribution, this band dispersion consists of 10 subbands. As we mentioned earlier, in the complex eigenvalue method for large momentum k, the bands are bent towards higher energies because at high k values, E_k becomes close to assumed E_{max} (= 1 eV). Very good agreement is observed between the results calculated by iterative search method (pink circles) and the band dispersion calculated using the complex eigenvalue method of Eq. (7.23). The only difference is that in the complex eigenvalue approach each sub-band starts from $k = 0$ and continues to the maximum k considered. However, finding the summation of Lorentzians to fit with LCINS distribution is tricky as small differences in the distributions lead discrepancies in the band structure.

7.4.3 Fractional Γ character

The fractional Γ character can be calculated using Eq. (7.12). Pink stars in Fig. 7.8 display the fractional Γ character, calculated by SCGF including the full LCINS distribution using the iterative search method for GaN_xAs_{1-x} with $x = 0.1\%$, $x = 0.36\%$ and $x = 1.2\%$. The parameters for sum of the Lorentzian fitted to LCINS distribution, including the energy peak E_j, weight x_j, width ζ_j and interaction β_j are given in Tables 7.1, 7.2, and 7.3 for $x = 0.36\%$, $x = 0.01\%$ and $x = 1.2\%$, respectively.

In the complex eigenvalue method of finding the poles, the fractional Γ character, for each sub-band, can also be obtained by the square of the first component of the eigenvector of Eq. (7.23). The contribution of each (Lorentzian broadened) localised state j can also be obtained by calculating j-th component of the eigenvector of Eq. (7.23). Circles in Fig. 7.8 show f_Γ calculated using the eigenvectors of Eq. (7.23) for GaN_xAs_{1-x} with $x = 0.1\%$, $x = 0.36\%$ and $x = 1.2\%$. For $x = 0.1\%$ and 1.2% we have considered sum of 13 and 15 Lorentzians, respectively, to fit to the LCINS distribution shown in Fig. (2.2).

It is seen in this figure, that the inclusion of the full LCINS distributions leads to sharp reductions in f_Γ at energies corresponding to pair N (close to the CBE), and higher clusters (just below the isolated N states). The states with low f_Γ, located about localised N states, have more localised character, while the state at the bottom of the CB, in the middle of lower band, (after N pairs), and above 0.3 eV have higher f_Γ, implying that they are more extended in nature. Fig. 7.8 shows that the states close to the mini-gaps have a very small Γ contribution.

As shown in Fig. 7.9, for low nitrogen composition ($x = 0.1\%$) only one Lorentzian-broadened component of the LCINS distribution (that corresponding

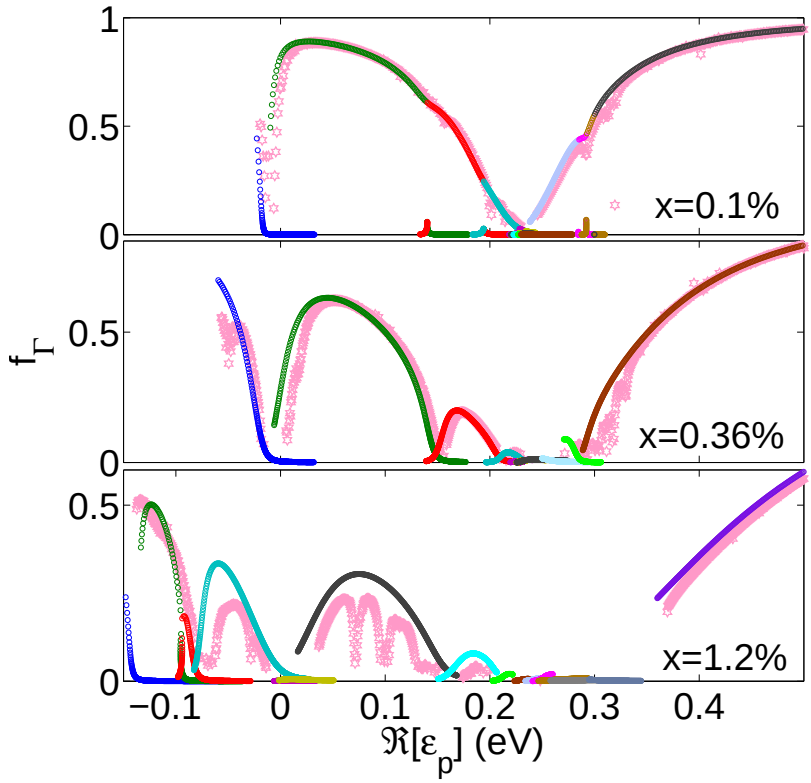

Figure 7.8: The fractional Γ character for GaN_xAs_{1-x} for different values of N concentration x, calculated by the SCGF approach and the full distribution of LCINS method. The pink stars show f_Γ calculated using the iterative search method in comparison with those calculated by the complex eigenvalue method, shown by the dotted lines.

to isolated N states) has sufficiently large concentration x_j to disrupt the topology of the parabolic band and open a gap between upper and lower bands, as discussed in § 7.3.1.1. For the other types of localised state (N-N pairs, etc.), the parabolic band connects continuously from energies below to energies above the localised state as the momentum k increases.

Figure 7.9 shows the energy variation with respect to the wavevector in GaN_xAs_{1-x} with x = 0.1, 0.5, 1.2 and 2.0%, calculated by the SCGF method in the framework of the LCINS approach to include the full N distribution and using the complex eigenvalue approach. In this plot the energy spectrum for each k state is given by a sum of Lorentzians centred at $\Re(\varepsilon_{p,n})$ with broadening $\Im(\varepsilon_{p,n})$ and weighted by $|\alpha_{M,n}|^2$ for each sub-band n. It is seen that the overall band dispersion is similar to BAC model dispersion, but the inhomogeneous broadening of localised states leads to an increased energy broadening at each k point. The dispersion at each k point is broadened over a range of energy values, with the broadening increasing around the nitrogen resonant state energies. The

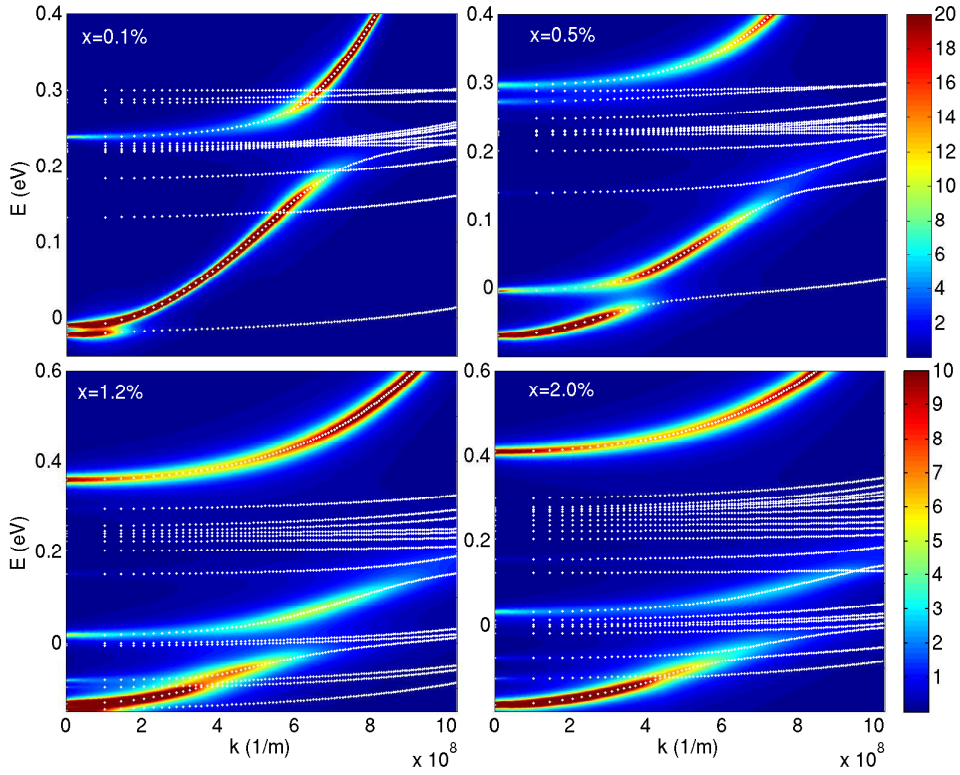

Figure 7.9: The band dispersion of GaN_xAs_{1-x} with $x = 0.1$, 0.5, 1.2 and 2.0%, calculated by the SCGF method and including the full distribution of localised states, while each k state its broadened by a Lorentzian with broadening equal to its decay rate and weighted by f_Γ. The white dots show the (N+1)-band dispersion calculated by Eq. (7.23).

Γ character of the states decreases toward zero around the gaps. Also Fig. 7.9 indicates the existence of a distribution of localised N-related states within these energy gaps. This plot also indicates that in the region that the iterative search method (Fig. B.2) fails to find the poles, the bands have a very small weight in the host conduction band but are primarily localised in character.

7.4.4 Group velocity

Figure 7.10 shows the group velocity for $GaN_{0.0036}As_{0.9964}$ calculated by Eq. (7.13), and using the full distribution of localised states from the LCINS model. The circles with different colors in Fig. 7.10 indicate the group velocity calculated using $(1/\hbar)\Re(\mathrm{d}\varepsilon_{p,n}/\mathrm{d}k)$ for n-th sub-band.

Overall group velocity is similar to BAC model's result, but with corresponding dips at energies near the N pair energy and larger clusters of N states. Moving

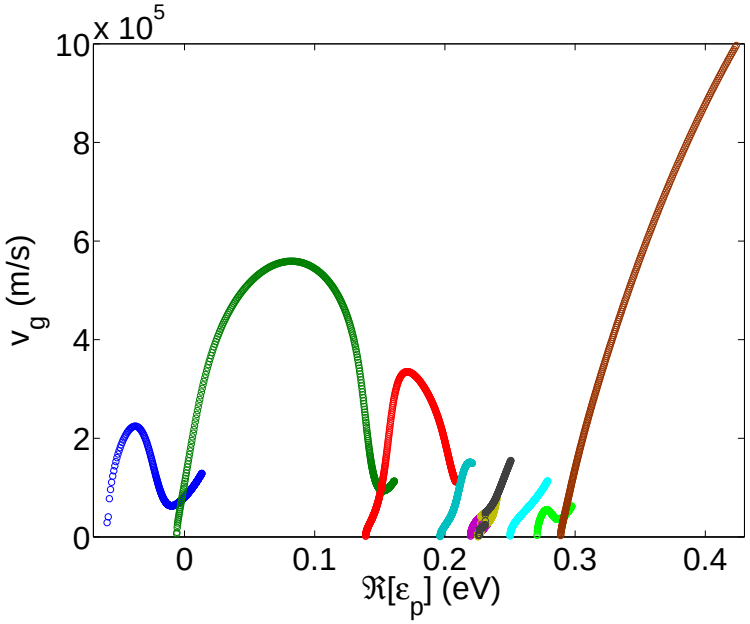

Figure 7.10: The group velocity of GaN_xAs_{1-x} with $x = 0.36\%$ calculated by the full LCINS distribution and the SCGF method. Each colors displays the group velocity for each sub-band calculated by the complex eigenvalue method. E_k is varied from 0 to 0.6 eV and E_{max} is taken to be 1 eV.

from bottom of the band to 0 eV, the group velocity increases from zero to around 2×10^5 (m/s), and then decreases rapidly where the band disappears due to a very high scattering rate at energies close to that of the N pair states. It again rises and reaches to around 5.5×10^5 (m/s) at energy 85 meV, 3.3×10^5 (m/s) at energy 170 meV. Also there is a large gap corresponding to the energy of isolated N states. Above this gap the group velocity again starts to increase.

7.5 Scattering rate

The decay rate is proportional to the imaginary part of the poles of the Green's function and given by [84]

$$R(E) = -\frac{2}{\hbar}\Im[\varepsilon_p]. \tag{7.24}$$

In Appendix D it has been shown that this decay rate can be written as

$$R(\varepsilon_p) = \frac{2\pi}{\hbar}\sum_j \frac{1}{N_c}\frac{|V_j|^4}{|\varepsilon_p - E_j - \Delta E_j(\varepsilon_p)|^2}\frac{f_\Gamma D_0(E_k)}{N_c}, \tag{7.25}$$

where $D_0(E_k)$ is the GaAs density of states and in the complex eigenvalue method is given by $-N_c/\pi\Im[G_{cb}]$. Therefore in this model the scattering rate for each

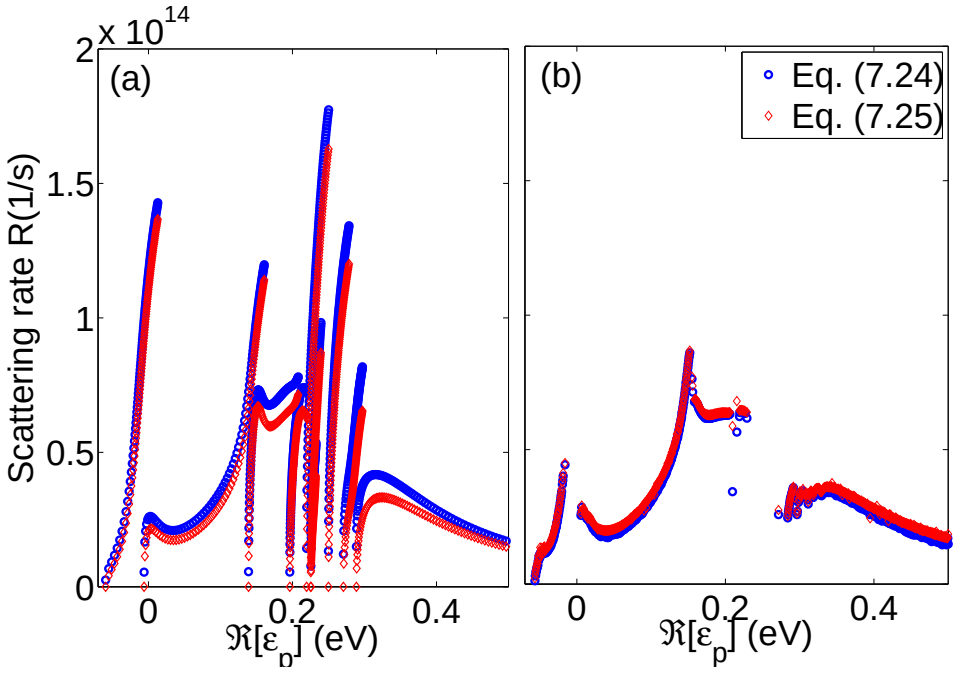

Figure 7.11: The comparison of the decay rates calculated by Eq. (7.24) (blue circles) and Eq. (7.25) (red diamonds), for $GaN_{0.0036}As_{0.9964}$ using the SCGF approach with the full LCINS distributions. (a) and (b) show the results calculated using the complex eigenvalue and iterative search methods, respectively.

sub-band n is given as

$$R_n(\varepsilon_{p,n}) = -\frac{2}{\hbar}\sum_j \frac{x_j \beta_j^4 f_\Gamma(\varepsilon_{p,n}) \Im(G_{cb})}{|\varepsilon_{p,n} - E_j - \beta_j^2 G_{cb} + i\zeta_j|^2}, \tag{7.26}$$

where $\varepsilon_{p,n}$ is the pole of the GF for the n-th sub-band. E_j, x_j, ζ_j and β_j here are respectively the peak energy, weight, width and interaction parameter of Lorentzian j. These parameters are given in Tables 7.2, 7.1 and 7.3 for $x = 0.1$, 0.36 and 1.2%.

Equation (7.25) is very similar to the expression that Fahy *et al.* already derived in Ref. [13]. However, in that earlier work a constant f_Γ, calculated at the bottom of the CB, has been considered. They also did not take into account the nonparabolicity of the CB in the DOS. Here we apply the energy dependence of the localised states broadening $\Delta E_j(\varepsilon)$ calculated by the SCGF approach, instead of constant broadening calculated by second order perturbation theory.

Figure 7.11 compares the decay rates calculated using Eqs. (7.24) and (7.25) with the full LCINS distribution of localised states in $GaN_{0.0036}As_{0.9964}$, obtained by the complex eigenvalue (a) and the iterative search (b) methods. As we expected, the scattering rates calculated by Eq. (7.24) and Eq. (7.25) lead to com-

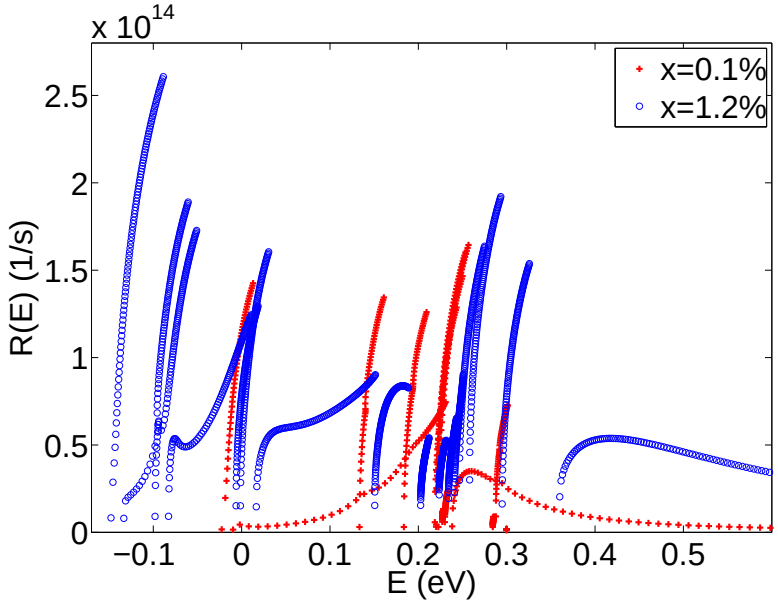

Figure 7.12: The decay rates calculated by Eq. (7.24) for GaN_xAs_{1-x} with $x = 0.1$ and 1.2%, using the SCGF approach with the full LCINS distributions, while the poles the Green's function are calculated using the iterative search method.

pletely similar results, which are almost indistinguishable.

The comparison between the scattering rates obtained by the complex eigenvalue and the iterative search methods indicates that their results are very similar for energies far from localised states. However, as the iterative search method is unable to find the poles of Green's function around N state energies, this method omits the states with very high scattering rates around sub-band edges. Fig. 7.12 shows the scattering rate for $x = 0.1$ and 1.2% in GaN_xAs_{1-x} calculated using Eq. (7.26).

It is seen that the peaks of the decay rate increase with x. These results also demonstrate that the N pair states are much more important than previously thought. In comparison with the corresponding results in Ref. [13] (reproduced in Fig. 2.4), here we see much stronger concentration dependence of the decay rates. The scattering rates associated to N-N states are very similar to what obtained in Ref. [13], but the peaks related to isolated N states show the lower decay rates (up to an order of magnitude), compared with results of Ref. [13], especially at lower concentrations. As mentioned earlier different factors are causing these differences. The most important one is considering an energy independent f_Γ in that work. They estimated f_Γ at CBE and use that for all energies, as they were interested in the scattering at the bottom of the conduction band. For instance, for N composition $x = 0.36\%$ they used $f_\Gamma = 0.805$, that is a good approximation for energies close to the CBE. This is the reason of observing the similar scattering

rates in both calculations for energies close to the CBE, e.g. around the N pair states. But as we saw in Fig. 7.8 the Γ character of the states tend to zero around N states. That is why the peaks of the decay rate corresponding to N states with higher energies are much smaller in the current work in comparison with Ref. [13].

7.6 Carrier mobility

As we have seen in Chapter 6, for carriers in a applied electric field, F, the Boltzmann transport equation, in the relaxation time approximation, gives the current density [76]

$$j = -\frac{e^2 F}{3} \int \tau(E) v_g^2(E) \frac{\mathrm{d}f_0}{\mathrm{d}E} D_T(E) \mathrm{d}E. \tag{7.27}$$

Here f_0 is the symmetric part of the distribution function, where at low electric field is given by Fermi-Dirac distribution, $f_0 = \{\exp\left[(E - E_F)/k_B T\right]+1\}^{-1}$. $\tau(E)$ in Eq. (7.27) is the scattering time for the distribution at energy E, which we set equal to the inverse of carrier scattering rate $R(E)$. The carrier mobility is given by $\mu = j/(enF)$, where the density of carriers is given by

$$n = \int_o^\infty f_0(E) D_T(E) \mathrm{d}E, \tag{7.28}$$

where $D_T(E)$ in Eqs. (7.27) and (7.28) represents the total density of states, that is given by the summation of Eq. (5.8) and Eq. (5.9).

Equation (7.27) cannot be evaluated directly, either from density of states alone or from the bands calculated from the poles of the Green's function. On the one hand, the density of (exact) eigenstates at the real energy axis gives us no information about group velocities or scattering rates. On the other hand, the bands calculated from the poles of the Green's function cannot be used to give us a correct density of states, which would be related to the number of carriers per unit volume in the semi-classical Boltzmann equation.

To resolve this, we reinterpret the standard Eq. (7.27) , using the dispersion of the poles $\varepsilon_{p,n} = E_{p,n} + i\delta_{p,n}$ of the Green's function with k to obtain the group velocity $v_g = (1/\hbar) dE_{p,n}/dk$ and the scattering rate $1/\tau_{p,n} = R = -2\delta_{p,n}/\hbar$ for a given band at a given energy $E_{p,n}$. The components of the eigenvector of the Hamiltonian, Eq. (7.23), gives the participation, f_Γ or $|\alpha_j|^2$, of a given band n in the host conduction band density of states $D_{cb} = -\Im[G_{cb}(E_{p,n})]/\pi$ or localised state j density of states $D_j = -\Im[G_{jj}(E_{p,n})]/\pi$, respectively. Then the n-th band

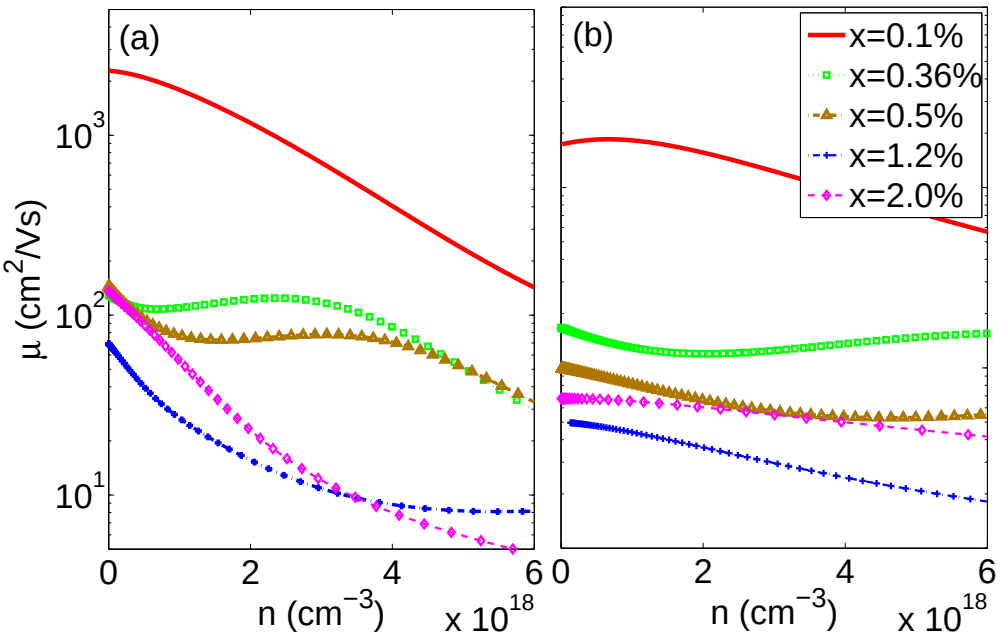

Figure 7.13: The calculated carrier mobility versus n-type carrier concentration for different values of x in GaN_xAs_{1-x}, using the SCGF approach with the full LCINS distributions, at room temperature. figure (a) and (b) show the results calculated using the complex eigenvalue and iterative search methods, respectively.

contributes

$$j_n = \frac{e^2 F}{3} \int \tau_{p,n} v_g^2(\varepsilon_{p,n}) \frac{df_o}{dE_{p,n}} \left\{ f_\Gamma(\varepsilon_{p,n}) D_{cb}(E_{p,n}) + \sum_j |\alpha_j(\varepsilon_{p,n})|^2 D_j(E_{p,n}) \right\} dE_{p,n}, \tag{7.29}$$

to the current. $D_j(E_{p,n})$ is the density of localised state j

$$D_j(E_{p,n}) = \frac{N_c}{\pi} \frac{x_j[\Im(\Delta E_j(E_{p,n})) + \zeta_j]}{|E_{p,n} - E_j - \Im(\Delta E_j(E_{p,n})) + i\zeta_j|^2}. \tag{7.30}$$

In order to calculate carrier mobility, we vary the chemical potential E_F around the CBE of the alloy, E_c, from $E_c - 20$ meV to $E_c + 20$ meV, which gives a maximum n of 6×10^{18} and 1×10^{19} cm^2(Vs)$^{-1}$ for $x = 0.1\%$ and $x = 0.36\%$, respectively. Fig. 7.13 shows the carrier mobility for GaN_xAs_{1-x} versus n-type carrier concentration at room temperature, calculated using complex eigenvalue (a) and iterative search (b) methods. There is good agreement between two methods of finding the poles. The discrepancies are due to the small differences in the band structure predicted by each method. We observe that even for a very small nitrogen composition ($x = 0.1\%$) the mobility of carriers reduces

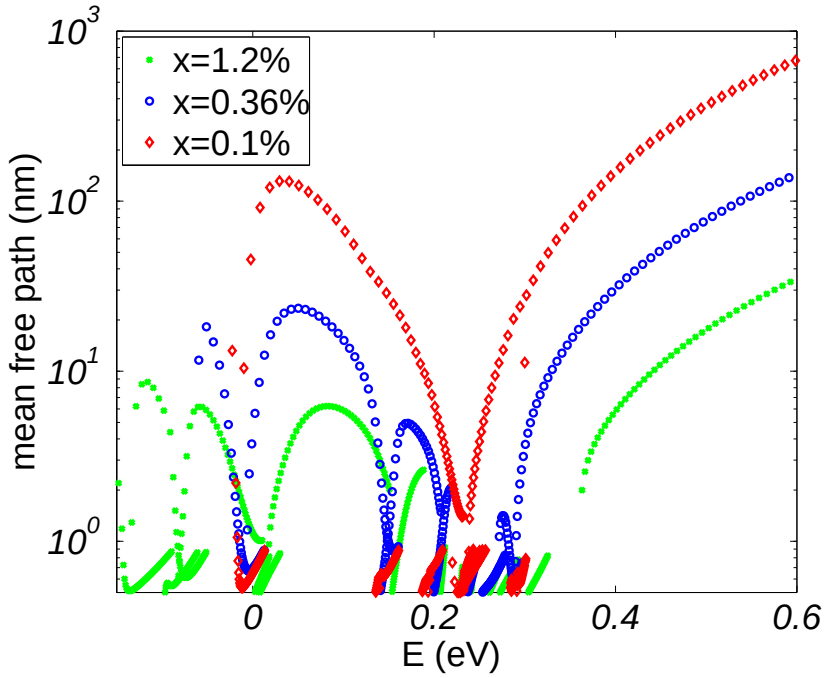

Figure 7.14: The mean free path calculated for in GaN_xAs_{1-x} with $x = 0.1$, 0.36 and 1.2%„ using the SCGF approach with the full LCINS distributions. The energy is referred to the CBE of GaAs.

dramatically from about 8000 $cm^2(Vs)^{-1}$ in GaAs to around 2000 $cm^2(Vs)^{-1}$ in GaN_xAs_{1-x}. Further reduction in mobility is observed by increasing the N concentration x. However $x = 2.0\%$ is an exception that has a higher mobility with respect to the $x = 1.2\%$. These results are lower than those calculated in Ref. [13], giving better overall agreement with experiments [42–44] (see Fig. 2.3).

Another quantity of interest is the mean free path that can be calculated by $l = v_g/R(E)$. The energy-dependence of mean free path is shown in Fig. 7.14 for various N concentrations calculated by the complex eigenvalue method. The iterative search approach predicts very similar results for the mean free path. The mean free paths given in Fig. 7.14 are very similar to the mean free path previously calculated by Fahy *et al.* [13], although there were no gaps in the CB structure in that work. Similar to the group velocity calculated by SCF, Fig. 7.14 shows that carriers have very short mean free path around the localised state energies. This very short mean free path, especially for higher x, is due to the strong scattering by N states and also the lower group velocity.

7.7 Discussion and conclusions

Following the results of Chapter 5,where we implemented a self-consistent Green's function approach to calculate the density of states, in this chapter, we have found the poles of the Green's function corresponding to carrier states of well-defined momentum in dilute nitride alloys. Using the poles of the Green's function the band structure, scattering and carrier mobility has been calculated for GaNAs dilute nitride alloys.

Two approaches have been considered; (i) the 2-band model; which assumes all localised N states have the same energy, and (ii) the LCINS model which gives a distribution of localised state energies, arising from direct interaction between nitrogen states and nearby lattice sites. We compared the 2-band model's results with those calculated by the numerical diagonalisation of large random supercell and by the BAC model.

We calculated the poles ε_p of the Green's function in the complex lower half plane, by (i) calculating $\Delta E_j(E+i\delta)$ self-consistently for all values of its real (E), and imaginary part (δ), and find the poles using the iterative search approach, (ii) using a complex eigenvalue method for calculating the poles ε_p without doing the iterations. These methods give similar results for the band structure of GaNAs alloys. However the iterative search method is unable to find the poles around the band edges. The complex eigenvalue method does not have this problem and is much faster in implementation as it only calculates ΔE_j's the poles ε_p of the Green's function. But this method requires fitting the LCINS distribution with a number of Lorentzians, a process which can be tedious.

Including the full distribution of localised states, the dispersion relation shows series of mini-gaps, corresponding to isolated, pair and larger clusters of N states. Increasing the N concentration makes these mini-gaps more pronounced, and they are wider for larger nitrogen compositions.

Having the poles of the Green's function, ε_p, we calculate the decay rate of states as $-2\Im(\varepsilon_p)/\hbar$, and compare that with those already calculated by Fahy *et al.* [13]. In that work they assumed f_Γ and ΔE_j to be independent of energy, as well as using the DOS of the host semiconductor. In the current work we have the appropriate energy-dependent form of these parameters. We have also included the density of states of the perturbed CB, rather than assuming a parabolic band.

The results for the full LCINS distribution provides a very good understanding of the effect of the N states on the electronic structure of dilute nitride alloys. The calculated mobilities here are lower than the previous calculations, giving better agreement with experiments. The previous calculated electron mobilities

by Fahy *et al.* [13], and Vaughan *et al.* [34] were respectively, about a factor of two, and an order of magnitude higher than the highest measured values (see Fig. 2.3).

Young *et al.* [42] have measured the mobility of GaN_xAs_{1-x} for several N concentrations from 0.01% up to 1.3% for carrier concentrations of $(5-7)\times 10^{18}$ cm^{-3}. For $x = 0.1\%$, ($n = 5\times 10^{18}$ cm^{-3}) we obtained $\mu = 720$ cm^2(Vs)$^{-1}$ and $\mu = 2600$ cm^2(Vs)$^{-1}$ in the iterative search and complex eigenvalue methods, respecively. Fahy *et al.* [13] predicted mobility around 2200 cm^2(Vs)$^{-1}$ for this concentration. These are close to the experimental data reported by Jin [12] (see Fig. 2.3). Also Fowler *et al.* [85] measured $\mu = 720$ cm^2(Vs)$^{-1}$ in a quantum well sample with a density equivalent to a bulk value of $n = 7\times 10^{17}$ cm^{-3}. However these are higher than the mobility reported by Young *et al.* [42] (262 cm^2(Vs)$^{-1}$). This variation in experimental data indicates that there are some material factors in the experiments that we do not consider in our calculations.

For $x = 0.4\%$, Young *et al.* reported $\mu = 187$ cm^2(Vs)$^{-1}$, which is close to our predicted values for mobility for $x = 0.36\%$ ($\mu = 150$ and 110 cm^2(Vs)$^{-1}$ in iterative search and complex eigenvalue methods, respectively). Their measured mobility for $x = 1.3\%$ is 165 cm^2(Vs)$^{-1}$ is close but higher than our calculated value of 20 cm^2(Vs)$^{-1}$ in iterative search method and 60 cm^2(Vs)$^{-1}$ in the complex eigenvalue approach, for $x = 1.2\%$.

Ishikawa *et al.* [43] measured the mobility of GaN_xAs_{1-x} for $x = 0.8, 1.7$ and 2.2% with several carrier concentrations. For $x = 0.8\%$, they measured $\mu = 413, 208$ and 89 cm^2(Vs)$^{-1}$ for $n = (0.1, 1.0$ and $5.1)\times 10^{18}$ cm^{-3} , respectively, in comparison with our theoretical values, $\mu = 93, 75$ and 70 cm^2(Vs)$^{-1}$ (Linear interpolation between values at $x = 0.5$ and 1.2% in the complex eigenvalue method.). Their mobility for $x = 1.7\%$ at $n = 5.3\times 10^{17}$ cm^{-3} is 185 cm^2(Vs)$^{-1}$, in comparison with 80 cm^2(Vs)$^{-1}$ in our calculations.

Reason *et al.* [44] have also measured mobility of Si-doped GaN_xAs_{1-x} for several N compositions from 0.01% up to 2% ($n = (0.3-1)\times 10^{18}$). Their value for $x = 0.1\%$, is around 600 cm^2(Vs)$^{-1}$ that is about one-third of our calculated value. For $x = 0.5$ and 1.2% they measured $\mu = 300$ and 200 cm^2(Vs)$^{-1}$, respectively.

In summary, we have presented the self-consistent Green's function approach to study the band structure and electronic properties of dilute nitride alloys. Although in this chapter we have applied the method only to GaN_xAs_{1-x}, this method can be easily applied for different dilute nitride and bismide semiconductors. This approach provides a useful tool for the examination of the electronic structure of these materials.

7. Band dispersion, scattering rate and carrier mobility using the poles of the Green's function

Chapter 8

Absorption spectrum of dilute nitride alloys

8.1 Introduction

In previous chapters of this thesis we developed models to describe the band structure of dilute nitride alloys. One way to test the accuracy of these is to look at optical absorption spectra for dilute nitride samples, where we expect the absorption spectra to show features related to the N states present in the samples. The absorption spectrum arises from transitions between valence and conduction band states. It provides the knowledge of the energy gap in semiconductors, and also gives significant information about the band structure of materials. Experimental measurements of absorption spectrum as a function of energy can be used to benchmark the band structure calculation. In this chapter we are going to investigate two different materials; $In_yGa_{1-y}N_xAs_{1-x}$ for which the band structure has been widely studied and many of the features are well established, and GaN_xSb_{1-x} for which much less information has been reported in the literature.

We consider two different models for the band structure of dilute nitride alloys, firstly a 5-level BAC model, including the host semiconductor CB and valence bands, isolated N and pair N-N states and secondly, the LCINS model where the band structure of the alloys is calculated using the self consistent Green's function method.

For $In_yGa_{1-y}N_xAs_{1-x}$ alloys we find that the BAC model reproduces the main features in the absorption spectrum. However this model shows some additional features which are related to the N and N-N states energies, reflecting that we have ignored the distribution of localised states in the BAC model. Including

the LCINS distribution of N states in $In_yGa_{1-y}N_xAs_{1-x}$ using the SCGF approach presented in Chapter 5, removes the additional features found in the BAC calculations and gives absorption spectra that are in very good agreement with experimental data.

We then apply our methods to GaN_xSb_{1-x}, where much less information is known theoretically and experimentally. The overall width of the optical spectrum can be well fitted by our models for the absorption spectrum. Both the BAC and LCINS models account for the absorption edge of GaNSb alloys supporting the presence of band anti-crossing interaction in these alloys. The 5-level BAC model gives more features than seen experimentally in the absorption spectrum. Including the distribution of localised states, by modifying those calculated for GaNAs, makes the calculated absorption smoother and gives better agreement with experimental data, but still shows some discrepancies around the localised state peak energies. These results suggest the presence of more disorder in GaNSb samples than what we found in the InGaNAs case. This disorder may be due to sample inhomogeneities or due to an intrinsically broader distribution of N states in GaNSb than in InGaNAs.

8.2 Absorption spectrum

The absorption spectrum $\alpha(E)$ is the fraction of photons with energy $E = \hbar\omega$ absorbed per unit distance

$$\alpha = \frac{\text{Number of photons absorbed per second per unit volume}}{\text{Number of injected photons per second per unit area}}. \tag{8.1}$$

Optical absorption can be described using a "single-electron" approximation. In this approach, the absorption spectrum for direct allowed transitions between valence band v and conduction band c is given by [86–88]

$$\alpha_{cv}(\hbar\omega) = \frac{\pi e^2}{n_r c\epsilon_0 m_0^2 \omega} \sum_{k_v} \sum_{k_c} |\mathbf{P}_{cv}|^2 \delta(E_c - E_v - \hbar\omega)(f_v - f_c), \tag{8.2}$$

where ω is the photon frequency, e and m_0 are the electron charge and mass, respectively, c is the speed of light and n_r is the refractive index. f is the Fermi-Dirac distribution function. Here we assume a filled valence and empty conduction band, so that $(f_v - f_c) = 1$. The matrix element in Eq. (8.2) is

$$\mathbf{P}_{cv} = \int_V \mathrm{d}\mathbf{r} \phi_c^*(\mathbf{k}_c, \mathbf{r})(\hat{e}.\mathbf{p})\phi_v(\mathbf{k}_v, \mathbf{r}), \tag{8.3}$$

where $\hat{e}$ is a vector along the polarisation in the direction of the incoming photon, $\mathbf{p}$ is the carrier momentum operator and V is the volume of the crystal. Writing $\phi_c(\mathbf{k}_c, \mathbf{r}) = \phi_c(\mathbf{r})u(\mathbf{r})$, and using the property that each $\phi_c(\mathbf{r})$ is slowly varying with $\mathbf{r}$, the $\mathbf{P}_{cv}$ can be separated into a Bloch term and an envelope term as [88]

$$|\mathbf{P}_{cv}|^2 = M_b^2 M_{env}^2, \tag{8.4}$$

where

$$M_b = \frac{1}{V}\int \mathrm{d}\mathbf{r} u_c^*(\mathbf{r})(\hat{e}.\mathbf{p})u_v(\mathbf{r}), \tag{8.5}$$

and

$$M_{env} = \int \mathrm{d}\mathbf{r}\phi_c^*(\mathbf{r})\phi_v(\mathbf{r}). \tag{8.6}$$

Using perturbation theory Kane derived for transitions between p- and s-like Bloch functions averaged near all polarisation as

$$M_b^2 = \frac{m_0 E_p}{3}, \tag{8.7}$$

where $E_p = (2m_0/\hbar^2)p^2$ is the interaction energy, and the momentum interband matrix element, p, is given by

$$p^2 = \left(1 - \frac{m_e^*}{m_0}\right)\frac{\hbar^2 E_g(E_g + \Delta_{so})}{2m_e^*(E_g + \frac{2}{3}\Delta_{so})}, \tag{8.8}$$

where m_0, m_e^* are the free electron and conduction band effective masses, respectively, E_g is the band gap (between conduction and valence band), and Δ_{so} is the spin orbit splitting energy. Several values of M_{env} have been reported. Eagles [89], for instance, assumed a localised acceptor wave function ϕ_v of hydrogenic form and a delocalised electronic state ϕ_c of plane wave form, that gives

$$|M_{env}|^2 = \frac{64\pi a^3 V^{-1}}{(1 + a^2 k_c^2)^4}, \tag{8.9}$$

where a is a Bohr radius. For a transition at the band edge $k_c = 0$ and therefore $|M_{env}|^2 = 64\pi a^3/V$. Therefore, Eq. (8.2) can be written as

$$\alpha_{cv}(\hbar\omega) = \frac{\pi e^2 \hbar}{n_r c \epsilon_0 m_0^2}\frac{M_b^2}{\hbar\omega} J_{c,v}(E)\Big|_{E=\hbar\omega}, \tag{8.10}$$

where $E = E_c - E_v$ is the transition energy, E_c and E_v are the conduction and valence band state energies, respectively, for the same wavevector k, $J_{cv}(E)$ is the joint density of states, and we ignore for now the energy dependence of M_b.

The hole electron interaction can be included assuming Elliot's theory, which applies to parabolic and nondegenerate bands. According to Elliot's model, the absorption spectrum is modified because of the hole-electron interaction through a multiplicative function F_{ex} given by [87]

$$F_{ex} = \frac{2\pi\varsigma}{1 - \exp(-2\pi\varsigma)}, \tag{8.11}$$

where

$$\varsigma = \left(\frac{R_y}{\hbar\omega - E_g}\right)^{1/2}, \tag{8.12}$$

and R_y is the exciton Rydberg energy, given by [90, 91]

$$R_y = \frac{e^4}{8h^2\epsilon_0^2}\left(\frac{\mu}{m_0\kappa^2}\right) = 13.61\left(\frac{\mu}{m_0\kappa^2}\right) \text{ eV}, \tag{8.13}$$

where κ is the static dielectric constant, h is the Planck constant, $\mu = 1/(m_c^{-1} + m_v^{-1})$ is the reduced mass, and $m_v = (m_h^{3/2} + m_l^{3/2})^{2/3}$, where m_h and m_l are the heavy hole and light hole effective masses.

Including the hole-electron interaction the total absorption spectrum can be then obtained by

$$\alpha_{tot} = F_{ex}\left(\alpha_{lh} + \alpha_{hh} + \alpha_{so}\right), \tag{8.14}$$

where α_{lh}, α_{hh} and α_{so} are the absorption spectra for transitions from the light hole (LH), heavy hole (HH) and spin orbit split-off (SO) bands to the conduction band, respectively.

In the rest of this chapter we first explain our method for calculating the absorption spectrum for III-V semiconductors and present the results for GaAs in § 8.3. Then in § 8.4 we extend our method to obtain the absorption spectrum for dilute nitride alloys, in the frame of the BAC model and the SCGF approach. We present in § 8.5 and 8.6 our results for (In)GaNAs and GaNSb alloys, and compare them with experimental optical absorption measurements. Finally we summarise our conclusion in § 8.7.

8.3 Optical absorption for III-V semiconductors

In order to calculate the absorption spectrum of GaAs we first need to calculate the joint density of state in GaAs. We do this taking into account the non-parabolicity in the GaAs CB calculated by the Kane model, as well as the light hole nonparabolicity using the 6-band Luttinger-Kohn valence band Hamiltonian.

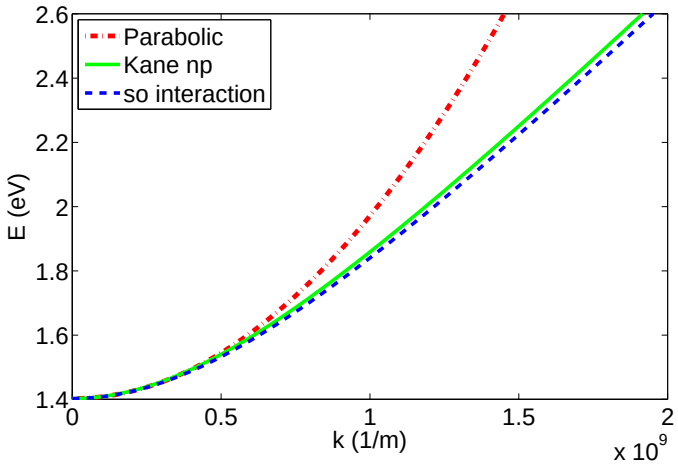

Figure 8.1: The conduction band of GaAs calculated for a parabolic band (dash-dotted red line), including the Kane interband nonparabolicity(solid green line), and the interaction with the valence and split-off bands (the dashed blue line).

8.3.1 CB nonparabolicity using the Kane model

The conventional 2-level BAC model treats the III-V conduction band dispersion as parabolic with

$$E_c(k) = E_{c0} + \frac{\hbar^2 k^2}{2m_c^*}, \tag{8.15}$$

where E_{c0} is the CB edge. However, in practice the conduction band dispersion is non-parabolic, and is better described using a Kane-type model, with the CB dispersion in the simplest Kane model given by the upper eigenvalue of

$$H = \begin{bmatrix} E_{c0} & kp \\ kp & E_{v0} \end{bmatrix}, \tag{8.16}$$

where E_{v0} is the energy of the valence band maximum.

The green solid line in Fig. 8.1 shows the conduction band dispersion of GaAs calculated by Eq. (8.16) in comparison with the parabolic band of Eq. (8.15) (dash-dotted red line). It can be seen that introduces significant nonparabolicity in Fig. 8.1 for values of $k \geq 5 \times 10^8$ m^{-1}.

Equation (8.16) does not include the spin-orbit interaction in the valence band. When this is included Eq. (8.16) should be replaced by [93]

$$H = \begin{bmatrix} E_{c0} & \sqrt{\frac{2}{3}}kp & \sqrt{\frac{1}{3}}kp \\ \sqrt{\frac{2}{3}}kp & E_{v0} & 0 \\ \sqrt{\frac{1}{3}}kp & 0 & E_{v0} - \Delta_{so} \end{bmatrix}, \tag{8.17}$$

where Δ_{so} indicates the spin orbit splitting energy. The upper eigenvalue of Eq. (8.17) gives the CB dispersion $E_c(k)$, shown by the dashed line in Fig. 8.1. It can be seen that the results of using Eqs. (8.16) and (8.17) are in good agreement with each other for the conduction band dispersion of GaAs.

8.3.2 LH band non-parabolicity

The light-hole (LH) band dispersion varies in the parabolic band model as

$$E_{LH} = E_{v0} - \frac{\hbar^2 k^2}{2m_0 m_L}, \tag{8.18}$$

where m_0 is the free electron mass and m_L is the relative light-hole mass. This model ignores that the light-hole band is nonparabolic, due both to the interaction with the conduction band and an anti-crossing interaction with the split-off band. The later of these is more important for GaAs. Using the 6-band Luttinger Kohn (LK) valence band Hamiltonian [94], the band dispersion of the light-hole band can be calculated by evaluating the upper eigenvalue of the 2×2 Hamiltonian, given by

$$H = \begin{bmatrix} E_{LH} & \sqrt{3}\gamma_2 \dfrac{\hbar^2 k^2}{2m_0} \\ \sqrt{3}\gamma_2 \dfrac{\hbar^2 k^2}{2m_0} & E_{so} \end{bmatrix}, \tag{8.19}$$

Table 8.1: Electrical and optical parameters in GaAs.

Parameter	*Symbol*	GaAs
Lattice constant [92]	a_0	$5.653 + 3.88 \times 10^{-5}(T_e - 300)$ (Å)
Electron effective mass(T_e) [91]		10/ 300 K
conduction	m_c^*	$0.063/ \quad 0.067(m_0)$
light hole	m_l	$0.076/ \quad 0.082(m_0)$
heavy hole	m_h	$0.5/ \quad 0.1(m_0)$
split-off	m_{so}	$0.145/ \quad 0.154(m_0)$
Energy gap ($T = 0$)	E_{g0}	1.519 eV
Varshni parameters [92] $\left(E_g = E_{g0} - \dfrac{\alpha_T T_e^2}{(\beta_T + T_e)}\right)$	α_T	5.408×10^{-4} (eV/K)
	β_T	204
SO splitting energy [92]	Δ_{so}	0.34 eV
Refractive index [91]	n_r	$3.255(1 + 4.5 \times 10^{-5} T_e)$
Static dielectric constant [77]	κ	$12.4(1 + 1.2 \times 10^{-4} T_e)$

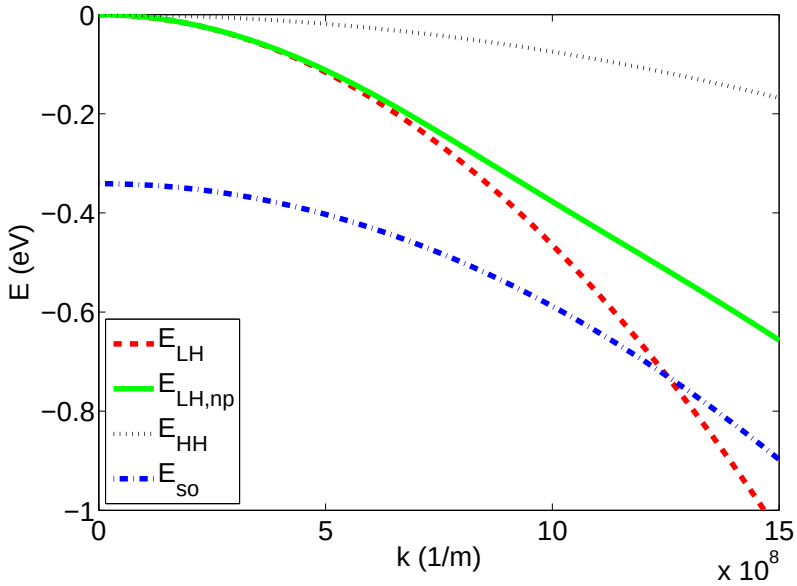

Figure 8.2: The valence bands of GaAs. The nonparabolic light hole band is shown by solid green line, in comparison with parabolic band (given by dashed red line). The dotted black and dash-dotted blue lines show the heavy hole and split-off dispersion bands, respectively, assuming parabolic band dispersion.

where E_{so} is the split-off band dispersion, given as

$$E_{so} = E_{v0} - \Delta_{so} - \frac{\hbar^2 k^2}{2m_0}\gamma_1. \tag{8.20}$$

In the LK 6-band Hamiltonian, the light hole inverse mass $(m_L)^{-1} = (\gamma_1 + 2\gamma_2)$ and the heavy-hole inverse mass $(m_H)^{-1} = (\gamma_1 - 2\gamma_2)$ so that you can evaluate γ_1 as

$$\gamma_1 = \frac{1}{2}\left(\frac{1}{m_L} + \frac{1}{m_H}\right), \tag{8.21}$$

and γ_2 as

$$\gamma_2 = \frac{1}{4}\left(\frac{1}{m_L} - \frac{1}{m_H}\right). \tag{8.22}$$

We evaluate the upper eigenvalue of the determinant in Eq. (8.19) as

$$E_{LH,np} = \frac{E_{LH} + E_{so}}{2} + \sqrt{\left(\frac{E_{LH} - E_{so}}{2}\right)^2 + 3\left(\gamma_2 \frac{\hbar^2 k^2}{2m_0}\right)^2}. \tag{8.23}$$

The solid green line in Fig. 8.2 shows the nonparabolic light hole band dispersion given by Eq. (8.23) for GaAs. The dashed red line shows the parabolic LH band, and the dash-dotted blue line displays the split-off band dispersion. The heavy hole and split-off band are assumed to be parabolic as shown in this figure. It

can be seen that the interaction with the split-off band introduces an observable nonparabolicity in the GaAs LH band dispersion for $k \geq 5 \times 10^8$ m^{-1}, which we take into account in the absorption calculations presented below.

8.3.3 The joint density of states

In order to calculate the absorption spectrum we first need to calculate the joint density of states, between conduction band c, and valence band vi, as

$$J_{c,vi} = \frac{k^2}{\pi^2} \frac{|\alpha_c(k)|^2}{(\mathrm{d}E_{c,vi}/\mathrm{d}k)}, \tag{8.24}$$

where $E_{c,vi} = E_c - E_{vi}(k)$ and vi refers to either light hole (LH), heavy hole (HH), or split-off (SO) band. $\alpha_c(E)$ is included in Eq. (8.24) to describe the energy dependence of the momentum matrix element squared, which is assumed for Eq. (8.16) to vary as

$$|\alpha_c(k)|^2 = \left(1 + \frac{k^2 p^2}{E_v^2}\right)^{-1}. \tag{8.25}$$

Therefore,

$$J_{c,LH} = \frac{k^2}{\pi^2} \frac{|\alpha_c(k)|^2}{(\mathrm{d}E_c/\mathrm{d}k) - (\mathrm{d}E_{LH}/\mathrm{d}k)}, \tag{8.26}$$

$$J_{c,HH} = \frac{k^2}{\pi^2} \frac{|\alpha_c(k)|^2}{(\mathrm{d}E_c/\mathrm{d}k) - (\mathrm{d}E_{HH}/\mathrm{d}k)}, \tag{8.27}$$

and

$$J_{c,SO} = \frac{k^2}{\pi^2} \frac{|\alpha_c(k)|^2}{(\mathrm{d}E_c/\mathrm{d}k) - (\mathrm{d}E_{SO}/\mathrm{d}k)}. \tag{8.28}$$

Having the joint densities of states the total absorption spectrum can then be obtained, using Eq. (8.14), as

$$\alpha_{tot} = F_{ex} \frac{\pi e^2 \hbar}{n_r c \epsilon_0 m_0^2} \frac{M_b^2}{\hbar\omega} \left(J_{c,LH} + J_{c,HH} + J_{c,SO}\right). \tag{8.29}$$

The nonparabolicity of the light hole valence band, E_{LH}, is taken into account by Eq. (8.23), while here (for GaAs) the heavy hole and split-off bands are considered to be parabolic as

$$E_{HH} = E_{v0} - \frac{\hbar^2 k^2}{2m_h}, \tag{8.30}$$

and

$$E_{so} = E_{v0} - \Delta_{so} - \frac{\hbar^2 k^2}{2m_{so}}. \tag{8.31}$$

Perlin *et al.* [95, 96] and Skierbiszewski [41, 97, 98] measured the absorption spectrum for GaAs and $In_{0.04}Ga_{0.96}N_{0.01}As_{0.99}$. The solid black line in Fig. 8.3 shows the GaAs absorption spectra measured by Skierbiszewski [41]. The dashed blue line in this figure shows the absorption coefficient, calculated ignoring electron-hole interaction ($F_{ex} = 1$). Including the electron-hole interaction given by Eq. (8.11), gives the red circles, which show a very good agreement with the experimental result.

However we observed a 20 meV downward shift in the experimental absorption spectra. This could be explained by the shrinkage of the CB due to heavy doping. It has been shown that the CB shrinks downward relative to the valence band, due to the exchange energy of donor electrons in the conduction band or acceptor holes in the valence band [88]. By fitting to experimental values of absorption spectrum, Casey and Stern [99] determined an empirical expression for this energy shrinkage for p-type GaAs at room temperature as

$$\Delta E_g = -1.6 \times 10^{-8} (n)^{1/3}, \tag{8.32}$$

where n is in cm^{-3} and ΔE_g is in eV. For instance, considering $n = 2 \times 10^{18}$ cm^{-3} gives $\Delta E_g = -20$ meV. Applying this shift in the CB of GaAs leads to the absorption spectrum shown by the green line (with diamonds) in Fig. 8.3, that is in excellent agreement with experimental result, for energies up to 2 eV, including a kick in the absorption spectrum close to 1.75 eV, at the onset of transitions between the spin-split-off band and the conduction band.

8.4 Optical absorption of dilute nitride alloys

The effect of the incorporation of N in (In)GaNAs alloys can be described in different ways. We investigate here how the model chosen influences the calculated alloy absorption spectrum. We first present a simple model including isolated and pair N states using the BAC model. We then modify this model by including the nonparabolicity of the conduction and light hole and split-off bands, and the interaction between the split-off and conduction bands. In the second model we then include the full LCINS distribution of localised states using the SCGF model in § 8.4.2.

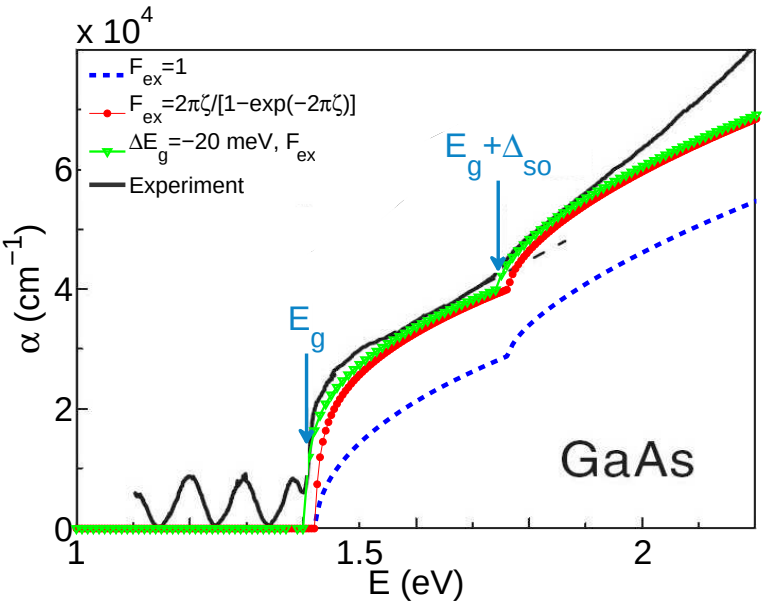

Figure 8.3: The absorption spectrum of GaAs at room temperature measured by Skierbiszewski [41] (solid black line), in comparison with absorption spectrum calculated by Eq. (8.29) with (red circles) and without (dashed green line) including the electron-hole interaction. The green line with triangles represents the effect of shrinkage in energy gap by $\Delta E_g = -20$ meV. The energy gap E_g and $E_g + \Delta_{so}$ are indicated for GaAs.

8.4.1 Five-level BAC model

In this section we first consider a simpler model, including isolated and pair N states and their interaction with the host semiconductor conduction, valence and spin orbit split-off bands. The conventional BAC model treats III-V conduction band dispersion as a parabolic band given by Eq. (8.15). Here we include the Kane nonparabolicity of the CB and of the light-hole and split-off bands, by combining and the 3-level BAC model explained in Chapter 3. Therefore, we can construct a 5×5 Hamiltonian as

$$H = \begin{bmatrix} E_{c0} & V_{Nc} & V_{NNc} & \sqrt{\frac{2}{3}}kp & \sqrt{\frac{1}{3}}kp \\ V_{Nc} & E_N & 0 & 0 & 0 \\ V_{NNc} & 0 & E_{NN} & 0 & 0 \\ \sqrt{\frac{2}{3}}kp & 0 & 0 & E_{v0} & 0 \\ \sqrt{\frac{1}{3}}kp & 0 & 0 & 0 & E_{v0} - \Delta_{so} \end{bmatrix}, \tag{8.33}$$

The energy of the isolated N levels (E_N), N-N pair states (E_{NN}) and the conduction band edge E_{c0} are assumed to vary with composition, x, and temperature,

T, as [21]

$$E_N = E_{N0} + \gamma_N x + a_N T, \tag{8.34}$$

$$E_{NN} = E_{NN0} + \gamma_{NN} x + a_{NN} T, \tag{8.35}$$

and

$$E_{c0} = E_g - \gamma_x x. \tag{8.36}$$

As mentioned in Chapter 3 the interaction parameters are given by $V_{Nc} = \beta_N \sqrt{x_N}$ and $V_{NNc} = \beta_{NN} \sqrt{x_{NN}}$, where the concentrations of single N and N-N pair states x_N and x_{NN} respectively, are determined from the total N concentration x as $x_{NN} = 6x^2$ and $x_N = x - 2x_{NN}$. The chosen values of the above parameters for (In)GaNAs are given in Table 8.2.

Calculating eigenvalues (the determinant of the characteristic equation) of this matrix gives the dispersion for 5 bands, namely the light-hole and split-off valence bands, and three conduction bands denoted by E_l, E_m, and E_u for lower, middle and upper bands, respectively. Fig. 8.4 displays the band dispersion for $In_{0.04}Ga_{0.96}N_{0.01}As_{0.99}$ where we have included also a parabolic heavy hole band given by Eq. (8.30) and nonparabolic light hole band given by Eq. (8.23).

The fractional Γ character, defined as the contribution of the host matrix CB states, can be calculated by finding the eigenvectors of Eq. (8.33)

$$\begin{bmatrix} E_{c0} & V_{Nc} & V_{NNc} & \sqrt{\frac{2}{3}}kp & \sqrt{\frac{1}{3}}kp \\ V_{Nc} & E_N & 0 & 0 & 0 \\ V_{NNc} & 0 & E_{NN} & 0 & 0 \\ \sqrt{\frac{2}{3}}kp & 0 & 0 & E_{v0} & 0 \\ \sqrt{\frac{1}{3}}kp & 0 & 0 & 0 & E_{v0} - \Delta_{so} \end{bmatrix} \begin{bmatrix} \alpha_c \\ \alpha_N \\ \alpha_{NN} \\ \alpha_v \\ \alpha_{SO} \end{bmatrix} = E \begin{bmatrix} \alpha_c \\ \alpha_N \\ \alpha_{NN} \\ \alpha_v \\ \alpha_{SO} \end{bmatrix}. \tag{8.37}$$

Following a method similar to Appendix A, the fractional Γ character ($f_\Gamma(E) = |\alpha_c|^2$) is given by

$$f_\Gamma(E) = \left[1 + \frac{V_{Nc}^2}{(E - E_N)^2} + \frac{V_{NNc}^2}{(E - E_{NN})^2} + \frac{(2/3)k^2p^2}{(E - E_{v0})^2} + \frac{(1/3)k^2p^2}{(E - E_{v0} + \Delta_{so})^2}\right]^{-1}. \tag{8.38}$$

Here, for each conduction sub-band we use the appropriate energy E, as shown in Fig. 8.4 by E_l, E_m and E_u.

The joint density of states for transitions from the valence band vi to the

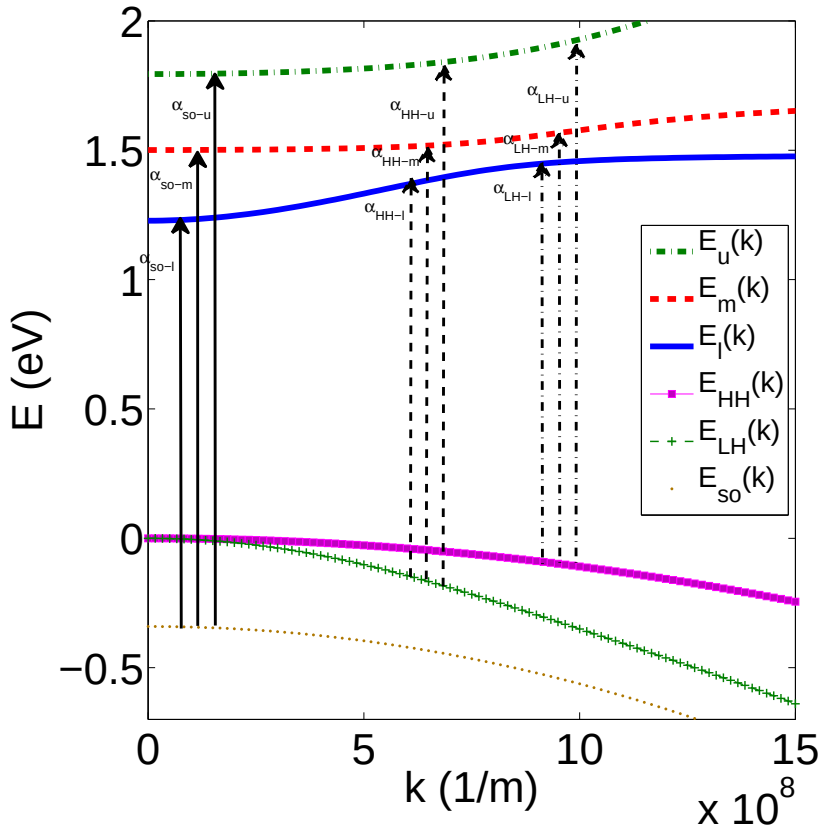

Figure 8.4: The band dispersion for $In_{0.04}Ga_{0.96}N_{0.01}As_{0.99}$ in 5-level BAC model.

conduction band cf, is given by Eq. (8.24)

$$J_{cf,vi} = \frac{k^2}{\pi^2} \frac{f_\Gamma(E_f)}{(\mathrm{d}E_{f,i}/\mathrm{d}k)}, \tag{8.39}$$

where $E_{f,i} = \hbar\omega = E_{vi} - E_{cf}$ is the energy separation between the CB cf and the valence band vi. The absorption spectrum for this transition, using Eq. (8.10) is given by

$$\alpha_{cf,vi}(\hbar\omega) = \frac{\pi e^2 \hbar}{n_r c \epsilon_0 m_0^2} \frac{M_b^2}{\hbar\omega} J_{cf,vi}(\hbar\omega). \tag{8.40}$$

Figure 8.4 represents the band dispersion of $In_{0.04}Ga_{0.96}N_{0.01}As_{0.99}$ and all possible transitions. The total absorption spectrum is given by the summation of nine individual absorption spectra for optical transitions from LH, HH and spin-orbit bands to CB sub-bands calculated using 5-level BAC model, i.e. E_l, E_m and E_u.

The total absorption is the sum of the contribution from all the transitions, shown in Fig. 8.4, between different valence and conduction bands. In total nine

individual transitions should be considered as

$$\begin{aligned}\alpha_T &= F_{ex}\sum_{cf,vi}\alpha_{cf,vi}\\ &= F_{ex}\Big(\alpha_{l,HH}+\alpha_{m,HH}+\alpha_{u,HH}+\alpha_{l,LH}\\ &+ \alpha_{m,LH}+\alpha_{u,LH}+\alpha_{l,SO}+\alpha_{m,SO}+\alpha_{u,SO}\Big).\end{aligned} \tag{8.41}$$

where α_{SO-l}, α_{SO-m} and α_{SO-u} are the absorption spectra from split-off band to lower, middle and upper sub-bands, respectively, and with a similar notation used for transitions from the HH and LH bands. The absorption spectrum for each transition is given by Eq. (8.40). For instance for transition from the light hole band E_{LH} to the lower conduction band, E_l

$$\alpha_{l,LH}(\hbar\omega) = \frac{\pi e^2\hbar}{n_r c\epsilon_0 m_0^2}\frac{M_b^2}{\hbar\omega}J_{l,LH}(\hbar\omega), \tag{8.42}$$

where $J_{l,LH}(\hbar\omega)$ is the joint density of states of the lower CB , E_l, and respect to the light hole band E_{LH}, and is given by

$$J_{l,LH}(\hbar\omega) = \frac{k^2}{\pi^2}\frac{f_\Gamma(E_l)}{\left(\dfrac{\mathrm{d}(E_l-E_{LH})}{\mathrm{d}k}\right)}. \tag{8.43}$$

8.4.2 The LCINS model

In order to include the full distribution of N states we need to use the Green's function method in the framework of the LCINS model. In Chapter 5 we showed that the conduction band Green's function could be written as

$$G_{kk}(E) = \left\{E - E_k - \frac{1}{N_c}\sum_j \frac{|V_j|^2}{E-E_j-\Delta E_j(E)}\right\}^{-1}, \tag{8.44}$$

where the (complex) energy shift of each localised state j is given by

$$\Delta E_j(E) = \frac{|V_j|^2}{N_c}\sum_k G_{kk}(E). \tag{8.45}$$

The density of states of the CB is given by

$$D_{cb} = -\frac{L^3}{\pi^2}\int \Im\left(G_{kk}\right)k^2\mathrm{d}k. \tag{8.46}$$

Replacing the integral by a sum over k this equation can be written as

$$D_{cb} = -\frac{L^3}{\pi^2} \sum_{k_i=0}^{k_{i,max}} k_i^2 \Im \left[G_{k_i k_i}(E) \right]. \tag{8.47}$$

The joint density of state between the CB and valence band vi can be obtained using

$$J_{c,vi} = -\frac{L^3}{\pi^2} \sum_{k_i=0}^{k_{i,max}} k_i^2 \Im \Big[G_{k_i k_i}\left(E - E_{vi}\right) \Big], \tag{8.48}$$

where E_{vi} is the energy of the valence band vi which, similar to previous section, can be the light hole (LH), heavy hole (HH), or split-off (SO) band. We take into account the nonparabolicity of the LH band given by Eq. (8.23), but assume parabolic heavy hole and split-off bands given by Eq. (8.30) and Eq. (8.31), respectively.

Having the joint DOS the optical absorption spectrum can be calculated using

$$\alpha_{tot} = F_{ex} \frac{\pi e^2 \hbar}{n_r c \epsilon_0 m_0^2} \frac{M_b^2}{\hbar\omega} \left(J_{c,LH} + J_{c,HH} + J_{c,SO} \right), \tag{8.49}$$

The Green's function given by Eq. (8.44) ignores the nonparabolicity of the host semiconductor CB. In order to consider the Kane non-parabolicity, the Green's function given by Eq. (8.44) could be modified as

$$G_{kk}(E) = \left\{ E - E_c - \frac{p^2 k^2}{E - E_v} - \frac{1}{N_c} \sum_j \frac{|V_j|^2}{E - E_j - \Delta E_j(E)} \right\}^{-1}, \tag{8.50}$$

8.5 Results for $In_yGa_{1-y}N_xAs_{1-x}$

Perlin, Skierbiszewski and their coworkers [41, 95–98] measured the absorption spectra for $In_{0.04}Ga_{0.96}N_{0.01}As_{0.99}$ and $In_{0.08}Ga_{0.92}N_{0.015}As_{0.985}$, and compared them with GaAs absorption data. Turcotte *et al.* [100, 101] recently measured the optical absorption spectrum of GaN_xAs_{1-x} and $In_yGa_{1-y}N_xAs_{1-x}$ for several values of x and y. Here, we calculate absorption spectra for $In_{0.04}Ga_{0.96}N_{0.01}As_{0.99}$ and compare them with Skierbiszewski measurements at different temperatures.

8.5.1 5-level model

The interaction between the InGaAs valence and conduction bands and with isolated and pair N states in $In_yGa_{1-y}N_xAs_{1-x}$ can be described using Eq. (8.33).

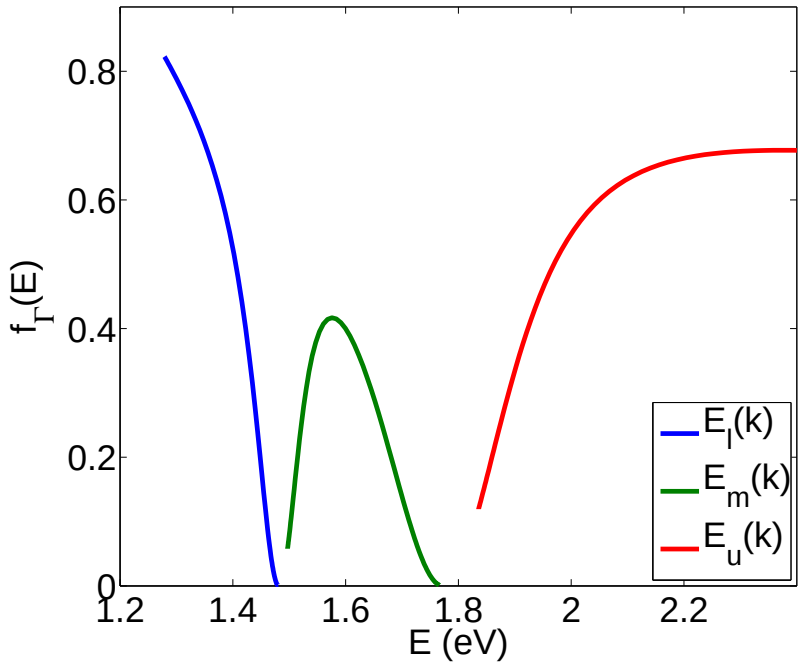

Figure 8.5: The fractional Γ character for $In_{0.04}Ga_{0.96}N_{0.01}As_{0.99}$, calculated by 5-level BAC model, at $T = 10$ K.

The band structure parameters for $In_yGa_{1-y}As$ are taken to vary with In composition, y, and temperature, T, as shown in Table 8.2. Also the energy and the interaction of isolated and pair N states are taken to vary with In composition and temperature as given in Tables 8.1 and 8.2. Fig. 8.4 shows the calculated band structure of $In_{0.04}Ga_{0.96}N_{0.01}As_{0.99}$ where the three conduction sub-bands ($E_u(k)$, $E_m(k)$ and $E_l(k)$) are determined as the eigenvalues of Eq. (8.33). Also we consider the lowest eigenvalue of Eq. (8.33) as the split-off band energy (E_{SO}). The non-parabolic light hole (E_{LH}) is given by Eq. (8.23), and the heavy hole

Table 8.2: BAC model parameters for $In_yGa_{1-y}N_xAs_{1-x}$ [6, 19, 100].

Parameter	*Symbol*	GaAs
N energy	E_{N0}	$1.706(1-y)+1.44y-0.38y(1-y)$ (eV)
N-N energy	E_{NN0}	$1.486(1-y)+1.44y-0.38y(1-y)$ (eV)
dE_N/dT	a_N	-2.5×10^{-4} (eV/K)
dE_{NN}/dT	a_{NN}	-2.5×10^{-4} (eV/K)
dE_N/dx	γ_N	-0.22 (eV)
dE_{NN}/dx	γ_{NN}	-0.22 (eV)
dE_c/dx	γ_x	-2.1 eV
N interaction	β_N	$1.97(1-y)+2y-3.5y(1-y)$ (eV)
N-N interaction	β_{NN}	$2.69(1-y)+2y-3.5y(1-y)$ (eV)
Energy gap	E_{c0}	$E_{g,GaAs}-1.33y+0.27y^2$ (eV)

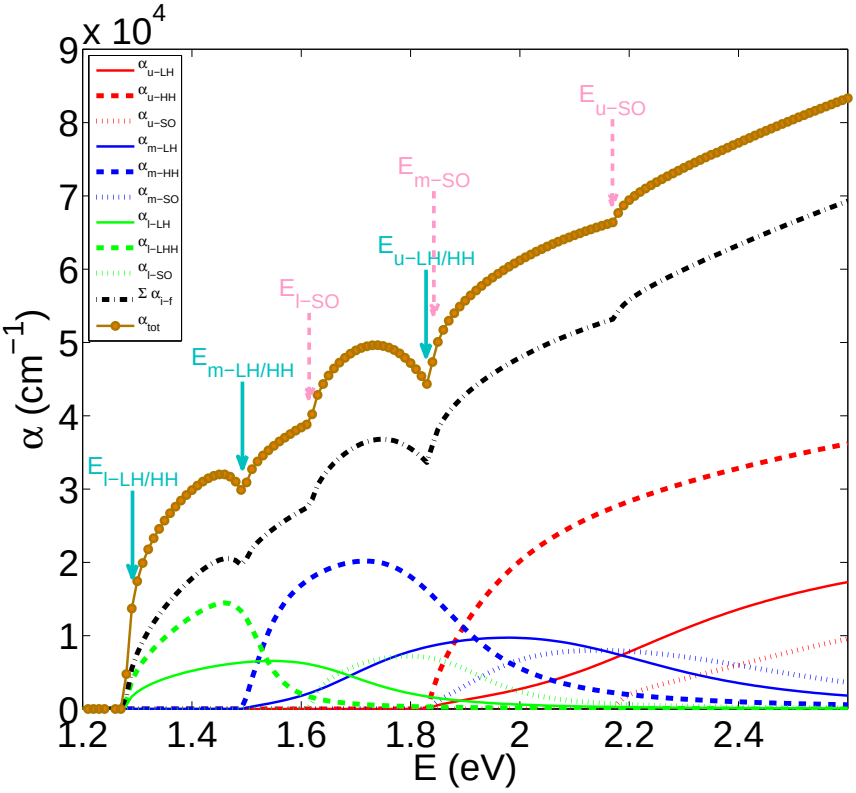

Figure 8.6: The absorption spectrum for $In_{0.04}Ga_{0.96}N_{0.01}As_{0.99}$ calculated using the 5-level BAC model at $T = 10$ K. The contribution of the transitions between three valence bands and three conduction sub-bands are shown. The solid arrows designate the transitions from heavy (HH) and light (LH) hole bands to lower (l), middle (m), and upper (u) conduction sub-bands. The dashed arrows indicate the transitions from spin-orbit split-off band to conduction sub-bands.

band (E_{HH}) has been considered to be parabolic, as given by Eq. (8.30).

The fractional Γ character of the conduction sub-bands is also required in order to calculate the joint density of states between the conduction and valence bands. Fig. 8.5 shows the Γ character of the CB for $In_{0.04}Ga_{0.96}N_{0.01}As_{0.99}$, obtained using Eq. (8.38). It is observed that in the lower sub-band it starts from its maximum value at the CBE, and decreases toward zero at the top of the lowest band. It increases again from zero to its maximum around 0.4 and goes back to zero in the middle band. Then in the upper band it increases gradually from its minimum at the bottom of the upper band, approaching an approximately constant value around $E = 2.1$ eV.

Figure 8.6 shows the calculated contributions of the different transitions to the total absorption spectrum. The solid, dashed and dotted lines in this figure represent the contribution for transition from LH, HH, and SO bands, respectively, to the conduction sub-bands. The red, blue and green lines indicate transition to

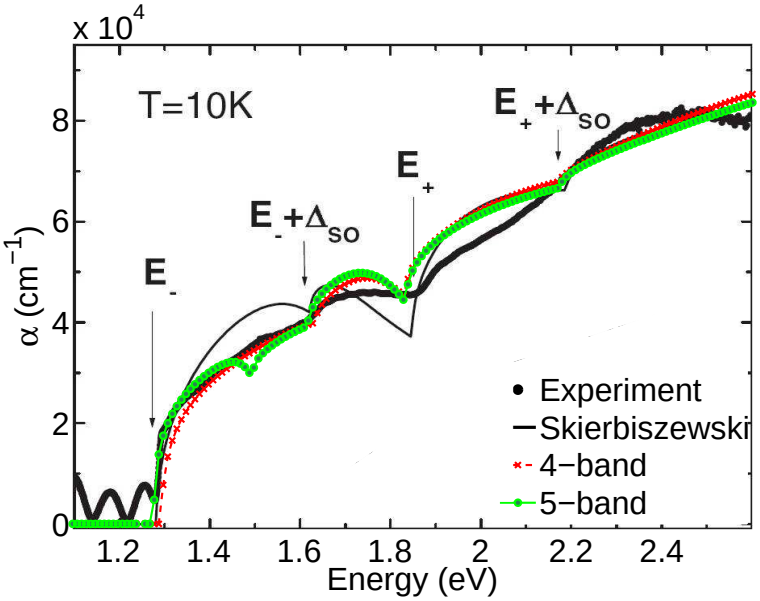

Figure 8.7: The absorption spectrum for $In_{0.04}Ga_{0.96}N_{0.01}As_{0.99}$ calculated using the 4-level (red line with crosses) and the 5-level BAC model (green line with circles). The black dots and line show the measured and calculated spectrum by Skierbiszewski [41] at temperature 10 K.

the upper, middle, and lower conduction sub-bands, respectively. The summation of these nine transitions is shown by the black dash-dotted line in this figure. Multiplying this by F_{ex} gives the total absorption spectrum, shown by the brown circles in this figure.

In Chapter 3 we have seen that the two and three-level BAC models predict a gap in the DOS. However it is clear from Fig. 8.6 that the joint DOS for different transitions overlap and fill this gap. Therefore no gap is seen in the absorption spectrum in (In)GaNAs alloys.

Figure 8.7 compares the calculated absorption spectrum using the 5-level BAC model with that measured and calculated by Skierbiszewski [41]. The 4-band model here refers to calculations which ignore the N-N pair states. The black dots in this figure are the experimental results for the absorption spectrum of $In_{0.04}Ga_{0.96}N_{0.01}As_{0.99}$ at $T = 10$ K. The solid black line shows the calculated absorption coefficient using the 2-level BAC model [96] with constant $V_{Nc} = 2.7$ eV and $E_N = 1.65$ eV. This line shows some discrepancies with the experimental data, especially around the transition to the upper sub-band of the BAC model. The arrows in this figure indicate the different transitions from the split-off, heavy and light hole band edges to the lower and upper sub-band band edges, in the BAC model. Our 4- and 5-level BAC models show much better agreement with the experimental measurements. The absorption spectrum, calculated by our

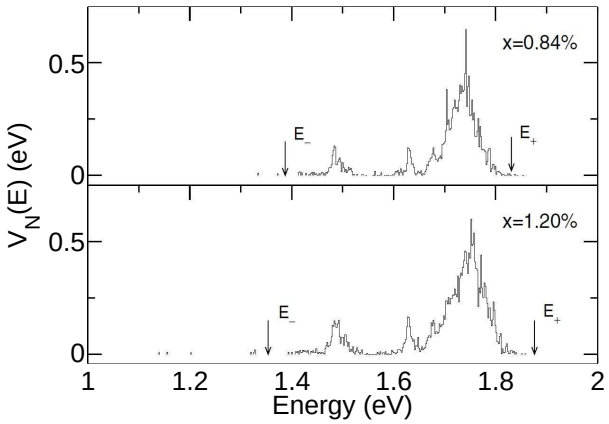

Figure 8.8: Calculated distribution of N cluster state energies at low temperature, weighted by their interactions with the conduction band edge state for GaN_xAs_{1-x} with $x = 0.84\%$ and $x = 1.2\%$.

four-level BAC model, shows a much better agreement with the experiment than the result of the BAC model by Perlin *et al.* [96]. This is because of using better BAC parameters taken in this work in comparison with earlier study [96], as well as including the valence band nonparabolicity in our calculations. However, the absorption edge predicted by this model is a bit higher than that seen in the experimental spectrum, and including the effect of N pair states in the 5-band model eliminates this difference. In our parameterisation, the N pair states push the CBE down to 1.28 eV, close to the value of the experimental absorption edge. This model still shows some steps corresponding to the transitions from the HH and LH band to the lower, middle and upper conduction sub-bands (see Fig. 8.6), whereas the experiment shows a much smoother absorption spectrum and has only one pronounced step around $E = 1.85$ eV. This is due to the fact that in the five-band model, we have considered isolated and pair N states. Considering the full distribution of N states can make the calculated absorption spectrum smoother and more similar to the experimental data.

8.5.2 LCINS approach

In order to calculate the absorption spectrum using the LCINS model, we first calculate the Green's function for the CB, given by Eq. (8.50). Fig. 8.8 shows histograms of the LCINS distribution of localised states for GaN_xAs_{1-x} with $x = 0.84\%$ and $x = 1.2\%$. This figure shows that the LCINS distributions for $x = 0.84\%$ and $x = 1.2\%$ are very similar. This implies that the LCINS distribution for GaN_xAs_{1-x} with $x = 1.0\%$ can be approximated by the one for $x = 1.2\%$. However, the calculated CBE at $x = 1.2\%$ (indicated by E_-) is

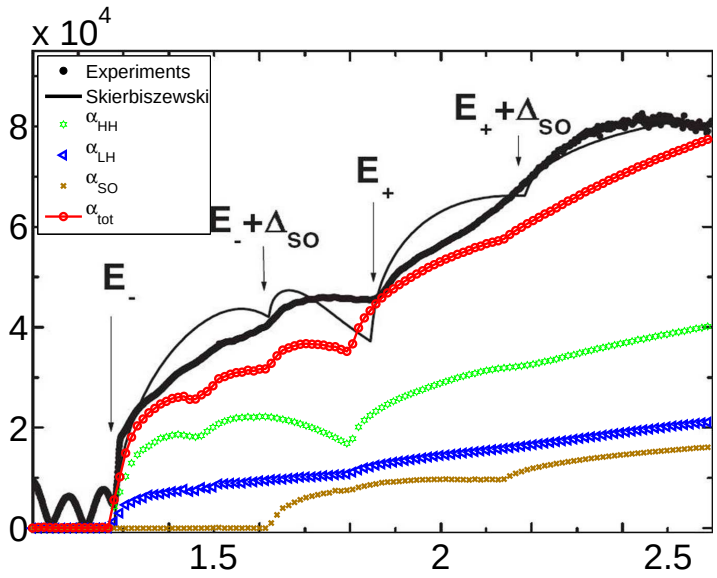

Figure 8.9: The absorption spectrum for $In_{0.04}Ga_{0.96}N_{0.01}As_{0.99}$ calculated by the SCGF approach, and LCINS distribution of N states at $T = 10$ K (red line with circles). The black dots and line respectively show the measured and calculated spectrum by Skierbiszewski [41] at this temperature. The contribution of transitions from HH, LH, and SO bands to the CB are shown by green stars, blue triangles and brown crosses, respectively.

about 30 meV lower than the CBE for $x = 0.84\%$. In the 5-band BAC model we assumed that the energy gap in $In_yGa_{1-y}As$ is given by $E_{g,GaAs} - 1.33y + 0.27y^2$. Also, the BAC model parameters in Table 8.2 suggest that including 4% In in $In_{0.04}Ga_{0.96}N_{0.01}As_{0.99}$ reduces the interaction $V_N(E)$ by about 5%, which we ignore in the LCINS model. Therefore, as we do not have the LCINS distribution for $In_{0.04}Ga_{0.96}N_{0.01}As_{0.99}$, We approximate it here by the LCINS distribution calculated for $GaN_{0.012}As_{0.988}$.

We can then calculate the Green's function for $In_{0.04}Ga_{0.96}N_{0.01}As_{0.99}$ alloy using Eq. (8.50). Fig. 8.9 displays the calculated absorption spectrum at $T = 10$ K including the full LCINS distribution of N states, and compares it with the absorption spectrum measured by Skierbiszewski [41]. Clearly the sharp steps that we saw in the 4 and 5-level BAC model disappear due to the inclusion of the distribution of localised states. This gives a better overall agreement with the experimental data. The remaining discrepancies between the calculated and experimental data may be due to the fact that we have approximated the N distribution by the one that was previously calculated for $GaN_{0.012}As_{0.988}$.

The room temperature absorption coefficient calculated from the SCGF method including the full LCINS distribution of N states is shown in Fig. 8.10. The solid black line in this figure displays the absorption spectrum measured by

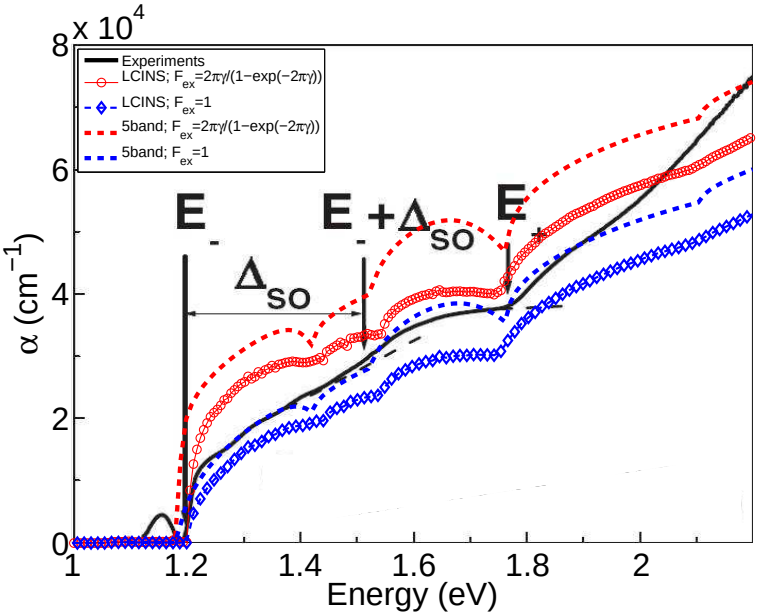

Figure 8.10: The room temperature absorption spectrum for $In_{0.04}Ga_{0.96}N_{0.01}As_{0.99}$ calculated using the LCINS (red circles and blue diamonds) and 5-level BAC (dashed lines) models. The red and blue curves display the results with and without including the electron-hole interaction. The solid black line shows the experimental data.

Skierbiszewski [41] at $T = 300$ K. The red circles in this figure show the absorption spectrum calculated in the LCINS model, where F_{ex} is calculated using Eq. (8.11). The blue diamonds here indicate the result when we consider $F_{ex} = 1$. The dashed blue and red lines in this figure show the optical absorption calculated using the 5-level BAC model, assuming $F_{ex} = 1$ and given by Eq. (8.11), respectively. Here, we again observe that the results calculated using the LCINS model have lower values in comparison with those calculated by the 5-level BAC model. This is because of the differences in the band non-parabolicity that we have considered for the valence bands, in the LCINS and 5-level LCINS models.

Figures 8.9 and 8.10 suggest that F_{ex} might have a stronger temperature dependence than what we have considered in our calculation. [1]

Comparison between the absorption spectrum of $In_{0.04}Ga_{0.96}N_{0.01}As_{0.99}$ (shown in Fig. 8.10) and GaAs (shown in Fig. 8.3) confirms that the absorption edge shifts towards lower energies with increasing N composition x. Also comparing the absorption spectrum of $In_{0.04}Ga_{0.96}N_{0.01}As_{0.99}$ at low and room temperatures, shown by Figs. 8.9 and 8.10, respectively, indicates that the band edge of $In_yGa_{1-y}N_xAs_{1-x}$ decreases by about 80 meV when we increase the tem-

[1] The temperature dependence is considered only in the static dielectric constant as shown in Table 8.1 in calculating exciton Rydberg energy in Eq. (8.12) .

perature from 10 to 300 K.

8.6 The absorption spectrum for GaN_xSb_{1-x}

Our focus in this thesis have been on the electrical and optical properties of (In)GaNAs alloys. We can apply our calculations to other dilute nitride alloys. Here we extend our calculations to investigate the absorption spectrum of GaNSb. The room temperature band gap of GaSb is about 725 meV, around half that of GaAs. Lindsay and O'Reilly [6, 103] have reported that N-related defect levels lie close to the CBE in GaNSb, and therefore strongly perturb the lowest conduction states in this alloy. The band gap and optical properties in GaN_xSb_{1-x} are shown to be strongly affected and highly sensitive to the distribution of the nitrogen atoms. Lindsay *et al.* [103] found that there is a wide distribution of N levels lying close to and below the CBE. The higher-lying N states push the CBE down in energy, as in GaAs, but the large number of lower-energy N states mix in strongly with the conduction band edge states, severely disrupting the band edge dispersion in GaNSb.

Here, we first investigate the band structure and optical absorption spectra of GaN_xSb_{1-x} in the 5-level BAC model, and compare the results with the absorption spectra measured by Jefferson *et al.* and by Veal *et al.* [102, 104]. We then apply the SCGF method to GaN_xSb_{1-x} in § 8.6.2. As the LCINS distributions have not yet been calculated for these alloys, we modify those calculated for GaNAs alloys and use them in our calculations.

Table 8.3: GaN_xSb_{1-x} parameters at room temperature.

Parameter	*Symbol*	GaAs
Lattice constant [92]	a_0	6.09593 (Å)
Electron effective mass [92]		
conduction	m_c^*	$0.039(m_0)$
light hole	m_l	$0.0439(m_0)$
heavy hole	m_h	$0.25(m_0)$
split-off	m_{so}	$0.12(m_0)$
SO splitting energy	Δ_{so}	0.76 (eV)
Energy gap [102]	E_g	0.725 (eV)
Refractive index [92]	n_r	3.8
N energy [6]	E_{N0}	$0.82 - 2.3 \times x$ (eV)
N-N energy [6]	E_{NN0}	$0.48 - 2.3 \times x$ (eV)
N interaction [6]	β_N	2.4 (eV)
N-N interaction [6]	β_{NN}	3.39 (eV)

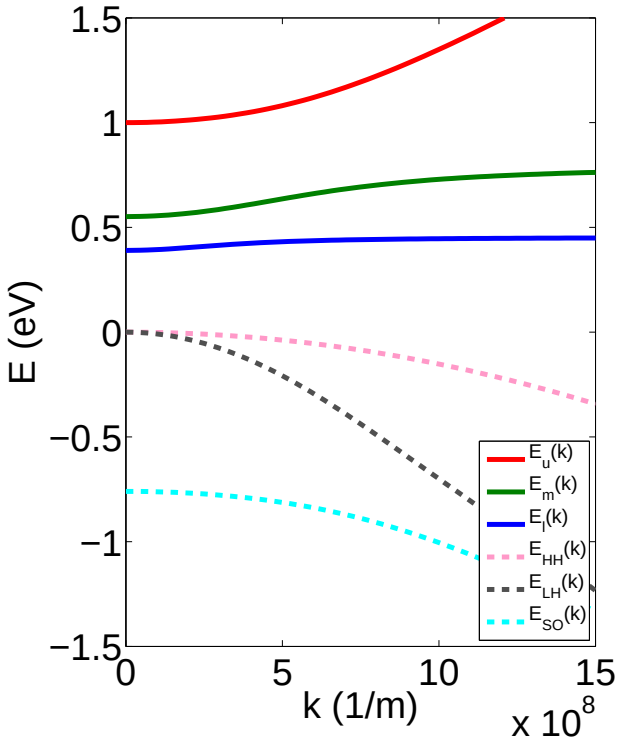

Figure 8.11: The band dispersion of $GaN_{0.012}Sb_{0.988}$ calculated by the 5-level BAC model. The sold lines display the conduction bands including upper (E_u), middle (E_m), and lower (E_l) sub-bands. The dashed lines show the spin orbit split-off (E_{SO}), light hole (E_{LH}) and heavy hole (E_{HH}) bands.

8.6.1 Absorption spectrum in the 5-level BAC model

When a single Sb atom is replaced by N in GaSb, the N atom introduces a localised state with energy E_N. However, a GaNSb alloy can also contain clusters of N atoms, such as N-N nearest neighbour pairs as well as larger clusters that introduce states in the band gap of GaSb. Table 8.3 contains the band parameters that we use for GaN_xSb_{1-x} and including the isolated N state energies, N energy states, E_N and N pair state energies, E_{NN} relative to the valence band maximum energy, and the BAC interaction parameters β_N and β_{NN}. As shown in this table, isolated N states are calculated to be less than 0.1 eV above the conduction band minimum, while the N pair states have energies in the middle of the GaSb band gap. The calculated energy gap of GaN_xSb_{1-x} depends strongly on the assumed N distribution, reflecting that N cluster states introduce a series of defect levels close to the CBE in this alloy. Also calculated values of the interaction parameters (β_N and β_{NN}) in GaN_xSb_{1-x} indicate that the interaction between these states and the host semiconductor CB is about 20% stronger than for GaNAs alloys.

Figure 8.11 shows the conduction and valence bands dispersion, calculated

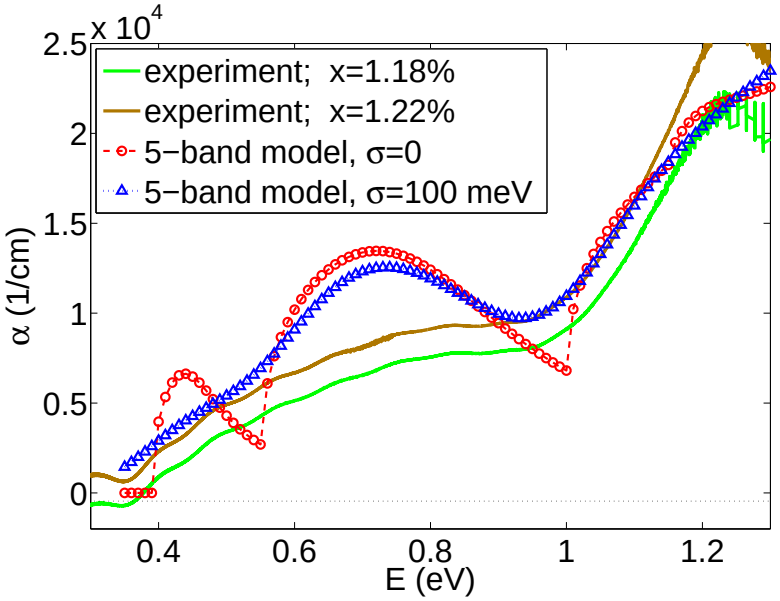

Figure 8.12: The absorption spectrum of $GaN_{0.012}Sb_{0.988}$ calculated by the 5-level BAC model (red line with circles), in comparison with experimental data measured for GaN_xSb_{1-x} with $x = 1.18\%$ and $x = 1.22\%$ (solid lines). Blue triangles show the calculated result broadened to a Gaussian of width 0.1 eV.

using the five-level BAC model given by the Hamiltonian of Eq. (8.33). The solid lines in this figure show the conduction sub-bands. Here we include the isolated and pair N states and their interaction with the GaSb conduction and valence bands, as explained in § 8.4. Since E_N is very close to the GaSb CBE, we observe that the lower sub-band (E_l) is almost flat and located within the GaSb band gap. The band edge minimum for this band is 0.39 eV and its maximum energy is 0.45 eV. This implies that substitution of only $x = 1.2\%$ N by Sb in GaSb reduced the energy gap rapidly from 725 meV to 390 meV. This value for the band gap of GaN_xSb_{1-x} with $x = 1.2\%$ is very close to that which was previously measured [102] and calculated using **k.p** [103] and *ab initio* pseudopotential [105] calculations.

The middle sub-band (E_m) lies between 0.55 and 0.78 eV, and the upper sub-band (E_u) minimum is close to 1.0 eV. The blue dashed line in Fig. 8.11 shows the non-parabolic spin orbit split-off band (E_{SO}), calculated by the lowest eigenvalue of Eq. (8.33). Also, the non-parabolicity of the light hole band (E_{LH}) has been taken into account using Eq. (8.23), while we assumed that the heavy-hole (E_{LH}) band has a parabolic dispersion.

Given the band dispersion we can calculate the optical absorption as described in § 8.5. The red circles in Fig. 8.12 display the absorption spectrum of $GaN_{0.012}Sb_{0.988}$ calculated using the 5-level BAC model. Green and brown

solid lines in this figure show the absorption spectra measured by Veal [106] for GaN_xSb_{1-x} with $x = 1.18\%$ and $x = 1.22\%$. Our calculated absorption edge is in good agreement with these experiments. However, there are two sharp steps in the calculated spectra corresponding to transitions from the light and heavy hole bands to the middle and upper sub-bands. We observe that the experimental absorption spectrum, $\alpha(E)$, increases from zero at the CBE, to about 3×10^3 cm^{-1} at energy $E = 0.55$ eV, that is the band edge of the middle sub-band. After this point the slope of the spectra decreases up to $E = 1$ eV, the minimum of the upper conduction sub-band. Then due to the transition from valence bands to the upper conduction sub-band, after this point the magnitude of the calculated absorption spectra increases rapidly. The spin-orbit splitting energy, Δ_{so}, is 0.76 eV. Therefore transitions from this band to the conduction sub-bands do not have any effect for energies up to 1.15 eV, where we see a small increase in the calculated absorption spectrum due to transition from the spin orbit split off band to the lowest conduction sub-band E_{SO}. The calculated optical absorption using a 5×5 **k.p** Hamiltonian, accounts well for the absorption edge. Wang *et al.* [107] have also measured the absorption edge of GaN_xSb_{1-x} with $x = 0.3\%$, $x = 0.7\%$ and $x = 1.4\%$, with the measured band edge energies in very good agreement with those calculated by the 5-level model of this chapter.

Note that there are two sharp features in this calculated result that are not observed in experiments. This could be due to the fact that we included only isolated and pair N states in this model and ignored the distribution of N states and their inhomogeneous broadening. We can consider the effects of localised states broadening by broadening the calculated spectrum using a Gaussian function. The blue triangles in Fig. 8.12 show the calculated absorption spectrum when it is broadened by a Gaussian with width 0.1 eV. We observe that this result agrees better with the experiments. The results for the calculated absorption spectrum using a 5-level BAC model suggest that we need to include the full distribution of N states in optical absorption calculations.

8.6.2 Absorption spectrum in the LCINS model

It has been shown that the calculated electronic structure of GaN_xSb_{1-x} strongly depends on the assumed distribution of N atoms [103]. Therefore, in order to calculate an accurate band dispersion for this alloy, we need to have the distribution of localised states. Unfortunately, such a distribution has not been calculated for GaN_xSb_{1-x}. However, we expect that the distribution of N states in GaN_xSb_{1-x} should be very similar to the LCINS distribution that Lindsay *et al.* [11] have

calculated for GaN_xAs_{1-x} alloys. Therefore, here we consider the LCINS distribution of N states in GaN_xAs_{1-x}, and, with some small modifications, use that for GaN_xSb_{1-x} alloys.

In the previous section we have seen that the energy of an isolated N state E_N is about 0.82 eV. So, we first need to shift the LCINS distribution of $GaN_{0.012}As_{0.988}$ to locate the highest peak at this energy. The dashed red line in Fig. 8.13 displays the LCINS distribution of N states, weighted by $V_j^2/\sqrt{N_c}$, calculated for GaN_xAs_{1-x} with $x = 1.2\%$, and shifted down in energy by 888 meV. This distribution can be approximated by three Gaussian distributions, each corresponding to different N environments. It is observed in this figure that if we align the main peak at $E = 0.82$ eV, the lowest peak corresponding to pair N-N states is located at 0.55 eV, which is higher than the values that we considered for E_{NN} in the BAC model. Therefore, we shift the Gaussian distributions corresponding to pairs and larger clusters of N states down by a further 70 meV. Moreover, the BAC model parameters in Table 8.3 suggest that in GaNSb the interaction parameters, β_N and β_{NN}, are 20% stronger than in GaNAs. Therefore we multiply the N LCINS values by 1.44 to account for this difference. The blue solid line in Fig. 8.13 presents the distribution of N states that we consider for $GaN_{0.012}Sb_{0.988}$ in our calculation.

Having the distribution of N states we are able to calculate the Green's function for $GaN_{0.012}Sb_{0.988}$ using Eq. (8.44) and Eq. (8.45), self-consistently. Also the density of CB states can be calculated using Eq. (8.46). Fig. 8.14 shows the DOS of $GaN_{0.012}Sb_{0.988}$ calculated by the SCGF, and including the distribution of localised states shown by the solid blue line in Fig. 8.13. The gaps corresponding

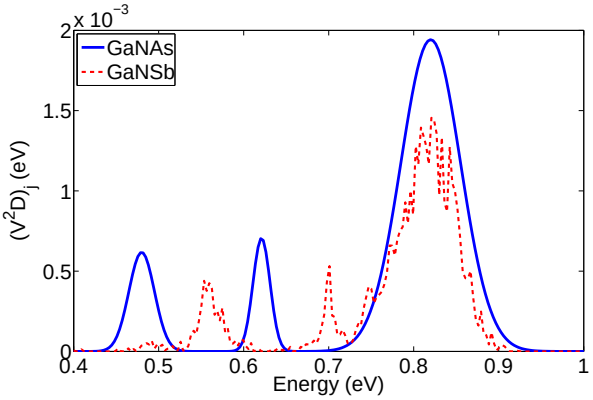

Figure 8.13: The distribution of N states assumed for $GaN_{0.012}Sb_{0.988}$ (blue line), in comparison with the LCINS distribution of $GaN_{0.012}As_{0.988}$, shifted down in energy by 888 meV (dashed red line). The zero of energy is taken to be at the top of the GaSb valence band.

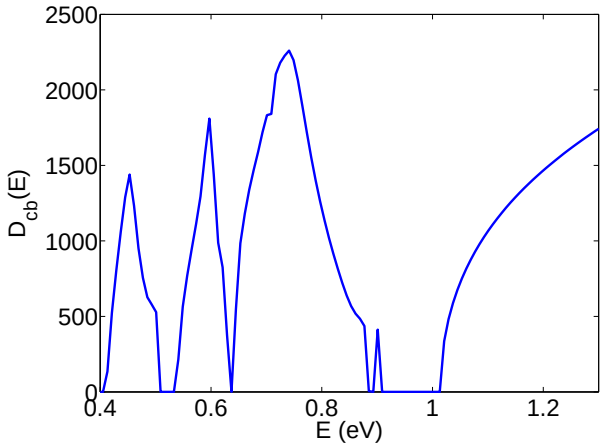

Figure 8.14: The density of states of $GaN_{0.012}Sb_{0.988}$ calculated using the SCGF method and including the distribution of N states given in Fig. 8.13.

to isolated and pair N states are clearly observed in this plot. Also, at energies around 0.65 eV the DOS has a small gap that is related to the higher cluster of N states.

We can also calculate the absorption spectrum in SCGF model explained in § 8.4.2. The blue line with diamonds in Fig. 8.15 shows the calculated absorption coefficient using this method. As we expected this method shows a better agreement with experiments, than the result of the 5-level BAC model (shown by red

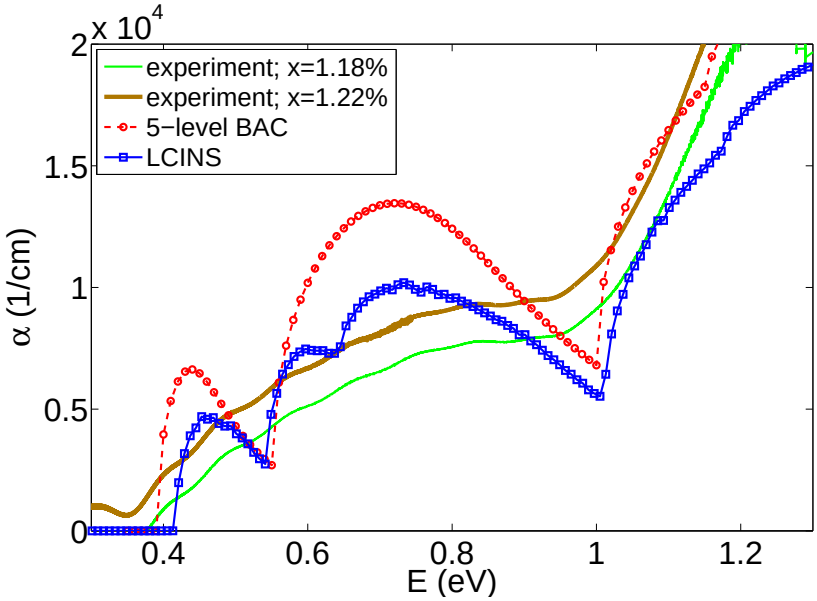

Figure 8.15: The absorption spectrum of $GaN_{0.012}Sb_{0.988}$ calculated by the SCGF model and including the distribution of localised states (blue diamonds), in comparison with experimental data measured for GaN_xSb_{1-x} with $x = 1.18\%$ and $x = 1.22\%$ (solid lines). The results calculated by the 5-level BAC model are displayed by the red line with circles.

circles in this plot).

For the considered N distribution, this calculation suggests more gaps in the DOS of $GaN_{0.012}Sb_{0.988}$ compared to what we have observed in Chapter 5 for $GaN_{0.012}As_{0.988}$. However, experimental data indicate that there are fewer features in the GaNSb absorption spectra than in the GaNAs ones. This could be because of the intrinsic differences between the distribution of N states in GaNSb and InGaNAs samples, or inhomogeneities in the samples investigated experimentally.

8.7 Summary

In this chapter we presented an analysis of the optical absorption spectra using the band structure calculations presented in previous chapters. We have considered two different models to calculate the absorption spectra in InGaNAs and GaNSb alloys and compared our results with experimental measurements. There are some discrepancies between experimental data in similar samples that make quantitative comparison difficult.

Two models have been considered to calculate the absorption spectrum in these materials: The 5-level BAC and LCINS models. The 5-level BAC model included isolated and pair N states and their interactions with the host semiconductor valence and conduction bands. The results of this model for InGaNAs alloys give an overall good agreement with experiments, and predict accurate absorption edge for these alloys. However, the results of 5-level BAC model confirms that we need to consider full distribution of N states in our calculations.

Then we extended our calculations to include the LCINS distribution using the SCGF approach presented in Chapter 5. The results of calculated absorption spectrum using the SCGF approach including the LCINS distribution provide very good agreement with experiments. This confirms the validity of using the SCGF approach including the distribution of localised states to study the band structure of dilute nitride alloys.

Our calculated absorption spectra for GaNSb alloys fit well with experiments at the absorption edge, and predict the correct band gap in these alloys. However, the absorption spectrum calculated in the BAC model contains some features associated with individual transitions to lower and upper sub-bands in the model that are not seen in the measured absorption spectra. Taking the distribution of localised states into account reduces the impact of these features and gives results more similar to experimental absorption. But we still see some dips in

our calculated spectra that are not seen in any experiment. We conclude that the distribution of N states in GaNSb alloys are different from what we found for InGaNAs samples. The position and broadening of localised states seem to be different from (In)GaNAs alloys and more work is needed to address and resolve why more structure is observed in the calculated absorption than measured spectra.

Chapter 9

Conclusions and further work

9.1 Conclusions

In this thesis we investigated the effects of substitutional N atoms on the electrical and optical properties of dilute nitride semiconductors. Our focus was on the band structure, carrier scattering, mobility and high field transport in these materials. In Chapters 3 to 5 we first tried to understand the band structure of dilute nitride alloys using the BAC and Green's function approaches and examined their accuracy by comparing their results with numerical diagonalisation of the Hamiltonian of large supercells containing localised states randomly distributed throughout the cell along with momentum eigenstates. This comparison led us to develop the self-consistent Green's function method which gives excellent agreement with the supercell model. Then in chapters 6 and 7 we used these models to study hot electron transport and carrier mobility in GaN_xAs_{1-x} alloys. Finally in Chapter 8 we tested the band structure methods developed in this thesis by calculating absorption coefficients for $In_yGa_{1-y}N_xAs_{1-x}$ and GaN_xSb_{1-x} alloys and compared them with experimental absorption spectra.

In Chapter 3 we first modified the BAC model to include N state energy broadening and energy shift, which were calculated using second order perturbation theory. This modified BAC model with complex N energy predicts similar DOS to those calculated by the Green's function approach. The gap in the DOS above the N state energy level predicted by the BAC model (without N broadening), is filled in both calculations. In this chapter the N-N pair states have been included in the 3-level BAC model. We extended this method to the LCINS model to include the full distribution of localised states. The DOS and the band dispersion of GaN_xAs_{1-x} were compared in different models. The DOS in the LCINS model contains features associated to N-N pairs and other N clusters.

In order to investigate the accuracy of the BAC and Green's function models discussed in Chapter 3, we presented a supercell model in Chapter 4, where we solved a random impurity Hamiltonian, based on the Anderson many impurity model. We considered a very large supercell with randomly placed nitrogen atoms. We simplified the model assuming that all N states have the same energy E_N. We then compared calculated DOS and fractional Γ character calculated by the eigenvalues and eigenvectors of this Hamiltonian, with the results of the 2-level BAC model (with broadening). This comparison confirmed the validity of the BAC model to study the band structure and the DOS in dilute nitride alloys. However it also highlighted discrepancies around N state energies. Contrary to the two-level Green's function and the BAC (with N broadening) models, the DOS calculated by the supercell calculation predicts a gap in the conduction band for the Anderson impurity Hamiltonian used. Also the comparison between the total DOS and the fractional Γ character in the supercell and BAC model revealed some differences around N state energies. These results suggested that the N broadening and the shift in the real part of the energy should be energy-dependent. Moreover, the BAC model introduces errors in the DOS as there is no maximum cut-off wave vector in this model. In fact it requires an infinite density of N levels interacting with the host matrix extended conduction states.

In Chapter 5 we modified the Green's function approach developed by Martin Vaughan [33] by including an energy-dependent complex energy shift $\Delta E_j(E)$, where the imaginary and real parts of $\Delta E_j(E)$ were interpreted as N broadening and the shift in the localised states energy, respectively. We calculated the energy shift $\Delta E_j(E)$, self-consistently, enabling us to then calculate the Green's function, G_{kk}. The DOS obtained by the imaginary part of the Green's function provide excellent agreement with those calculated in the supercell calculations. The 2-level SCGF, which ignores the N-N pairs and higher cluster of N states, predicts a gap in the DOS as seen in the supercell model. Including the N state distribution, given by the LCINS model, fills this gap (for N composition $x < 2\%$), in agreement with experimental measurements. The DOS and the band dispersion calculated using the SCGF method, including LCINS distribution, show additional features associated with N-N pairs and higher N clusters.

In Chapters 6 and 7 we turned to investigate the consequences of N incorporation on carrier scattering and high field mobility. In Chapter 6 we solved the steady state Boltzmann transport equation and calculated drift velocity and carrier mobility for GaNAs alloys. As it is very difficult to treat the Green's function band structure in the Boltzmann transport equation, we used and compared the

results of two approaches: the parabolic band model and the BAC model. The former is likely to provide a lower bound on the effects of N incorporation, while the second approach clearly overestimates the effects of N on the band structure. In the parabolic band model we ignored the effect of N states on the band structure of the GaNAs alloys and assumed that the conduction band retains a parabolic dispersion, but included explicitly the strong resonant scattering associated both with isolated N atoms and also with an LCINS distribution of N states. We observed that the strong scattering by N states limits the mobility and the acceleration of carriers to higher energy. This means that carriers require much higher electric field to scatter to the higher energy L valley. In the BAC model we assumed carriers are constrained in the lower band of the BAC model and scattered by phonons and nitrogen states. This model gives good results at lower field but because of the unphysical constraint of limiting carriers to the lower BAC band, it breaks down at intermediate and high field. We showed, for lower N concentration, in agreement with previous Monte-Carlo calculations [16, 58] and experimental results [15], that a negative differential velocity (NDV) can still be present, but at higher electric fields than those where NDV occurs in GaAs. However, for higher N compositions NDV disappears, as seen in experimental measurement [57].

Then in Chapter 7 we expanded the mobility calculations of Chapter 6 by including the band structure and the carrier scattering calculated using the SCGF approach. The poles of the Green's function calculated in this chapter provided an accurate band structure and scattering rate for GaNAs alloys that enabled us to calculate group velocity, mobility and mean free path of carriers for dilute nitride alloys. The carrier mobility calculated in Chapter 7 showed better agreement with experiment than previous calculations using a parabolic band model.

Finally in Chapter 8 we tested the band structure models developed in Chapters 3 to 5 by comparing the absorption spectra predicted by these models with experimental data. The results of absorption coefficients calculated for $In_yGa_{1-y}N_xAs_{1-x}$ alloys in this chapter showed very good agreement with experiments. This confirms the validity of the SCGF approach presented in Chapter 5. In this chapter we extended our calculations to examine the DOS and absorption coefficient for GaN_xSb_{1-x} alloys for which much less studies have been done. Our calculated optical absorption for GaNSb alloys fits well with experiments at the absorption edge, and provides the correct band edges for these alloys. However, the absorption spectrum we calculated has more features than seen experimentally. We conclude that further work is required to identify whether this is due

to inhomogeneities in the samples investigated experimentally or to intrinsic differences between the distribution of N states in GaNSb and InGaNAs samples.

9.2 Future work

Although in this thesis we investigated the band structure, scattering and high field mobility for GaNAs alloys, our methods can be easily applied to other highly mismatched semiconductors, including different dilute nitride alloys and dilute bismide semiconductors, containing bismuth (Bi). In Chapter 8 we applied our band structure methods to study the band structure and absorption spectra of $In_yGa_{1-y}N_xAs_{1-x}$ and GaN_xSb_{1-x} alloys. Our studies for GaN_xSb_{1-x} show that in order to accurately calculate band structure for dilute nitride alloys, it is imperative to take in to account the actual distribution of localised states.

In order to study the high carrier transport, in Chapter 6 of this thesis, we have considered two models that provide upper and lower limits of actual results. The combination of information from these models gives a clear analysis of the strong influence of N scattering on electron transport in dilute nitride alloys, consistent with the observed experimental behavior across the complete range of electric fields considered. However, it remains a challenging problem to describe exactly high field carrier transport in these materials, including details of the CB dispersion such as we presented in Chapter 5 by the SCGF approach.

Moreover, in high field studies in Chapter 6 we used the N scattering rate calculated by Fahy *et al.* [13]. In Chapter 7 we obtained more accurate decay rates using the poles of the Green's function, which are much lower than previous results [13], for energies far from the CBE of dilute nitride alloys. Using the decay rates obtained by the SCGF method in Chapter 7 in the Boltzmann transport equation, can give more accurate mobility and drift velocity in high electric filed.

In this thesis we studied the band structure and transport of bulk dilute nitride alloys. However, to understand the behaviour of carriers in quantum well structure, we can lower the dimensions of our calculations to 2-D, to get a more realistic picture of carrier transport in these alloys. This requires modification of the band structure calculations to obtain an appropriate DOS and band dispersion for 2-D alloys. This can be done by calculating the Green's function in two dimensions, self-consistently. The poles of the Green's function can then be used to find the band structure, scattering rate, and carrier mobility for 2-D dilute nitride alloys.

Another possible interesting problem is the low temperature transport and

investigation of the carrier behaviour in this regime. Also the effect of pressure on electron transport in dilute nitride alloys can be studied using the methods presented in this thesis.

Overall, we conclude that the methods presented here are very well suited to further investigations of the electronic structure and its consequences for the transport properties of a wide range of highly mismatched semiconductor alloys.

Appendix A

Calculating the fractional Γ character

The DOS projected onto the k^{th} conduction band state, $|k\rangle$, can be found from the imaginary part of the Green's function G_{kk} of Eq. (5.2). It can be shown that this is equivalent to solving the Hamiltonian H_k [30], given by

$$\begin{pmatrix} E_k & V_1/\sqrt{N_c} & V_2/\sqrt{N_c} & \cdots & V_n/\sqrt{N_c} \\ V_1/\sqrt{N_c} & E_1+\Delta E_1 & 0 & \cdots & 0 \\ V_2/\sqrt{N_c} & 0 & E_2+\Delta E_2 & \cdots & 0 \\ \vdots & \vdots & \cdots & \ddots & \cdots \\ V_n/\sqrt{N_c} & 0 & 0 & \cdots & E_n+\Delta E_n \end{pmatrix} \times \begin{pmatrix} \alpha_M \\ \alpha_1 \\ \alpha_2 \\ \vdots \\ \alpha_n \end{pmatrix} = H_k \begin{pmatrix} \alpha_M \\ \alpha_1 \\ \alpha_2 \\ \vdots \\ \alpha_n \end{pmatrix} = E \begin{pmatrix} \alpha_M \\ \alpha_1 \\ \alpha_2 \\ \vdots \\ \alpha_n \end{pmatrix}, \tag{A.1}$$

where E_k is the host matrix state of momentum k, and E_i is the energy of the ith localised state, with complex energy shift ΔE_i arising from its interaction with the continuum of delocalised states. Note that $\Delta E_j(\varepsilon_p)$ incorporates the coupling of other than k excited state j to all host states of momentum k and is an energy dependent quantity. Therefore

$$\frac{V_j}{\sqrt{N_c}}\alpha_M + (E_j + \Delta E_j(E))\alpha_j = E\alpha_j. \tag{A.2}$$

Rearranging this equation we have

$$\alpha_j = \frac{\alpha_M}{\sqrt{N_c}} \frac{V_j}{E - E_j - \Delta E_j(E)}, \tag{A.3}$$

Multiplying Eq. (A.3) by its complex conjugate we have

$$|\alpha_j|^2 = \frac{|\alpha_M|^2}{N_c} \frac{|V_j|^2}{|E - E_j - \Delta E_j(E)|^2}. \tag{A.4}$$

The normalisation condition implies

$$|\alpha_M|^2 + \sum_j |\alpha_j|^2 = 1, \tag{A.5}$$

and therefore the fractional Γ character is given by

$$f_\Gamma = |\alpha_M|^2 = \left(1 + \frac{1}{N_c} \sum_j \frac{|V_j|^2}{|E - E_j - \Delta E_j(E)|^2}\right)^{-1}. \tag{A.6}$$

The complex poles ε_p of the Green's function G_{kk} can be expressed as eigenvalues of the Hamiltonian of Eq. (A.1) if we substitute the real energy E by the complex poles ε_p and also the energy shift $\Delta E_j(E)$ by $\Delta E_j(\varepsilon_p)$ in this equation. In this case the contribution of localised state j to the poles at ε_p is given by

$$W_{j,p} = |\alpha_j|^2 = \frac{|\alpha_M|^2}{N_c} \frac{|V_j|^2}{|\varepsilon_p - E_j - \Delta E_j(\varepsilon_p)|^2}. \tag{A.7}$$

and therefore Eq. (A.6) becomes

$$f_\Gamma = |\alpha_M|^2 = \left(1 + \frac{1}{N_c} \sum_j \frac{|V_j|^2}{|\varepsilon_p - E_j - \Delta E_j(\varepsilon_p)|^2}\right)^{-1}. \tag{A.8}$$

Appendix B

Iterative search method for finding the poles of GF

In order to calculate Green's function given in Eq. (7.1) we need to calculate $\Delta E_j(\varepsilon)$ for all values of $E = \Re(\varepsilon)$ and $\delta = \Im(\varepsilon)$. We first solve Eqs. (5.2) and (5.3) self-consistently for real values of the energy, as we already explained in Chapter 5, and determine $\Delta E_j(\varepsilon)$ for real values of ε (i.e. for $\delta = 0$). Then we vary δ from 0 to $-\Delta_{max}$ by small steps, $d\delta$, where Δ_{max} is the maximum negative imaginary part of ΔE_j. For each value of imaginary part of the energy δ, we use $\Delta E_j(E + i(\delta - \mathrm{d}\delta))$ as an initial value for $\Delta E_j(E + i\delta)$ to solve Eqs. (7.1) and (7.2) self-consistently, by the iteration method described in Chapter 5.

To find the poles of the Green's function $\varepsilon_p(k)$, we need to find values of ε where $[G_{kk}(\varepsilon_p)]^{-1} = 0$. Defining $\gamma(\varepsilon)$ by

$$\gamma(\varepsilon) = \varepsilon - \frac{1}{N_c} \sum_j \frac{|V_j|^2}{\varepsilon - E_j - \Delta E_j(\varepsilon)}, \tag{B.1}$$

we have

$$\gamma(\varepsilon) = [G_{kk}(\varepsilon_p)]^{-1} + E_k, \tag{B.2}$$

and the poles $\varepsilon_p(k)$ of G_{kk} occur where

$$\gamma(\varepsilon_p) = E_k. \tag{B.3}$$

One approach for finding the solution of Eq. (B.3) is to calculate $\gamma(\varepsilon)$ along the lines in the complex plane, for which $\Re[\varepsilon] = E$ is constant. Thus, for fixed E, we vary δ from 0 to $-\Delta_{max}$. We then search for where the resulting $\gamma(E + i\delta)$ crosses the positive real axis at some value, $E_k = \hbar^2 k^2/2m$. The wavevector is then $k = \sqrt{2m\gamma(\varepsilon)}/\hbar$, and $\varepsilon_p(k) = E + i\delta$. (If the curve of $\gamma(\varepsilon)$ does not cross the

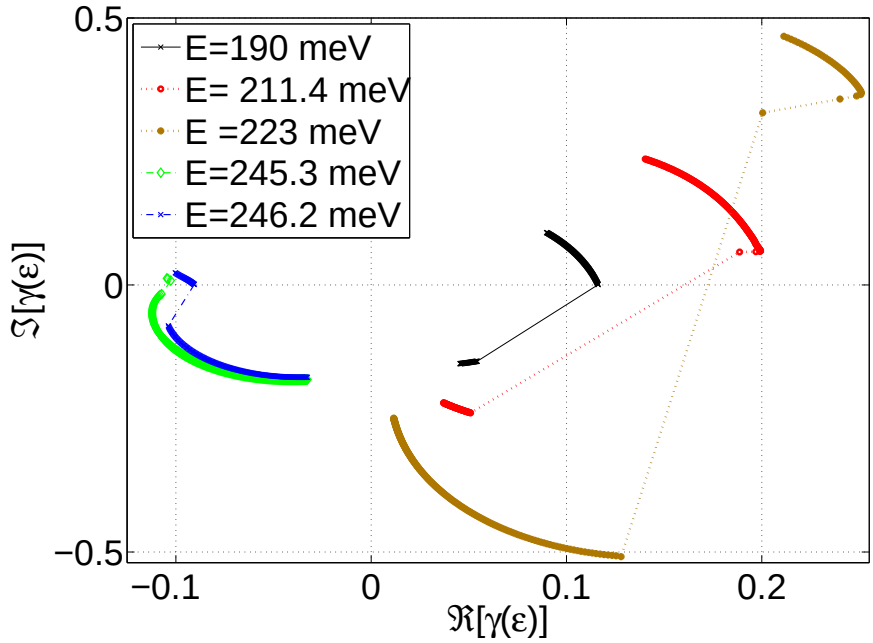

Figure B.1: The real and imaginary parts of $\gamma(\varepsilon)$ for some chosen energies close to the nitrogen localised stat energy, E_N. For each curve, for the given $\Re(\varepsilon) = E$, $\Im(\varepsilon)$ is varied from 0 to -26 meV.

positive real axis, then there is no value of k for which the band energy equals this value of E.) We now have the real and imaginary parts of $\varepsilon_p(k)$. Varying $\Re[\varepsilon_p]$ allows us to plot the complex bands E versus real k. For each k, $\Re[\varepsilon_p]$ gives the physical energy of the state and $-2\Im[\varepsilon_p]/\hbar$ is its decay rate.

B.1 The two-band model

In the two-band model, we include only isolated nitrogen with energy E_N. For all values of E and δ, we vary δ from 0 to $-\Delta_{max}$ (e.g. -26 meV for $x = 0.2\%$) in the steps of 0.1 meV, and for each value of δ we iterate Eqs. (7.1) and (7.2) 40 times to assure we have reached convergence in $\Delta E_N(E + i\delta)$.

Now, having the $\Delta E_N(\varepsilon)$ on the whole complex surface we can calculate the poles of the Green's function ε_p. In the 2-level model $\gamma(\varepsilon)$ is simplified as

$$\gamma(\varepsilon) = \varepsilon - \frac{V_{Nc}^2}{\varepsilon - E_N - \Delta E_N(\varepsilon)}, \tag{B.4}$$

where $V_{Nc}^2 = x\beta^2$. Finding the corresponding values of δ that $\gamma(E + i\delta)$ crosses the real axis we have $\Re(\varepsilon_p)(= E)$ and $\Im(\varepsilon_p)$.

Figure B.1 illustrates the method of searching for the poles of the Green's func-

tion, showing $\gamma(E + i\delta)$ for fixed values of E and δ varying from 0 to -26 meV. Finding the poles for energies, E, inside the (lower and upper) bands is straightforward: by varying δ, $\gamma(E + i\delta)$ crosses the positive real axis. For instance, we can easily find the appropriate pole at $E = 190$ meV, shown by the black line in Fig. B.1. For some energy values E we can not find the poles of the Green's function, as $\gamma(E + i\delta)$ does not cross the positive real axis. Therefore, there is no pole corresponding to this energy. This indicates that such an energy E is located inside the gap of the CB, e.g. $E = 245.3$ meV and $E = 246.2$ meV shown by the green and blue squares, respectively, in Fig. B.1.

For energies E near the top of the lower band (e.g. the red and the brown circles in Fig. B.1), despite the fact that $\gamma(\varepsilon)$ has some values on both sides of the positive real axis, no value of ε is found for which $\gamma(\varepsilon)$ is real. Therefore we exclude these states from the band. This failure to find poles at these energies is due to the failure of the iterative search method for solution of Eqs. (7.1) and (7.2) to converge to a value of ΔE_N with negative imaginary part. Moreover, as we will see in Figs. 7.2 and 7.3, at the bottom of the upper band, we also can not find any value of δ that gives $\Im(\gamma(E + \delta)) = 0$. That is the reason for observing the wider gap for the calculations at the poles of the Green's function in § 7.3.

B.2 The LCINS method

In the LCINS method the we include the distribution of N states, we can calculate $\Delta E_N(\varepsilon)$ in a similar way to the method that was described in previous section, by solving the pair of equations (7.1) and (7.2), self-consistently. We then search for the poles ε_p of the Green's function and calculate and calculate E_k and the poles ε_p as discussed in previous section for the two-level model.

The blue circles in Fig. B.2 display the calculated dispersion relation for GaN_xAs_{1-x} with $x = 0.1, 0.36, 1.2$ and 2.0%, using the LCINS distribution and the SCGF approach, while the poles of Green's function, ε_p are calculated using the iterative search method. As we mentioned in § 7.4, finding the poles of the Green's function is tricky. For instance the red stars in Fig. B.2 show the energies E where $\gamma(\varepsilon)$ discontinuously crosses the positive real axis but it is not possible to find a value of imaginary part of the energy, δ, for which $\Im[\gamma(E + i\delta)] = 0$. The green areas below the CBE and around the isolated N states energy, show the energies for which $\gamma(E + i\delta)$ does not cross the positive real axis of energy. (See Fig. 7.2.) Fig. B.2 shows that, besides a gap corresponding to isolated N states, we have other mini-gaps related to pairs and larger clusters, that are more

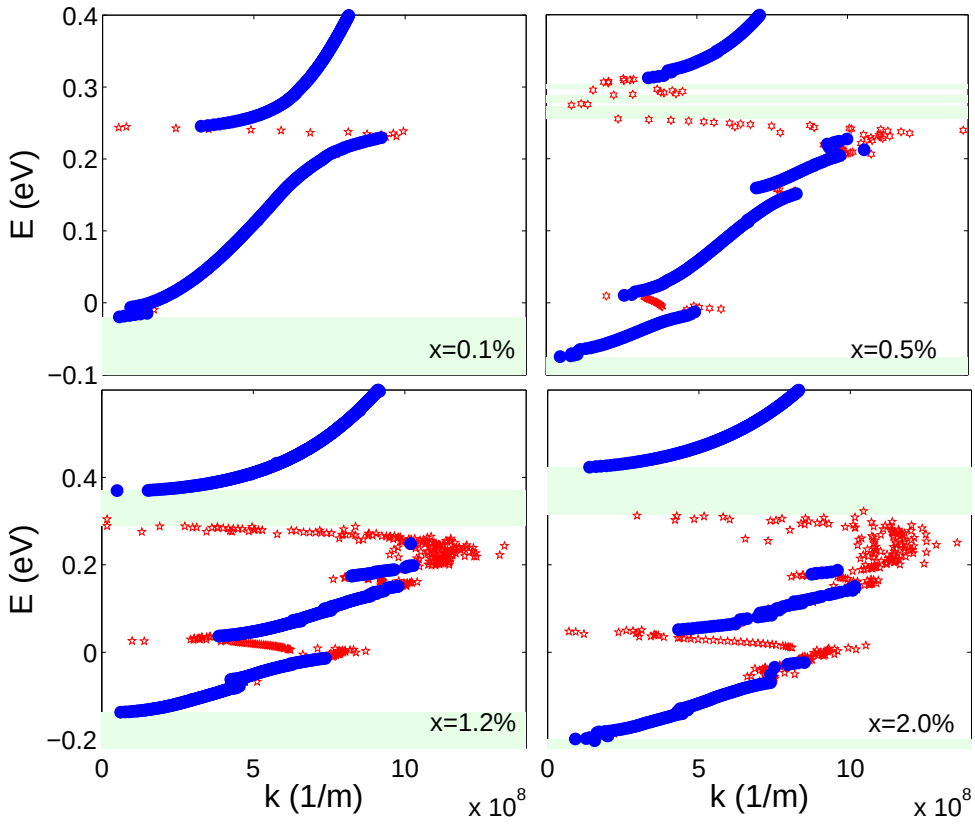

Figure B.2: The dispersion relation of GaN_xAs_{1-x} with $x = 0.1, 0.5, 1.2$ and 2.0% calculated by the SCGF approach using the full distribution of nitrogen localised states from the LCINS method (blue circles). The red stars show the values of E where $\gamma(\varepsilon)$ discontinuously crosses the positive real axis, but where no value of δ gives $\gamma(E + i\delta) = 0$. The green shaded areas show the energies, E, for which $\gamma(E + i\delta)$ does not cross the positive real axis.

pronounced for higher N concentration x.

Figure B.2 also shows that the upper sub-band (above isolated N states) does not start from $k = 0$, in contrast to the band dispersion predicted by the BAC model. As mentioned before this is because of the problem in stability of iterative search method to find $\Delta E_j(\varepsilon_p)$, and we can fix that by using the complex eigenvalue method as discussed in § 7.3.1.

Appendix C

Contribution of individual poles of G_{nn} to the density of states

If we apply the residue theorem to the full circular contour C' of radius R in the complex plane, we can obtain a sum rule for the residues of G_{nn} at its poles ε_p in the lower half-plane

$$2\pi i = \int_{C'} G_{nn}(E)\mathrm{d}E = 2\pi i \sum_p Res[\varepsilon_p], \tag{C.1}$$

where ε_p are the (complex) roots of the equation,

$$\varepsilon_p - E_n - \Delta E_n(\varepsilon_p) = 0, \tag{C.2}$$

and the residue is defined as

$$Res[\varepsilon_p] = \lim_{E\to\varepsilon_p} \frac{E-\varepsilon_p}{\varepsilon_p - E_n - \Delta E_n(\varepsilon_p)} = \left\{1 - \frac{\mathrm{d}\Delta E_n}{\mathrm{d}E}\bigg|_{E=\varepsilon_p}\right\}^{-1}. \tag{C.3}$$

Thus, we have a sum rule for the residues at the poles ε_p

$$1 = \sum_p Res[\varepsilon_p] = \sum_p \left\{1 - \frac{\mathrm{d}\Delta E_n}{\mathrm{d}E}\bigg|_{E=\varepsilon_p}\right\}^{-1}, \tag{C.4}$$

and the contribution of each pole ε_p of the Green's function to the integrated the density of states might naturally be taken to be

$$W_p = \Re\left\{1 - \frac{\mathrm{d}\Delta E_n}{\mathrm{d}E}\bigg|_{E=\varepsilon_p}\right\}^{-1}. \tag{C.5}$$

$$Res[\varepsilon_p] = (\frac{d\gamma}{dE})^{-1} \quad at \quad E = \varepsilon_p. \tag{C.6}$$

Then $\sum_p W_p = 1$. But, from Eq. (B.3), we have that

$$\frac{\mathrm{d}\varepsilon_p}{\mathrm{d}E_k}\frac{\mathrm{d}\gamma}{\mathrm{d}E}\Big|_{E=\varepsilon_p} = 1, \tag{C.7}$$

and therefore

$$Res[\varepsilon_p] = \frac{\mathrm{d}\varepsilon_p}{\mathrm{d}E_k}. \tag{C.8}$$

This is consistent with the contribution $\mathrm{d}\varepsilon_p/\mathrm{d}E_k$ of an exact eigenstate of energy E to the k-projected DOS. From Eq. (5.11), the derivative of $\gamma(E)$ with respect to energy is given by

$$\frac{d\gamma}{dE} = 1 - \frac{1}{N_c}\sum_j \frac{|V_j|^2}{[E - E_j - \Delta E_j(E)]^2}\left\{1 - \frac{\mathrm{d}\Delta E_j}{dE}\right\}. \tag{C.9}$$

From Eq. (C.7) we can calculate $\mathrm{d}\varepsilon_p/\mathrm{d}E_k$ as

$$\begin{aligned}
\Re\left[\frac{\mathrm{d}\varepsilon_p}{\mathrm{d}E_k}\right] &= \Re\left[\frac{\mathrm{d}\varepsilon_p}{\mathrm{d}\gamma(\varepsilon_p)}\right] = \Re\left[\left(\frac{\mathrm{d}\gamma(\varepsilon_p)}{\mathrm{d}\varepsilon_p}\right)^{-1}\right] \\
&= \Re\left[\left\{1 - \frac{1}{N_c}\sum_j \frac{|V_j|^2}{[\varepsilon_p - E_j - \Delta E_j(\varepsilon_p)]^2}\right. \right. \\
&\quad \left. \left. \times\left(1 - \frac{\mathrm{d}\Delta E_j(\varepsilon_p)}{d\varepsilon_p}\right)\right\}^{-1}\right].
\end{aligned} \tag{C.10}$$

Appendix D

The real and imaginary parts of $\gamma(E)$ and the decay rate of momentum states.

We have defined $\gamma(E)$ as

$$\gamma(\varepsilon) = \varepsilon - \frac{1}{N_c}\sum_j \frac{|V_j|^2}{\varepsilon - E_j - \Delta E_j(\varepsilon)}, \tag{D.1}$$

Having $\varepsilon = E + i\delta$ we can separate the real and imaginary parts of $\gamma(E)$ as

$$\begin{aligned}
& \gamma(E) = E + i\delta - \frac{1}{N_c} \\
\times \quad & \sum_j \frac{|V_j|^2}{\Big(E - E_j - \Re[\Delta E_j(\varepsilon)]\Big) + i\Big(\delta - \Im[\Delta E_j(\varepsilon)]\Big)} \\
= \quad & \left[E - \frac{1}{N_c}\sum_j \frac{|V_j|^2\Big(E - E_j - \Re[\Delta E_j(\varepsilon)]\Big)}{\Big|\varepsilon - E_j - \Delta E_j(\varepsilon)\Big|^2}\right] \\
+ \quad & i\left[\delta - \frac{1}{N_c}\sum_j \frac{|V_j|^2\Big(\Im[\Delta E_j(\varepsilon)] - \delta\Big)}{\Big|\varepsilon - E_j - \Delta E_j(\varepsilon)\Big|^2}\right].
\end{aligned} \tag{D.2}$$

At the poles ε_p, of Green's function, the imaginary part of $\gamma(\varepsilon_p)$ should be zero and its real part is equal to E_k, where

$$E_k = \Re[\varepsilon_p] - \frac{1}{N_c}\sum_j \frac{|V_j|^2\Big(\Re(\varepsilon_p) - E_j - \Re[\Delta E_j(\varepsilon_p)]\Big)}{\Big|\varepsilon_p - E_j - \Delta E_j(\varepsilon_p)\Big|^2}. \tag{D.3}$$

The derivative of this expression with respect to $\Re[\varepsilon_p]$ is

$$\begin{aligned}\frac{\mathrm{d}\Re[\gamma(\varepsilon_p)]}{\mathrm{d}\Re[\varepsilon_p]} &= \Re\left[\frac{\mathrm{d}\gamma}{\mathrm{d}E}\right]_{E=\varepsilon_p} \\ &= \Re\left[1+\frac{1}{Nc}\sum_j \frac{|V_j|^2\left\{1-\frac{\mathrm{d}\Delta E_j(\varepsilon_p)}{\mathrm{d}\varepsilon_p}\right\}}{\Big(\varepsilon_p - E_j - \Delta E_j(\varepsilon_p)\Big)^2}\right].\end{aligned} \tag{D.4}$$

The vanishing of the imaginary part of γ in Eq. (D.2) at ε_p gives

$$\Im[\varepsilon_p] = \frac{1}{N_c}\sum_j \frac{|V_j|^2\Big(\Im[\Delta E_j(\varepsilon_p)] - \Im(\varepsilon_p)\Big)}{\Big|\varepsilon_p - E_j - \Delta E_j(\varepsilon_p)\Big|^2}, \tag{D.5}$$

and, using Eq. A.7 for $W_{j,p}$, the imaginary part of ε_p can be written as

$$\Im[\varepsilon_p] = \sum_j \frac{W_{j,p}}{|\alpha_M|^2}\Big(\Im[\Delta E_j(\varepsilon_p)] - \Im(\varepsilon_p)\Big). \tag{D.6}$$

Rearranging, and using the fact that $|\alpha_M|^2 + \sum_j W_{j,p} = 1$ we have

$$\Im[\varepsilon_p] = \sum_j W_{j,p}\Im[\Delta E_j(\varepsilon_p)]. \tag{D.7}$$

Therefore, the decay rate from Eq. (7.24) can be written as

$$\begin{aligned}R(E) &= -\frac{2}{\hbar}\Im[\varepsilon_p] = -\frac{2}{\hbar}\sum_j W_{j,p}\Im[\Delta E_j(\varepsilon_p)] \\ &= \Re\left\{-\frac{2}{\hbar}\frac{1}{N_c}\sum_j \frac{|V_j|^2 f_\Gamma(\varepsilon_p)\Im[\Delta E_j(\varepsilon_p)]}{|\varepsilon_p - E_j - \Delta E_j(\varepsilon_p)|^2}\right\}.\end{aligned} \tag{D.8}$$

Also from Eqs. (5.3) and (5.15) we have

$$\Im[\Delta E_j(E)] = \frac{|V_j|^2}{N_c}\sum_k \Im[G_{kk}(E)] = -\frac{\pi|V_j|^2}{N_c}\frac{(2m^*)^{3/2}}{4\pi^2\hbar^3}\Re\Big[(\gamma(E))^{1/2}\Big], \tag{D.9}$$

where at the poles of Green's function it becomes

$$\Im[\Delta E_j(\varepsilon_p)] = -\frac{\pi|V_j|^2}{N_c}\frac{(2m^*)^{3/2}}{4\pi^2\hbar^3}E_k^{1/2} = -\frac{\pi|V_j|^2}{N_c}D_0(E_k), \tag{D.10}$$

where $D_0(E_k)$ is the DOS of the host semiconductor CB. Hence, Eq. (D.8) is given by

$$R(\varepsilon_p) = -\frac{2\pi}{\hbar}\sum_j \frac{1}{N_c}\frac{|V_j|^4}{|\varepsilon_p - E_j - \Delta E_j(\varepsilon_p)|^2}\frac{f_\Gamma D_0(E_k)}{N_c} \tag{D.11}$$

having in mind that the denominator in the brackets can be written in the form

$$\Big(\varepsilon_p - E_j - \Re[\Delta E_j(\varepsilon_p)]\Big)^2 + \Big(\Im(\varepsilon_p) - \Im[\Delta E_j(\varepsilon_p)]\Big)^2$$

Eq. (D.11) is equivalent to the expression that Fahy *et al.* [13] derived for the scattering rate as

$$R(E) = -\frac{2\pi}{\hbar}\sum_j \frac{1}{N_c}\frac{|V_j|^4}{|(E - E_j)^2 + (\Gamma/2)^2}\frac{f_\Gamma D(E_k)}{N_c} \tag{D.12}$$

where $D(E_k)$ was the DOS the CB of the GaAs was assumed to be parabolic. If we consider $E_j' = E_j + \Re[\Delta E_j(\varepsilon_p)]$, $\Gamma/2 = \Im(\varepsilon_p) - \Im[\Delta E_j(\varepsilon_p)]$ and taking DOS for a parabolic band.

D. The real and imaginary parts of $\gamma(E)$ and the decay rate of momentum states.

References

[1] I. Buyanova and W. Chen. *Physics and applications of dilute nitrides*, volume 21. CRC Press, 2004.

[2] M. Henini. *Dilute nitride semiconductors*. Elsevier Science, 2004.

[3] A. Erol. *Dilute III-V nitride semiconductors and material systems: physics and technology*. Springer Verlag, 2008.

[4] M. Weyers, M. Sato, and H. Ando. Red shift of photoluminescence and absorption in dilute GaAsN alloy layers. *Japanese Journal of Applied Physics*, 31(7A):L853–L855, 1992.

[5] M. Kondow, K. Uomi, A. Niwa, T. Kitatani, S. Watahiki, and Y. Yazawa. GaInNAs: a novel material for long-wavelength-range laser diodes with excellent high-temperature performance. *Japanese Journal of Applied Physics*, 35(part 1):1273–1275, 1996.

[6] E. P. O'Reilly, A. Lindsay, P. J. Klar, A. Polimeni, and M. Capizzi. Trends in the electronic structure of dilute nitride alloys. *Semiconductor Science and Technology*, 24:033001, 2009.

[7] X. Liu, M. E. Pistol, L. Samuelson, S. Schwetlick, and W. Seifert. Nitrogen pair luminescence in GaAs. *Applied Physics Letters*, 56(15):1451, 1990.

[8] D. J. Wolford, J. A. Bradley, K. Fry, and J. Thompson. -. *Proc. 17th Int. Conf. on the Physics of Semiconductors (New York: Springer)*, page 627, 1984.

[9] W. Shan, W. Walukiewicz, J. W. Ager, E. E. Haller, J. F. Geisz, D. J. Friedman, J. M. Olson, and S. R. Kurtz. Band Anticrossing in GaInNAs Alloys. *Physical Review Letters*, 82(6):1221–1224, Feb 1999.

[10] E. P. O'Reilly, A. Lindsay, S. Tomic, and M. Kamal-Saadi. Tight-binding and $k \cdot p$ models for the electronic structure of Ga(In)NAs and related alloys. *Semiconductor Science and Technology*, 17(8):870–879, 2002.

[11] A. Lindsay and E. P. O'Reilly. A tight-binding-based analysis of the band anti-crossing model in $GaAs_{1-x}N_x$. *Physica E: Low-dimensional Systems and Nanostructures*, 21(2-4):901–906, 2004.

[12] Y. Jin. *Influence of N incorporation on the electronic properties of dilute nitride (In) GaAsN alloys*. PhD thesis, University of Michigan, 2010.

[13] S. Fahy, A. Lindsay, H. Ouerdane, and E. P. O'Reilly. Alloy scattering of n-type carriers in $GaAs_{1-x}N_x$. *Physical Review B*, 74:035203, 2006.

[14] A. R. Adams. Band-structure engineering to control impact ionisation and related high-field processes. *Electronics Letters*, 40(17):1086–1088, 2004.

[15] A. Patanè, A. Ignatov, D. Fowler, O. Makarovsky, L. Eaves, L. Geelhaar, and H. Riechert. Hot-electrons and negative differential conductance in $GaAs_{1-x}N_x$. *Physical Review B*, 72(3):033312, Jul 2005.

[16] N. Vogiatzis and J. M. Rorison. Negative differential velocity in ultradilute $GaAs_{1-x}N_x$ alloys. *Journal of Applied Physics*, 109:083720, 2011.

[17] E. P. O'Reilly, A. Lindsay, and S. Fahy. Theory of the electronic structure of dilute nitride alloys. *Journal of Physics: Condensed Matter*, 16:S3257–S3276, 2004.

[18] J. Wu, W. Walukiewicz, and E. E. Haller. Band structure of highly mismatched semiconductor alloys: Coherent potential approximation. *Physical Review B*, 65(23):233210–1, 2002.

[19] A. Lindsay and E. P. O'Reilly. Theory of enhanced bandgap nonparabolicity in $GaAs_{1-x}N_x$ and related alloys. *Solid State Communications*, 112:443–447, 1999.

[20] S. Tomić, E. P. O'Reilly, P. J. Klar, H. Grüning, W. Heimbrodt, W. M. Chen, and I. A. Buyanova. Influence of conduction-band nonparabolicity on electron confinement and effective mass in GaN_xAs_{1-x}/GaAs quantum wells. *Physical Review B*, 69(24):245305, Jun 2004.

[21] S. B. Healy, A. Lindsay, and E. P. O'Reilly. Influence of N cluster states on band dispersion in GaInNAs quantum wells. *Physica E: Low-dimensional Systems and Nanostructures*, 32(1-2):249–253, 2006.

[22] A. Patanè, J. Endicott, J. Ibáñez, P. N. Brunkov, L. Eaves, S. B. Healy, A. Lindsay, E. P. O'Reilly, and M. Hopkinson. Breakup of the conduction band structure of dilute $GaAs_{1-x}N_x$ alloys. *Physical Review B*, 71(19):195307, May 2005.

[23] T. Dannecker, Y. Jin, H. Cheng, C. F. Gorman, J. Buckeridge, C. Uher, S. Fahy, C. Kurdak, and R. S. Goldman. Nitrogen composition dependence of electron effective mass in $GaAs_{1-x}N_x$. *Physical Review B*, 82(12):125203, Sep 2010.

[24] A. Lindsay and E. P. O'Reilly. Unification of the band anticrossing and cluster-state models of dilute nitride semiconductor alloys. *Physical Review Letters*, 93(19):196402, 2004.

[25] F. Masia, G. Pettinari, A. Polimeni, M. Felici, A. Miriametro, M. Capizzi, A. Lindsay, S. B. Healy, E. P. O'Reilly, A. Cristofoli, et al. Interaction between conduction band edge and nitrogen states probed by carrier effective-mass measurements in GaAs1-xNx. *Physical Review*, 73(78):073201, 2006.

[26] A. Polimeni, F. Masia, G. Pettinari, R. Trotta, M. Felici, M. Capizzi, A. Lindsay, E. P. O'Reilly, T. Niebling, W. Stolz, and P. J. Klar. Role of strain and properties of N clusters at the onset of the alloy limit in $GaAs_{1-x}N_x$. *Physical Review B*, 77(15):155213, Apr 2008.

[27] A. Polimeni, G. Pettinari, R. Trotta, F. Masia, M. Felici, M. Capizzi, A. Lindsay, E. P. O'Reilly, T. Niebling, W. Stolz, et al. Photoluminescence under magnetic field and hydrostatic pressure for probing the electronic properties of GaAsN. *Physica Status Solidi A*, 205(1):107–113, 2008.

[28] G. Pettinari, F. Masia, A. Polimeni, M. Felici, A. Frova, M. Capizzi, A. Lindsay, E. P. O'Reilly, P. J. Klar, W. Stolz, G. Bais, M. Piccin, S. Rubini, F. Martelli, and A. Franciosi. Influence of nitrogen-cluster states on the gyromagnetic factor of electrons in $GaAs_{1-x}N_x$. *Physical Review B*, 74(24):245202, Dec 2006.

[29] L. Ivanova, H. Eisele, M. P. Vaughan, Ph. Ebert, A. Lenz, R. Timm, O. Schumann, L. Geelhaar, M. Dähne, S. Fahy, H. Riechert, and E. P.

O'Reilly. Direct measurement and analysis of the conduction band density of states in diluted $GaAs_{1-x}N_x$ alloys. *Physical Review B*, 82(16):161201, Oct 2010.

[30] M. P. Vaughan. *Alloy and phonon scattering-limited electron mobility in dilute nitrides*. University of Essex , PhD Thesis, 2007.

[31] P. W. Anderson. Localized magnetic states in metals. *Physical Review*, 124(1):41–53, 1961.

[32] M. P. Vaughan and B. K. Ridley. Effect of non-parabolicity on the density of states for high-field mobility calculations in dilute nitrides. *Physica Status Solidi C*, 4(2):686–688, 2007.

[33] M. P. Vaughan. *Alloy and Phonon Scattering*. VDM Verlag, 2009.

[34] M. P. Vaughan and B. K. Ridley. Electron-nitrogen scattering in dilute nitrides. *Physical Review B*, 75(15):195205, 2007.

[35] N. Vogiatzis and J. M. Rorison. Density of states for dilute nitride systems: calculation of lifetime broadening. *Journal of Physics: Condensed Matter*, 21:255801, 2009.

[36] N. Vogiatzis and J. M. Rorison. Single impurity Anderson model and band anti-crossing in the $Ga_{1-x}In_xN_yAs_{1-y}$ material system. *Physica Status Solidi A*, 205(1):120–128, 2008.

[37] Y. G. Hong, C. W. Tu, and R. K. Ahrenkiel. Improving properties of GaInNAs with a short-period GaInAs/GaNAs superlattice. *Journal of Crystal Growth*, 227:536–540, 2001.

[38] S. R. Kurtz, A. A. Allerman, C. H. Seager, R. M. Sieg, and E. D. Jones. Minority carrier diffusion, defects, and localization in InGaAsN, with 2% nitrogen. *Applied Physics Letters*, 77(3):400–402, 2000.

[39] I. Suemune, K. Uesugi, and W. Walukiewicz. Role of nitrogen in the reduced temperature dependence of band-gap energy in GaNAs. *Applied Physics Letters*, 77(19):3021–3023, 2000.

[40] W. Li, M. Pessa, J. Toivonen, and H. Lipsanen. Doping and carrier transport in $Ga_{1-3x}In_{3x}N_xAs_{1-x}$ alloys. *Physical Review B*, 64(11):113308, 2001.

[41] C. Skierbiszewski. Experimental studies of the conduction-band structure of GaInNAs alloys. *Semiconductor Science and Technology*, 17(8):803, 2002.

[42] D. L. Young, J. F. Geisz, and T. J. Coutts. Nitrogen-induced decrease of the electron effective mass in GaAsN thin films measured by thermomagnetic transport phenomena. *Applied Physics Letters*, 82:1236, 2003.

[43] F. Ishikawa, G. Mussler, K. J. Friedland, H. Kostial, K. Hagenstein, L. Daweritz, and K. H. Ploog. Impact of N-induced potential fluctuations on the electron transport in Ga (As, N). *Applied Physics Letters*, 87(26):262112–262112, 2005.

[44] M. Reason, Y. Jin, H. A. McKay, N. Mangan, D. Mao, R. S. Goldman, X. Bai, and C. Kurdak. Influence of N on the electronic properties of GaAsN alloy films and heterostructures. *Journal of Applied Physics*, 102(10):103710–103710, 2007.

[45] S. Fahy and E. P. O'Reilly. Intrinsic limits on electron mobility in dilute nitride semiconductors. *Applied physics letters*, 83:3731, 2003.

[46] S. Fahy, A. Lindsay, and E. P. O'Reilly. Intrinsic limits on electron mobility in disordered dilute nitride semiconductor alloys. *IEE Proceedings-Optoelectronics*, 151(5):352–356, 2004.

[47] S. Fahy and E. P. O'Reilly. Theory of electron mobility in dilute nitride semiconductors. *Physica E: Low-dimensional Systems and Nanostructures*, 21(2-4):881–885, 2004.

[48] E. P. O'Reilly and M. Seifikar. *Theory of Electronic Transport in Nanostructures*, page 41. 2012.

[49] M. P. Vaughan and B. K. Ridley. Solution of the Boltzmann equation for calculating the Hall mobility in bulk GaN_xAs_{1-x}. *Physical Review B*, 72(7):075211, August 2005.

[50] K. Volz, J. Koch, B. Kunert, and W. Stolz. Doping behaviour of Si, Te, Zn and Mg in lattice-matched (GaIn)(NAs)/GaAs bulk films. *Journal of Crystal Growth*, 248:451–456, 2003.

[51] P. R. C. Kent and A. Zunger. Theory of electronic structure evolution in GaAsN and GaPN alloys. *Physical Review B*, 64:115208, Aug 2001.

[52] J. S. Nga, S. L. Tan, Y. L. Goh, C. H. Tan, J. P. R. David, J. Allam, S. J. Sweeney, and A. R. Adams. InGaAsN as absorber in APDs for 1.3 micron wavelength applications. In *Indium Phosphide & Related Materials (IPRM), 2010 International Conference on*, pages 1–4. IEEE, 2010.

[53] D. Fowler, O. Makarovsky, A. Patanè, L. Eaves, L. Geelhaar, H. Reichert, and K. Uesugi. Electrical conduction properties of Ga (AsN) layers. In *AIP Conference Proceedings*, volume 772, page 497, 2005.

[54] G. Allison, S. Spasov, A. Patanè, L. Eaves, A. Ignatov, D. K. Maude, M. Hopkinson, and R. Airey. Magnetophonon oscillations in the negative differential conductance of dilute nitride $GaAs_{1-x}N_x$ submicron diodes. *Physical Review B*, 75(73):115325, 2007.

[55] A. Patanè, G. Allison, L. Eaves, M. Hopkinson, G. Hill, and A. Ignatov. Tailoring the electrical conductivity of GaAs by nitrogen incorporation. *Journal of Physics: Condensed Matter*, 21:174209, 2009.

[56] B. K. Ridley. *Quantum processes in semiconductors*. Clarendon Press in UK, 1999.

[57] Y. Sun, M. P. Vaughan, A. Agarwal, M. Yilmaz, B. Ulug, A. Ulug, N. Balkan, M. Sopanen, O. Reentilä, M. Mattila, et al. Inhibition of negative differential resistance in modulation-doped n-type $Ga_xIn_{1-x}N_yAs_{1-y}$/GaAs quantum wells. *Physical Review B*, 75(20):205316, 2007.

[58] N. Vogiatzis and J. M. Rorison. Electron transport in bulk GaAsN. *Physica Status Solidi B*, 248:1183–1186, 2011.

[59] U. Fano. Effects of configuration interaction on intensities and phase shifts. *Physical Review*, 124(6):1866–1878, Dec 1961.

[60] M. Seifikar, E. P. O'Reilly, and S. Fahy. Analysis of band-anticrossing model in GaNAs near localised states. *Physica Status Solidi B*, 248:1176–1179, 2011.

[61] P. J. Klar, H. Gruning, W. Heimbrodt, J. Koch, F. Hohnsdorf, W. Stolz, P. M. A. Vicente, and J. Camassel. From N isoelectronic impurities to N-induced bands in the GaN_xAs_{1-x} alloy. *Applied Physics Letters*, 76(23):3439–3441, jun 2000.

[62] P. J. Klar, H. Grüning, W. Heimbrodt, G. Weiser, J. Koch, K. Volz, W. Stolz, S. W. Koch, S. Tomić, S. A. Choulis, et al. Interband transitions of quantum wells and device structures containing Ga (N, As) and (Ga, In)(N, As). *Semiconductor Science and Technology*, 17(8):830, 2002.

[63] P. R. C. Kent, L. Bellaiche, and A. Zunger. Pseudopotential theory of dilute III–V nitrides. *Semiconductor Science and Technology*, 17(8):851, 2002.

[64] R. J. Bell and P. Dean. Atomic vibrations in vitreous silica. *Discuss. Faraday Soc.*, 50:55–61, 1970.

[65] B. Lee and L. W. Wang. Band gap bowing and electron localization of $Ga_xIn_{1-x}N$. *Journal of Applied Physics*, 100(9):093717–093717, 2006.

[66] M. Seifikar, E. P. O'Reilly, and S. Fahy. Theory of intermediate- and high-field mobility in dilute nitride alloys. *Physical Review B*, 84:165216, Oct 2011.

[67] A. Lindsay and E. P. O'Reilly. Influence of nitrogen resonant states on the electronic structure of GaN_xAs_{1-x}. *Solid State Communications*, 118(6):313–317, 2001.

[68] O. F. Sankey, J. D. Dow, and K. Hess. Theory of resonant scattering in semiconductors due to impurity central-cell potentials. *Applied Physics Letters*, 41(7):664–666, 1982.

[69] D. E. Aspnes. GaAs lower conduction-band minima: Ordering and properties. *Physical Review B*, 14(12):5331–5343, Dec 1976.

[70] D. E. Aspnes, C. G. Olson, and D. W. Lynch. Ordering and Absolute Energies of the L_6^c and X_6^c Conduction Band Minima in GaAs. *Physical Review Letters*, 37(12):766–769, Sep 1976.

[71] E. M. Conwell and M. O. Vassell. High-Field Transport in n-Type GaAs. *Physical Review*, 166(3):797–821, 1968.

[72] E. M. Conwell and M. O. Vassell. High-field distribution function in GaAs. *IEEE Transactions on Electron Devices*, 13(1):22–27, 1966.

[73] Th. Vogelsang and W. Hansch. The electron high-energy distribution function: A comparison of analytical models with Monte Carlo calculations. *Journal of Applied Physics*, 69(6):3592–3595, 1991.

[74] W. Fawcett, A. D. Boardman, and S. Swain. Monte Carlo determination of electron transport properties in gallium arsenide. *Journal of Physics and Chemistry of Solids*, 31(9):1963–1990, 1970.

[75] G. A. Baraff. Maximum anisotropy approximation for calculating electron distributions; application to high field transport in semiconductors. *Physical Review*, 133(1A):A26–A33, Jan 1964.

[76] M. Lundstrom. *Fundamentals of carrier transport*. Cambridge University Press, USA, 2000.

[77] M. A. Littlejohn, J. R. Hauser, and T. H. Glisson. Velocity-field characteristics of GaAs with Γ_6^c-L_6^c-X_6^c conduction-band ordering. *Journal of Applied Physics*, 48(71):9 – 11, 1977.

[78] D. Rakoczy, G. Strasser, C. Strahberger, and J. Smoliner. L-valley electron transport in GaAs-AlAs double-barrier resonant tunneling structures studied by ballistic electron emission microscopy. *Physical Review B*, 66(3):33309, 2002.

[79] J. S. Blakemore. Semiconducting and other major properties of gallium arsenide. *Journal of Applied Physics*, 53(72):123 – 159, 1981.

[80] N. Cavassilas, F. Aniel, G. Fishman, and R. Adde. Full-band matrix solution of the Boltzmann transport equation and electron impact ionization in GaAs. *Solid-State Electronics*, 46(4):559–566, 2002.

[81] M. V. Fischetti and S. E. Laux. Monte carlo analysis of electron transport in small semiconductor devices including band-structure and space-charge effects. *Physical Review B*, 38(14):9721–9745, Nov 1988.

[82] J. G. Ruch and G. S. Kino. Transport Properties of GaAs. *Physical Review*, 174(3):921–931, Oct 1968.

[83] J. W. Ager III and W. Walukiewicz. Current status of research and development of III–N–V semiconductor alloys. *Semiconductor Science and Technology*, 17:741, 2002.

[84] E. N. Economou. *Green's Functions in Quantum Physics*. Berlin, Heidelberg: Springer-Verlag Berlin Heidelberg, 3rd edition, 2006.

[85] D. Fowler, O. Makarovsky, A. Patanè, L. Eaves, L. Geelhaar, and H. Riechert. Electron conduction in two-dimensional $GaAs_{1-y}N_y$ channels. *Physical Review B*, 69:153305, Apr 2004.

[86] G. Lasher and F. Stern. Spontaneous and stimulated recombination radiation in semiconductors. *Physical Review*, 133(2A):A553–A563, 1964.

[87] C. Ghezzi, R. Magnanini, A. Parisini, B. Rotelli, L. Tarricone, A. Bosacchi, and S. Franchi. Optical absorption near the fundamental absorption edge in GaSb. *Physical Review B*, 52(3):1463, 1995.

[88] W. Sritrakool, V. Sa-Yakanit, and H. R. Glyde. Absorption near band edges in heavily doped GaAs. *Physical Review B*, 32(2):1090, 1985.

[89] D. M. Eagles. Optical absorption and recombination radiation in semiconductors due to transitions between hydrogen-like acceptor impurity levels and the conduction band. *Journal of Physics and Chemistry of Solids*, 16(1):76–83, 1960.

[90] J. S. Blakemore. Semiconducting and other major properties of gallium arsenide. *Journal of Applied Physics*, 53(1):0, 1982.

[91] J. S. Blakemore. *Gallium arsenide*, volume 1. Springer, 1961.

[92] I. Vurgaftman, J. R. Meyer, and L. R. Ram-Mohan. Band parameters for III-V compound semiconductors and their alloys. *Journal of Applied Physics*, 89(11), 2001.

[93] L. C. L. Y. Voon and M. Willatzen. *The kp method*. Springer, 2009.

[94] S. L. Chuang et al. *Physics of optoelectronic devices*. Wiley New York, 1995.

[95] P. Perlin, S. G. Subramanya, D. E. Mars, J. Kruger, N. A. Shapiro, H. Siegle, and E. R. Weber. Pressure and temperature dependence of the absorption edge of a thick GaInAsN layer. *Applied Physics Letters*, 73:3703, 1998.

[96] P. Perlin, P. Wisniewski, C. Skierbiszewski, T. Suski, E. Kaminska, S. G. Subramanya, E. R. Weber, D. E. Mars, and W. Walukiewicz. Interband optical absorption in free standing layer of $Ga_{0.96}In_{0.04}As_{0.99}N_{0.01}$. *Applied Physics Letters*, 76:1279, 2000.

[97] C. Skierbiszewski, P. Perlin, P. Wisniewski, W. Knap, T. Suski, W. Walukiewicz, W. Shan, K. M. Yu, J. W. Ager, and E. E Haller. Large, nitrogen-induced increase of the electron effective mass in $In_yGa_{1-y}N_xAs_{1-x}$. *Applied Physics Letters*, 76(17), 2000.

[98] C. Skierbiszewski, P. Perlin, P. Wisniewski, T. Suski, J. F. Geisz, K. Hingerl, W. Jantsch, D. E. Mars, and W. Walukiewicz. Band structure and optical properties of $In_yGa_{1-y}N_xAs_{1-x}$ alloys. *Physical Review B*, 65(3):035207, 2001.

[99] H. C. Casey and F. Stern. Concentration-dependent absorption and spontaneous emission of heavily doped GaAs. *Journal of Applied Physics*, 47(2):631–643, 1976.

[100] S. Turcotte, J-N. Beaudry, R. A. Masut, P. Desjardins, G. Bentoumi, and R. Leonelli. Experimental investigation of the variation of the absorption coefficient with nitrogen content in GaAsN and GaInAsN grown on GaAs (001). *Journal of Applied Physics*, 104(8):083511–083511, 2008.

[101] S. Turcotte, S. Larouche, J-N. Beaudry, L. Martinu, R. A. Masut, P. Desjardins, and R. Leonelli. Evidence of valence band perturbations in GaAsN/GaAs (001): Combined variable-angle spectroscopic ellipsometry and modulated photoreflectance investigation. *Physical Review B*, 80(8):085203, 2009.

[102] T. D. Veal, L. F. J. Piper, S. Jollands, B. R. Bennett, P. H. Jefferson, P. A. Thomas, C. F. McConville, B. N. Murdin, L. Buckle, G. W. Smith, et al. Band gap reduction in GaNSb alloys due to the anion mismatch. *Applied Physics Letters*, 87(13):132101–132101, 2005.

[103] A. Lindsay, E. P. O'Reilly, A. D. Andreev, and T. Ashley. Theory of conduction band structure of InN_xSb_{1-x} and GaN_xSb_{1-x} dilute nitride alloys. *Physical Review B*, 77(16):165205, 2008.

[104] P. H. Jefferson, T. D. Veal, L. F. J. Piper, B. R. Bennett, C. F. McConville, B. N. Murdin, L. Buckle, G. W. Smith, and T. Ashley. Band anticrossing in GaN_xSb_{1-x}. *Applied Physics Letters*, 89(11):111921–111921, 2006.

[105] A. Belabbes, M. Ferhat, and A. Zaoui. Giant and composition-dependent optical band gap bowing in dilute $GaSb_{1-x}N_x$ alloys. *Applied physics letters*, 88(15):152109–152109, 2006.

[106] J. J. Mudd, N. J. Kybert, W. M. Linhart, L. Buckle, T. Ashley, P. D. C. King, S. Jones, T, M. J. Ashwin, and T. D. Veal. Optical absorption by dilute GaNSb alloys: Influence of N pair states. *Applied Physics Letters*, 103:042110, 2013.

[107] D. Wang, S. P. Svensson, L. Shterengas, G. Belenky, C. S. Kim, I. Vurgaftman, and J. R. Meyer. Band edge optical transitions in dilute-nitride gansb. *Journal of Applied Physics*, 105(1):014904–014904, 2009.